GEMS & GEMOLOGY

SPRING 2017
VOLUME LIII

THE QUARTERLY JOURNAL OF THE GEMOLOGICAL INSTITUTE OF AMERICA

Brazilian Diamonds: Past and Present

Cuprian Liddicoatite

Silicon's Role in the Color of Corundum

2017 Tucson Report

Editorial Staff

Editor-in-Chief
Duncan Pay
dpay@gia.edu

Managing Editor
Stuart D. Overlin
soverlin@gia.edu

Editor
Jennifer-Lynn Archuleta
jennifer.archuleta@gia.edu

Technical Editors
Tao Z. Hsu
tao.hsu@gia.edu

Jennifer Stone-Sundberg

Editors, Lab Notes
Thomas M. Moses
Shane F. McClure

Editors, Micro-World
Nathan Renfro
Elise A. Skalwold
John I. Koivula

Editors, Gem News
Emmanuel Fritsch
Gagan Choudhary
Christopher M. Breeding

Editorial Assistants
Brooke Goedert
Erin Hogarth

Contributing Editors
James E. Shigley
Andy Lucas
Donna Beaton

Editor-in-Chief Emeritus
Alice S. Keller

Customer Service
Martha Erickson
(760) 603-4502
gandg@gia.edu

Production Staff

Creative Director
Faizah Bhatti

Image Specialist
Eric Welch

Illustrator
Peter Johnston

Photographers
Robert Weldon
Kevin Schumacher

Video Production
Pedro Padua
Nancy Powers
Betsy Winans

Production Specialist
Juan Zanahuria

Multimedia Specialist
Lynn Nguyen

Editorial Review Board

Ahmadjan Abduriyim
Tokyo, Japan

Timothy Adams
San Diego, California

Edward W. Boehm
Chattanooga, Tennessee

James E. Butler
Washington, DC

Alan T. Collins
London, UK

John L. Emmett
Brush Prairie, Washington

Emmanuel Fritsch
Nantes, France

Eloïse Gaillou
Paris, France

Gaston Giuliani
Nancy, France

Jaroslav Hyršl
Prague, Czech Republic

A.J.A. (Bram) Janse
Perth, Australia

E. Alan Jobbins
Caterham, UK

Mary L. Johnson
San Diego, California

Anthony R. Kampf
Los Angeles, California

Robert E. Kane
Helena, Montana

Stefanos Karampelas
Basel, Switzerland

Lore Kiefert
Lucerne, Switzerland

Ren Lu
Wuhan, China

Thomas M. Moses
New York, New York

Aaron Palke
Brisbane, Australia

Nathan Renfro
Carlsbad, California

Benjamin Rondeau
Nantes, France

George R. Rossman
Pasadena, California

Andy Shen
Wuhan, China

Guanghai Shi
Beijing, China

James E. Shigley
Carlsbad, California

Elisabeth Strack
Hamburg, Germany

Fanus Viljoen
Johannesburg, South Africa

Wuyi Wang
New York, New York

Christopher M. Welbourn
Reading, UK

GEMS & GEMOLOGY®

gia.edu/gems-gemology

Subscriptions
Copies of the current issue may be purchased for $29.95 plus shipping. Subscriptions are $79.99 for one year (4 issues) in the U.S. and $99.99 elsewhere. Canadian subscribers should add GST. Discounts are available for group subscriptions, GIA alumni, and current GIA students. To purchase print subscriptions, visit store.gia.edu or contact Customer Service. For institutional rates, contact Customer Service.

Database Coverage
G&G is abstracted in Thomson Reuters products (Current Contents: Physical, Chemical & Earth Sciences and Science Citation Index—Expanded, including the Web of Knowledge) and other databases. For a complete list of sources abstracting *G&G*, go to gia.edu/gems-gemology, and click on "Publication Information."

Manuscript Submissions
Gems & Gemology, a peer-reviewed journal, welcomes the submission of articles on all aspects of the field. Please see the Author Guidelines at gia.edu/gems-gemology or contact the Managing Editor. Letters on articles published in *G&G* are also welcome. Please note that Field Reports, Lab Notes, Gem News International, Micro-World, and Charts are not peer-reviewed sections but do undergo technical and editorial review.

Copyright and Reprint Permission
Abstracting is permitted with credit to the source. Libraries are permitted to photocopy beyond the limits of U.S. copyright law for private use of patrons. Instructors are permitted to reproduce isolated articles and photographs/images owned by *G&G* for noncommercial classroom use without fee. Use of photographs/images under copyright by external parties is prohibited without the express permission of the photographer or owner of the image, as listed in the credits. For other copying, reprint, or republication permission, please contact the Managing Editor.

Gems & Gemology is published quarterly by the Gemological Institute of America, a nonprofit educational organization for the gem and jewelry industry.

Postmaster: Return undeliverable copies of *Gems & Gemology* to GIA, The Robert Mouawad Campus, 5345 Armada Drive, Carlsbad, CA 92008.

Our Canadian goods and service registration number is 126142892RT.

Any opinions expressed in signed articles are understood to be opinions of the authors and not of the publisher.

About the Cover

The lead article of this issue covers Brazilian diamond production,which reached its peak in the late 1700s. Our cover shows a brooch dating back to the mid-19th century. This piece contains a 0.77 ct natural Fancy Light pink antique pear-shaped diamond set in darkly patinated silver ribbons over gold. The total weight of the diamonds exceeds 5.20 carats. Photo by Robert Weldon/GIA, courtesy of Lang Antique & Estate Jewelry.

Printing is by L+L Printers, Carlsbad, CA.
GIA World Headquarters The Robert Mouawad Campus 5345 Armada Drive Carlsbad, CA 92008 USA
© 2017 Gemological Institute of America All rights reserved.
ISSN 0016-626X

FSC
www.fsc.org
MIX
Paper from responsible sources
FSC® C006300

GEMS & GEMOLOGY

Spring 2017
VOLUME 53, No. 1


pg. 3


pg. 49


pg. 83

EDITORIAL

FEATURE ARTICLES

NOTES AND NEW TECHNIQUES

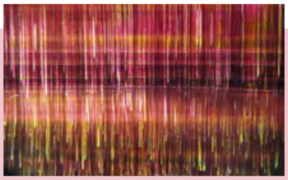
pg. 106


pg. 132

REGULAR FEATURES

Brazil's Enigmatic Diamonds, Cuprian Liddicoatite, and Silicon in Corundum

Welcome to the first *Gems & Gemology* of 2017! This is an unusually diverse issue, combining Brazilian diamonds, cuprian liddicoatite tourmaline, Japanese jadeite, iris quartz, synthetic zincite, and a short but important contribution on the fundamental role of the element silicon in generating blue color in many fine sapphires.

> *"The original geologic sources of Brazil's most valuable diamonds remain elusive..."*

In our lead article, authors Darcy Svisero, James Shigley, and Robert Weldon survey Brazil's diamond deposits. This region has produced a significant number of large rough diamonds. It's also a source of valuable colored diamonds from predominantly alluvial deposits, but today's diamond production is small and the original geologic sources remain mostly elusive. Although economically viable kimberlite pipes have been discovered in recent years, the outlook for increased production appears challenging.

Most researchers assume the bulk of copper-bearing tourmaline on the market today is elbaite, but some is undoubtedly another tourmaline species: liddicoatite. Yusuke Katsurada and Ziyin Sun report on the chemistry of copper-bearing liddicoatite tourmaline submitted to GIA's Tokyo laboratory. Their study shows elevated gallium and lead content in cuprian liddicoatite, which displays stronger fluorescence under long-wave ultraviolet light than cuprian elbaite due to high concentration of rare earth elements.

In our third paper, John Emmett, Jennifer Stone-Sundberg, Yunbin Guan, and Ziyin Sun discuss the critical role of silicon in the color of gem-quality corundum. Although the effect of trace elements such as iron, titanium, and magnesium within the corundum lattice is well understood, the chemical interaction of these trace elements is not widely appreciated. The authors demonstrate that silicon's presence is vital to the process that allows titanium to pair with iron and create blue color in sapphire. To the best of the authors' knowledge, this topic has not been addressed in the gemological literature.

Our next paper, by Ahmadjan Abduriyim, Kazuko Saruwatari, and Yusuke Katsurada, covers the history and characteristics of Japanese jadeite and compares this highly valued gem with jadeite from other sources. Their study examines the chemical composition and chromophores of jadeite varieties from the Itoigawa and Omi regions of Niigata Prefecture and the Wakasa region of Tottori Prefecture and compares them with samples from Myanmar, Guatemala, and Russia.

Next, Xiayang Lin and Peter Heaney analyze iris quartz crystals from geodes in the Deccan Trap basalts of west-central India using scanning and transmission electron microscopy and atomic force microscopy. Their investigation reveals that certain crystal faces exhibit etching, which acts as a diffraction grating to produce iridescence.

Our final paper, by Ji Zhang, Yujie Gao, and Guanghai Shi, provides a gemological characterization of an intriguing industrial by-product: gem-quality synthetic zincite from foundries in Poland.

Be sure to investigate our three regular sections: Lab Notes documents GIA staff gemologists' most recent findings, Micro-World reveals fascinating gemstone inclusions, and this issue's Gem News International reports on the 2017 Tucson gem shows, including an important update on Ethiopian emerald.

We offer congratulations to the winners of our 2016 Dr. Edward J. Gübelin Most Valuable Article Award (p. 109), and thank all of the readers who voted. Don't forget to take this year's *G&G* Challenge (pp. 110–111), our annual multiple-choice quiz. Thank you for all your support through 2016!

Duncan Pay | Editor-in-Chief | dpay@gia.edu

BRAZILIAN DIAMONDS: A HISTORICAL AND RECENT PERSPECTIVE

Darcy P. Svisero, James E. Shigley, and Robert Weldon

Brazil, which commanded global production in the 1700s and early 1800s, has remained a continuous source of diamonds for three centuries. Even though the country represented less than 1% of world production in 2015, a number of large famous diamonds, as well as fancy-color diamonds, have originated there. The sources are primarily alluvial, with diamonds transported by and deposited along a multitude of rivers. The diamonds are found mainly by independent miners (*garimpeiros)* in riverbeds, in unconsolidated sediments, and in compacted sedimentary conglomerates. After a century of exploration for the primary sources, some economically viable kimberlite pipes have been discovered in recent years, with one occurrence now being developed for mining. This article traces the country's fascinating diamond history before focusing on the geologic setting of the diamond occurrences, as well as the challenges and future outlook for production. The locations of the secondary deposits, principally in the states of Minas Gerais and Mato Grosso, are presented.

While Brazil is widely known for the production of colored gemstones, it is often not recognized as a source of gem diamonds (figure 1). Yet diamonds were discovered in the early 1700s by artisanal miners looking for gold along the banks of the Jequitinhonha River near the village of Arraial do Tijuco (later named Diamantina) in the state of Minas Gerais (Calógeras, 1904; Leonardos, 1959; Barbosa, 1991; Cornejo and Bartorelli, 2010). For the next 150 years, Minas Gerais was the world's major supplier of gem diamonds. Beginning in the early 1840s, unusual polycrystalline black diamonds (or carbonados) were also recovered, mainly from the state of Bahia (Karfunkel et al., 1994).

As Africa emerged as the major diamond source in the 1870s, Brazilian mining decreased dramatically within a decade, principally because of the low grade of the alluvial deposits. According to Kimberley Process statistics, Brazil produced 31,825 carats in 2015, although this figure is likely a low estimate considering the lack of accurate reporting there. Despite its low output relative to other sources, Brazil has produced a significant number of large rough diamonds (Svisero, 1995; Hoover and Karfunkel, 2009; also see table 1). The geologic explanation for this abundance of large crystals is not yet clear. Highly valued colored diamonds are also found, including yellows and occasionally greens, pinks, and reds.

In Brief

- For approximately 150 years between the early 1700s to the 1870s, Brazil was the world's most productive diamond source.
- Although it accounts for less than 1% of global production today, Brazil has yielded a number of large diamonds as well as fancy-color and superdeep diamonds and carbonado.
- Due to the absence of obvious primary sources, the geologic origin of these diamonds remains elusive.
- Production is expected to increase significantly with large-scale kimberlite mining in Bahia State.

In most countries, diamonds are usually recovered from primary kimberlite pipes of volcanic origin. Brazilian diamonds, however, occur in secondary deposits over large watersheds or sedimentary rock for-

---

See end of article for About the Authors and Acknowledgments.

Gems & Gemology, Vol. 53, No. 1, pp. 2–33,
http://dx.doi.org/10.5741/GEMS.53.1.2

Figure 1. The Portuguese Placa dos Três Militares, *or Badge of the Three Military Orders, was made in 1789, and is now part of the crown jewelry collection of the Ajuda National Palace in Lisbon. The badge consists of Brazilian diamonds as well as emeralds and rubies, and it is designed in a way to conceal the metal mounting and emphasize the gems. Photo by Manuel Silveira Ramos, courtesy of the Ajuda National Palace.*

mations. The diamonds are recovered by artisanal miners called *garimpeiros*, using simple tools and operating individually or in small groups. The diamonds are found as loose crystals obtained either by panning or dredging in the rivers, or by washing and/or breaking down the sediments that contain them (figure 2). Kimberlite bodies have been found in Brazil, but only one in Bahia is now being mined. Despite extensive exploration, none of the known kimberlites seems to account for Brazil's abundance of alluvial diamonds. The long history of diamond production in the country, combined with the absence of obvious primary sources, has led to various theories on the geologic origin of these diamonds (see Chaves et al., 2001). This article will review the history of diamonds in Brazil, the locations and geologic settings of the principal diamond deposits, and the mining methods used to recover them.

BACKGROUND

The first European explorers to reach the New World in the late 1400s were focused on finding spices and gold rather than diamonds. The Italian explorer and navigator Christopher Columbus set sail under the Spanish flag in 1492 in search of a more direct route to the "Indies," the region of the Indian subcontinent and eastern Africa that was rich in spices, gemstones, pearls, and gold (Fernandez-Armesto, 2009). After a five-week westward voyage, Columbus discovered an island in the Caribbean and called it San Salvador. Portugal and Spain, the global powers of the day, understood that to avoid future confrontation, they had to subdivide the recently discovered lands in the New World. The Treaty of Tordesilhas, drawn up by Pope Alexander VI and signed by the two empires in 1494, drew a meridian that would effectively divide South America (which had yet to be discovered by Euro-

Figure 2. This selection of diamonds recovered from the Abaeté River in Minas Gerais, weighing a total of 77.82 carats, is typical of the material being found today in Brazil's alluvial deposits. Photo by Robert Weldon/GIA, courtesy of Giovani de Deus Borges.

peans) from north to south (figure 3). Spain would receive the lands west of the meridian, including modern-day Venezuela, Colombia, Ecuador, and Peru, while Portugal gained the eastern side. On his third trip to the New World in 1498, Columbus discovered the mouth of the Orinoco River in what is today Venezuela. Here was the key to reaching a vast continental interior concealed in the jungles behind the Atlantic coastline.

To open a new trade route to India that did not require passing through the Mediterranean, Portuguese nobleman Pedro Álvares Cabral was dispatched in early 1500 with a fleet of ships. His mission was to reach India by traveling south around the tip of Africa. His fleet landed instead on the coast of Brazil, which he claimed for Portugal on April 22 of that year. The voyages of Amerigo Vespucci, the Florentine navigator after whom the continent is named, took place around the same time. As he sailed south along the Brazilian coast, Vespucci realized that the continent was much larger than previously recognized. These expeditions were the first to bring back

Figure 3. The 1494 Treaty of Tordesilhas effectively divided the South America continent between Portugal and Spain. The Cantino planisphere map, produced around 1502, shows the north-south Tordesilhas meridian line passing through South America, whose geography was still largely unknown. Courtesy of Biblioteca Estense.

Figure 4. Ouro Preto, once the settlement of Vila Rica in Minas Gerais, was the site of Brazil's first significant gold discovery, in 1695. This attracted explorers and fortune-seekers to Brazil. Over the next three centuries diamonds and other gem minerals were found throughout the region. Photo by Robert Weldon/GIA.

shipments to Portugal of *pau brasil* (Brazilwood), a tree sought after not only for timber but for a desirable red dye (Reid, 2014). Over the next two centuries, more European adventurers came to South America, most of them seeking riches in the form of gold, silver, and emeralds.

Between 1534 and 1536, King John III of Portugal divided the coastal regions of Brazil into 15 captaincy colonies to encourage development; these areas were given to Portuguese noblemen to administer and explore. Within a few years, most of these captaincies failed for a number of reasons. With this setback as well as the presence of French ships along the coast, the Portuguese crown decided to turn Brazil into a royal enterprise in 1549. Several successive governors-general were appointed to administer the colony, which was divided in 1621 into the states of Maranhão (in the north) and Brazil (in the south).

The exploration of Brazil's vast interior was left to Portuguese adventurers, known as *bandeirantes* (flag bearers), who claimed territories for Portugal and the Catholic Church. While Spanish conquests in the New World met resistance from powerful empires—the Aztecs in Mexico and the Incas in Peru—the Portuguese were confronted with numerous small native tribes and a forbidding interior.

Exploration and conquest on both sides of the Tordesilhas meridian would soon rewrite the gemological texts of the time. For example, Spanish exploitation of emeralds in the territory of New Granada (modern-day Colombia) would vastly change the world's understanding and appreciation for the gem, particularly in Europe (Weldon and Jonathan, 2013). Brazil would emerge as a major source for dozens of colorful gem species. It would also become, for a period, the world's most prolific source of diamonds (Cornejo and Bartorelli, 2010).

PORTUGUESE EXPLORERS

Much of the early exploration and colonization of Brazil was undertaken by the bandeirantes. The *bandeiras*, funded by the crown and the Catholic Church, were large quasi-military expeditions comprised of hundreds of free men and slaves who ventured into the interior, capturing and enslaving indigenous groups they encountered (de Galvão Bueno, 1922). Along with a Jesuit priest, explorer Francisco Bruzo Espinoza mounted the first bandeira in 1554, in search of emerald. It was a short-lived and fruitless expedition. Successive expeditions also failed, though in 1572 Sebastião Fernandes Tourinho found green and blue gems (likely tourmaline) along the tributaries of the Jequitinhonha and Doce Rivers in what is now Minas Gerais. The success of Tourinho's discoveries attracted more adventurers (Draper, 1950a).

In 1695, at Rio das Velhas, Manuel Borba Gato finally discovered gold, triggering a rush that would lead to the settlement of Vila Rica (later Ouro Preto) in 1698 (figure 4). The town played a leading role in Brazilian history for the next two centuries as the capital of Minas Gerais from 1720 to 1897 (Dodge, 1922). Settlements at Mariana, São Bento, Serro Frio, and Arraial do Tijuco soon followed the gold discoveries in those areas of Minas Gerais, and dozens more sprang up in Brazil's interior. The north-south road

TABLE 1. The largest rough diamond and carbonado discoveries in Brazil.[a]

Name	Weight[b] (ct)	Year	Location[c]
Diamond			
Presidente Vargas	726.6	1938	Santo Antônio do Bonito River, MG
Unnamed	657	1936	Santo Inácio River, MG
Unnamed	630	1938	Santo Inácio River, MG
Santo Antônio	602	1994	Santo Antônio do Bonito River, MG
Goiás	600 (?)	1906	Veríssimo River, GO
Darcy Vargas	460	1939	Santo Antônio do Bonito River, MG
Charneca I	428	1940	Santo Inácio River, MG
Presidente Dutra	407.7	1949	Dourados River, MG
Coromandel VI	400.6	1940	Santo Inácio River, MG
Diário de Minas	375.1	1941	Santo Antônio do Bonito River, MG
Vitória I	375	1945	Abaeté River, MG
Tiros I	354	1940	Abaeté River, MG
Bonito I	346	1948	Santo Antônio do Bonito River, MG
Vitória II	328.3	1943	Abaeté River, MG
Unnamed	328	Unknown	Santo Antônio do Bonito River, MG
Patos	324	1937	São Bento River, MG
Unnamed	309	Unknown	Santo Antônio do Bonito River, MG
Star of the South	261.4	1853	Bagagem River, MG
Cruzeiro	261	1942	Santo Antônio do Bonito River, MG
Carmo do Paranaíba	245	1937	Bebedouro River, MG
Abaeté	238	1926	Abaeté River, MG
Coromandel III	228	1936	Santo Inácio River, MG
Mato Grosso	227	1963	MT
Regente de Portugal	215	1732	Abaeté River, MG
João Neto de Campos	201	1947	Paranaíba River, GO
Tiros II	198	1935	Abaeté River, MG
Cedro do Abaeté	194	1967	Abaeté River, MG
Tiros III	182	1935	Abaeté River, MG
Coromandel IV	180	1934	Santo Inácio River, MG
Estrela de Minas	179.4	1910	Dourados River, MG
Rio Preto	177	1972	Preto River, MG
Brasília	176.2	1944	Preto River, MG
Juscelino Kubitschek	174.5	1954	Bagagem River, MG
Tiros IV	173	1938	Abaeté River, MG
Minas Gerais	172.5	1937	Santo Antônio do Bonito River, MG
Princesa do Carmo de Paranaíba	165	1986	São Bento River, MG
Abaeté	161.5	1791	Abaeté River, MG
Portuguese	150	1790	Abaeté River, MG
Unnamed	147	1970	Abaeté River, MG
Coromandel V	141	1935	Santo Inácio River, MG
Nova Estrela do Sul	140	1937	Abaeté River, MG
Minas Vermelhas	140	1960	Santo Antônio do Bonito River, MG
Unnamed	139.5	1797	Abaeté River, MG
Charneca III	132	1972	Santo Antônio do Bonito River, MG
Great Brazilian	130	1791	Abaeté River, MG
Dresden Branco	122.5	1857	Bagagem River, MG
Cruzeiro do Sul	118	1929	Bagagem River, MG
Vargem I	110	1940	Santo Inácio River, MG
Jalmeida	109.5	1924	Tesouro, MT
Governador Valadares	108.3	1940	Bagagem River, MG
Independência	107	1941	Tejuco River, MG
Vargem II	105	1942	Santo Inácio River, MG
Abadia dos Dourados	104	1940	Dourados River, MG
Empress Eugénie	>100	1760	Chapada Diamantina, BA
Carbonado			
Sérgio	3,167	1905	Lençóis, BA
Casco de Burro	2,000	1906	Lençóis, BA
Xique-Xique	931.6	Unknown	Andaraí, BA
Abaeté	827.5	1935	Abaeté River, MG
Bahia	350	1851	BA
Santa Ana	319.5	1960	Rosário do Oeste, MT
Pau de Óleo	113	1932	Andaraí, BA

[a] *Sources: Moreira (1955), Abreu (1973), Svisero (1995), and Hoover and Karfunkel (2009)*
[b] *Carat weights are rounded to the nearest 0.1 ct*
[c] *Abbreviations: BA = Bahia, GO = Goiás, MG = Minas Gerais, MT = Mato Grosso*

Figure 5. The Estrada Real, or "royal highway," was the principal 18th century route to transport goods from Minas Gerais to the ports of Parati and Rio de Janeiro, a distance of several hundred miles, for shipment to Europe.

system in Minas Gerais, known as the Estrada Real or "royal highway," begun in 1697, was built to promote trade, economic development, and communication. Minerals, wood, and other natural resources were transported along the road from the interior to the coast for shipment to Lisbon (figure 5). Manufactured goods from Portugal were also carried inland. The road was strictly regulated by the crown to prevent smuggling and unauthorized movement of goods. It was also the only official route for traveling inland (Cheney, 2005).

As Brazil's population grew from European settlement, larger farms were required to grow crops, and indigenous tribes were used as a source of slave labor. Slaves were also imported from Portugal's African colonies to work the farms. The combination of slave labor and the colony's immense wealth of minerals and wood provided Portugal with unique imports for the European market (Reid, 2014).

EARLY REPORTS ON BRAZILIAN DIAMONDS

Early indications of Brazil's diamond potential were sporadic, but there is evidence that crystals were found in Bahia within a century of Columbus's discovery of the New World. In one of the earliest descriptions, historian Pero de Magalhães Gândavo (1576) mentioned the existence of "certain mines of white stones such as diamonds." In another account, Gabriel Soares de Sousa (1587) noted that fine, eight-sided crystals—possibly diamond—had been found during the dry winter months along certain rivers.

English adventurer Anthony Knivet, who was captured and later escaped during a raid of Portuguese settlements in southern Brazil led by the English privateer Thomas Cavendish, described seeing what he believed to be diamond crystals while living among the natives in the late 1590s (Lessa de Sá, 2015). This would have been another of the earliest accounts of Brazilian diamonds, though no details were provided and the crystals could have been other gems such as quartz.

In 1695, gold was discovered in the mountainous region near Ouro Preto (Southey, 1819), and over the following decade thousands of miners flocked from the coast to the interior in search of the precious metal (Machado and Figueirôa, 2001). Near the village of Arraial do Tijuco in the northern part of Minas Gerais, unusually bright transparent crystals kept showing up in the panned river gravels in the early 1700s. In some cases, the miners disregarded them. Dos Santos (1868) recalled that men sometimes used these crystals as small markers in card games. A similar account says that in 1721 a gold miner secured several of these markers, which were later recognized as diamonds by someone who had traveled in the Golconda region of India (Oakenfull, 1919; see also Cornejo and Bartorelli, 2010).

The discovery of Brazilian diamonds is supported by the account of the Dutch explorer Jacob Roggeven (or Roggewein). As reported in Kerr (1824), Roggeven's three ships anchored off the coast near São Paulo for a short time in November 1721 before resuming their voyage to the Pacific Ocean. Several crewmembers deserted to go to the diamond mining area:

> A little time before the arrival of Roggewein, the Portuguese had discovered a diamond mine not far from St Sebastian [a coastal village near São Paulo], of which at that time they were not in full possession, but were meditating an expedition against the Indians, in order to become sole masters of so valuable a prize; and with this view they invited the Dutch to join them, promising them a share in the riches in the event of success. By these means, nine of our soldiers were tempted to desert. I know not the success of this expedition; but it is probable that it succeeded, as great quantities of diamonds have since been imported from Brazil into Europe. They are said to be found on the tops of mountains among a peculiar red earth containing a great deal of gold; and, being washed down by the great rains and torrents into the vallies, are there gathered.

Figure 6. The village of Arraial do Tijuco in Minas Gerais became famous for Brazil's first alluvial diamond discoveries in the early 1700s. As the settlement grew into a colonial city, it became known as Diamantina. Photo by Robert Weldon/GIA.

Eventually, reports of diamonds in Minas Gerais began to reach Europe. Accounts from the colonial governor came to the attention of both King John V and the Catholic Church in Portugal, and the discovery was officially announced in 1729 (Ball, 1929). As Lisbon's economic clout in Europe had waned somewhat, this was welcome news. In Minas Gerais, there was a diamond rush in the many rivers and streams around Arraial do Tijuco. Portugal moved aggressively to control the area, restricting gold and diamond mining and imposing high taxes. Despite efforts by the crown, clandestine mining and diamond smuggling increased. Draper (1950b) noted:

> The diamonds played a prominent part in shaping the destiny of Portugal. Wealth derived from its diamonds not only helped place that country at the zenith of its glory but also contributed, at a later stage, to its release from the French occupation by paying part of the indemnity exacted by France during the Napoleonic wars (1807-1814).

The occurrence of alluvial diamonds around Arraial do Tijuco was reported in the scientific literature by de Castro Sarmento (1731). Over time, Arraial do Tijuco became the town of Diamantina (figure 6), the diamond trading center during Brazil's tenure as the world's leading exporter. To properly dredge, reroute, and mine the rivers around Diamantina required hard manual labor. This need coincided with the growth of the sugarcane business in Brazil's northeast, and slaves were imported from modern-day Angola, Congo, and Mozambique to fill the needs of both industries. Much like Ouro Preto, Diamantina grew into a rich and picturesque city in the 18th and 19th centuries.

Oakenfull (1919) reported that between 1732 and 1771, "at least 1,666,500 carats of diamonds were exported to Europe." That figure represents an average of about 42,000 carats per year. While miniscule by today's standards, it placed Brazil squarely as the world's top diamond producer at the time, eclipsing India's Golconda region. The glut of Brazilian diamonds pouring into Europe caused for a time a steep decline in prices. Consequently, there were efforts to protect the value of the Indian diamonds on the market by disparaging the quality of Brazilian diamonds (Cassedanne, 1989). Oversupply was put to an end in 1739 when Portugal stepped in to monopolize the Brazilian mines, but by then the Golconda mines had stopped producing. An arrangement with financiers in Amsterdam ensured a steady supply of Brazilian rough for the city's diamond cutters. And despite Portuguese oversight, smuggled Brazilian diamonds also found their way to London, another major center for rough diamonds and jewelry production (Hofmeester, 2013a). For more on the early cutting styles for Brazilian diamonds, see figure 7 and box A.

During this period, additional alluvial sources were discovered. Diamonds were found in the Mato Grosso region in 1746, and subsequently in other rivers in Minas Gerais. The Jequitinhonha River near Diamantina and the surrounding area yielded impressive quantities of alluvial diamonds as well (fig-

Figure 7. This star motif necklace with "Old Mine" cut Brazilian diamonds was made in 1865. Photo by Luisa Oliveira, courtesy of Ajuda National Palace.

ure 8), including treasure troves in "potholes" or traps in the river bedrock. But the primary source of diamonds in Minas Gerais—actual diamondiferous kimberlites—remains elusive. As Sinkankas (1977) noted:

> The original host rocks of the diamond crystals remain unknown despite much past speculation, "proof" of host rock sources by some authorities, and modern intensive geologic exploration of the regions presently yielding diamonds. Brazilian diamonds are found in a sort of matrix to be sure, this being a conglomerate of well-rounded pebbles cemented together with sand and iron oxides.

In 1733, Portuguese authorities began granting royal licenses to individuals to work portions of the diamond deposits. Guarded mule trains transported the diamonds along the Estrada Real to Parati and Rio de Janeiro ("Diamond carriers," 1842). This licensing system eventually broke down, as bands of runaway slaves and garimpeiros clandestinely worked the areas or stole the recovered diamonds. In 1772, the government abandoned this system and took full control of the workings around Diamantina (von Spix and von Martius, 1824).

The English mineralogist John Mawe is probably the most celebrated European traveler to Brazil's interior, having been the first foreigner to reach the diamond mines. In 1809 he received ap-

BOX A: THE EVOLUTION OF THE OLD MINE CUT

Demand for diamonds and experimentation with cutting styles dovetailed with Brazilian diamond discoveries in the 1700s. This convergence of marketing and manufacturing led to the rapid growth of diamond mining in Brazil. As diamonds suddenly became available to a larger audience, cutters in Amsterdam and London embarked on a new cutting style that became the precursor to the modern brilliant cut.

Demand. Jewelry historian Marcia Pointon (1999) wrote that by the late 1600s, diamond adornment was one of the "publically recognized criteria for gauging social success…" Louis XIV's thirst for diamonds best illustrated this trend among Europe's wealthy classes: "While also influencing concepts of taste, the demand of the King himself was hugely significant… in 1669, Louis had purchased an unprecedented 1.5 million livres worth of diamonds (about US$21.45 million), including 900,000 livres worth from gem merchant Jean-Baptiste Tavernier; all of course were Indian diamonds" (McCabe, 2008). In 1691, an inventory of the king's collection showed it was composed almost exclusively of diamonds cut in the brilliant style (Tillander, 1995). By 1715, just prior to his death, the king displayed a collection of cut diamonds worth 12 million livres, or more than US$170 million today (DeJean, 2005).

Global Trade. While diamond rough from India had been sporadic by the early 1700s, the new finds in Brazil stimulated the global diamond trading network (Inveness, 2014). Within the country, the Portuguese crown authorized "exploiters," who oversaw individual miners, to work the deposits in Minas Gerais. In turn, these individuals paid the Portuguese treasury with a tax per miner in their employ (Hofmeester, 2013b). The arrangement worked well. Diamond supplies increased fivefold in Europe, followed by a 50% drop in prices (Lenzen, 1970; Yogev, 1978). The Brazilian production triggered a restructuring of the global diamond supply chain, as lower prices only served to compound the demand. More people could afford them, thereby stoking a continued exploration within the country. Furthermore, the increasing market stirred a growth in the European diamond cutting industry.

Cutting Styles. Increased supplies of rough diamonds also allowed for experimentation in cutting styles by French cutters (figure A-1). The brilliant cut, introduced around 1660–1670 in France, was also associated with London by the mid-1700s (Tillander, 1995).

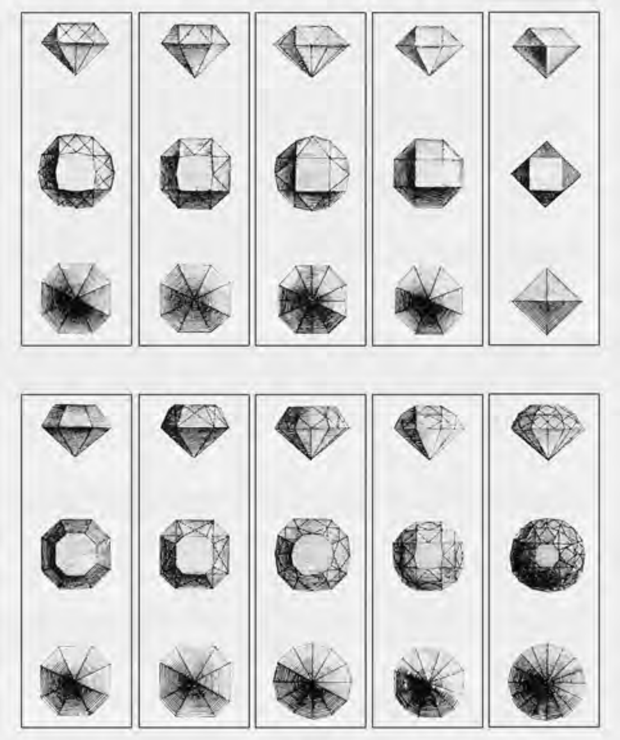

Figure A-1. Illustrations of the diamond faceting arrangements known in France by the mid-1700s. These were compiled by Denis Diderot, chief editor from 1745 to 1772 of the 28-volume Encyclopédie, ou Dictionnaire Raisonné des Sciences, des Arts et des Métiers, *one of the principal works of the Enlightenment. This page is taken from his 1771 volume entitled* Recuiel de Plances, sur Les Sciences, Les Arts Liberauz, et Les Arts Mechaniques *(p. 732).*

Soon after the Brazilian discoveries, the most prominent cutting styles in Europe were the brilliant and, for smaller stones, the rose cut (Jeffries, 1750). Originally the "brilliant" cut represented an arrangement of 58 facets, typically cut in a cushion or somewhat squarish shape following the outline of the most common type of rough, the octahedron. The brilliant was also cut in round, oval, and pear shapes, as seen in figure A-2.

The brilliant style of cutting, favored by Louis XIV in the late 1600s, was suddenly available to many. The re-

proval and funding from the Portuguese crown for his visit. His descriptions of the diamond region are still some of the most detailed. A vivid portrayal of the washing plants and the diamond discovery methods emerges in his 1812 account, *Travels in the Interior of Brazil*:

> A shed is erected in the form of a parallelogram…consisting of upright posts which support a roof thatched

sult was that diamonds cut in this style glittered in the candlelit ballrooms of the 1700s.

Rise of the Mine Cut. India and Brazil were the classic sources for high-color diamonds in the 1700s and most of the 1800s. In comparing the sources, gem expert Edwin Streeter extolled the virtues of Brazilian stones. "A fair portion of the South-African stones are diamonds of the first-water [i.e, best clarity and colorless], rivalling in beauty and purity the finest Brazilian and Indian Stones" (Streeter, 1882).

In 1891, one diamond manufacturer wrote: "Many diamond dealers sell African diamonds at an enhanced price to the uninitiated public as 'old mine stones,' presumably referring to diamonds from the 'old mines' of Brazil or India… Great variations in color and purity of course exist, but it is not fair to assume that all the best come from Brazil or India" (Stonestreet, 1891). Although India is included in this definition, it does not refer to diamonds cut in India; rather, it only pertains to Indian diamonds fashioned in Europe using the brilliant cutting style.

Not all of Brazil's diamonds were "of the first-water," however. Streeter (1882) did make a distinction between Brazil's various sources. "The Diamonds of Brazil are known in commerce as (1) Diamantina diamonds, and (2) Cincora [sometimes spelled Sincora] diamonds," he wrote. "The latter are of less value than the former, because they are not of such pure water, nor of so good a shape. In Matto-Grosso, the diamonds are small, but of purest water, and in their rough state have a peculiar lustre, which is seen in none other than Brazilian diamonds" (Streeter, 1882). He also noted that diamonds from Bahia were of lesser quality.

By the early 1900s, the "Old Mine" designation had evolved to refer to aspects of the cut as high-color quality also became associated with diamonds from the mines in South Africa:

> Specifically, Brazil diamonds from the old diggings (probably the Diamantina area); as generally used, old-cut diamonds of good color…. This quality of color was long-termed 'Old Mine,' from Brazil... Since the opening of the African mines, a new name has been given to material of this character. A mine called Jagersfontein yielded many bluish-tinted diamonds, and it soon became customary in trade circles to call everything of that grade 'Jagers' (pronounced Yahgers). (Cattelle, 1903)

Thus, the appearance of African high-quality diamonds began to shift the definition of "Old Mine." Cattelle (1903) wrote,"This is now the trade term for blue goods, the name 'Old Mine' being confined to the old cut stones of that quality [referred to in the early 1900s as blue-white] which occasionally drift back into the market from private hands" (Cattelle, 1903). More recently, diamond historian Herbert Tillander (1995) indicated that "Old Mine or Old Miner…were introduced at the end of the last century to describe the type of cut applied to most Brazilian rough." He later noted that this term is a "popular but inaccurate term for the cushion-shaped brilliant, which dates back to the seventeenth century." He pointed out that "Old Mine," once the epitome of cutting style, came to be viewed with disdain. It was seen as a less desirable cut, referring simply to an old style of shape outline (squarish) and cutting style, with steeper pavilions and crowns, shorter half facets, and large culets. This cut was replaced with a more light-efficient shape and style of cutting known as the round brilliant.

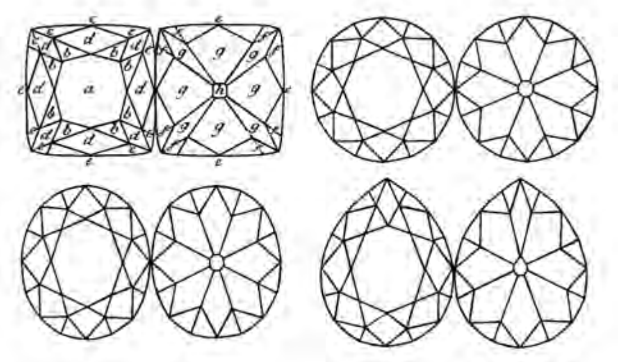

Figure A-2. The most common outlines for "brilliant cut" diamonds, as illustrated in A Treatise on Diamonds and Pearls *by David Jeffries in 1750. Note that all have 58 facets in a similar layout, and the only differences are their outlines.*

Today, nostalgia for historic diamonds and that style of cut has shed a kinder light on the so-called Old Mine cut. Such gems, when they are found, are often viewed as collectors' items (figure 8). Because Old Mine cuts have enjoyed such a storied history, some contemporary jewelry designers continue to use them successfully in their creative expressions. Out of strong demand for this vintage look, several companies now deliberately cut Old Mine faceted diamonds, but with thicker girdles than in their heyday.

with long grass. Down the middle of the area of this shed a current of water is conveyed through a canal covered with strong planks, on which the *cascalhão* [a Portuguese term for gravel] is laid two or three feet thick. On the other side of the area is a flooring of [sloped] planks… The flooring is divided into about twenty compartments or troughs…by means of planks placed on their edge. The upper ends of these troughs

Figure 8. Crystals such as this group from the Jequitinhonha River were once used as markers in card games, as they were not recognized as diamonds. Photo by Robert Weldon/GIA, courtesy of Gar Mineração.

> communicate with the channel, and are so formed that water is admitted into them…The negroes enter the troughs, each provided with a rake…with which he rakes into the trough…[the] cascalhão. The water being let in upon it, the cascalhão is spread abroad and continually raked up to the head of the trough, so as to be kept in constant motion. [After the finer sediment is removed], the gravel-like matter is raked up to the end of the trough, and…then the whole is examined with great care for diamonds. When a negro finds one, he immediately stands upright and claps his hands, then extends them, holding the gem between his fore-finger and thumb; an overseer receives it from him, and deposits it in a gamella or bowl…In this vessel all the diamonds found in the course of the day are placed, and at the close of work are taken out and delivered to the principal officer, who, after they have been weighed, registers the particulars in a book kept for that purpose.

Mawe's successful journey prompted other European explorers to follow in his footsteps. His account, and the illustrations in his book by noted mineralogist James Sowerby, inspired many European scientists from a variety of disciplines to explore Brazil. Swiss botanist Auguste de Saint-Hilaire, who traveled there in 1817, described Diamantina as a "valley of diamonds" (de Saint-Hilaire, 1833). He also painted a dismal image of the conditions for both the garimpeiros and slaves around Diamantina. The slaves received little food or rest, and their panning and sorting of diamonds was subject to strict punishment. The only reprieve was good luck:

> From this wretched mode of life a fortunate accident sometimes frees a slave. When he happens to find a diamond weighing an octavo, or 17 ½ carats… his value is ascertained by the administration, the price is paid to his owner, he is dressed, and set at liberty. (Mawe, 1812)

German nobleman Baron Wilhelm Ludwig von Eschwege fought alongside the Portuguese during the Napoleonic Wars, and for his service he was granted access to Minas Gerais as a consultant for the government. In 1811, he settled in Ouro Preto to lend his qualifications there as a mining engineer. Having traveled throughout Minas Gerais over the course of a decade, he was instrumental in not only documenting existing techniques used for diamond and gold mining, but also offering recommendations for the use of more modern procedures (von Eschwege, 1833).

Richard Francis Burton, an English explorer, was noted for his travel in sub-Saharan Africa in search of the origins of the Nile River as well as other exploits in the 1850s. In 1865, he was given a diplomatic post in Brazil by the British government. An 1867 expedition in the Brazilian highlands took him to Diamantina and the São Francisco River. His account of reaching the city, and his description of the diamond mining region, are well chronicled in his 1869 book, *Explorations of the Highlands of Brazil*.

When Brazil gained independence in 1822, Portuguese control of diamond mining ceased in Minas Gerais. It was replaced with a system of free exploitation except along the Jequitinhonha River Valley, which remained under some government control until 1845. By the 1880s, production had dropped significantly due to several factors—the low grade of the alluvial deposits, competition from diamonds from South Africa, and Brazil's abolition of slavery in 1888, which meant the loss of cheap labor.

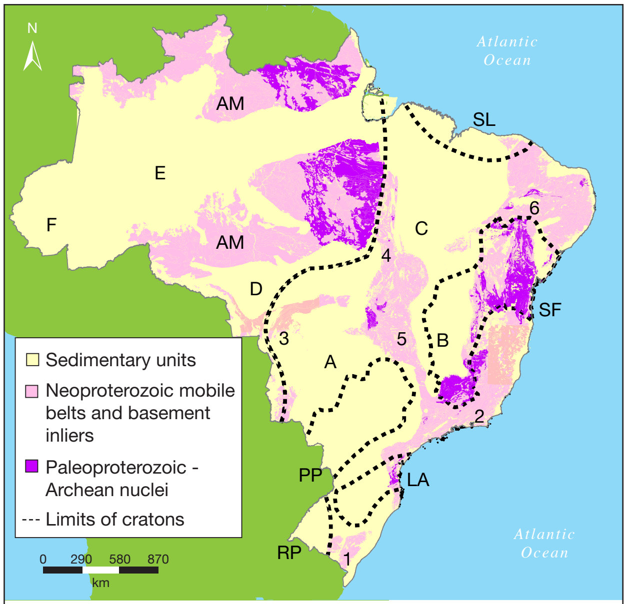

Sedimentary units - intracontinental basin:
(A) Paraná, (B) San Franciscana, (C) Parnaíba, (D) Parecis, (E) Solimões-Amazonas, (F) Acre

Neoproterozoic mobile belts and basement inliers:
(1) Dom Feliciano, (2) Ribeira, (3) Paraguai, (4) Tocantins, (5) Brasília, (6) Rio Negro-Sergipano

Paleoproterozoic - Archean nuclei:
(RP) Rio de la Plata, (LA) Luis Alves, (PP) Paranapanema, (SF) São Francisco, (SL) São Luíz, (AM) Amazonas

Figure 9. A simplified map of the major geological regions of Brazil.

GEOLOGIC SETTING

Brazil contains a variety of rocks and geotectonic structures (see Branner, 1919; de Almeida, 1967; de Almeida et al., 1981). The present-day land masses in the Southern Hemisphere were assembled as part of a large Precambrian supercontinent called Gondwana (de Brito-Neves and Cordani, 1991; Cordani et al., 2003, 2009). Much of the current geological setting of Brazil was established in the Pan-African/Brasiliano orogenic cycle (approximately 440–1000 Ma). During this time, preexisting Archean cratons were brought together by plate tectonics and assembled along mountain (or orogenic) fold belts representing the zones of continental collision. At about 180 Ma, Gondwana began to break up into separate pieces, with South America and Africa gradually drifting apart to create the Atlantic Ocean (Hasui, 2012). Since the two continents were connected prior to this breakup, corresponding rock types and certain geological structures occur on either side of the ocean. As shown in the simplified map in figure 9, the main geological units consist of:

1. Ancient Archean or Proterozoic "basement" cratons that are covered in many places by geologically younger sedimentary rocks
2. Weathered Proterozoic mountain fold belts that separate the cratons
3. Paleozoic sediments that fill topographic basins within the cratons
4. Mafic and/or ultramafic igneous intrusions of Mesozoic and Cenozoic age

DIAMOND OCCURRENCES

Diamonds occur in several different geologic settings across Brazil. They are usually recovered as loose crystals along rivers in unconsolidated alluvial or glacial sediments, or they are embedded in conglomer-

Figure 10. A map showing the distribution of various categories of diamonds found in Brazil. The name of the mining area is shown (with the abbreviation of the Brazilian state), preceded by its location number on the map.

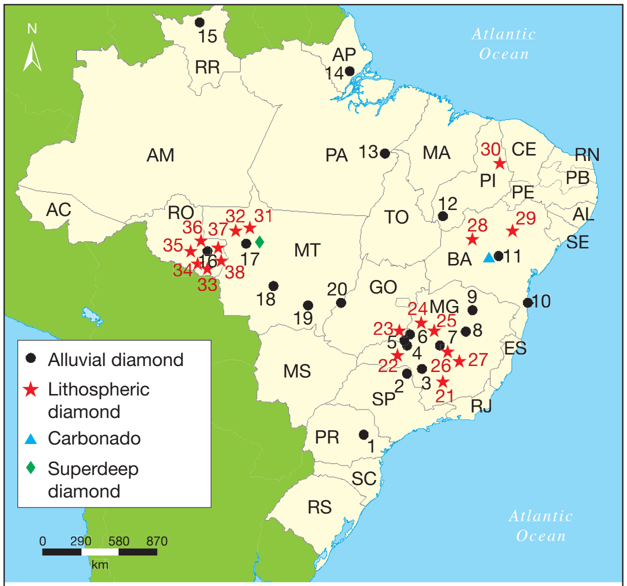

Alluvial diamonds:
(1) Tibagi, (2) Franca, (3) Vargem Bonita (4) Romaria, (5) Estrela do Sul, (6) Coromandel, (7) Abaeté, (8) Diamantina, (9) Grão Mogol, (10) Canavieiras, (11) Lençóis, (12) Gilbués, (13) Marabá, (14) Vila Nova, (15) Tepequém, (16) Pimenta Bueno, (17) Juína, (18) Diamantino, (19) Poxoréu, (20) Barra do Garças

Lithospheric diamonds:
(21) Canastra 1, (22) Romaria, (23) Três Ranchos 4, (24) Tucano, (25) Abel Régis, (26) Cana Verde, (27) Maravilhas, (28) Salvador 1, (29) Braúna 3, (30) Moana 11, (31) Juína 5, (32) Collier 4, (33) Carolina 1, (34) Comet 1, (35) Cosmos 1, (36) Cosmos 2, (37) Cosmos 3, (38) Tumeleiro 3

Carbonado:
Lencóis (BA)

Superdeep diamonds:
Juína

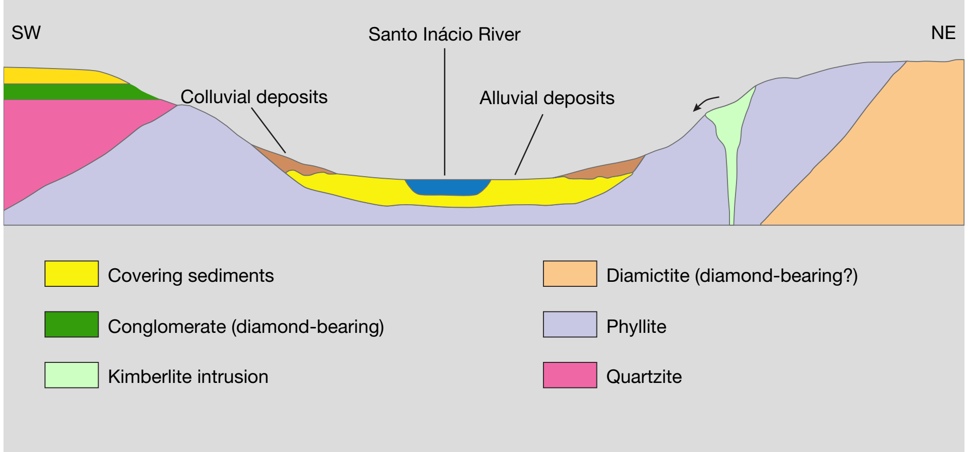

Figure 11. This diagram illustrates the kinds of secondary diamond deposits found along the Santo Inácio River in Minas Gerais—alluvial and colluvial deposits along the river channel, occasional kimberlite pipes (often unrecognized because they are deeply weathered and covered by younger sediments), and sedimentary conglomerates exposed on the adjacent hillsides.

ates or metamorphosed sedimentary rocks. They are also found in small amounts in a few known kimberlite bodies. Figure 10 shows the locations of the major mining areas (both historical and current) for the different categories of diamond deposits that will be discussed.

The general geology of Brazil and its important mineral resources have been reviewed by Berbert et al. (1981), Delgado et al. (1994), and Machado and Figueirôa (2001). Further information on the diamond occurrences themselves can be found in Gorceix (1882), Pearson (1909), Cassedanne (1989), and Cornejo and Bartorelli (2010).

Alluvial Diamonds. Alluvial diamonds are recovered as loose crystals directly from rivers or streams, or from geologically recent unconsolidated sediments nearby. These deposits occur throughout Brazil, but the sources in Minas Gerais and Mato Grosso have been the most economically important over the past three centuries.

The recovery of diamonds has involved simple methods used by artisanal miners. Loose diamonds and other heavy minerals are panned directly from a flowing river, or are washed from sediments through a series of sieves. The diamond-carrying sediments are mixtures of clay, sand, silt, gravel, and angular or rounded pebbles; they are often found in horizontal bands or layers, with their contents washed down from higher terrain.

The main detrital diamond deposits are called *cascalhos* (river gravels). Besides quartz, the gravels may contain heavier pebbles of iron oxide minerals. They are geologically classified as eluvial, colluvial, or alluvial gravels depending on their topographic location and distance from the source.

Figure 12. At larger alluvial mining operations, such as the Duas Barras mine on the Jequitinhonha River (left), sediments are passed through a washing plant (right) where high-pressure water hoses are used to remove larger pebbles as well as clays and other lighter materials. Diamonds along with heavy minerals are collected as a concentrate. Photos by Robert Weldon/GIA.

Figure 13. At the Duas Barras mine, a miner pans the finest-size heavy-mineral concentrate to recover small particles of gold, the production of which helps offset the cost of diamond recovery. Photos by Robert Weldon/GIA.

Figure 11 illustrates several types of diamond deposits in relation to the topography. The diamond-bearing gravels occur as deposits along the bottom or banks of rivers, and along paleo-river channels that are buried beneath younger rocks. Remnants of the buried channels outcrop along riverbanks. The diamonds may also occur in sediments exposed on hillsides. The garimpeiros use various approaches—past discoveries, rumors, intuition, and other means—to identify potential mining areas. They often wait for the dry season to explore the accessible riverbeds, as diamonds can be concentrated in depressions or potholes on the underlying bedrock. In some cases, the course of a river is blocked with a dam, or the water is diverted using a large sluice, providing access to the gravels. Once a potential spot is selected, it may be necessary to remove overlying layers of silt, clay, or sand to reach the diamond-bearing gravels, which tend to lie on or above the solid bedrock. Larger pebbles are removed, and the gravels are then washed using sieves or pans to pick any diamonds by hand (figure 12). The finest-size material is then checked for diamonds as well as small particles of gold (figure 13).

Larger hydraulic systems have sometimes been used to wash diamond-bearing sediments exposed in an outcrop. In the late 1800s and early 1900s, diving suits were used by some miners to retrieve sediments from the river depths. These traditional mining activities have been supplemented by mechanized methods; for example, gravel may be extracted from the river by suction pumps. The pumped water and gravel is then passed through a sluice box that removes the lighter material to recover diamonds and other heavy minerals (Barbosa, 1991). Large, expensive dredges are less common because the low grade of the deposits makes them too costly to exploit with this kind of equipment.

Jequitinhonha River, Minas Gerais. Following the discovery of diamonds in alluvial gravels around Diamantina in the early 1700s, exploration took place along the Jequitinhonha River as well as other rivers and streams in the mountainous Serra do Espinhaço (Derby, 1906; Thompson, 1928). Diamonds occur in metamorphosed sediments of the Mesoproterozoic-age Espinhaço Supergroup. As a result of the weathering of these sediments, diamonds are found in the rivers and streams and in exposed gravels (Karfunkel et al., 1994; Chaves et al., 2001). Mining in this region has been carried out by garimpeiros and later by larger companies, though the peak of activity occurred between about 1740 and 1830.

The alluvial deposits of the Jequitinhonha River have been responsible for most of Brazil's historic diamond production (Chaves and Uhleim, 1991). In this region, the alluvium consists of a 10- to 45-meter-thick layer of gravel capped by a sand-clay layer. The diamond content of the gravel is approximately 0.6 carats per cubic meter of sediment (ct/m^3; Dupont, 1991). In 1966, Mineração Tejucana SA, a diamond mining company based in Diamantina, began using dredges to work the alluvium of this river. The company processed 9 million cubic meters of alluvium per year to recover 70,000 carats of mostly gem-quality diamonds (along with 150 kg of gold) over a period of several years (Dupont, 1991).

Between December 2007 and April 2008, the Peçanha mine near Diamantina, owned and operated by Recursos Mineração Ltda. (a subsidiary of Brazil Minerals Inc.) yielded 4,512 carats of diamonds and 8.95 kg of gold, with average grades of 0.06 ct and 0.14 g per cubic meter, respectively (Watkins, 2009).

Mineraçao Rio Novo is a subsidiary of Andrade Gutierrez SA, a private multinational company headquartered in Belo Horizonte that has been mining along the Jequitinhonha River since 1988. The deposit has a diamond content of about 1.1 ct/m^3 and an average production of 25,000 carats per year (Chaves and Uhlein, 1991; Watkins, 2009). Mining involves removing the overlying sediments and using a bucket dredger to excavate the mineralized gravel. Diamonds are recovered from the coarser concentrate in a vibrational circular sieve, while gold is retrieved from the finer concentrate.

Another important project in the Diamantina region is run by Mineraçao Duas Barras, a subsidiary of Brazil Minerals Inc. Data released by the company showed a yield in 2008 of 32,008 carats, with an average value of US$145 per carat (Watkins, 2009). Geological studies of this deposit gave an indicated resource of approximately 1,639,000 m^3 of diamondiferous gravel with an average grade of 0.16 ct/m^3. A weekly output of nearly 0.5 kg of gold provides a source of revenue to support mining operations.

Poxoréu, Mato Grosso. Poxoréu is located on the northwestern edge of the Paraná Basin. Diamonds were discovered in the Coité River in the 1930s, causing an influx of prospectors. The alluvial deposits are distributed along the Coité, São João, Poxoréu, Alcantilados, Pomba, and Jácomo rivers.

Until the mid-1970s, mining was carried out using only picks, sieves, and panning. St. Felix Ltda. subsequently conducted studies in the Coité River Valley to characterize the diamond reserves—38.6 million cubic meters of gravels were processed, of which about 42% contained diamonds. The average diamond content was 0.05 ct/m^3, with an estimated recoverable reserve of 662,000 carats, 27% of it gem-quality (Souza, 1991). According to this reference, there were about 2,500 miners and 150 dredges in the region in the 1980s.

Approximately 70% of the diamond crystals from Poxoréu and Chapada dos Guimarães, both located near the state capital of Cuiabá, display a dodecahedral habit, while the rest display octahedral and mixed habits (Zolinger et al., 2002). All of the diamonds are recovered from sedimentary rocks of the Upper Cretaceous-age Bauru formation (Souza, 1991). Similarly, diamonds mined elsewhere in southeastern Mato Grosso, around the cities of Tesouro, Guiratinga, Alto Garças, Barra do Garças, and Batovi, are related to conglomerates of the same formation (Weska, 1996).

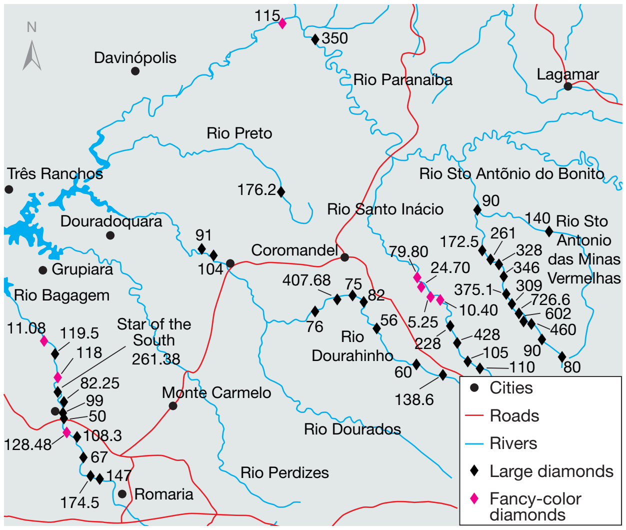

Figure 14. The Alto Paranaíba region of western Minas Gerais has produced large diamonds along river systems near the towns of Coromandel and Romaria. The symbols indicate where individual large diamonds were found; the value shown next to each symbol represents their carat weight. The site where the famous Star of the South diamond was recovered in 1853 along the Bagagem River is indicated in the lower left corner.

Coromandel, Minas Gerais. The mines around Coromandel began operating in the late 18th century (Des Genettes, 1859). The town was probably named by Portuguese traders for the Coromandel region of India, an important diamond source since antiquity (Legrand, 1980). Also known as the Alto Paranaíba province or the Triângulo Mineiro, this area is the second most important source of diamonds in Minas Gerais, serving as the center of the local diamond trade (figure 14; Leonardos, 1956; Kaminsky et al., 2001; Karfunkel et al., 2014).

The town itself is located on the eroded rocks of the Brasilia fold belt in western Minas Gerais. The mines occur in alluvial deposits of Cenozoic age,

Figure 15. The Bagagem River, shown near the town of Romaria, has yielded numerous large diamonds over the past two centuries, including the Star of the South. Photo by Robert Weldon/GIA.

mainly along rivers that cut through the recent sediments as well as metamorphic rocks of the crystalline basement.

The main diamond-mining areas are situated along the Paranaíba, Santo Inácio, Dourahinho, Santo Antônio do Bonito, Santo Antônio das Minas Vermelhas, and Bagagem rivers, and to a lesser extent the Preto and Dourados rivers. In the Paranaíba River, the largest waterway in the region, most mining is done by means of rafts anchored at various points along the riverbed. Heavy mineral concentrates from all of these rivers and streams contain traditional kimberlite indicators: pyrope garnet and magnesian ilmenite in similar proportions, followed by zircon and chromite.

The Coromandel region is famous for its periodic discoveries of large rough diamonds (table 1). The best-known examples are the 726.6 ct Presidente Vargas and the 261.38 ct Star of the South (Hussak, 1894; Reis, 1959; Smith and Bosshart, 2002; Balfour, 2011; also see Abreu, 1973; Svisero, 1995). The Presidente Vargas was found in 1938 along the Santo Antônio do Bonito River. The Star of the South was discovered in 1853 in the Bagagem River, near a village then known by the same name (Dufrenoy, 1855). The area continues to occasionally yield large diamonds, attesting to the great economic potential of these deposits (figure 15).

Colored diamonds finds are not rare in Brazil, and they are often not officially registered. Still, there are some notable examples. In 1998, a 7.0 ct pink diamond found in the Vargem mining area near Coromandel was purchased by a diamond dealer for US$650,000. The Giacampos Red, a 5.25 ct crystal found in 2005 in the Santo Inácio River, yielded a 1.57 ct faceted oval. In May 1993, a 602 ct brown diamond discovered in the Santo Antonio do Bonito River (Haralyi et al., 1994) became the second-largest recorded Brazilian gem diamond (surpassed only by the colorless Presidente Vargas). In the fall of 2014, at a site along the Dourahinho River, the mine owners found a flattened 138.6 ct pink crystal, which they were able to sell almost immediately.

In the Coromandel region, large diamonds have also been recovered from the Abaeté, São Bento, Borrachudo, and Indaiá rivers, all occurring in the São Francisco River Basin (figure 16). They are also recovered in the alluvium eroded from Cretaceous conglomerates of the Capacete formation (Read et al., 2004). Examples of large diamonds include the 27.09 ct vivid pink Queen Giacampos and the 13.90 ct Moussaieff Red, both found in the Abaeté River (King and Shigley, 2003). Other discoveries include the 0.59

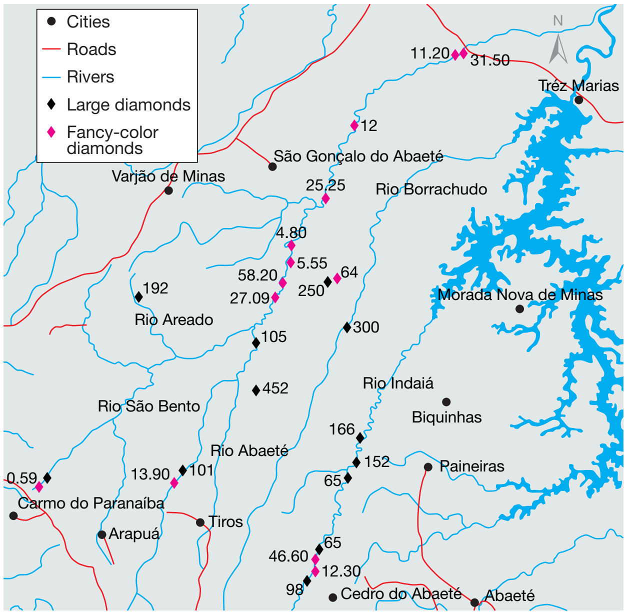

Figure 16. This map shows the Abaeté and nearby river systems in Minas Gerais that have produced large diamonds for many years. Again, the value shown next to each symbol represents the carat weight of the rough crystal found at the location. Discoveries of colored diamonds are indicated by colored symbols. The rivers shown on the map, some of which flow into the Tres Marias reservoir, are all located within the southern portion of the São Francisco River basin.

ct Rob Red, from the São Bento River, and two rough stones of 41.44 and 58.2 carats from the Abaeté River (see references listed in table 1).

The remarkable Bragança diamond—either 1,680 ct (Mawe, 1812) or 1,730 ct (Ferry, in Reis, 1959), depending on the source—was found in 1797 in the Abaeté region. For many years, the Bragança belonged to the Portuguese crown jewels (Balfour, 2011). Because of its large size and pale appearance, it was once considered a topaz by some historians and traders (Reis, 1959; Balfour, 2011). More recently, Galopim de Carvalho (2006) discussed the possibility that it was a pale aquamarine. Yet this region's geology is not favorable to the occurrence of either topaz or aquamarine, and it is more likely that the Bragança was indeed a diamond. Its current whereabouts are unknown.

The origin of these large diamonds continues to elude both researchers and mining companies. The geological literature reflects two opposing views. One theory holds that diamonds of all sizes, weathered from kimberlite pipes, were recycled into the alluvium from the conglomerates of the Capacete formation and distributed throughout the Coromandel region (Svisero et al., 1981; Sgarbi and Chaves, 2005). Based on field evidence that seems incompatible with a kimberlite "pipe" origin, the other theory proposes that the diamonds were transported westward into the region from the São Francisco craton by glacial events in the Neoproterozoic and Paleozoic periods (Tompkins and Gonzaga, 1987; Gonzaga and Tompkins, 1991). This alternate view has been difficult for some to accept because there is little understanding of the transport, concentration, and dispersion mechanisms of diamonds in glacial systems in South America (Gonzaga et al., 1994).

Juína, Mato Grosso. The Juína diamond region lies in the southern part of the Amazonian craton and in the northwest of Mato Grosso. Alluvial diamond deposits are located in the basins of the Juína Mirim, Vinte e Um de Abril, and Cinta Larga rivers, all situated southwest of the city of Juína. The alluvium comes from erosion of the crystalline basement rocks and from overlying sediments of the Parecis basin, located on the southeastern edge of the Amazonian craton (Tassinari and Macambira, 1999). The Parecis basin, encompassing an area of 500,000 km^2, contains sediments about 6,000 m deep. The Pimenta Bueno and Paranatinga regions in the neighboring state of Rondônia also contain diamond-bearing alluvium.

During the 1980s, the Juína region was the country's largest producer of industrial diamonds. At its peak, some 30,000 miners produced around 400,000 carats per month (Costa, 2013). Examination of 2,200 crystals by one of the authors (DPS) in 1985 revealed that 90% were of industrial quality, gray to dark brown in appearance. Most were malformed or corroded crystals and crystal fragments.

Late in the decade, large variations were recognized in the abundance of alluvial diamonds in the area. The Cinta Larga River basin and its tributaries—the São Luiz, Porcão, Samanbaia, Mutum, and Central rivers, as well as the Sorriso and Duas Barras streams—all contained large amounts of alluvial diamonds (up to 6–7 ct/m^3). In the Juína Mirim River basin, however, there were much lower amounts (0.6–0.8 ct/m^3). Besides the high yield of industrial diamonds, the alluvial deposits were also noteworthy for their large diamonds, similar to Coromandel and Abaeté in western Minas Gerais. Haralyi (1991) reported finding eight crystals between 49.5 and 232 ct, along with six industrial diamonds between 52 and 263 ct. According to Costa (2013), in September 1992 a garimpeiro found a 413 ct diamond in the village of Poção. Le Noan (2008) mentioned the discovery of a 452 ct "megadiamond" in alluvial deposits of the São Luiz River. Although sporadic, these finds indicate that the area around Juína also has potential for large diamonds. Watkins (2009) reported that Juína remains the country's leading producer of industrial diamonds. In the last decade, the estimated output has been on the order of five million carats.

Other Sources. Diamonds were discovered in the state of Roraima in the early 20th century in the Mau River region and later near Vila do Tepequém (located in the Serra do Tepequém). The deposits occur in sediments that originated from conglomerates of the Neoproterozoic Tepequém formation. Present-day alluvial placers occur where the diamondiferous gravel ranges up to 0.80 m thick, and where indicator minerals are present. In some locations, gold is also recovered (Grazziotin and Andrade, 2011).

In the state of Piauí, diamonds mainly occur near the city of Gilbués in alluvial deposits along the Riachão stream, and in colluvium near the towns of Gioninha, Bom Jardim, Compra Fiado, and Boqueirão. At these locations, the diamonds are usually small but of good quality, sometimes reaching values of US$100 per carat or more (Watkins, 2009).

Sublithospheric Diamonds. Juína drew the attention of geoscientists with the discovery of so-called su-

Figure 17. A section of the diamond-bearing sediments left by past mining operations at the abandoned Romaria mine in Minas Gerais. The diamondiferous conglomerates lie beneath the lower portion of the reddish brown sediments along the center of the photo; they are covered by about 10 meters of brown sediments. These conglomerates extend across a large area of the countryside near the town of Romaria. Photo by Robert Weldon/GIA.

perdeep diamonds in the São Luiz River area in the early 1990s (Wilding et al., 1991; Stachel et al., 2005; Harte, 2010; Kaminsky, 2012). They are believed to have formed at 400 to 800 km, considerably deeper than most diamonds that formed in the continental lithosphere at approximately 140 to 200 km (Thomson et al., 2014). These "sublithospheric" diamonds are characterized by unusual syngenetic mineral inclusions indicating greater formation depth (such as majorite, periclase-wustite, wollastonite, diopside, moissanite, tetragonal garnet, and perovskite). They are mainly low-nitrogen type IIa diamonds. More recently, similar mineral inclusions have been found in samples from the Collier 4 kimberlite in southwest Juína (Bulanova et al., 2010).

Diamonds in Conglomerates. In several locations, sedimentary conglomerates are the host rocks for diamonds. Diamonds are seldom recovered directly from conglomerates, since most mines are developed in unconsolidated sediments. The classic example of a diamond-bearing conglomerate is the Romaria mine (figure 17), located in western Minas Gerais about 500 km from Belo Horizonte.

According to Des Genettes (1859), diamonds were first discovered in the Bagagem River in 1722 by the explorer João Leite da Silva Hortis. Large-scale exploration in the Romaria region began in the second half of the 19th century (Hussak, 1894). In the early 20th century, this mine was visited by many foreigners (Porcheron, 1903; Draper, 1911). It was subsequently controlled by various companies, the last of which was Extratífera de Diamantes do Brazil (EXDIBRA), which operated it from 1969 until 1983, when the mine was closed for financial reasons.

The Romaria mine, located near the town of the same name, was excavated using tractors to remove the overlying sediment layer. Trucks transported the ore for washing at a plant that processed up to 600 m^3 of ore per day, with the final separation of the diamonds performed manually (Svisero et al., 1981). The mine, located in the northeastern edge of the Paraná basin, covers an area of approximately 1.2 km^2. On the property, the Uberaba formation consists of a sequence of conglomerates, sandstones, and mudstones; at the base of this formation are diamond-bearing conglomerates approximately six meters thick (Suguio et al., 1979; Coelho, 2010; see figure 17). The concentrates obtained by washing the conglomerates contain indicator minerals. Chemical analysis revealed that the garnet and ilmenite are of a kimberlitic origin (Svisero, 1979; Svisero and Meyer, 1981; Coelho, 2010). In 1981, during the final phase of the EXDIBRA operation, one of the authors (DPS) examined a parcel of 450 carats of diamonds comprising 5,250 stones of various size, shape, and color. The crystals were predominantly rhombododecahedral in shape; most were colorless, and 70% were of gem quality (Svisero et al., 1981).

During this period, drill core samples were taken to determine the extent of the mineralized conglomerates (Feitosa and Svisero, 1984). The results revealed the presence of small "basins" formed by depressions in both the sandstone and the underlying mica schist. These paleostructures on the crystalline basement were filled by mud flows, giving rise to di-

Figure 18. The town of Lençois in the Chapada Diamantina region of Bahia has long been an important source of diamonds and carbonado. Garimpeiros *found diamonds in conglomerates (left) or in the bottoms of water-worn potholes formed in the river bed. The conglomerate specimen on the right, called the "Madonna" because of its shape, contains a small diamond. Photos by Robert Weldon/GIA; conglomerate sample courtesy of Gar Mineração.*

amond-rich layers within the conglomerate. Samples also revealed that the diamond-bearing layers measured up to 9.6 m thick, while the average diamond content ranged from 0.33 to 0.69 ct/m^3.

Diamonds in Glacial Deposits. Most researchers now accept that diamonds in the Tibagi region of Paraná come from sedimentary glacial deposits (Oppenheim, 1936; Maack, 1968; Liccardo et al., 2012). Tibagi is one of the country's oldest centers of diamond mining, having been discovered in 1754 by gold prospectors (Leonardos, 1959).

The mines of the Tibagi River basin and the adjacent areas have been worked since the latter half of the 18th century (Derby, 1878). Diamonds occur in the riverbeds in both old and recent alluvium and colluvium. The deposits are distributed in small groups in the southeastern border of the Paraná basin (Perdoncini et al., 2010), and there have been alternating periods of intense mining activity and neglect. The Tibagi deposits were especially active in the first decades of the 1900s, when Oppenheim (1936) noted 60 alluvial occurrences in production.

In the 1980s, Paraná Minerals (MINEROPAR) and the Companhia de Pesquisa de Recursos Minerais (CPRM) conducted fieldwork to assess the deposits in the Tibagi region. They found that the gravels had an average grade of 0.62 ct/m^3 (Watkins, 2009). Currently, Jezzini Minerals and Tibagiana Mineração are using ferries to dredge and concentrate the alluvial sediments in the riverbed. The average value of the diamond mined by these companies is US$150 per carat.

This region is characterized by small crystals (0.1–0.3 ct), and historically there have not been discoveries of large diamonds there (Reis, 1959). Sampling of heavy-mineral concentrates from the Tibagi, Laranjinha, Cinzas, Itararé, and Verde river valleys revealed no traditional kimberlite indicator minerals (Chieregati and Svisero, 1990).

In 1985, a diversion of the river channel allowed mining of the sediments in the Tibagi riverbed. This afforded one of the authors (DPS) the opportunity to examine a group of 2,210 diamonds (about 90% of them gem quality). The crystals were generally well formed and euhedral, with a small number of cleavage fragments.

Existing field evidence of glacial striations on local rocks, and the absence of kimberlite indicator minerals, indicates that diamonds in this region were dispersed as the result of glacial transport (Maack, 1968; Chieregati, 1989; Chieregati and Svisero, 1990; Liccardo et al., 2012). The diamonds' small size, euhedral shape, and overall high quality all suggest that these deposits were subjected to transport processes that favored the retention of the better crystals. In addition, studies have shown that the region contains diamonds with mineral inclusions characteristic of a peridotitic paragenesis, pointing to a kimberlitic initial source (Meyer and Svisero, 1975). Paleogeographic reconstructions (dos

Santos et al., 1996) indicate that the original centers where glacial flow took place were located in southern Africa.

Diamonds in Metasedimentary Rocks. Diamonds from metasedimentary deposits occur mainly around the town of Diamantina in Minas Gerais and in the larger region known as Chapada Diamantina in Bahia (figure 18). Both areas are located along the Serra do Espinhaço, a mountain range extending approximately 1,100 km from the center of Minas Gerais north into Bahia (figure 19). Minor deposits are located at Grão Mogol and Serra do Cabral.

Diamantina. This town is located near the Jequitinhonha River in Minas Gerais. Diamonds occur in metaconglomerates and metabreccias of the Sopa-Brumadinho formation (Mesoproterozoic-age Espinhaço Supergroup; see Chaves and Uhlein, 1991) and in alluvial placers. The primary sources of these diamonds still have not been found.

The diamond-bearing metaconglomerates were deposited in plains and alluvial fans, while the metabreccias were deposited by debris flows, possibly in flat tidal environments (Chaves and Uhlein, 1991). In the Diamantina district, the most important diamond fields are located near São João da Chapada, Sopa, Guinda, Extração, and Datas (Chaves, 1997; Haralyi et al., 1991).

The Sopa metaconglomerates, which are about 12 to 15 m thick, have diamond concentrations ranging from 0.04 to 0.076 ct/m^3. Most of the heavy minerals in these sediments are derived from the crystalline basement rocks. Noteworthy is the absence of the traditional kimberlite indicator minerals that are common in the Coromandel region (Chaves, 1997; Svisero et al., 2005). Diamonds from this district are generally small: 90% weigh less than 2 ct, with only 1% above 8 ct. The typical size range is from 0.55 to 0.85 ct (Chaves and Uhlein, 1991).

Large "megadiamond" crystals, such as those recovered near Coromandel and the Abaeté River, have apparently been found in the Diamantina district (Barbosa, 1991). While there are references to stones as large as 140 ct (Renger, 2005), these discoveries occurred during the 18th century, when record keeping was inadequate or nonexistent. In recent decades, crystals above 10 carats have occasionally been found (Chaves, 1997; Renger, 2005).

Most of the diamond crystals from the area are colorless; some exhibit a green or brown surface coloration. The predominant crystal morphology is a dodecahedral habit followed by other shapes, and the majority is of gem quality (Chaves, 1997).

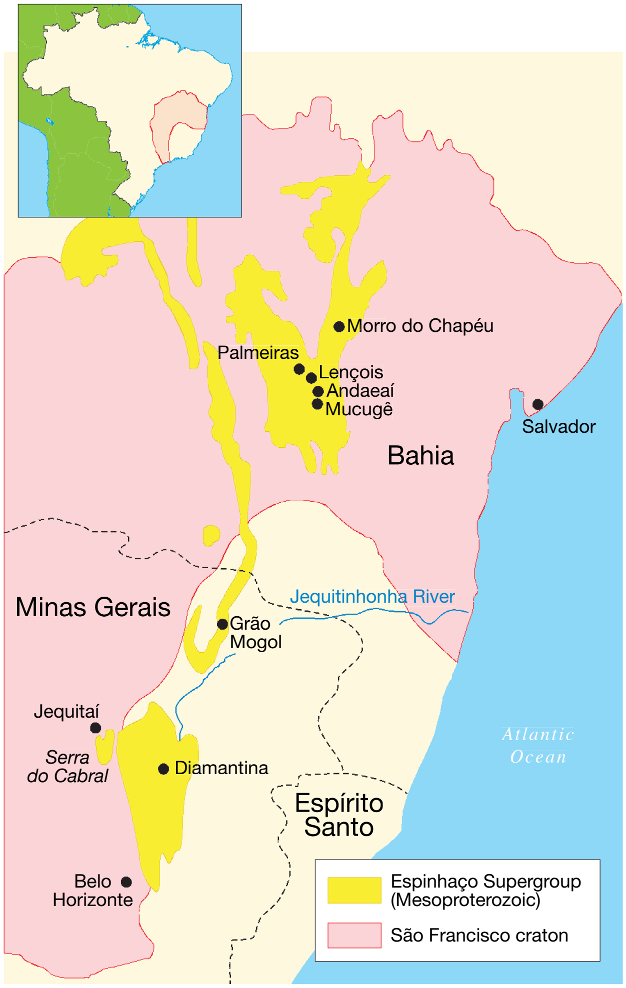

Figure 19. A simplified map of the São Francisco craton, showing the areas covered by sediments of the geological formation called the Espinhaço Supergroup. The locations of several diamond districts are also shown, including Diamantina, Grão Mogol, and Serra do Cabral in Minas Gerais, and the Chapada Diamantina region (Lençóis, Palmeiras, Andaraí, Mucugê and Morro do Chapéu) in Bahia.

Chapada Diamantina. Bahia was Brazil's largest diamond producer in the second half of the 19th century. The most important areas are in Chapada Diamantina in the eastern portion of the state, including the towns of Lençóis, Palmeiras, Andaraí, Mucugê, Utinga, and Morro do Chapéu. Around 1821, diamonds were discovered by German explorers Johann Baptist von Spix and Carl Friedrich Phillipp von Martius in the Sincorá Mountains of the Mucugê River

Figure 20. The polycrystalline form of diamond known as carbonado was first found in Bahia in about 1841. During the late 19th century, this very hard material was of great economic importance for industrial use. Shown here is a privately held collection of samples in the town of Lençois. Photo by Robert Weldon/GIA.

region (Abreu, 1973). The explorers had previously visited the deposits of the Diamantina district; based on geological similarities, they searched for and discovered diamonds in Bahia. Mining began in the Mucugê River and then spread throughout the headwaters of the Upper Paraguaçu River. Around 1842, discovery of the Mucugê River placers caused a rush of about 30,000 miners into the region (Leonardos, 1937; Abreu, 1973). The secondary sources of these diamonds are the metaconglomerates of the Tombador formation (Chapada Diamantina Group, part of the Mesoproterozoic-age Espinhaço Supergroup).

In general, these diamonds have dodecahedral habits, or curved forms intermediate between octahedral and dodecahedral. Colorless crystals are the most common, followed by browns and grays. As in Minas Gerais, there are no kimberlite indicator minerals. The primary source of diamonds from the Serra do Espinhaço remains unknown.

Diamond production in Chapada Diamantina peaked between 1850 and 1860, reaching 70,000 carats per year, followed by alternating phases of activity and decline. In 1929, mechanized mining equipment was installed on the Paraguaçu River. After two years of operation, a yield of 2,008 carats of diamond and 4,109 carats of carbonado was recorded. The diamond content at this location was 1 ct per 28 m^3 of washed gravel; the carbonado content was 1 ct per 14 m^3 (see Abreu, 1973).

Carbonado. Around 1841, miners in Chapada Diamantina discovered that some dark grains in the heavy mineral concentrates had the same hardness as conventional diamonds. They had discovered a new type of "diamond" with completely different physical properties, which they called *carbonado* (Rivot, 1848; Leonardos, 1937; Herold, 2013; see figure 20). Derby and Branner (1905) and Branner (1909) described the washings in Bahia where carbonado and diamond are found.

Carbonado is a polycrystalline aggregate—opaque, solid but porous—consisting of a mixture of diamond, graphite, and amorphous carbon (Haggerty, 2014). Compared with monocrystalline diamonds, which have perfect cleavage and a density of 3.51 g/cm^3, carbonados are free of cleavage and have slightly lower densities (ranging from 3.0 to 3.4 g/cm^3). They can display a glass film, or patina, that is never observed on diamond crystals (Haggerty, 2014). Besides having the same hardness of conventional diamond, carbonado has great toughness, and its resistance to impact made it an excellent material for industrial use by the late 1800s (Herold, 2013).

Carbonados are generally about 1 cm in size but occasionally weigh tens or even hundreds of carats. Decades ago, several "megacarbonados" emerged from the mines of Chapada Diamantina. The greatest was the Sérgio—at 3,167 carats, the largest diamond ever found in nature—discovered at Brejo da Lama near Lençóis in 1905. Another example is the 2,000 ct Casco de Burro, found in Lençóis a year later (Leonardos, 1937).

Although Chapada Diamantina is the traditional source of carbonado, this material is also mined in Minas Gerais, Mato Grosso, Goiás, Paraná, and Roraima (Reis, 1959; Chaves, 1997). Some famous carbonados are the Pontesinha (267.53 ct) from West Rosário, Mato Grosso (Reis, 1959), and an 827.5 ct specimen found in the Abaeté River in 1934 (Leonardos, 1937). In each of these localities, carbonados occur in alluvial deposits associated with normal crystalline diamond (Chaves, 1997).

The production and trade of carbonados in Chapada Diamantina peaked in the second half of the 19th century. At the time France maintained a consulate in Lençóis to facilitate the purchase and export of this material to Europe (Abreu, 1973; Herold, 2013). Production went into decline after 1929, when the price fell by nearly 97% due to increased availability of industrial diamonds from African countries (Reis, 1959). Prospecting dwindled before officially ending on September 17, 1985, with the establishment of Chapada Diamantina National Park (Andrade, 1999).

The origin of carbonados remains controversial. Typical monocrystalline diamond is related to three distinct geological phenomena: (1) transport from the earth's deep interior by explosive volcanism (volcanic diamonds), (2) continental collision followed by subduction and exhumation (metamorphic diamonds), and (3) meteoritic impact (impact diamonds). Recent evidence indicates that carbonado does not fall into any of these categories. Haggerty (2014) suggested an extraterrestrial origin, in which the carbonados formed in a white dwarf star, a carbon-rich exoplanet, or a supernovae explosion during a cosmic bombardment between 4.1 and 3.8 billion years ago.

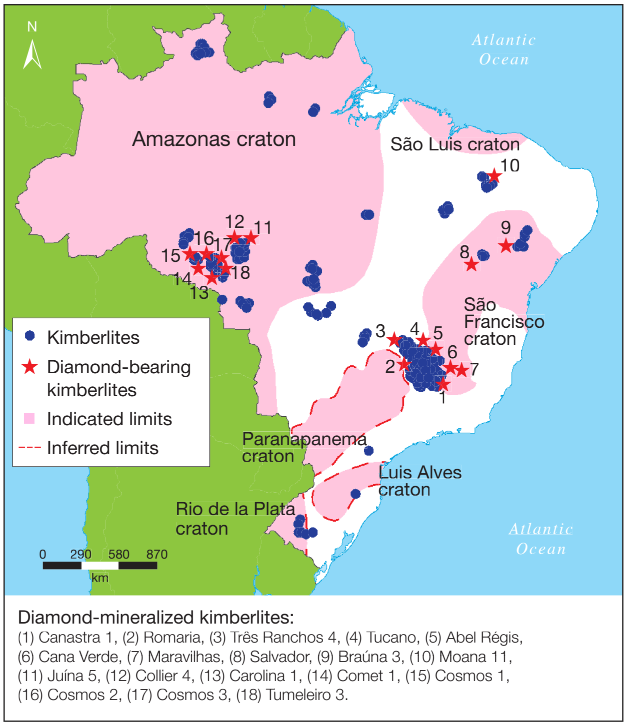

Diamond-mineralized kimberlites:
(1) Canastra 1, (2) Romaria, (3) Três Ranchos 4, (4) Tucano, (5) Abel Régis, (6) Cana Verde, (7) Maravilhas, (8) Salvador, (9) Braúna 3, (10) Moana 11, (11) Juína 5, (12) Collier 4, (13) Carolina 1, (14) Comet 1, (15) Cosmos 1, (16) Cosmos 2, (17) Cosmos 3, (18) Tumeleiro 3.

Figure 21. The distribution of kimberlites in the cratonic areas of Brazil. According to Companhia de Pesquisa de Recursos Minerais (2004), there are 1,212 known kimberlite bodies distributed throughout the country, most of them concentrated in the Alto Paranaíba region of Minas Gerais.

Kimberlite. The systematic exploration of Brazil's primary kimberlite sources only began in the late 1960s. Figure 21 presents a country map showing the locations of known kimberlite pipes. Karfunkel et al. (1994) cited several reasons for this lack of detailed exploration, including the wide areas over which alluvial diamonds are found, the historical control over these areas by garimpeiros who often prevented exploration, the intense tropical weathering and erosion that removed the upper sections of kimberlite pipes, and (until recently) the absence of published information from mining companies searching for kimberlite bodies.

The Redondão kimberlite was the first such body found, during geological mapping in the southern Parnaíba Basin in the 1960s. This pipe is located southeast of the city of Santa Filomena in Piauí state. It has a circular shape, with a diameter of 1,000 m and a negative relief of about 70 m in relation to the surrounding rocks.

Several mining companies have undertaken prospecting for kimberlites in Brazil, especially Pesquisa e Exploração de Minérios S/A (SOPEMI), a De Beers subsidiary that has operated for more than three decades. After finishing its exploration activities, this company transferred its database on 1,212 kimberlites to the state-owned CPRM. About 700 of these kimberlites occur in the Alto Paranaíba region in western Minas Gerais and southeastern Goiás.

The kimberlites of the Alto Paranaíba province, located southwest of the São Francisco craton, were mostly intruded into rocks of the Brasília fold belt. The Vargem 1 kimberlite, in the floodplain of the Vargem Fazenda near Coromandel, was the first body found in the region (Meyer et al., 1991). It is 700 m in diameter and consists of serpentinized kimberlitic rocks that intrude the Vazante phyllite formation (figure 22). The pipe contains abundant pyrope garnet, magnesian ilmenite, diopside, and chromite, as well as some zircon. The diamond potential of this body is still being investigated.

Other kimberlite bodies in the Coromandel region are Três Ranchos 4 (Fazenda Alagoinha), Limeira, and Indaiá. These consist of hypabyssal kimberlite rock facies with isotopic characteristics intermediate between Group 1 and Group 2 kimberlites (Bizzi et al., 1993; Melluso et al., 2008; Guarino et al., 2013).

Três Ranchos 4 was the first kimberlite in the area known to contain diamonds (Gonzaga and Tompkins, 1991), though not in sufficient quantity for commercial exploitation. Another well-known kimberlite is Abel Regis, a mineralized intrusion in the Serra da Mata da Corda (Cookenboo, 2005). This

Figure 22. An exposed portion of the Vargem 1 kimberlite seen on the banks of the Santo Inácio River near Coromandel. The kimberlite pipe, which has decomposed and altered to serpentine, giving it a brownish green appearance, is only exposed by removing several meters of overlying sediments. Material removed from the weathered kimberlite is panned to collect the heavy mineral concentrate. When the pan is turned over, the concentrate is seen as grains of red pyrope garnet and black ilmenite. The concentrate is then checked for diamonds. Photos by Robert Weldon/GIA.

pipe is located 20 km northwest of Coromandel (again, see figure 14), and it is intruded into the Neoproterozoic-age Bambuí Group (CPRM, 2013). It has an elliptical shape and an area of approximately 1 km^2. Serpentinization of the kimberlite yielded a green saprolite clay containing fragments of pyrope, magnesian ilmenite, and diopside. Most of the garnets from this kimberlite, and from several others of the Upper Paranaíba region, are lherzolitic in nature (G9). They are followed by eclogitic garnets (G4 and G5); G10 garnets are either rare or absent (Cookenboo, 2005; Svisero et al., 2005). These G-numbers represent a statistical classification of garnets from kimberlites and associated xenoliths, developed by Dawson and Stephens (1975), that is used in diamond exploration. According to local miners, diamonds up to 20 carats have been found in ravines in the area of the intrusion.

Other mineralized kimberlite pipes include Tucano, located west of Carmo do Paranaíba (Cookenboo, 2005), and the Romaria kimberlite located northeast of the Romaria mine (F.M. Coelho, pers. comm., 2008). Another important diamond-bearing kimberlite is the Canastra 1, located in the headwaters of the São Francisco River near São José do Barreiro in the Serra da Canastra region (Cookenboo, 2005). It intrudes quartzites of the Canastra Group (Barbosa et al., 1970) that are part of the Brasília fold belt of Mesoproterozoic age (Chaves et al., 2008). Canastra 1, dated at 120 million years, comprises two subcircular bodies oriented along the regional northwest-southeast trend of the Canastra Group metasediments. Trial mining conducted in 2007 indicated the presence of 16 carats of diamond per 100 tons of rock (Chaves et al., 2008). Eighty percent of the recovered diamonds were gem quality; the crystals were octahedral in shape and colorless to faint yellow. These characteristics make the diamonds from this area some of Brazil's most valued. Other mineralized bodies include the Maravilhas kimberlite located near the city of the same name, and the Cana Verde pipe located north of the city of Luz, both in the southern portion of the São Francisco craton (O. Barbosa, pers. comm., 1978).

Several diamond-bearing kimberlites occur in Juína, where they intrude into the Rio Negro–Juruena mobile belt (1.55 to 1.8 Ga). Among others, the Collier 4 kimberlite has an average grade of 0.62 ct/m^3. Mining companies have recovered 6,000 diamonds from this pipe, including a 17.08 ct stone (Costa, 2013). The pipe contains sublithospheric diamonds, which have mineral inclusions and other features that suggest they formed at great depth (Bulanova et al., 2010). Another pipe, Juína 5, also contains sublithospheric diamonds—mainly contact-twinned and octahedral crystals—that appear corroded and are covered with a graphite film (Thomson et al., 2014).

Rondônia has 62 kimberlites distributed in the Pimenta Bueno, Colorado do Oeste, and Ariquemes fields. According to Neto et al. (2014), it ranks fourth in terms of known occurrences after Minas Gerais (765), Goiás (197), and Mato Grosso (102). Among the mineralized kimberlites in Rondônia, perhaps the most important is the Carolina 1 pipe, located near Pimenta Bueno. It intrudes into rocks of the Rio Negro–Juruena mobile belt (Tassinari and Macambira, 1999); the age of the intrusion is 230 Ma (Hunt et al., 2009). Although diamond-bearing, this kimberlite is characterized by the absence of G10 garnets in the heavy mineral concentrates obtained by washing the ore. Such garnets are rare in other kimberlites in Minas Gerais, Bahia, and Mato Grosso (Cookenboo, 2005; Svisero et al., 2005). Analysis of a small batch of diamonds indicated that the predominant color is gray (48%), followed by colorless (23%) and others (Hunt et al., 2009). Other mineralized pipes include Cosmos 1, 2, and 3; Comet 1; and Tumeleiro 3 (Neto et al., 2014).

There are two areas with kimberlite concentrations in Piauí. The first is located in the southern region where, besides the famous Redondão kimberlite, several intrusions are distributed in the municipalities of Santa Filomena, Gilbués, Currais, and Baixa Grande do Ribeiro. The second is in the eastern region, covering the municipalities of Picos, Ipiranga do Piauí, Elesbão Veloso, Jardim do Mulato, and Regeneração. The Moana 11 kimberlite near Picos contains diamonds, but it has been little studied to date.

Diamond-bearing kimberlites also occur in Bahia State (Watkins, 2009) in the northeastern São Francisco craton. The Salvador 1 kimberlite, located near Barra do Mendes, intrudes metaconglomerates of the Tombador formation. Rb/Sr dating of the intrusion indicates an age of 1,152 Ma, making it the oldest known intrusion in the country. Also, the pipe's intrusion into rocks in the Serra do Espinhaço provides evidence of a period of diamond-bearing kimberlite magmatism generated in the region.

The most important kimberlite pipe at present is Braúna 3 (see box B), which contains diamonds in commercial concentrations. This pipe is located about 260 km from Salvador, in the northeast portion of the São Francisco craton. It occurs as part of a kimberlite field consisting of three pipes and 19 dikes, all diamond bearing and intruding the Nordestina granodiorite (a batholith of Paleoproterozoic age; see Donatti-Filho et al., 2013). The dikes range from 0.5 to 5.0 m thick, and they are controlled by northwest-trending fractures that can be followed for 15 km. All volcanic pipes and dikes of the Braúna field belong to the hypabyssal facies. The age of the kimberlites, obtained by U/Pb dating of perovskites, is 642 +/- 6 Ma. The Braúna kimberlites have mineralogical and geochemical similarities to those in the Guaniamo region of Venezuela (Donatti-Filho et al., 2013). The Braúna 3 pipe is now being commercially exploited by Lipari Mineração Ltda.

PRODUCTION

Since the discovery of diamonds in South Africa, Brazil has never regained its standing, and in recent decades it has accounted for less than 1% of global production. According to *Minérios & Minerales* (2014), the estimated production between 1725 and 1870 was 50,000 to 250,000 carats per year; if the larger value is assumed, this would yield a total of 37.5 million carats over the 150-year period. As most Brazilian occurrences are alluvial, it has always been difficult to determine the amount and commercial value of what is recovered.

Production increased with the discovery of diamonds in other Brazilian states in the 19th and 20th centuries, but under limited government oversight. Production in the early 1970s was approximately 300,000 carats per year, before jumping to 670,000 carats in 1980. This significant increase was due to the Juína mines, and Mato Grosso became the country's principal source of diamonds. In recent years, production has declined significantly, to less than 32,000 carats in 2015 (http://kimberleyprocess

BOX B: THE FIRST KIMBERLITE MINE IN BRAZIL

Figure B-1. A recent view of the open pit at the Lipari diamond mine near Nordestina in Bahia (left). The Braúna 3 kimberlite pipe lies beneath serpentinized soil and sedimentary rocks. Also shown is the processing plant on-site where kimberlite ore is broken down to recover the diamonds (right). Photos by Andrew C. Johnson, courtesy of Lipari Mineração Ltda.

Explosive volcanic eruptions are the transport mechanism that brings diamonds to the earth's surface. Most of these kimberlite pipes are not diamondiferous or commercially viable to exploit. But some are, and most of the annual production of diamonds today comes through mining of these pipes, particularly in southern Africa (Linde et al., 2014).

Economic diamondiferous pipes in Brazil have until recently remained elusive. With the discovery of diamond-bearing kimberlites in South Africa in 1867, Brazil lost its standing as the world's primary source. Its total production, an estimated 45 million carats over three centuries, is alluvial in nature and has mostly been recovered through the work of garimpeiros (K. Johnson, pers. comm., 2014).

This situation is changing. The consequences of these transformations may have implications for Brazil's reemergence as a global producer of diamonds.

Nordestina Kimberlite Diamonds. Following a few years of exploration and development by Lipari Mineração Ltda., a new mine has been established there to exploit a kimberlite field called the Braúna complex in the São Francisco craton. De Beers initially explored the largest of these kimberlites—Braúna 3, with a surface area of 15,000 square meters—in the early 1990s (figure B-1). The

Figure B-2. Left: A selection of rough Brazilian diamonds, 262 carats total, photographed in Antwerp. The crystal at the center weighs 7.46 ct. The diamonds are from the Braúna kimberlite field near Nordestina. Right: These larger diamond crystals from the Lipari mine include a 3.87 ct resorbed yellow crystal, a 3.49 ct octahedral crystal, and a 2.94 ct macle. Photos by Robert Weldon/GIA, courtesy of Aftergut N. & Zonen and Lipari Mineração Ltda.

operating license was sold in 2004 to Valdiam Resources Ltd., which runs the operation today as the Lipari mine.

"We have invested $45 million in exploration, development, and drilling," says Ken Johnson, president and CEO of Lipari. "Our attention is on Braúna 3, where we've developed a resource containing an estimated 2.5 million carats of high-quality diamonds. In 2014, our initial bulk sampling activities yielded some 2,500 diamonds with an average value of over US$322 per carat. Since then, much has changed, with our accrued exploration and development costs at about US$ 70 million by early 2017."

Commercial production at Braúna started in July 2016, and the projected production for 2017 is 210,000 carats valued at US$42 million. "We are now recovering diamonds from the central zone of the kimberlite pipe, and our current average sale value of $200 per carat is in line with our expectations" (figure B-2).

The new mine is expected to produce up to 340,000 carats a year during an open-pit mine lifetime of seven years, and Johnson estimates a nearly US$750 million revenue stream. "The Braúna 3 project has excellent potential to transition from an open pit to an underground mine. Our current exploration efforts are focused on development of additional diamond resources below the bottom of the open pit (at a depth of 260 meters)—identification of these resources will support a decision to transition to an underground mine." In addition to the current open pit, 22 other kimberlite pipes have been discovered so far in the vicinity.

Future of Large-Scale Kimberlite Mining in Brazil. More than 1,300 kimberlites are known in Brazil, though only about 70 are expected to yield diamond on a commercial basis. Kimberlite mining is a new scenario, but one that offers advantages over small-scale artisanal mining. For one, mining occurs in a known location, and the reserves can be far better estimated than in the scattered alluvial deposits around Brazil. "In 2014, revenue from taxation on small-scale activities was very small (about US$78 per carat on average value for export), with even lower revenue in 2015" Johnson explained. He believes it could be, and should be, much higher. Preliminary 2016 data from the Brazilian Ministry of Mines and Energy (MME) indicate an average value of US$727 per carat, which is a significant increase in value over previous years. This would rank Brazil fourth in the world for the average value of rough diamond production.

Many of the traditional obstacles to diamond mining in Brazil will be overcome, added Johnson. "We will put kimberlite production on the map and will go on record as the first company to develop a diamond mine in a kimberlite primary source of rock. As such it is an historic event for Brazil, and for us."

statistics.org). This number is expected to increase significantly with the mining of the Braúna 3 kimberlite in Bahia. Open-pit mining is expected until 2021, with the potential for mining to continue underground.

Brazil has participated in the Kimberley Process Certification Scheme (KPCS) since 2003. Underreporting of annual production, along with corruption and criminal activity in diamond exporting and sales, has been endemic (see Partnership Africa Canada, 2005, 2006). Experts believe the stringent certification requirements of the KPCS have caused exports to be underreported, particularly for valuable material such as fancy-color diamonds (Gomes dos Santos, 2015).

Considering the widespread distribution and mode of occurrence of Brazilian diamonds, and the lack of historical controls over mining, underreporting is not surprising. In countries where diamonds are recovered from kimberlite pipes, control is more easily maintained over the small area. But Brazil is one of the world's largest countries, and the secondary deposits cover vast areas. Alluvial mining and initial diamond sales are carried out by garimpeiros, individually or in small groups, with no large companies exerting control. With Brazil's long coastline and remote borders with neighboring countries, diamond smuggling is an ever-present concern.

CONCLUSIONS

Brazil's significance as a diamond producer spans three centuries, making it the world's longest continuous commercial source of diamonds (figure 23). Brazil reached its peak production in the mid-1700s as adventurers and explorers made their way into the country's vast interior. Most of its diamond supply—then and now—comes from the multitude of alluvial sources spread across the country.

Alluvial diamonds have been mined in most Brazilian states since the beginning of the 18th century, when the colony was still under Portuguese rule. Besides alluvial occurrences, there are other important deposits related to conglomerates (Romaria, Minas Gerais), glacial rocks (Tibagi, Paraná), and mid-Paleozoic metasedimentary rocks (Diamantina District, Minas Gerais and Chapada Diamantina, Bahia). Among the alluvial deposits, the Coromandel and Abaeté regions have occasionally yielded "mega-diamonds" reaching hundreds of carats in size, as well as crystals with pink, yellow, green, red, and blue "fancy colors." The mines of the Juína region in Mato Grosso are known for the quantity of their production.

Figure 23. Brazilian diamonds were shipped to Europe from the 1720s through the 1860s. The rose-cut diamonds, seen in this necklace and brooch, are part of the Danish crown jewels on display in the Rosenborg Castle in Copenhagen. The necklace was originally worn by Queen Louise, consort of King Frederik VIII (1843–1912). The brooch could be taken apart and the components worn separately. The jewelry was fashioned by the firm of C.M Weishaupt & Söhne of Hanau, Germany in 1840 using diamonds most likely of Brazilian origin. Photo by Iben Kaufmann.

Although systematic exploration of Brazilian kimberlites began relatively late, there are several known mineralized bodies in the states of Minas Gerais, Bahia, Mato Grosso, Rondônia, Goiás, and Piauí. Large mining groups such as De Beers have worked in Brazil but never at a reported kimberlite source. However, more than 1,300 kimberlite pipes have been identified through exploration in the last century.

The past three centuries have shown the importance of mining to Brazil's economic development. Since the beginning, garimpeiros have worked the remote regions, founding towns that later became cities such as Diamantina, Coromandel, and Juína. In the ongoing search for new mineral deposits, the garimpeiros pushed west beyond the boundaries of the Treaty of Tordesilhas, helping expand Brazilian territory. Beginning in the 1700 and 1800s, Brazilian diamonds were used in European jewelry—the larger and better-quality diamonds found their way into royal jewelry collections at a time when production from India had ceased and the African deposits had yet to be discovered.

Another important development was the discovery of carbonado in Chapada Diamantina in the 1840s. In the early 1990s, sublithospheric diamonds were discovered in the kimberlites of Juína in Mato Grosso. These unusual diamonds contain inclusions of minerals formed in the transition zone and lower mantle. Their study has increased our awareness of the mineralogy of Earth's interior.

Brazil's diamond production remains enigmatic. The country's enormous expanse, and the fact that diamonds have been found at numerous alluvial sources, weathered over the millennia from their primary sources and dispersed throughout the continent in riverbeds and conglomerates, contributes to the confusion. A lack of expertise in large-scale diamond mining, and industry regulation, have also hampered growth in the sector (A. Epstein, pers. comm., 2015). According to Constance (2011), recent production has stalled for several reasons: government efforts to comply with the Kimberley Process Certification Scheme, its crackdown in 2006 on diamond smuggling, and the 2008 global financial crisis. When combined with the shortage of skilled labor and the limited availability of geological resources that can be applied to mineral exploration, an expanded diamond mining program seems unlikely in the near future.

However, Brazil's diamond production may yet be rewritten in the early 21st century. Despite considerable geological fieldwork, the sources of most alluvial diamonds in Brazil are still uncertain. As large-scale mining will be conducted in at least one location, the traditional scene of garimpeiros panning for alluvial diamonds likely represents a vanishing way of life.

ABOUT THE AUTHORS
Dr. Svisero is a professor in the Institute of Geosciences of the University of São Paulo, Brazil. Dr. Shigley is a distinguished research fellow, and Mr. Weldon is manager of photography and visual communications, at GIA in Carlsbad, California.

ACKNOWLEDGMENTS
The authors wish to thank the following individuals: Ken Johnson, CEO and president of Lipari Mineração Ltda.; Lauro de Freitas; and José Paulo Donatti Filho, Lipari exploration manager at Nordestina, for the opportunity to visit the Lipari kimberlite mine. Ari Epstein of Antwerp World Diamond Centre for insight into Brazil's diamond industry. Dr. Stephen Haggerty of Florida International University in Miami for information on carbonado. Prof. Miguel A.S. Basei for suggestions on the geological map in figure 9. Dr. Otavio Barbosa, Fernando M. Coelho, and Rafael Rodrigues for information on Brazilian kimberlites. Al Gilbertson of GIA in Carlsbad for the history of the Old Mine cut presented in box A, and for information on Anthony Knivet. Francisco de Assis Ribeiro and Robledo Delatorre Ribeiro of Gar Mineração in Belo Horizonte for the opportunity to visit alluvial diamond mining operations in Minas Gerais, and for selections of rough diamonds made available for photography. Dr. Joachim Karfunkel of Federal University of Minas Gerais in Belo Horizonte, and Dr. Donald B. Hoover of Springfield, Missouri, for discussions of Brazilian diamond geology. Luis Alberto de Deus Borges of Petrus Mineração, and Giovanni de Deus Borges of Gem Eireli Company, Patos de Minas, for information on diamond occurrences in Minas Gerais and for selections of rough diamonds made available for photography. Rui Galopim de Carvalho in Lisbon and Niels Ruddy Hansen in Brøndby, Denmark, for assistance in obtaining images of European historical jewelry.

REFERENCES

Abreu S.F. (1973) *Recursos Minerais do Brasil*. Editora Edgard Blucher, São Paulo, two volumes.

de Almeida F.F.M. (1967) *Origem e evolução da Plataforma Brasileira*. Bulletin of the National Department of Mineral Production (DNPM)/Division of Geology and Mineralogy (DGM), No. 241, Rio de Janeiro.

de Almeida F.F.M., Hasui Y., de Brito-Neves B.B. (1981) Brazilian structural provinces: An introduction. *Earth-Science Reviews*, Vol. 17, No. 1/2, pp. 1–29, http://dx.doi.org/10.1016/0012-8252(81)90003-9

Andrade C.M. (1999) Aspectos mineralógicos, gemológicos e econômicos de diamantes e carbonados da Chapada Diamantina, Bahia. MSc. thesis, Institute of Geosciences, University of São Paulo, 165 pp.

Balfour I. (2011) *Famous Diamonds*. Antique Collectors' Club Ltd., London.

Ball S.H. (1929) Diamond mining in Brazil. *Jewelers' Circular*, Vol. 99, No. 11, pp. 37–39, 45.

Barbosa O. (1991) *Diamante no Brasil: Histórico, Ocorrência, Prospecção e Lavra*. Companhia de Pesquisa de Recursos Minerais (CPRM), Brasília.

Barbosa O., Braun O.P.G., Dyer R.C., Cunha C.A.B.R. (1970) *Geologia da região do Triângulo Mineiro*. Bulletin DNPM, No. 136, Rio de Janeiro.

Berbert C.O., Svisero D.P., Sial A.N., Meyer H.O.A. (1981) Upper mantle material in the Brazilian Shield. *Earth-Science Reviews*, Vol. 17, No. 1/2, pp. 109–133, http://dx.doi.org/10.1016/0012-8252(81)90008-8

Bizzi L.A., Smith C.B., Wit M.J., Armstrong R.A., Meyer H.O.A. (1993) Mesozoic kimberlites and related alkali rocks in the south-western São Francisco craton, Brazil. In H.O.A. Meyer and O.H. Leonardos, Eds., *Proceedings of the 5th International Kimberlite Conference*, Araxá (MG), CPRM Special Publication, Vol. 2, pp. 156–171.

Boxer C.R. (1962) *The Golden Age of Brazil, 1695–1750: Growing Pains of a Colonial Society*. University of California Press, Oakland.

Branner J.C. (1909) The diamond-bearing highlands of Bahia. *Engineering and Mining Journal*, Vol. 87, No. 20, pp. 981–986 and No. 21, pp. 1029–1033.

——— (1919) Outlines of the geology of Brazil to accompany the geologic map of Brazil. *Bulletin of the Geological Society of America*, Vol. 30, pp. 189–338.

de Brito-Neves B.B., Cordani U.G. (1991) Tectonic evolution of South America during the late Proterozoic. *Precambrian Research*, Vol. 53, No. 1/2, pp. 23–40, http://dx.doi.org/10.1016/0301-9268(91)90004-T

Bulanova G.P., Walter M.J., Smith C.B., Kohn S.C., Armstrong, L.S., Blundy J., Gobbo L. (2010) Mineral inclusions in sublithospheric diamonds from Collier 4 kimberlite pipe, Juina, Brazil: Subducted protoliths, carbonated melts and primary kimberlite magmatism. *Contributions to Mineralogy and Petrology*, Vol. 160, No. 4, pp. 489–510, http://dx.doi.org/10.1007/s00410-010-0490-6

Burton R.F. (1869) *Explorations of the Highlands of the Brazil, with a Full Account of the Gold and Diamond Mines*. Tinsley Brothers, London, two volumes.

Calógeras J.P. (1904) *As Minas do Brasil e sua Legislação*, Vol. 1. National Press, Rio de Janeiro.

Cassedanne J.P. (1985) Chercheurs de diamant au Brésil. *Monde et Mineraux*, No. 70, pp. 36–39.

——— (1989) Diamonds in Brazil. *Mineralogical Record*, Vol. 20, No. 5, pp. 325–336.

de Castro Sarmento J. (1731) A letter from Jacob de Castro Sarmento, M.D. and F.R.S., to Cromwell Mortimer, M.D. and Sec. R.S., concerning diamonds found in Brazil. *Philosophical Transactions of the Royal Society of London*, Vol. 37, pp. 199–201.

Cattelle W.R. (1903) *Precious Stones: A Book of Reference for Jewellers*, J.B. Lippincott & Co., Philadelphia.

Chaves M.L.S.C. (1997) Geologia e mineralogia do diamante da Serra do Espinhaço em Minas Gerais. PhD thesis, Institute of Geosciences, University of São Paulo.

Chaves M.L.S.C., Uhlein A. (1991) Depósitos diamantíferos da região do alto/médio Rio Jequitinhonha, Minas Gerais. In C. Schobbenhaus, E.T. Queiroz, and C.E.S. Coelho, Eds., *Principais Depósitos Minerais do Brasil*, Vol. 4, DNPM/CPRM, Brasília, pp. 117–138.

Chaves M.L.S.C., Karfunkel J., Hoppe A., Hoover D.B. (2001) Diamonds from the Espinhaço Range (Minas Gerais, Brazil) and their redistribution through the geologic record. *Journal of South American Earth Sciences*, Vol. 14, No. 3, pp. 277–289, http://dx.doi.org/10.1016/S0895-9811(01)00024-4

Chaves M.L.S.C., Brandão P.R.G., Girodo A.C., Benitez L. (2008) Kimberlito Canastra-1 (São Roque de Minas, MG): Mineralogia e reservas diamantíferas. *Revista Escola de Minas*, Vol. 61, No. 3, pp. 357–364, http://www.scielo.br/pdf/rem/v61n3/a14

Cheney G.A. (2005) *Journey on the Estrada Real – Encounters in the Mountains of Brazil*. Chicago Review Press, Chicago.

Chieregati L.A. (1989) Aspectos mineralógicos, genéticos e econômicos das ocorrências diamantíferas da região nordeste do Paraná e sul de São Paulo. MSc thesis, Institute of Geosciences, University of São Paulo.

Chieregati L.A., Svisero D.P. (1990) Estudo de minerais pesados da região diamantífera do Rio Tibagi (PR) e as possibilidades de existência de fontes primárias de diamante na região. *Acta Geológica Leopoldênsia*, Vol. 13, No. 10, pp. 171–186.

Coelho F.M. (2010) Aspectos geológicos e mineralógicos da mina de diamantes de Romaria, Minas Gerais. MSc thesis, Institute of Geosciences, University of São Paulo.

Companhia de Pesquisa de Recursos Minerais (2004) *Cartas Geológicas do Brasil ao Milionésimo*, Escala 1:1.000.000, Brasília, Distrito Federal, Brasil.

Constance D. (2011) Brazilian diamond mining stalls. *Rapaport Magazine*, Vol. 34, No. 11, pp. 56–60.

Cookenboo H.O. (2005) Exploration for diamond-bearing kimberlite in the Brasilia Belt of Minas Gerais. *Proceedings of the Fourth Brazilian Diamond Geology Symposium*, Bulletin No. 14, Diamantina, Brazil, pp. 51–53.

Cordani U.G., de Brito-Neves B.B., D'Agrella-Filho M.S. (2003) From Rodinia to Gondwana: A review of available evidence from South America. *Gondwana Research*, Vol. 6, No. 2, pp. 275–283, http://dx.doi.org/10.1016/S1342-937X(05)70976-X

Cordani U.G., Teixeira W., D'Agrella-Filho M.S., Trindade R.I. (2009) The position of the Amazonian craton in supercontinents. *Gondwana Research*, Vol. 15, No. 3/4, pp. 396–407, http://dx.doi.org/10.1016/j.gr.2008.12.005

Cornejo C., Bartorelli A. (2010) *Minerals and Precious Stones of Brazil*. Solaris Cultural Publications, São Paulo.

Costa V.S. (2013) Mineralogia e petrologia de xenólitos mantélicos da Província Kimberlítica de Juína, MT. PhD thesis, Institute of Geosciences, University of São Paulo.

Dawson J.B., Stephens W.E. (1975) Statistical classification of garnets from kimberlites and associated xenoliths. *Journal of Geology*, Vol. 83, No. 5, pp. 589–607, http://dx.doi.org/ 10.1086/628143

DeJean J.E. (2005) *The Essence of Style: How the French Invented High Fashion, Fine Food, Chic Cafe*s*, Style, Sophistication and Glamour*, Simon Shuster, New York.

Delgado I. de M., Pedreira A.J., Thorman C.H. (1994) Geology and mineral resources of Brazil: A review. *International Geology Review*, Vol. 36, No. 6, pp. 503–544, http://dx.doi.org/10.1080/00206819409465474

Derby O.A. (1878) Geologia da região diamantífera do Paraná, Brazil. *Archivo Museu Nacional do Rio de Janeiro*, Vol. 3, pp. 89–98.

——— (1898) Brazilian evidence on the genesis of the diamond. *Journal of Geology*, Vol. 6, No. 2, pp. 121–146.

——— (1906) The Serra do Espinhaço, Brazil. *Journal of Geology*, Vol. 14, No. 5, pp. 374–401.

Derby O.A., Branner J.C. (1905) The geology of the diamond and carbonado washings of Bahia, Brazil. Economic Geology, Vol. 1, No. 2, pp. 134–142.

Des Genettes H.R. (1859) Diamantes na Bagagem. *Revista do Archivo Publico Mineiro*, Vol. 4, Imprensa Official de Minas Gerais, Belo Horizonte, Brazil, pp. 287–292.

Diamond carriers (1842) *Penny Magazine*, Vol. 11, (March 12), pp. 100–101.

Diderot D. (1771) *Recuiel de Plances, sur les Sciences, les Arts Liberauz, et les Arts Mechaniques*. Briasson, Paris.

Dodge F.H. (1922) Ouro Preto – The old capital of Minas Gerais, Brazil. *The Pan-American Magazine and New World Review*, Vol. 34, No. 4, pp. 29–38.

Donatti-Filho J.P., Tappe S., Oliveira E.P., Heaman L.M. (2013) Age and origin of the Neoproterozoic Brauna kimberlites: Melt generation within the metasomatized base of the São Francisco Craton, Brazil. *Chemical Geology*, Vol. 353, No. 1, pp. 19–35, http://dx.doi.org/10.1016/j.chemgeo.2012.06.004

Draper D. (1911) The diamond-bearing deposits of Bagagem and Agua Suja in the State of Minas Gerais, Brazil. *Transactions of the Geological Society of South Africa*, Vol. 14, pp. 8–19.

Draper T. (1949) Diamond mining in Brazil. *G&G*, Vol. 7, No. 8, pp. 231–242.

——— (1950a) The gemstones of Brazil. *G&G*, Vol. 6, No. 12, pp. 369–375.

——— (1950b) The origin and distribution of diamonds in Brazil.

G&G, Vol. 6, No. 10, pp. 298–306.

——— (1951) The diamond mines of Diamantina – Past and present. *G&G*, Vol. 7, No. 2, pp. 49–57.

Dufrenoy A. (1855) Note sur un cristal de diamant provenant du district Bogagem, au Brésil. *Comptes Rendus Hebdomadaires des Séances de l'Académie des Sciences*, Vol. 40, No. 1, pp. 3–5.

Dupont H. (1991) Jazida aluvionar de diamante do rio Jequitinhonha em Minas Gerais. In C. Schobbenhaus, E.T. Queiroz, and C.E.S. Coelho, Eds., *Principais Depósitos Minerais do Brasil*, Vol. 4. DNPM/CPRM, Brasília, pp. 139–148.

von Eschwege W.L. (1833) *Pluto Brasiliensis*. G. Reimer, Berlin.

Fausto B. (1999) *A Concise History of Brazil*. Cambridge University Press, Cambridge.

Feitosa V.M.N., Svisero D.P. (1984) Conglomerados diamantíferos da região de Romaria, Minas Gerais. *Proceedings of the 33rd Brazilian Congress of Geology*, Rio de Janeiro, Vol. 10, pp. 4995–5005.

Fernandez-Armesto F. (2009) *Columbus*. Oxford University Press, Oxford.

Galopim de Carvalho R. (2006) The Bragança 'diamond' discovered? *G&G*, Vol. 42, No. 3, pp. 132–133.

de Galvão Bueno A. (1922) The bandeirantes: Their deeds and descendants. *Bulletin of the Pan American Union*, Vol. 54, pp. 456–480.

Gomes dos Santos E. (2015) The Kimberley Process Certification System – KPCS and diamond production changes in selected African countries and Brazil. *Revista Escola de Minas*, Vol. 68, No. 3, pp. 279–285, http://dx.doi.org/10.1590/0370-44672015680024

Gonzaga G.M., Tompkins L.A. (1991) Geologia do diamante. In C. Schobbenhaus, E.T. Queiroz, and C.E.S. Coelho, Eds., *Principais Depósitos Minerais do Brasil*, Vol. 4. DNPM/CPRM, Brasília, pp. 53–116.

Gonzaga G.M., Teixeira N.A., Gaspar J.C. (1994) The origin of diamonds in western Minas Gerais, Brazil. *Mineralium Deposita*, Vol. 29, No. 5, pp. 414–421, http://dx.doi.org/10.1007/BF01886959

Gorceix H. (1882) Brazilian diamonds and their origins. *Popular Science Monthly*, Vol. 21, No. 37, pp. 610–620.

Grazziotin H.F., Andrade J.B.F. (2011) Recursos minerais e indicadores metalogenéticos da folha NA.20-X-A-III, Vila de Tepequém. *Thirteenth Brazilian Congress of Geochemistry*, Expanded Abstracts, pp. 1725–1728.

Guarino V., Wu F-Y., Lustrino M., Melluso L., Brotzu P., Gomes C. de B., Ruberti E., Tassinari C.C.G., Svisero D.P. (2013) U-Pb ages, Sr-Nd-isotope geochemistry, and paragenesis of kimberlites, kamafugites and phlogopite-picrites of the Alto Paranaíba igneous province, Brazil. *Chemical Geology*, Vol. 353, No. 1, pp. 65–82, http://dx.doi.org/10.1016/j.chemgeo.2012.06.016

Haggerty S.E. (2014) Carbonado: Physical and chemical properties, a critical evaluation of proposed origins, and a revised genetic model. *Earth-Science Reviews*, Vol. 130, pp. 49–72, http://dx.doi.org/10.1016/j.earscirev.2013.12.008

Haralyi N.L.E. (1991) Os diamantes de Juína, Mato Grosso. In C. Schobbenhaus, E.T. Queiroz, and C.E.S. Coelho, Eds., *Principais Depósitos Minerais do Brasil*, Vol. 4. DNPM/CPRM, Brasília, pp. 155–160.

Haralyi N.L.E., Hasui Y., Morales N. (1991) O diamante pré-cambriano da Serra do Espinhaço, Minas Gerais. In C. Schobbenhaus, E.T. Queiroz, and C.E.S. Coelho, Eds., *Principais Depósitos Minerais do Brasil*, Vol. 4. DNPM/CPRM, Brasília, pp. 209–222.

Haralyi N.L.E., Hasui Y., Rodrigues A. S. (1994) O segundo maior diamante brasileiro: 602 Quilates. *Geociências*, Vol. 13, No. 1, pp. 213–221.

Harte B. (2010) Diamond formation in the deep mantle - The record of mineral inclusions and their distribution in relation to mantle dehydration zones. *Mineralogical Magazine*, Vol. 74, No. 2, pp. 189–215, https://dx.doi.org/10.1180/minmag.2010.074.2.189

Hasui Y., (2012) Compartimentação geológica do Brasil. In Y. Hasui, C.D. Carneiro, F.F.M. de Almeida, and A. Bartorelli, Eds., *Geologia do Brasil*, Editora Beca, São Paulo, pp. 112–122.

Herold M.W. (2013) The black diamonds of Bahia (carbonados) and the building of Euro-America: A half-century supply monopoly (1880-1930s). *Commodities of Empire Working Paper*, No. 21, 37 pp., Ferguson Center for African and Asian Studies, The Open University, Milton Keynes, United Kingdom, http://commoditiesofempire.org.uk/publications/working-papers/working-paper-21/

Hofmeester K. (2013a) Working for diamonds from the 16th to the 20th century. From Working on *Labor: Essays in Honor of Jan Lucassen*. Brill Publishers, Leiden, pp. 19–46.

Hofmeester K. (2013b) Shifting trajectories of diamond processing: From India to Europe and back, from the fifteenth century to the twentieth. *Journal of Global History,* Vol. 8, No. 1, pp. 25–49.

Hoover D.B., Karfunkel J. (2009) Large Brazilian diamonds. *Australian Gemmologist*, Vol. 23, No. 10, pp. 440–446.

Hunt L., Stachel T., Morton R., Grütter H., Creaser R.A. (2009) The Carolina kimberlite, Brazil – Insights into an unconventional diamond deposit. *Lithos*, Vol. 112, Supp. 2, pp. 843–851, http://dx.doi.org/10.1016/j.lithos.2009.04.018

Hussak E. (1894) Sobre o depósito diamantífero de Água Suja perto de Bagagem, Minas Gerais. In L. Cruls, Ed., *Relatório da Commissão Exploradora do Planalto Central do Brasil*, Annex 5, Rio de Janeiro, pp. 281–319.

Inveness J (2014). Reinterpreting the role of non-Europeans in the 'English private trade': The globalisation of diamonds via East India Company networks in the late-seventeenth century. Unpublished manuscript, accessed July 17, 2016, https://www.academia.edu/8372856/The_globalisation_of_diamonds_via_East_India_Company_networks_in_the_late-seventeenth_century_Reinterpreting_the_role_of_non-Europeans_in_the_English_private_trade

Janse A.J.A. (2007) Global rough diamond production since 1870. *G&G*, Vol. 43, No. 2, pp. 98–119, http://dx.doi.org/10.5741/GEMS.43.2.98

Jeffries D. (1750) *A Treatise on Diamonds and Pearls*, C. and J. Ackers, London.

Kaminsky F. (2012) Mineralogy of the lower mantle: A review of 'super-deep' mineral inclusions in diamond. *Earth-Science Reviews*, Vol. 110, No. 1/4, pp. 127–147, http://dx.doi.org/10.1016/j.earscirev.2011.10.005

Kaminsky F.V., Zakharchenko O.D., Khachatryan G.K., Shiryaev A.A. (2001) Diamonds from the Coromandel area, Minas Gerais, Brazil. *Revista Brasileira de Geociências*, Vol. 31, pp. 583–596.

Kaminsky F.V., Sablukov S.M., Sablukova L.I., Zakharchenko O.D. (2009) The Fazenda Largo off-craton kimberlites of Piauí State, Brazil. *Journal of South American Earth Sciences*, Vol. 28, No. 3, pp. 288–303.

Karfunkel J., Chaves M.L.S.C., Svisero D.P., Meyer H.O.A. (1994) Diamonds from Minas Gerais, Brazil: An update on sources, origin and production. *International Geology Review*, Vol. 36, No. 11, pp. 1019–1032, http://dx.doi.org/ 10.1080/00206819409465502

Karfunkel J., Hoover D.B., Fernandes A.F., Sgarbi G.N.C., Kambrock K., Oliveira G.D. (2014) Diamonds from the Coromandel Area, West Minas Gerais State, Brazil: An update and new data on surface sources and origin. *Brazilian Journal of Geology*, Vol. 44, No. 2, pp. 325–338, http://dx.doi.org/10.5327/Z2317-4889201400020011

Kerr R. (1824) *A General History and Collection of Voyages and Travels, Arranged in Systematic Order*, Vol. 11, William Blackwood, Edinburgh, pp. 65–200.

King J.M., Shigley J.E. (2003) An important exhibition of seven rare gem diamonds. *G&G*, Vol. 39, No. 2, pp. 136–143,

http://dx.doi.org/10.5741/GEMS.39.2.136

Le Noan C. (2008) *Technical Report on the Juina Diamond Project*, Report No. 43-101, Diagem Inc., Quebec.

Legrand J. (1980) *Diamonds: Myth, Magic and Reality*. Crown Publishers, New York.

Lenzen G. (1970) *History of Diamond Production and the Diamond Trade*. Barrie and Jenkins, New York.

Lessa de Sá V.K., ed. (2015) *The Admirable Adventures and Strange Fortunes of Master Anthony Knivet – An English Pirate in Sixteenth-Century Brazil*. Cambridge University Press, New York.

Leonardos O.H. (1937) Diamante e carbonado no Estado da Bahia. *Mineração e Metalurgia*, pp. 183–192.

——— (1956) Recursos minerais do Triângulo Mineiro. Engenharia, *Mineração e Metalurgia*, Vol. 14, No. 140, pp. 71–77; No. 141, pp. 133–142; No. 142, pp. 219–226.

——— (1959) Diamante. *Revista Engenharia, Mineração e Metalurgia*, No. 175, pp. 5–8.

Liccardo A., Barbosa T.A., Hornes K.L. (2012) Diamante de Tibagi no Paraná – Patrimônio geológico-mineiro e cultural. *Anuário do Instituto de Geociências*, Vol. 35, No. 1, pp. 142–151, http://dx.doi.org/10.11137/2012_1_142_151

Linde O., De Meo R., Epstein A., Fischler S. (2014) *The Global Diamond Report 2014 – Diamond: Timeless Gem in a Changing World*. Bain & Company and Antwerp World Diamond Centre, Dec. 9, http://www.bain.com/publications/articles/global-diamond-report-2014.aspx

Maack R. (1968) Diamante no tilito de Tibagi, Paraná. *Anais da Academia Brasileira de Ciências*, Vol. 40, p. 96.

Machado I.F., Figueirôa S.F. de M. (2001) 500 years of mining in Brazil: A brief review. *Resources Policy*, Vol. 27, No. 1, pp. 9–24, http://dx.doi.org/10.1016/S0301-4207(01)00004-6

Mawe J. (1812) *Travels in the Interior of Brazil*. Longman, Hurst, Rees, Orme, Brown, and Green, London.

McCabe I.B. (2008) *Orientalism in Early Modern France, Eurasian Trade, Exoticism and the Ancient Règime*. Bloomsbury Academic Press, Oxford.

Melluso L., Lustrino M., Ruberti E., Brotzu P., Gomes C.B., Morbidelli L., Morra V., Svisero D.P., D'Amelio F. (2008) Major and trace-element composition of olivine, perovskite, clinopyroxene, Cr-Fe-Ti oxides, phlogopite and host kamafugites and kimberlites, Alto Paranaíba, Brazil. *Canadian Mineralogist*, Vol. 46, No. 1, pp. 19–40, http://dx.doi.org/ 10.3749/canmin.46.1.19

Meyer H.O.A., Svisero D.P. (1975) Mineral inclusions in Brazilian diamonds. *Physics and Chemistry of the Earth*, Vol. 9, pp. 785–795, http://dx.doi.org/10.1016/0079-1946(75)90051-8

Meyer H.O.A., Waring M., Posey E.F. (1991) Diamond deposits of the Santo Inácio river and the Vargem intrusions, near Coromandel, Minas Gerais. In *Fifth International Kimberlite Conference Field Guidebook*, pp. 50–57.

Minérios & Minerales (2014), Vol. 38, No. 363, pp. 14-18.

Moreira P.S. (1955) Os grandes diamantes Brasileiros. *Gemologia*, Vol. 1, No. 1, pp. 5–12.

Neto I.C., Castro C.C., Silveira F.V. (2014) Intrusões kimberlíticas de Rondônia: uma síntese com base no conhecimento atual. *Proceedings of the Sixth Brazilian Symposium on Diamond Geology*, pp. 97–102.

Oakenfull J.C. (1919) *Brazil: Past, Present, and Future*. John Bayles and Sons and Danielsson Ltd., London.

Oppenheim V. (1936) *Sedimentos diamantíferos do Paraná*. Bulletin No. 9, Rio de Janeiro, DNPM/DGM.

Partnership Africa Canada (2005) *The Failure of Good Intentions: Fraud, Theft and Murder in the Brazilian Diamond Industry*. The Diamonds and Human Security Project, Occasional Paper No. 12, Ottawa, http://www.pacweb.org/images/PUBLICATIONS/Conflict_Diamonds_and_KP/12_Failure_good_intentions_electr-Eng.pdf

——— (2006) *Fugitives and Phantoms: The Diamond Exporters of Brazil*. The Diamonds and Human Security Project, Occasional Paper No. 13, Ottawa, http://www.pacweb.org/images/PUBLICATIONS/Conflict_Diamonds_and_KP/13_Fugitives_and_Phantoms_Revised_2015.pdf

Pearson H. (1909) The diamond fields of Brazil. *Journal of the Royal Society of Arts*, Vol. 58, No. 2978, pp. 101–129.

Perdoncini L.C., Soares P.C., Góis J.R. (2010) Geologia e ocorrências diamantíferas da região de Tibagi. *Proceedings of the Fifth Brazilian Diamond Geology Symposium*, pp. 92–101.

Pointon M. (1999) Jewellery in Eighteenth Century England. In M. Berg and H. Clifford, Eds., *Consumer and Luxury: Consumer Culture in Europe, 1650–1850*. Manchester University Press, Manchester.

Porcheron H. (1903) *Rapport sur les Mines de Diamants de Agua Suja dans l'Etat de Minas Gerais, Brésil*. Lecog et Mathorel, Paris.

Read G., Grütter H., Winter S., Luckman N., Gaunt F., Thomsen F. (2004) Stratigraphic relations, kimberlite emplacement and lithospheric thermal evolution, Quiricó Basin, Minas Gerais State, Brazil. *Lithos*, Vol. 77, No. 1/4, pp. 803–818, http://dx.doi.org/10.1016/j.lithos.2004.04.011

Reid M. (2014) *Brazil: The Troubled Rise of a Global Power*. Yale University Press, New Haven, Connecticut.

Reis E. (1959) *Os grandes diamantes brasileiros*. Bulletin No. 191, Rio de Janeiro, DNPM/DGM.

Renger F.E. (2005) Regimes de extração e produção de diamantes do Serro Frio no século XVIII. *Proceedings of the Fourth Brazilian Diamond Geology Symposium*, Bulletin No. 14, pp. 139–142.

Rivot L.E. (1848) D'un diamant en masse amorphe et compacte provenant du Brésil. *Annales des Mines*, Vol. 57, pp. 419–422.

de Saint-Hilaire A. (1833) *Voyage dans le District des Diamans et sur le Littoral du Brésil*. Librairie Gide, Paris, two volumes (excerpt from *The Museum of Foreign Literature and Science*, Vol. 26, 1835, pp. 6–15).

dos Santos J.F. (1868) *Memorias do Districto Diamantino da Cormarca do Serro Frio (Provincia de Minas Geraes)*. Americana, Rio de Janeiro.

dos Santos P.R., Rocha-Campos A.C., Canuto J.R. (1996) Patterns of late Paleozoic deglaciation in the Paraná Basin, Brazil. *Palaeogeography, Palaeoclimatology, Palaeoecology*, Vol. 125, No. 1/4, pp. 165–184, http://dx.doi.org/10.1016/S0031-0182(96)00029-6

Sgarbi G.N.C., Chaves A.O. (2005) Kimberlitos e diamantes no oeste mineiro: uma discussão. *Proceedings of the Fourth Brazilian Diamond Geology Symposium*, Bulletin No. 14, pp. 153–157.

Sinkankas J. (1977) Historical notes on South American gemstones. *G&G*, Vol. 15, No. 11, pp. 334–344.

Smith C.P., Bosshart G. (2002) Star of the South: A historic 128 ct diamond. *G&G*, Vol. 38, No. 1, pp. 54–64, http://dx.doi.org/10.5741/GEMS.38.1.54

Southey R. (1819) *History of Brazil*, Vol. 3. Longman, Hurst, Rees, Orme and Browne, London.

de Souza G.S. (1587) *Tratado Descritivo do Brasil em 1587*. Typographia de João Ignacio da Silva, Rio de Janeiro, https://archive.org/stream/tratadodescriti00varngoog#page/n7/mode/1up

Souza N. B. (1991) Depósitos diamantíferos de Poxoréo, Mato Grosso. In C. Schobbenhaus, E.T. Queiroz, and C.E.S. Coelho, Eds., *Principais Depósitos Minerais do Brasil*, Vol. 4. DNPM/CPRM, Brasília, pp. 149–154.

Stachel T., Brey G.P., Harris J.W. (2005) Inclusions in sublithospheric diamonds: Glimpses of deep earth. *Elements*, Vol. 1, No. 2, pp. 73–78, http://dx.doi.org/10.2113/gselements.1.2.73

Stonestreet G.D. (1891) Diamond Mining in South Africa. *Factory and Industrial Management*, Vol. 1, No. 5, p. 590.

Streeter E.W. (1882) *Precious Stones and Gems*. George Bell & Sons, London, 3rd ed.

Suguio K., Svisero D.P., Felitti-Filho W. (1979) Conglomerados polimíticos diamantíferos de idade cretácea de Romaria (MG): Um exemplo de sedimentação de leques aluviais. *Minutes of the 2nd Regional Geology Symposium*, Vol. 1, pp. 217–229.

Svisero D.P. (1979) Piropos cromíferos da mina de diamantes de Romaria: composição química e origem. *Bulletin Mineralógico*, Vol. 6, pp. 7–14.

——— (1995) Distribution and origin of diamonds in Brazil: An overview. *Journal of Geodynamics*, Vol. 20, No. 4, pp. 493–514, http://dx.doi.org/10.1016/0264-3707(95)00017-4

Svisero D.P., Meyer H.O.A. (1981) Ilmenitas kimberlíticas da mina de diamantes de Romaria, Minas Gerais. *Revista Brasileira de Geociências*, Vol. 11, No. 4, pp. 217–221.

Svisero D.P., Felliti-Filho W., Almeida J.S. (1981) Geologia da mina de diamantes de Romaria, município de Romaria, Minas Gerais. *Mineração e Metalurgia*, Vol. 425, pp. 4–14.

Svisero D.P., Ulbrich M.N.C., Vlach S.R. (2005) Composição, origem e significado geológico de minerais resistatos de intrusões kimberlíticas da região de Coromandel, Minas Gerais. *Proceedings of the Fourth Brazilian Congress of Diamond Geology*, Bulletin No. 14, Diamantina, Brazil, pp. 169–172.

Tassinari C.C.G., Macambira M.J.B. (1999) Geochronological provinces of the Amazonian Craton. *Episodes*, Vol. 22, No 3, pp. 174–182, http://www.episodes.org/index.php/epi/article/view/62773/48972.

Thompson L.S. (1928) The upland diamond deposits of the Diamantina District, Minas Gerais, Brazil. *Economic Geology*, Vol. 23, No. 7, pp. 705–723.

Thomson A.R., Kohn S.C., Bulanova G.P., Smith C.B., Araujo D., EIMF, Walter M.J. (2014) Origin of sub-lithospheric diamonds from the Juina-5 kimberlite (Brazil): Constraints from carbon isotopes and inclusion compositions. *Contributions to Mineralogy and Petrology*, Vol. 168, No. 6, http://dx.doi.org/10.1007/s00410-014-1081-8

Tillander H. (1995) *Diamond Cuts in Historic Jewellery, 1381–1910*. Art Books International, Slovenia.

Tompkins L.A., Gonzaga G.M. (1989) Diamonds in Brazil and a proposed model for the origin and distribution of diamonds in the Coromandel Region, Minas Gerais, Brazil. *Economic Geology*, Vol. 84, No. 3, pp. 591–602, http://dx.doi.org/10.2113/gsecongeo.84.3.591

von Spix J.B., von Martius C.F.P. (1824) *Travels in Brazil in the Years 1817–1820*. Longman, Hurst, Rees, Orme, Browne, and Green, London.

Watkins J.M. (2009) *Relatório Técnico 50, Perfil do Diamante (Gema e Diamante Industrial)*, Vol. 1. Ministry of Mines and Energy, Brasília.

Weldon R., Jonathan C. (2013) The Museum of London's extraordinary Cheapside Hoard. *G&G*, Vol. 49, No. 3, pp. 126–137, http://dx.doi.org/10.5741/GEMS.49.3.126

Weska R.K. (1996) Geologia da região diamantífera de Poxoréo e áreas adjacentes, Mato Grosso. PhD thesis, Institute of Geosciences, University of São Paulo, 219 pp.

Wilding M.C., Harte B., Harris J.W. (1991) Evidence for a deep origin for São Luiz diamonds. *Fifth International Kimberlite Conference Extended Abstracts, Araxa*, pp. 456–458.

Yogev G. (1978) Diamonds and Coral: *Anglo-Dutch Jews and Eighteenth Century Trade*. Holmes & Meier Publishers, New York.

Zolinger I.T., Svisero D.P., Weska R.K. (2002) Morfologia cristalina de diamantes provenientes das regiões de Chapada dos Guimarães, Poxoréo, Paranatinga, Diamantino e Alto Paraguai, Mato Grosso. *Revista do Instituto Geológico*, Vol. 23, pp. 23–33, http://dx.doi.org/10.5935/0100-929X.20020007.

For More on Brazilian Diamonds

Watch slideshows and videos from this historical diamond source, where large-scale production could resume. Visit https://www.gia.edu/gems-gemology/spring-2017-brazilian-diamonds, or scan the QR code on the right.

FEATURE ARTICLES

CUPRIAN LIDDICOATITE TOURMALINE

Yusuke Katsurada and Ziyin Sun

Cuprian (copper-bearing) tourmaline, known as "Paraíba" tourmaline in the trade, has been an important gem since its discovery in 1989. Until now, almost all of the material reported has been classified as the elbaite species of the tourmaline supergroup. Chemical analyses by laser ablation–inductively coupled plasma–mass spectroscopy (LA-ICP-MS), a common technique for origin determination of Paraíba tourmalines, revealed that 13 copper-bearing samples submitted to GIA's Tokyo laboratory contained substantial amounts of Ca in the X-site. Consequently, they are classified as liddicoatite tourmaline. The origin of these stones is unknown.

Minerals of the tourmaline supergroup are cyclosilicates with the general formula $XY_3Z_6(T_6O_{18})(BO_3)_3V_3W$, where X = ($Na^+$, Ca^{2+}, K^+, and vacancy); Y = (Fe^{2+}, Mg^{2+}, Mn^{2+}, Cu^{2+}, Al^{3+}, Li^+, Fe^{3+}, and Cr^{3+}); Z = (Al^{3+}, Fe^{3+}, Mg^{2+}, and Cr^{3+}); T = (Si^{4+}, Al^{3+}, and B^{3+}); B = (B^{3+}); V = (OH^- and O^{2-}), and W = (OH^-, F^-, and O^{2-}) (e.g., Henry et al., 2011). Tourmaline-supergroup minerals can be classified into three primary groups based on the X-site occupancy: the alkali group (Na^+ and K^+ dominant), the calcic group (Ca^{2+} dominant), and the X-site vacant group (vacancy dominant). In each primary tourmaline group, specific species are further determined based on the occupancy of other sites. Thirty-four species have been recognized by the International Mineralogical Association's Commission on New Minerals, Nomenclature and Classification (IMA-CNMNC; e.g., Henry et al., 2011; Hawthorne and Dirlam, 2011; B. Dutrow, pers. comm., 2017). Elbaite is a sodium-, lithium-, and aluminum-rich species in the alkali group, with the general formula $(Na)(Li_{1.5}Al_{1.5})Al_6Si_6O_{18}(BO_3)_3(OH)_3(OH)$. Liddicoatite is a calcium- and lithium-rich species in the calcic group, with the general formula $(Ca)(Li_2Al)Al_6Si_6O_{18}(BO_3)_3(OH)_3(OH)$. Most gem-quality tourmaline has been reported as elbaite. Liddicoatite was first distinguished as a separate mineral species in 1977 (Dunn et al., 1977). Gem-quality liddicoatite tourmaline from Madagascar has been prized for its remarkable color zoning that is typically characterized by triangular zones and three-rayed stars surrounded by oscillatory zonings when it is cut perpendicular to the c-axis (e.g., Dirlam et al., 2002; Pezzotta and Laurs, 2011).

Cuprian (copper-bearing) tourmalines with vivid blue, green-blue, green, and violet colors were first reported in 1989 from Paraíba State in northeastern Brazil (Koivula and Kammerling, 1989). They are now commonly called "Paraíba" or "Paraíba-type" tourmaline in the trade. Fritsch et al. (1990) and Bank et al. (1990) reported that the blue to green colors were primarily due to the presence of trace (or minor) amounts of copper. Years after the initial discovery in the state of Paraíba, similar gem-quality elbaite tourmalines colored by copper and manganese were found elsewhere in Brazil (Shigley et al., 2001; Furuya, 2007), in Nigeria (Smith et al., 2001), and in Mozambique (Abduriyim and Kitawaki, 2005; Laurs et al., 2008). The composition of cuprian tourmaline from all of these deposits has been determined with energy-dispersive X-ray fluorescence spectrometry (EDXRF), electron microprobe analysis, and laser ablation–inductively coupled plasma–mass spectroscopy (LA-ICP-MS; see Abduriyim et al., 2006; Okrusch et al., 2016). No mineral species other than elbaite has been previously reported for "Paraíba" tourmalines except for four pieces of Cu-bearing liddicoatite first reported by Karampelas and Klemm (2010) showing Ca-rich X-site occupancy and three

---

See end of article for About the Authors and Acknowledgments.
GEMS & GEMOLOGY, Vol. 53, No. 1, pp. 34–41,
http://dx.doi.org/10.5741/GEMS.53.1.34

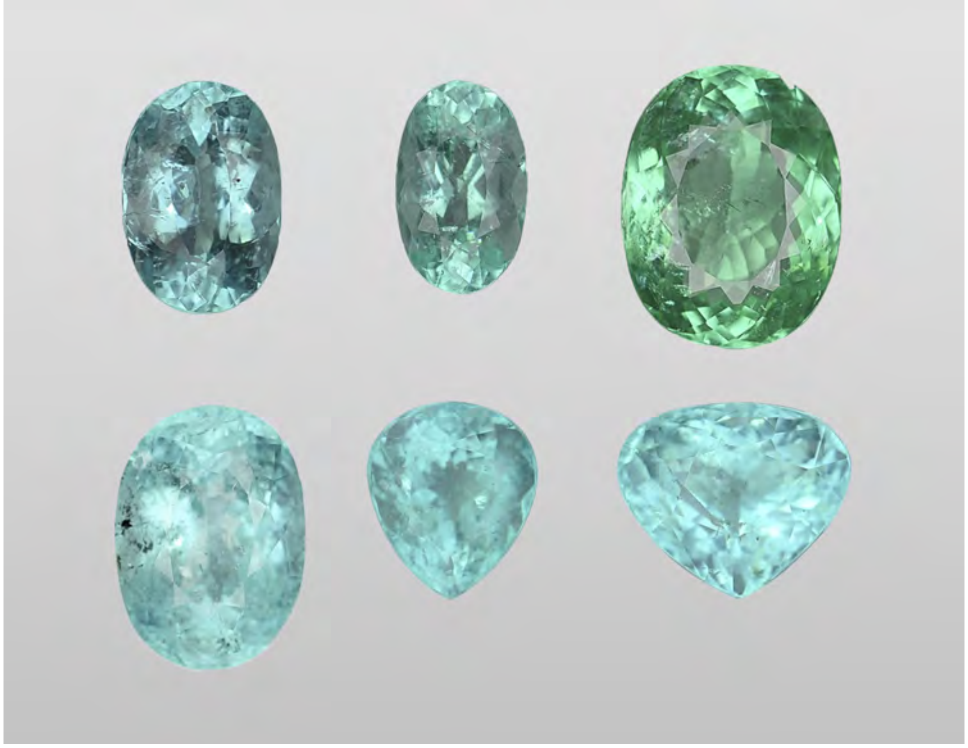

Figure 1. Six of the 13 cuprian liddicoatite tourmalines from this study. The faceted stones weigh 1.59–9.63 ct (average 3.95 ct). They are transparent and have greenish blue, green-blue, and green colors. Photos by Masumi Saito.

pieces of possible liddicoatite conjectured from the qualitative analysis indicating high Ca (Leelawatanasuk and Jakkawanvibul, 2011). This article reports on the same type of cuprian tourmalines that belong to the liddicoatite species based on the evidence supported by quantitative analysis.

MATERIALS AND METHODS

Thirteen tourmaline samples of Paraíba-type colors (figure 1) from unknown geographic origins were examined in GIA's Tokyo laboratory. These were submitted by different clients in 2016. Standard gemological testing was followed by analyses of the major, minor, and trace element concentration for each sample with LA-ICP-MS. Fluorine was not measured. A Thermo Fisher Scientific's iCAP Qc ICP-MS was connected to an Electro Scientific Industries NWR213 laser ablation unit with a frequency-quintupled Nd:YAG laser (213 nm wavelength) running at 4 ns pulse width. NIST SRM 610 and 612 glass standards were used for external calibration. Ablation was achieved using a 40 μm diameter laser spot size, a fluence (energy density) of approximately 10 J/cm^2, and a 7 Hz repetition rate. Three laser spots were acquired from the girdle of each sample. The composition was initially internally standardized with ^{29}Si using a calculated amount of Si based on the weight percent of pure elbaite in the chemical formula. Twenty-six additional cuprian tourmaline samples submitted by clients were analyzed with LA-ICP-MS for comparison. Their geographical origin was identified using GIA's tourmaline database. Eighteen of these additional samples were from Brazil, one from Nigeria, and seven from Mozambique.

The data was converted to wt.% oxides and normalized to 100 wt.% and then converted back to ppmw to obtain individual element concentrations, based on 27 O^{2-} and 4 OH^{-} anions per formula. LA-ICP-MS analysis for tourmaline is an incomplete characterization, with critical light elements (H and F) and

In Brief

- Almost all copper-bearing tourmaline has been classified as the elbaite species. Cuprian liddicoatite exists, however, and may have entered the "Paraíba" tourmaline market.
- Only sophisticated quantitative chemical analysis can effectively separate liddicoatite from elbaite.
- Cuprian liddicoatite shows high Ga and high Pb. Under long-wave UV, it displays stronger fluorescence than cuprian elbaite due to high concentrations of rare earth elements.

TABLE 1. Chemical composition of 13 cuprian tourmaline samples, obtained by LA-ICP-MS.

Sample no	CT1	CT2	CT3	CT4	CT5	CT6	CT7	CT8	CT9	CT10	CT11	CT12	CT13
							ppmw						
Li	11,600	11,700	12,300	13,600	12,300	12,800	12,500	13,000	13,900	11,700	12,100	12,600	15,300
B	33,900	34,400	33,200	35,200	32,500	34,700	35,200	31,500	33,600	34,400	37,600	34,100	40,300
Na	8920	8480	8050	8390	8960	7600	9130	9860	8170	7910	7120	8220	7810
Al	220000	218,000	230,000	220,000	224,000	217,000	218,000	228,000	225,000	217,000	216,000	222,000	197,000
Si	169,000	169,000	158,000	163,000	166,000	169,000	161,000	164,000	161,000	168,000	164,000	166,000	171,000
Ca	21,000	21,300	24,100	24,400	21,800	21,700	22,800	20,400	23,500	22,200	20,800	22,800	20,400
Mn^{2+}	2160	3110	5780	3610	3480	3340	12,300	2130	3480	6530	8000	2860	10,100
Cu	1490	1610	2120	1510	2140	1600	2790	1550	1460	2300	2510	1330	2970
							atoms per formula unit, 27 O + 4 OH anions normalization						
							X-site						
X site vacancy	0.14	0.15	0.09	0.08	0.11	0.17	0.08	0.11	0.10	0.15	0.22	0.12	0.20
Ca	0.50	0.50	0.57	0.58	0.52	0.51	0.54	0.48	0.56	0.52	0.49	0.54	0.48
Na	0.37	0.35	0.33	0.35	0.37	0.31	0.38	0.41	0.34	0.33	0.29	0.34	0.32
X-site total	1.00	1.00	1.00	1.00	1.00	1.00	1.00	1.00	1.00	1.00	1.00	1.00	1.00
							Y-site						
Al	1.42	1.36	1.46	1.22	1.49	1.30	1.15	1.59	1.37	1.31	1.08	1.37	0.63
Cu	0.02	0.02	0.03	0.02	0.03	0.02	0.04	0.02	0.02	0.03	0.04	0.02	0.04
Li	1.58	1.60	1.70	1.86	1.68	1.74	1.72	1.79	1.90	1.60	1.65	1.73	2.08
Mn^{2+}	0.04	0.05	0.10	0.06	0.06	0.06	0.21	0.04	0.06	0.11	0.14	0.05	0.17
Y-site total	3.06	3.04	3.29	3.16	3.26	3.12	3.13	3.44	3.36	3.06	2.91	3.17	2.92
							Z-site						
Al	6.00	6.00	6.00	6.00	6.00	6.00	6.00	6.00	6.00	6.00	6.00	6.00	6.00
Z-site total	6.00	6.00	6.00	6.00	6.00	6.00	6.00	6.00	6.00	6.00	6.00	6.00	6.00
							T-site						
Si	5.70	5.71	5.35	5.50	5.62	5.68	5.46	5.55	5.46	5.67	5.53	5.58	5.74
Al	0.30	0.29	0.65	0.50	0.38	0.32	0.54	0.45	0.54	0.33	0.47	0.42	0.26
T-site total	6.00	6.00	6.00	6.00	6.00	6.00	6.00	6.00	6.00	6.00	6.00	6.00	6.00
							B-site						
B	2.97	3.01	2.92	3.08	2.85	3.04	3.10	2.77	2.95	3.02	3.29	2.99	3.50
B-site total	2.97	3.01	2.92	3.08	2.85	3.04	3.10	2.77	2.95	3.02	3.29	2.99	3.50
							Sum						
Cation sum	18.89	18.90	19.12	19.17	19.01	18.99	19.15	19.10	19.20	18.93	18.98	19.03	19.22
Anion sum	31.00	31.00	31.00	31.00	31.00	31.00	31.00	31.00	31.00	31.00	31.00	31.00	31.00

Detection limits (ppmw) are: Li (0.95–1.31), B (8.78–10.42), Na (18.91–19.34), Al (3.41–3.48), Ca (339–364), Mn (0.55), and Cu (0.42–0.45). Si is used as internal standard.

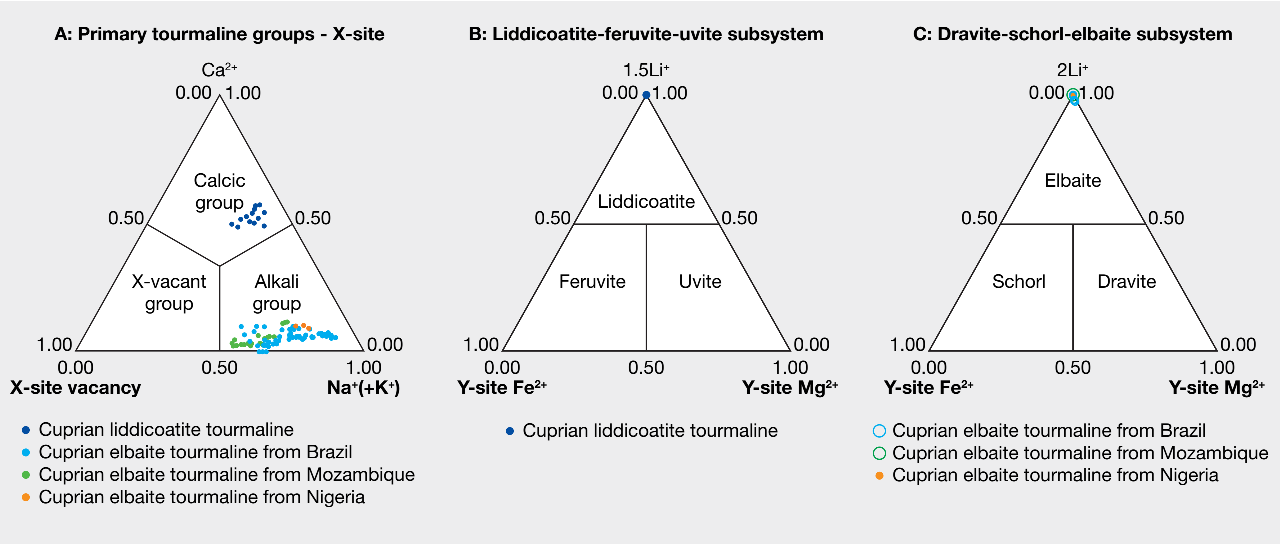

Figure 2. A: The 13 cuprian tourmaline samples belong to the calcic group, while the 26 additional cuprian tourmalines belong to the alkali group based on the dominant occupancy of X-site. B: Li, Y-site Fe^{2+}, and Y-site Mg^{2+} distinguish the tourmaline species as liddicoatite in a liddicoatite-feruvite-uvite subsystem ternary diagram. C: Li, Y-site Fe^{2+}, and Y-site Mg^{2+} of elbaite samples were further plotted in a dravite-schorl-elbaite subsystem ternary diagram (modified after Henry et al., 2011).

the oxidation states of transition elements (Fe and Mn) undetermined. In this article, it is assumed that Fe and Mn are divalent, that the B-site is fully occupied by B, and that the X-site is occupied by Na, Ca, and a vacancy equal to 1 atom per formula unit (apfu). Additional assumptions are that the Z-site is only occupied by Al^{3+} and equal to 6 apfu, while the T-site is occupied by Si^{4+} and Al^{3+} and equal to 6 apfu. If Si^{4+} is greater than 6, the T-site is only occupied by Si^{4+}. The excess Al goes into the Y-site. The priority of ions with different valence states entering the Y-site is ($R^{2+} > R^{3+} > R^{+} > R^{4+}$), such that the Y-site is occupied by Mn, Cu, Al, and Li. The common assumption that all iron is ferrous and that OH + F = 4 apfu can result in the misidentification of buergerite as "fluor-schorl" as well as misidentification of the oxy- and fluor- species. The chemical composition presented in this article is not affected by the minor amounts of Fe in the tourmaline (Clark, 2007). The assumption of 4 OH^- does not allow for the fluor- or oxy- species to be determined. The major elements, including Ca, Na, Si, Al, and Mg, were verified by comparison of LA-ICP-MS data with electron microprobe data of a secondary tourmaline standard with similar Ca:Na ratios (Dutrow and Henry, pers. comm., 2017).

RESULTS AND DISCUSSIONS

Microscopic examination of the 13 samples revealed two-phase inclusions, needle-like growth tubes, and fluid inclusions typical of tourmaline. Standard gemological testing resulted in the general range of gem tourmalines such as refractive indices of 1.62–1.64 and specific gravity of approximately 3.06, but the fluorescence under long-wave ultraviolet light was stronger than the usual Paraíba tourmalines, as described later. Chemical analysis demonstrated a calcium-dominant composition. The representative data in table 1 was selected to show the best stoichiometry. All the data points showed liddicoatite, and none were classified as elbaite. In all analyses, Mg was below the detection limit and Fe was less than 0.005 apfu. Based on the primary tourmaline group classification, all 13 calcium-rich cuprian samples are classified as calcic-group tourmaline and the 26 additional sodium-rich cuprian samples as alkali-group tourmaline (table 2, figure 2A). In addition, the 13 calcic-group samples plot as liddicoatite tourmaline in a liddicoatite-feruvite-uvite subsystem ternary diagram (figure 2B). The 26 tourmalines in the alkali group are shown as elbaite in a dravite-schorl-elbaite subsystem ternary diagram (figure 2C; Henry et al., 2011).

Comparing the data in table 1 with that of liddicoatitic tourmaline from Madagascar (Dirlam et al., 2002) shows that these cuprian samples have more sodium in the X-site—with a greater elbaitic component. Other liddicoatite tourmalines from Canada (Teertstra et al., 1999) have similar sodium (0.365–

TABLE 2. X-site occupancy of 26 cuprian elbaite samples in molecular proportions, obtained by LA-ICP-MS.

	Na	K	Ca	Vacancy
Brazil	0.705 (0.513–0.861)	0.003 (0.001–0.005)	0.063 (0.000–0.112)	0.229 (0.073–0.381)
Mozambique	0.596 (0.519–0.661)	0.002 (0.002–0.003)	0.057 (0.025–0.131)	0.346 (0.205–0.444)
Nigeria	0.724 (0.699–0.748)	0.003 (0.003–0.003)	0.111 (0.103–0.116)	0.162 (0.145–0.185)

0.395 apfu) and similar or lower calcium (0.420–0.498 apfu). The sodium contents of liddicoatite from Madagascar and Canada vary with their zonation.

Table 3 shows the samples' averaged chemical composition for selected minor and trace elements. In cuprian tourmalines from different origins, these have some distinguishable trends (Abduriyim et al., 2006; Okrusch et al., 2016). For example, Brazilian and Nigerian cuprian tourmalines tend to show higher concentrations of Cu than those from Mozambique—which typically have higher Ga than the other two sources. Nigerian stones tend to have higher Pb than those from Brazil and Mozambique. Figure 3 shows the Ga-Pb distribution of the 13 cuprian liddicoatite and 26 cuprian elbaite samples analyzed in this study. The cuprian liddicoatite samples show both high Ga (297–433 ppmw) and high Pb (420–827 ppmw). These combinations of trace elements plot well outside the ranges of any known reference samples in GIA's database, and therefore their geographic origin could not be determined.

Another remarkable point was the samples' high concentration of rare earth elements (REE; table 2)—in other words, lanthanides except Pm. Lighter REE (La, Ce, Pr, Nd, Sm, and Gd) showed a higher concentration than heavier REE (Tb, Dy, Ho, Er, Tm, Yb, and Lu). The samples show an exceptionally low Eu content. The high concentration of REEs is interpreted as the cause of their comparatively strong fluorescence under long-wave UV (figure 4).

Although the geographic origin of these cuprian liddicoatite is unknown, this unique chemical property offers directions for further research. Geological studies of the elbaitic cuprian tourmaline deposits in Brazil have been published (e.g., Shigley et al., 2001; Soares et al., 2008; Beurlen et al., 2011), but no detailed study has been carried out for Nigerian and Mozambican occurrences. Teertstra et al. (1999) reported that some liddicoatite crystals have cores that correspond to elbaite with rims of liddicoatite. They proposed three possibilities for the calcium needed to form liddicoatite: mobilization of Ca from earlier-formed pegmatite minerals, introduction of Ca from host rocks, and conservation of Ca through the crystallization of minerals in the pegmatite magma. Major elements can also be used to determine provenance. Henry and Guidotti (1985) established distinct regions to define potential different source rock types of tourmaline using Al-Fe(tot)-Mg and Ca-Fe(tot)-Mg ternary diagrams. Figure 5 indicates that the rock

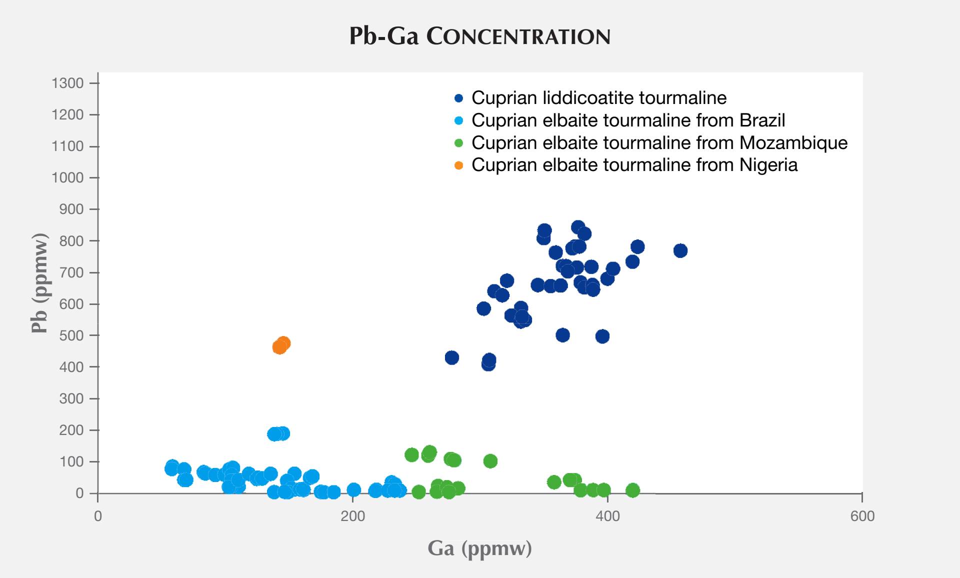

Figure 3. Pb vs. Ga concentration plot of the 13 cuprian liddicoatites of unknown origin and 26 cuprian elbaite tourmalines from Brazil, Mozambique, and Nigeria. The 13 cuprian liddicoatites have high Pb and high Ga. Cuprian elbaite tourmalines from Brazil have low Pb and low Ga. Cuprian elbaites from Mozambique have high Ga and low Pb, while those from Nigeria have low Ga and high Pb.

TABLE 3. Minor and trace element concentration (ppmw) of 13 cuprian liddicoatite samples and 26 cuprian elbaites from Brazil, Mozambique, and Nigeria.

Sample	CT1	CT2	CT3	CT4	CT5	CT6	CT7	CT8	CT9	CT10	CT11	CT12	CT13	Brazil (18 samples)	Mozambique (7 samples)	Nigeria (1 sample)
Mg	bdl	1.90	bdl	bdl	bdl	bdl	bdl	bdl	bdl	bdl	bdl	bdl	0.25	112 (0–1170)	bdl	0.73
Mn^{2+}	2220	3140	5740	3570	3510	3440	12300	2130	3430	6490	7900	2790	9820	11800 (420–26300)	4360 (99.5–12100)	18700
Fe^{2+}	bdl	261	72.4	66.0	34.9	20.0	208	bdl	36.0	155	241	42.9	201	164 (0–1060)	bdl	209
Cu	1530	1580	2100	1490	2140	1650	2850	1560	1530	2250	2550	1220	2860	9580 (420–23200)	2310 (1140–3430)	2470
Ga	397	373	333	368	382	375	297	433	359	324	319	376	349	139 (61.2–232)	321 (255–401)	143
La	4.99	17.0	76.9	42.6	27.9	42.2	108	4.28	42.8	87.3	99.9	27.5	93.2	0.69 (bdl–3.72)	0.01 (bdl–0.03)	0.04
Ce	20.3	54.2	230	131	88.1	131	316	20.0	137	277	304	92.0	319	0.97 (bdl–5.79)	0.02 (bdl–0.06)	0.04
Pr	4.89	9.62	31.2	18.9	15.5	19.6	40.5	5.06	19.8	32.6	39.9	11.8	39.5	0.07 (bdl–0.42)	0.00 (bdl–0.00)	0
Nd	36.5	47.1	111	76	72.2	71.9	126	37.3	72.4	115	123	65.0	120	0.12 (bdl–0.82)	bdl	bdl
Sm	40.0	29.5	27.0	26.7	58.3	26.6	26.0	45.7	27.8	25.6	28.8	23.0	28.0	0.02 (bdl–0.13)	bdl	bdl
Eu	1.26	0.79	0.63	0.64	1.57	0.75	0.64	1.64	0.73	0.77	0.71	0.69	0.71	0.00 (bdl–0.01)	bdl	bdl
Gd	12.2	8.25	7.65	6.84	15.1	6.43	7.59	13.3	7.48	7.15	8.22	6.44	6.71	0.01 (bdl–0.06)	0.00 (bdl–0.02)	bdl
Tb	0.89	0.51	0.43	0.40	1.18	0.41	0.48	0.86	0.39	0.45	0.51	0.34	0.46	0.00 (bdl–0.01)	bdl	0
Dy	1.48	1.00	0.82	0.66	1.67	0.79	0.79	1.44	0.71	0.77	0.92	0.84	0.75	0.00 (bdl–0.01)	bdl	bdl
Ho	0.08	0.06	0.04	0.04	0.07	0.05	0.05	0.10	0.05	0.05	0.06	0.03	0.06	0.00 (bdl–0.00)	0.00 (bdl–0.00)	bdl
Er	0.09	0.09	0.10	0.06	0.10	0.13	0.09	0.07	0.10	0.09	0.09	0.07	0.08	0.00 (bdl–0.00)	0.00 (bdl–0.01)	bdl
Tm	bdl	0.00	0.01	0.01	0.00	0.01	0.00	0.01	bdl	0.00	bdl	0.00	0.01	0.00 (bdl–0.01)	0.00 (bdl–0.00)	bdl
Yb	0.08	0.05	0.02	bdl	0.05	0.04	bdl	0.07	0.03	0.01	bdl	0.05	bdl	0.00 (bdl–0.01)	0.00 (bdl–0.01)	bdl
Lu	0.01	bdl	0.01	0.00	bdl	bdl	0.01	0.01	bdl	bdl	bdl	0.00	bdl	0.02 (bdl–0.40)	bdl	bdl
Ta	7.31	6.52	5.30	7.18	5.06	6.85	4.18	8.05	7.92	6.53	6.70	7.70	5.83	2.23 (0.04–8.35)	1.58 (0.54–3.62)	6.66
Pb	703	672	550	773	659	774	420	761	827	642	578	567	684	44.4 (2.74–188)	43.9 (3.85–123)	467
ΣREE	123	168	486	304	282	300	626	130	309	547	606	228	609	1.89	0.03	0.1

Abbreviation: bdl = below detection limit. Detection limits (ppmw) are: Mg (0.13–0.56), Mn (0.16–1.01), Fe (6.70–34.02), Cu (0.73–3.00), Ga (0.05–0.19), La (0.00–1.26), Ce (0.00–0.01), Pr (0.00–0.02), Nd (0.00–0.23), Sm (0.00–0.04), Eu (0.00–0.01), Gd (0.00–0.02), Tb (0.00–0.01), Dy (0.00–0.02), Ho (0.00), Er (0.00–0.01). Tm (0.00–0.01), Yb (0.01–0.02), Lu (0.00–0.01), Ta (0.00), and Pb (0.05–0.14).

types in which the cuprian liddicoatite was found are Li-rich granitoid pegmatites and aplites. Because these copper-bearing liddicoatite tourmalines are Ca-dominant, they must be from a Ca-rich host rock. Karampelas and Klemm (2010) noted that liddicoatite rough had been found near the Paraíba-type el-

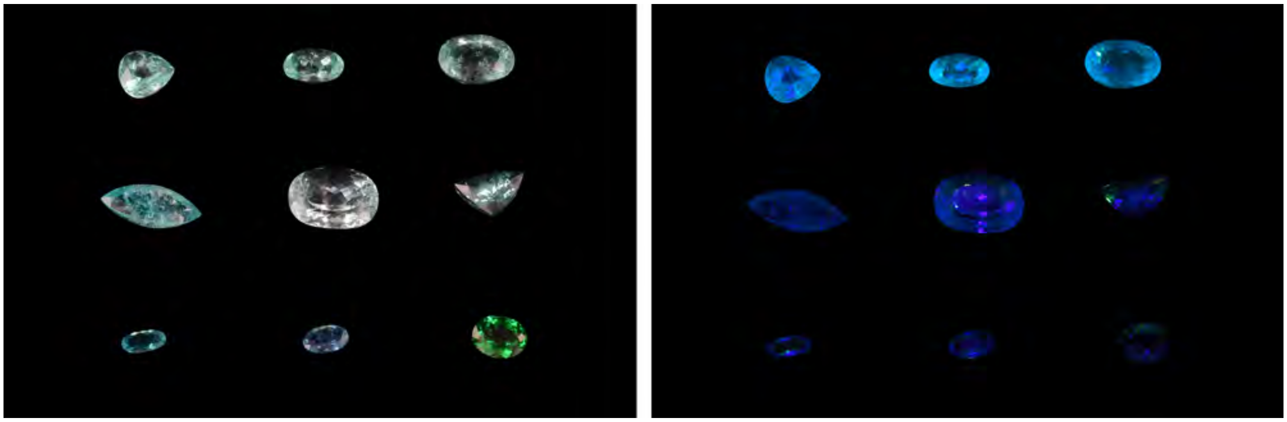

Figure 4. Randomly selected samples under daylight-equivalent light (left) and under long-wave UV light (right). Copper-bearing liddicoatite (CT05, CT03, and CT06 at the top) show stronger fluorescence than the cuprian elbaite (MZ04, MZ06, NG01, BR15, BR17, and BR08 at the middle and bottom) due to high REE concentrations. Photos by Yusuke Katsurada.

baite mine in Mozambique. Qualitative EDXRF analysis of Paraíba-type tourmaline from a new mine reportedly near Nampula, Mozambique, showed a Ca peak (Leelawatanasuk and Jakkawanvibul, 2011).

Figure 5. A: This Al-Fe(tot)-Mg diagram (in molecular proportions) reveals that the likely source rock of cuprian liddicoatite tourmaline is Li-rich granitoid pegmatite and aplite. Fe(tot) represents the total Fe. This diagram is divided into regions that define the compositional range of tourmaline from different rock types (modified after Henry and Guidotti, 1985). B: The Ca-Fe(tot)-Mg diagram (also in molecular proportions) shows that the likely source rock of cuprian liddicoatite tourmaline is Li-rich granitoid pegmatite and aplite. The rock types defined by the fields in this diagram (also modified after Henry and Guidotti, 1985) are somewhat different from those in figure 5A.

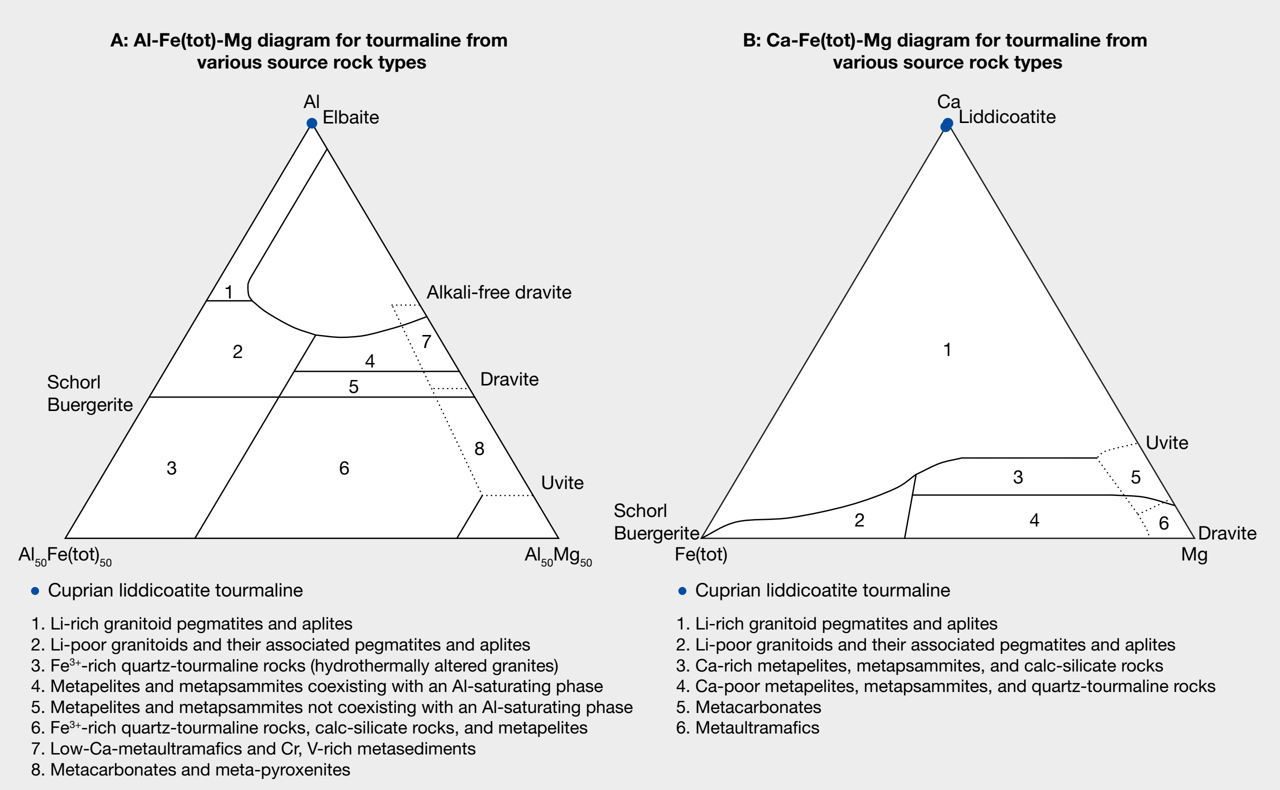

A: Al-Fe(tot)-Mg diagram for tourmaline from various source rock types

● Cuprian liddicoatite tourmaline

1. Li-rich granitoid pegmatites and aplites
2. Li-poor granitoids and their associated pegmatites and aplites
3. Fe^{3+}-rich quartz-tourmaline rocks (hydrothermally altered granites)
4. Metapelites and metapsammites coexisting with an Al-saturating phase
5. Metapelites and metapsammites not coexisting with an Al-saturating phase
6. Fe^{3+}-rich quartz-tourmaline rocks, calc-silicate rocks, and metapelites
7. Low-Ca-metaultramafics and Cr, V-rich metasediments
8. Metacarbonates and meta-pyroxenites

B: Ca-Fe(tot)-Mg diagram for tourmaline from various source rock types

● Cuprian liddicoatite tourmaline

1. Li-rich granitoid pegmatites and aplites
2. Li-poor granitoids and their associated pegmatites and aplites
3. Ca-rich metapelites, metapsammites, and calc-silicate rocks
4. Ca-poor metapelites, metapsammites, and quartz-tourmaline rocks
5. Metacarbonates
6. Metaultramafics

Analysis of the host rock geology around cuprian tourmaline mines in Mozambique may be an important approach.

CONCLUSIONS

Thirteen cuprian tourmaline samples were identified as liddicoatite tourmaline. Their Cu and Mn concentrations were within the range of other cuprian tourmalines—consistent with their similar blue to green colors. Except for their stronger fluorescence under long-wave UV, presumably caused by high REE concentrations, the samples' gemological properties were also similar to cuprian elbaite tourmalines. Only sophisticated quantitative chemical analyses can effectively separate liddicoatite from elbaite.

Cuprian liddicoatite tourmaline is not well known, but the material may have already entered the "Paraíba" tourmaline market. Discovering its origin could provide new insights into the geologic growth conditions and chemical variations of tourmaline crystals.

ABOUT THE AUTHORS

Dr. Katsurada is a scientist and a staff gemologist at GIA in Tokyo. Mr. Sun is a staff gemologist at GIA in Carlsbad, California.

ACKNOWLEDGMENTS

We wish to thank Dr. Makoto Miura and Takuya Sunaoshi of GIA's laboratory in Tokyo for assisting with LA-ICP-MS testing. We also appreciate the helpful comments and suggestions from Shane McClure of GIA Carlsbad and Dr. Barbara Dutrow of Louisiana State University.

REFERENCES

Abduriyim A., Kitawaki H. (2005) Gem News International: Cu- and Mn-bearing tourmaline—More production from Mozambique. *G&G*, Vol. 41, No. 4, pp. 360–361.

Abduriyim A., Kitawaki H., Furuya M., Schwarz D. (2006) "Paraíba"-type copper-bearing tourmaline from Brazil, Nigeria, and Mozambique: Chemical fingerprinting by LA-ICP-MS. *G&G*, Vol. 42, No. 1, pp. 4–21, http://dx.doi.org/10.5741/GEMS.42.1.4

Bank H., Henn U., Bank F.H., von Platen H., Hofmeister W. (1990) Leuchtendblaue Cu-führende Turmaline aus Paraiba, Brasilien. *Zeitschrift der Deutschen Gemmologischen Gesellschaft*, Vol. 39, No. 1, pp. 3–11 (in German).

Beurlen H., de Moura O. J.M., Soares D. R., Da Silva M. R.R., Rhede D. (2011) Geochemical and geological controls on the genesis of gem-quality "Paraíba tourmaline" in granitic pegmatites from northeastern Brazil. *The Canadian Mineralogist*, Vol. 49, No. 1, pp. 277–300, http://dx.doi.org/10.3749/canmin.49.1.277

Clark C.M. (2007) Tourmaline: Structure formula calculations. *The Canadian Mineralogist*, Vol. 45, No. 2, pp. 229–237, http://dx.doi.org/10.2113/gscanmin.45.2.229

Dirlam D.M., Laurs B.M., Pezzotta F., Simmons W.B. (2002) Liddicoatite tourmaline from Anjanabonoina, Madagascar. *G&G*, Vol. 38, No. 1, pp. 28–53, http://dx.doi.org/10.5741/GEMS.38.1.28

Dunn P.J., Appleman D.E., Nelen J.E. (1977) Liddicoatite, a new calcium end-member of the tourmaline group. *American Mineralogist*, Vol. 62, pp. 1121–1124.

Fritsch E., Shigley J.E., Rossman G.R., Mercer M.E., Muhlmeister S.M., Moon M. (1990) Gem-quality cuprian-elbaite tourmalines from São José da Batalha, Paraíba, Brazil. *G&G*, Vol. 26, No. 3, pp. 189–205, http://dx.doi.org/10.5741/GEMS.26.3.189

Furuya M. (2007) Copper-bearing tourmaline from new deposits in Paraíba State, Brazil. *G&G*, Vol. 43, No. 3, pp. 236–239, http://dx.doi.org/10.5741/GEMS.43.3.236

Hawthorne F.C., Dirlam D.M. (2011) Tourmaline the indicator mineral: From atomic arrangement to Viking navigation. *Elements*, Vol. 7, No. 5, pp. 307–312, http://dx.doi.org/10.2113/gselements.7.5.307

Henry D.J., Guidotti C.V. (1985) Tourmaline as a petrogenetic indicator mineral: an example from the staurolite-grade metapelites of NW Maine. *American Mineralogist*, Vol. 70, pp. 1–15.

Henry D.J., Novák M., Hawthorne F.C., Ertl A., Dutrow B.L., Uher P., Pezzotta F. (2011) Nomenclature of the tourmaline-supergroup minerals. *American Mineralogist*, Vol. 96, No. 5–6, pp. 895–913, http://dx.doi.org/10.2138/am.2011.3636

Karampelas S., Klemm L. (2010) Gem News International: "Neon" blue-to-green Cu- and Mn-bearing liddicoatite tourmaline. *G&G*, Vol. 46, No. 4, pp. 323–325.

Koivula J.I., Kammerling R.C., Eds. (1989) Gem News: Paraíba tourmaline update. *G&G*, Vol. 25, No. 4, pp. 248–249.

Laurs B.M., Zwaan J.C., Breeding C.M., Simmons W.B., Beaton D., Rijsdijk K.F., Befi R., Falster A.U. (2008) Copper-bearing (Paraíba-type) tourmaline from Mozambique. *G&G*, Vol. 44, No. 1, pp. 4–30, http://dx.doi.org/10.5741/GEMS.44.1.4

Leelawatanasuk T., Jakkawanvibul J. (2011) New Paraiba-type tourmaline from Mozambique. http://www.git.or.th/2014/eng/testing_center_en/lab_notes_en/glab_en/2011/GIT_Paraiba-new_Mine.pdf.

Okrusch M., Ertl, A., Schüssler U., Tillmanns E., Brätz H., Bank H. (2016) Major- and trace-element composition of Paraíba-type tourmaline from Brazil, Mozambique and Nigeria. *The Journal of Gemmology*, Vol. 35, No. 2, pp. 120–139.

Pezzotta F., Laurs B.M. (2011) Tourmaline: the kaleidoscopic gemstone. *Elements*, Vol. 7, No. 5, pp. 333–338, http://dx.doi.org/10.2113/gselements.7.5.333

Shigley J.E., Cook B.C., Laurs B.M., Oliveira Bernardes M. (2001) An update on "Paraíba" tourmaline from Brazil. *G&G*, Vol. 37, No. 3, pp. 260–276, http://dx.doi.org/10.5741/GEMS.37.4.260

Smith C.P., Bosshart G., Schwartz D. (2001) Gem News International: Nigeria as a new source of copper-manganese-bearing tourmaline. *G&G*, Vol. 37, No. 3, pp. 239–240.

Soares D.R., Beurlen H., Barreto S. d. B., Da Silva M.R.R., Ferreira A.C.M. (2008) Compositional variation of tourmaline-group minerals in the Borborema pegmatite province, northeastern Brazil. *The Canadian Mineralogist*, Vol. 46, No. 5, 1097–1116, http://dx.doi.org/10.3749/canmin.46.5.1097

Teertstra D.K., Černý P., Ottolini L. (1999) Stranger in paradise: Liddicoatite from the High Grade Dike pegmatite, southeastern Manitoba, Canada. *European Journal of Mineralogy*, Vol. 11, No. 2, pp. 227–235, http://dx.doi.org/10.1127/ejm/11/2/0227

THE ROLE OF SILICON IN THE COLOR OF GEM CORUNDUM

John L. Emmett, Jennifer Stone-Sundberg, Yunbin Guan, and Ziyin Sun

Natural corundum is colored by a variety of trace-element impurities and by the chemical reactions among them. Important to nearly all of the colors is the role played by the reactions among silicon, titanium, and magnesium. Characterization of the interactions between these aliovalent ions has been hindered by the fact that the laser ablation–inductively coupled quadrupole–mass spectrometry equipment used in most gem labs does not resolve the interferences for silicon. Thus Si has not been measured at relevant concentrations. Recent development of ion implant standards and the application of secondary ion mass spectrometry has allowed the accurate measurement of silicon in corundum for the first time. As an example of its importance, detailed analyses of sapphire from Montana's Yogo Gulch deposit are presented. These analyses show that without silicon, Yogo sapphire would not be blue.

Corundum, like many other transparent gemstones, is inherently colorless if pure. In fact, pure corundum has an excellent transmission window that can achieve good transparency between approximately 0.18 and 5 μm (Khattack and Schmid, 2001). Pure corundum is aluminum oxide, Al_2O_3. Thus, the only cation (positive ion) in pure corundum is Al^{3+} and the only anion (negative ion) is O^{2-}. Neither of these two ions arrayed in the corundum lattice structure absorbs light in the visible region of the spectrum. The color of corundum gems is therefore determined by trace element impurities that are in solution in the corundum lattice. Such gems are referred to as *allochromatic* ("other colored").

"In solution" is an important distinction to make. Sugar dissolved in water is "in solution." Fine sand stirred into water is not. "In solution" in corundum means that if the impurities are cations, they will primarily substitute for Al^{3+} in the corundum lattice. If they are anions, they will primarily substitute for O^{2-} in the corundum structure.

This paper discusses how trace elements chemically interact with each other, and thus concentrations will be expressed as atomic concentrations in units of parts per million atomic (ppma), not weight concentrations (ppm or ppmw). These units are chosen because it is the concentration of trace elements that determines how they chemically interact, not their relative weights.[1]

Al^{3+} is one of the smallest trivalent cations, with a radius of only 53 picometers (pm; 1 pm = 10^{-12} m) in sixfold coordination, which means six oxygen ions surround a single aluminum ion. This cation site in corundum is quite small, limiting the size and thus the variety of trace elements that can be easily incorporated. Whereas corundum has only a single small cation site, other gems (beryl, for example) can have multiple cation sites of different sizes.

For trivalent cations substituting for Al^{3+} at geologic temperatures, size is the primary factor in determining the solubility (Blundy and Wood, 2003; Karato, 2016). Trivalent ions in corundum are termed *isovalent* (same valence). Isovalent ions that are larger than aluminum stretch the lattice. The energy required to stretch the lattice results in a reduced solubility. Isovalent ions that are smaller than Al^{3+} also create substantial lattice distortion that reduces solubility.

Cations in corundum with a valence different than the +3 of aluminum are termed *aliovalent* (different valence). Since a solid must be rigorously electrically neutral, the incorporation of an aliovalent trace element requires either the incorporation of an-

---

See end of article for About the Authors and Acknowledgments.

Gems & Gemology, Vol. 53, No. 1, pp. 42–47,
http://dx.doi.org/10.5741/GEMS.53.1.42

other aliovalent ion to achieve an average charge of +3 for the pair, or the creation of a charged crystal defect such as an interstitial ion, a vacancy, or a change in valence of an existing ion. These requirements are energy intensive and result in very low solubilities for aliovalent ions as compared to isovalent ions of the same size (Blundy and Wood, 2003).

The overall result of size and valence constraints in corundum is that in nature only a small fraction of the elements in the periodic table are found in solution. The majority of these elements are listed in table 1, along with their radii in the sixfold coordination of corundum.

The foregoing rules are useful for growth of corundum at low temperatures, such as in geologic growth. However, it should be pointed out that for growth from a corundum melt at 2050°C (Czochralski, Verneuil, etc.), other factors can modify these general rules.

In Brief

- Due to advances in analytical techniques, the silicon concentration of gem corundum samples has been accurately measured for the first time.
- Si can have a major impact on all colors of corundum, as illustrated through the analysis of blue sapphire from Yogo Gulch, Montana.

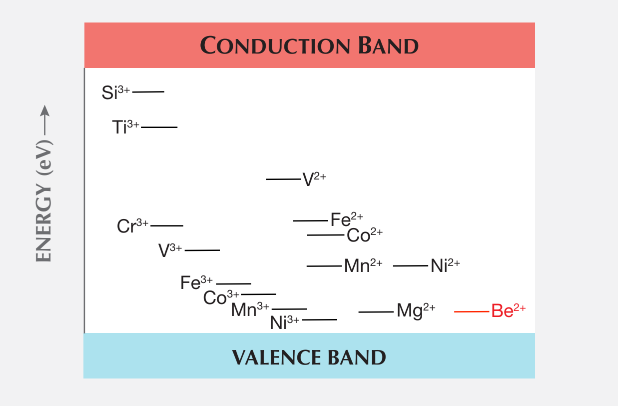

Figure 1. In this energy level diagram of trace elements in corundum, trivalent donor ions are shown on the left and divalent acceptor ions are shown on the right. A charge-compensating donor-acceptor pair can form when the donor level is significantly above the acceptor level. There is no significance to the lateral positions of the energy levels, but the vertical positions are very significant. Data from Kröger (1984b).

The trace elements in corundum chemically interact with each other, and this interaction is, in many cases, key to the resulting color we observe. In Emmett et al. (2003), this interaction and the resulting colors produced were discussed at length. Rather than recreate that discussion here, the reader is referred to that paper. However, as presented in that paper, the chemical reaction among trace elements is based on their relative energy level positions in the band gap as shown in figure B-1 in Emmett et al. (2003). The positions shown were based on a summary paper (Kröger, 1984a). That paper shows that the silicon donor level lies well *below* the titanium donor level, and we used that position in our analysis of the effect of silicon on the color of corundum.

Unknown at the time was that a second summary paper by the same author (Kröger, 1984b) corrected the silicon donor level based on measured data in a concurrent paper by Kröger and one of his students (Lee and Kröger, 1985). These later two publications clearly show that the correct silicon donor level lies well above the titanium donor level. The second summary paper also corrects the relative level positions of some of the transition metals. Figure 1 of this paper presents data from the second summary paper and clearly shows that the silicon donor level is well above the titanium donor level.

While the position of the silicon donor level with regard to the position of the titanium donor level may seem unimportant, it surely is not. Their relative positions have a significant impact on how trace elements react with each other, and in certain cases it is only the presence of silicon that allows the titanium to pair with iron, creating the blue coloration of the Fe^{2+}-Ti^{4+} pair in sapphire.

To understand how this comes about, we need to examine the corrected band gap chart in figure 1. This is a greatly simplified version of the correct chart from Kröger (1984b). The convention of label-

---

[1] The more commonly used units for trace element analyses are ppmw (parts per million by weight), usually written as *ppm*. One ppm means that there is one microgram of impurity in one gram of crystal. In this article we choose to use the unit *ppma* (parts per million atomic) to state trace element concentrations. One ppma means that there is one trace element atom for each million atoms. In corundum, that is 400,000 Al atoms + 600,000 O atoms.

$$\text{ppma} = \frac{(\text{molecular weight of } Al_2O_3)/5}{(\text{atomic weight of the element})} \bullet \text{ppmw}$$

TABLE 1. Radii of selected elements found in natural corundum.[a]

Cation	Valence	Ionic radii (pm)
Beryllium[b]	+2	45
Magnesium	+2	72
Aluminum	+3	53.5
Nickel	+3	56
Iron	+3	55
Manganese	+3	58
Chromium	+3	61.5
Gallium	+3	62
Vanadium	+3	64
Silicon	+4	40
Titanium	+4	60.5

[a] *Data from Shannon (1976) and Dyar and Gunter (2008)*

[b] *Beryllium is often found in natural corundum, but it is associated with inclusion clouds. Whether Be exists in solution is not yet clear.*

ing these levels is to show the donor level before donating an electron (e.g., Ti as Ti^{3+}), and the acceptor levels after accepting the electron (e.g., Fe as Fe^{2+}). As such, the vertical distance between the donor and acceptor states is a measure of the binding energy of the donor-acceptor pair.

The beryllium acceptor level in figure 1 is shown in red, as it was not presented in Kröger (1984b) and has not been accurately measured. It is estimated from the original beryllium diffusion experiments (Emmett et al., 2003).

From the defect chemical reactions and energy level positions, we can formulate a series of rules about impurity interactions (Smyth, 2000). These rules will not be valid for all concentration levels or all temperatures. They become less valid as concentrations of key elements (such as Mg, Si, and Ti) exceed a few hundred ppma or at temperatures substantially above room temperature. A correct formulation requires solving the equilibrium chemical defect reactions for all of the impurities simultaneously, but measurements of the equilibrium constants for all the reactions are unavailable. However, the following rules are useful for a wide variety of situations and, more importantly, will serve to illustrate the types of chemical reactions that occur among impurities in corundum. These rules correct those presented in Emmett et al. (2003), written when it was believed that the silicon donor level was *below* that of titanium.

1. If there are two acceptors and a single donor, the lowest acceptor preferentially pairs with the donor unless both acceptors are energetically close together in the band gap, in which case the donor will pair with both.
2. If there are two donors at different levels and a single acceptor, the highest donor will preferentially pair with the acceptor. If the two donor energy levels are energetically close together in the band gap, they will both take part in charge compensation of the acceptor.
3. If corundum contains Ti, Mg, and Fe, Ti will pair with Mg before Fe.
4. If corundum contains Si, Mg, and Fe, Si will pair with Mg before Fe.
5. If corundum contains Si, Ti, Mg, and Fe, Si will pair with both Mg and Fe before Ti will.
6. When the concentration of Mg exceeds the sum of both Si and Ti, the excess Mg will be charge compensated by *trapped holes* (see Emmett et al., 2003, p. 92) in oxidizing conditions, or by oxygen vacancies under reducing conditions, or by both.

Why are we still uncertain about the role of silicon in corundum? We certainly understand the roles of Ti, Fe, and Mg. It is because we have not been able to measure the silicon content of the sapphire samples we have studied. The instruments used for laser ablation–inductively coupled plasma–quadrupole mass spectrometry (LA-ICP-QMS) in use in most laboratories show significant interferences for the three silicon isotopes. Thus, when a very high-purity sample of synthetic sapphire is measured on these instruments, it shows nominally several tens to several hundreds of ppma silicon that is not there (Shen, 2010). The reason for this is that in the plasma, small quantities of unusual molecules are formed with a mass close to that of silicon; these molecules are recorded by the instrument as silicon. For example, ^{28}Si is the most abundant isotope of silicon, at 92.23% abundance. Its mass is 27.97693 atomic mass unit (amu). When ablating corundum, aluminum carried by the plasma can combine with hydrogen from even a miniscule amount of water vapor to form ^{27}AlH with a mass of 27.98936. The mass difference between ^{28}Si and ^{27}AlH is only about 4 parts in 10,000, which is too small for the instrument to resolve, and so the instruments record both as silicon. The mass resolution of quadrupole mass spectrometers used in normal gemological laboratories at mass 28 is only 2–

3 parts in one hundred in the normal resolution mode, and only about 1 part per hundred in the high-resolution mode. The required resolution of 4 parts in 10,000 far exceeds the capability of a commercial "desktop" design ICP-QMS in normal gemological laboratories. High-resolution QMS is not available commercially. This example dramatically shows why a zero trace element concentration, matrix-matched standard is critical for the interpretation of data from these and other analytical instruments. Similar interferences have been measured for the other two silicon isotopes (Shen, 2010).

A few years ago, GIA initiated a project to develop an improved set of matrix-matched standards for the analysis of corundum with the existing LA-ICP-QMS instruments. The approach was to make ion implant standards in sapphire for each element of interest and calibrate them with Rutherford backscattering spectrometry (RBS). For those trace elements lighter than or close in mass to aluminum (i.e., Be, Mg, and Si), secondary ion mass spectrometry (SIMS) was used against multiple highly characterized standards kept by Evans Analytical. With calibrated ion implant standards, the next step was to grow multi-element doped sapphire crystals for the laboratory standards, which was done by Scientific Materials Corporation. The calibration was then transferred from the ion implant standards to the multiply doped crystals with Caltech's SIMS facility (GIA, 2016). A silicon ion implant standard was also prepared with the hope that advanced instrumentation would eventually allow the analysis of silicon.

The plan for the standards was to have a three-point calibration—a zero, a mid-range value, and a high value for each element. Sapphire crystals were grown that accomplished these goals except for the high-range iron value. Iron and its oxides all have high vapor pressure at the Czochralski growth temperature (~2300°C) and thus distill out of the melt.

All of the multi-element doped crystals were calibrated at the SIMS facility against the ion implant standards. When the extremely high-purity sapphire crystal (the zero standard) was measured by SIMS, it demonstrated that SIMS could resolve the isotopic interferences for silicon. SIMS could therefore measure silicon in corundum samples against an ion implant standard.

To create a high-range iron standard, a different approach had to be employed. Natural sapphires from Montana's Yogo deposit (figure 2) were evalu-

Figure 2. Paula Crevoshay's "Yogo Columbine" pendant displays the remarkably consistent blue color of Yogo sapphires: 243 in all, with a total weight of 13.89 carats. The piece also contains 0.59 ct of yellow sapphires and 1.37 ct of diamonds, set in 18K yellow and white gold. Photo by Orasa Weldon.

TABLE 2. SIMS analysis of a typical Yogo sapphire sample (in ppma).

Trace elements	Mg	Si	Mg – Si = available Mg	Ti	Ti – available Mg = available Ti	V	Cr	Fe	Ga
Concentration	84.3	24.6	59.7	79.7	20.0	2.7	2.2	1130	10.4
Standard deviation (ppma)	1.32	0.44	1.4	0.72	1.6	0.05	0.08	20	0.3

ated for uniformity. The Yogo sapphire is almost unique for the extreme uniformity of its blue color, which indicates a high trace element concentration uniformity, at least for the Fe^{2+}-Ti^{4+} chromophore. A typical sample is shown in figure 3. It was hoped that this uniformity would also extend to Fe^{3+}. The SIMS analyses of nine pieces of Yogo sapphire at nine points each did show a very high iron uniformity, and thus it was chosen to be the high iron concentration standard. The nine Yogo samples were calibrated with SIMS for all elements for which ion implant standards had been prepared. Since we can easily resolve the mass interference for silicon in corundum using the high mass resolving power of SIMS, accurate silicon measurements of natural corundum samples have been obtained for the first time.

Figure 3. A typical polished Yogo wafer sample measuring 0.93 mm thick. The c-axis is perpendicular to the wafer surface. Note the distinct color uniformity and the lack of any color zoning. Ten LA-ICP-QMS measurement points can also be seen on this wafer. Photo by John L. Emmett.

Surprisingly, it also turned out that the Yogo sapphires provided an excellent example of the role of silicon in gem corundum. The trace element concentrations and color are extremely uniform, and thus the standard deviations (SDs) of the concentration measurements are quite small. SIMS analysis of the individual trace elements against corundum ion implant standards is shown in table 2. The data presented are the average of three measurement points on this particular sample.

Since Si is the highest-lying donor and Mg the lowest-lying acceptor, Si will pair with Mg first, leaving 59.7 ppma Mg^{2+} available to interact with other trace elements. Then Ti as a donor will pair with all the remaining available Mg, leaving 20.0 ppma Ti to pair with Fe, producing the blue coloration. It is interesting to note that without silicon, Yogo sapphire would not be blue because Mg>Ti, and thus no unpaired Ti would be available to pair with Fe. The analysis of this Yogo sapphire is not unusual but is typical of all of the Yogo samples analyzed.

This clearly demonstrates the critical role of silicon in the color of corundum, a factor that, to the best of our knowledge, has not been correctly addressed in the literature.

The SDs presented in table 2 only relate to the point-to-point analysis variations of the sample. For determining the SDs of the absolute measurement, it is necessary to correctly combine the point-to-point SDs with the SDs of the ion implant standards. When this is done, the SD result for the "available titanium" becomes 6.7 ppma, which is well below the stated concentration value of 20 ppma. While this addition to the SD is rarely applied in the gemological literature, it is presented here to emphasize the validity of the absolute result.

The SIMS analysis of Si conducted on nine Yogo samples resulted in Si concentrations from 22 to 26 ppma. In addition, ten other samples from Myanmar, the Rock Creek deposit in Montana (United States), the Garba Tula deposit in Kenya, the Subera deposit in Queensland (Australia), the Pailin deposit in Cambodia, and the Montepuez ruby deposit in Mozambique were also analyzed for silicon. The concentrations measured ranged from 3.5 to 150 ppma. In each case the silicon concentration was in the same range as the concentrations of the other aliovalent ions, and thus in each case it had a significant impact on color.

CONCLUSIONS

It is clear from the foregoing study that silicon is an important trace element in gem corundum, contributing substantially to the resulting color. The current analytical capabilities of most of the world's gem labs do not allow the quantification of silicon at relevant concentration levels. Consideration should be given to the possibility of obtaining higher-resolution mass detectors for the existing LA-ICP equipment, or to evaluating other analytical techniques such as laser-induced breakdown spectroscopy (LIBS).

ABOUT THE AUTHORS

Dr. Emmett is the director of Crystal Chemistry in Brush Prairie, Washington; he is also a consultant to GIA. Dr. Stone-Sundberg is the managing director of Crystal Solutions in Portland, Oregon, and a consultant to GIA. Dr. Guan is the laboratory director of the Microanalysis Center, Division of Geological & Planetary Sciences, at the California Institute of Technology in Pasadena, California. Mr. Sun is a staff gemologist at GIA in Carlsbad, California.

ACKNOWLEDGMENTS

Tom Moses and GIA have provided long-term support for numerous studies like this one. Tim Thomas initiated GIA's development of the new set matrix-matched standards on which this work depends. He had the foresight to include an ion implant standard for silicon, which made this work possible. Dr. George Rossman has facilitated access to Caltech's excellent SIMS analytical facility. In addition, he continues to provide an extremely helpful debate of the technical issues, which is greatly appreciated.

REFERENCES

Blundy J., Wood B. (2003) Partitioning of trace elements between crystals and melts. *Earth and Planetary Science Letters*, Vol. 210, No. 3-4, pp. 383–397, http://dx.doi.org/10.1016/S0012-821X(03)00129-8

Dyar M.D., Gunter M.E. (2008) *Mineralogy and Optical Mineralogy*. Mineralogical Society of America, Chantilly, Virginia.

Emmett J.L., Scarratt K., McClure S.F., Moses T., Douthit T.R., Hughes R., Novak S., Shigley J.E., Wang W., Bordelon O., Kane R.E. (2003) Beryllium diffusion of ruby and sapphire. *G&G*, Vol. 39, No. 2, pp. 84–135, http://dx.doi.org/10.5741/GEMS.39.2.84

Gemological Institute of America (2016). Final report for corundum standard sets for GIA LA-ICP-MS instruments. Internal report, June 10.

Karato S.-I. (2016) Physical basis of trace element partitioning: A review. *American Mineralogist*, Vol. 101, No. 12, pp. 2577–2593, http://dx.doi.org/10.2138/am-2016-5665

Khattak C.P., Schmid F. (2001) Growth of the world's largest sapphire crystals. *Journal of Crystal Growth*, Vol. 225, No. 2-4, pp. 572–579, http://dx.doi.org/10.1016/S0022-0248(01)00955-1

Kröger F.A. (1984a) Defect related properties of doped alumina. *Solid State Ionics*, Vol. 12, pp. 189–199, http://dx.doi.org/10.1016/0167-2738(84)90148-6

Kröger F.A. (1984b) Electrical properties of alpha-Al_2O_3. In W.D. Kingery, Ed., *Advances in Ceramics, Volume 10: Structure and Properties of MgO and Al_2O_3 Ceramics*. American Ceramic Society, Columbus, Ohio, pp. 1–15.

Lee C.H., Kröger F.A. (1985) Electrical conductivity of polycrystalline Al_2O_3 doped with silicon. *Journal of the American Ceramic Society*, Vol. 68, No. 2, pp. 92–99, http://dx.doi.org/10.1111/j.1151-2916.1985.tb15271.x

Shannon R.D. (1976) Revised effective ionic radii and systematic studies of interatomic distances in halides and chalcogenides. *Acta Crystallographica Section A*, Vol. 32, No. 5, pp. 751–767, http://dx.doi.org/10.1107/S0567739476001551

Shen A.H. (2010) Silicon in sapphires – Its role and detectability by LA-ICP-QMS. Goldschmidt Conference Abstracts, p. A945.

Smyth D.M. (2000) *The Defect Chemistry of Metal Oxides*. Oxford University Press, New York.

JAPANESE JADEITE: HISTORY, CHARACTERISTICS, AND COMPARISON WITH OTHER SOURCES

Ahmadjan Abduriyim, Kazuko Saruwatari, and Yusuke Katsurada

Even though Japanese jadeite lacks the transparency of the highest-quality Burmese imperial jadeite, its rarity and natural features make it a highly valued gemstone. In this study, jadeite from the Itoigawa and Omi regions in Niigata Prefecture and the Wakasa region in Tottori Prefecture, both on Japan's western coast, were divided into several color varieties corresponding to chromophores and mineral phases: white (nearly pure jadeite), green (Fe-rich, Cr-bearing), lavender (Ti-bearing), blue (Ti- and Fe-bearing), and black (graphite-bearing). White jadeite from Itoigawa-Omi was close to pure jadeite (X_{Jd} = 98, or 98% jadeite composition). Green jadeite from the same location had an X_{Jd} range from 98 to 82. The maximum CaO content in green jadeite was 5 wt.%, and its chromophores were Fe and Cr. Whereas lavender samples had a jadeite composition of X_{Jd} = 98 to 93 and tended to be high in TiO_2 and FeO_{tot} and low in MnO content, blue jadeite showed the highest TiO_2 concentration at 0.65 wt.% and had an X_{Jd} range of 97 to 93. A blue jadeite from Wakasa had a range of 97 to 91 and a similarly high TiO_2 concentration. In trace-element analysis, chondrite-normalized and primitive mantle–normalized patterns in lavender, violetish blue, and blue jadeite from Japan showed higher large-ion lithophile element contents (Sr, Ba) and higher field strength element contents (Zr, Nb) than those in green jadeite, while white and black jadeite had relatively low REE contents. The Japanese jadeites were compared to samples from Myanmar, Guatemala, and Russia.

Japan is an important source of jadeite, much of which comes from the Itoigawa and Omi regions in Niigata Prefecture. The Kotaki area upstream of the Hime River in Itoigawa-Omi was the first documented source of gem-quality jadeite and jadeite-bearing rocks in Japan (Kawano, 1939; Ohmori, 1939). This area is located in the high-pressure, low-temperature metamorphic Renge belt within a Late Paleozoic subduction zone (Shibata and Nozawa, 1968; Nishimura, 1998). Tsujimori (2002) suggested that blueschist to eclogite metamorphism was related to the subduction of oceanic crust. Miyajima et al. (1999, 2001, 2002) and Morishita (2005) proposed that the fluids that facilitated the formation of jadeite in Itoigawa-Omi were related to subduction zones. U-Pb zircon dating of jadeite-natrolite rocks in the area indicated that the age of jadeitization is about 519±17 Ma (Kunugiza et al., 2002; Tsutsumi et al., 2010).

This study introduces the historical background and sources of Japanese jadeite (figure 1). It describes

Figure 1. A large, attractive jadeite boulder from Itoigawa, Japan, characterized by mixed white and green colors. This boulder weighs 40.5 kg and measures approximately 39 cm high, 32 cm long, and 26 cm wide. Photo by Ahmadjan Abduriyim.

See end of article for About the Authors and Acknowledgments.
GEMS & GEMOLOGY, Vol. 53, No. 1, pp. 48–67,
http://dx.doi.org/10.5741/GEMS.53.1.48

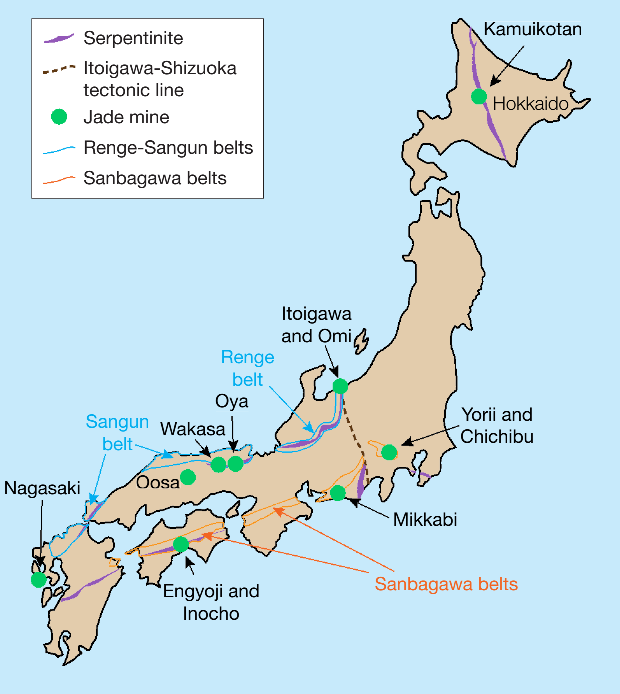

Figure 2. Japanese jadeite is found in eight locations, though the only significant source of gem-quality material is the Itoigawa-Omi region in Niigata Prefecture. Modified after Fossa Magna Museum.

the material's color varieties, internal texture, and chemical features using quantitative electron microprobe (EPMA) and laser ablation–inductively coupled plasma–mass spectroscopy (LA-ICP-MS) analysis.

HISTORICAL BACKGROUND

In addition to Japan, major jadeite localities include Myanmar, Russia, Central America, and the United States. Some of the world's earliest jadeite jade artifacts emerged from the Olmec, Maya, and Aztec civilizations of modern-day Mexico and Guatemala, which flourished from about 1200 BC until the Spanish conquest in the 16th century (Foshag and Leslie, 1955; Umehara, 1971; Taube, 2004). During the Jomon era, about 5,500 years ago, Japan's Itoigawa region became the birthplace of jadeite carving (figure 2), and it is no exaggeration to say that the Japanese gem culture was derived from this area. In the middle of the Jomon era, pendant-like jadeite pieces called *taishu* were produced and traded throughout many parts of Japan. Rough jadeite fashioning techniques, including spherical bead carving, were passed on in the late Jomon era. In the Yayoi era, curved *magatama* and tube-shaped *kudatama* beads became popular. According to legend dating from the early 8th century, the ancient state of Koshi (in modern-day Niigata Prefecture) was ruled by a beautiful empress who wore a mysterious curved green jadeite (figure 3). Koshi produced a variety of beautiful stones and cultivated a thriving trade with many other parts of Japan. Typically excavated from the tombs of powerful people, magatama jadeite appears to have been a sacred ornament as well as a symbol of wealth and prestige. Magatama carvings spread to the Korean Peninsula, where they have been excavated at many archaeological sites (Barnes, 1999).

Thousands of years of jadeite culture went into decline during the mid and late Kofun period (3rd to 7th century AD) before disappearing in the 6th century. Jadeite was rediscovered in Japan in 1938, more than a thousand years after vanishing, when researcher Eizo Ito uncovered it at the Kotaki River in the city of Itoigawa. The following year, Dr. Yoshi-

Figure 3. In this mosaic painting, made with pieces of Itoigawa jadeite, the magatama carving is worn by an empress of the ancient state of Koshi, in modern-day Niigata Prefecture. Courtesy of the Jade Ore Museum (Hisui Gensekikan).

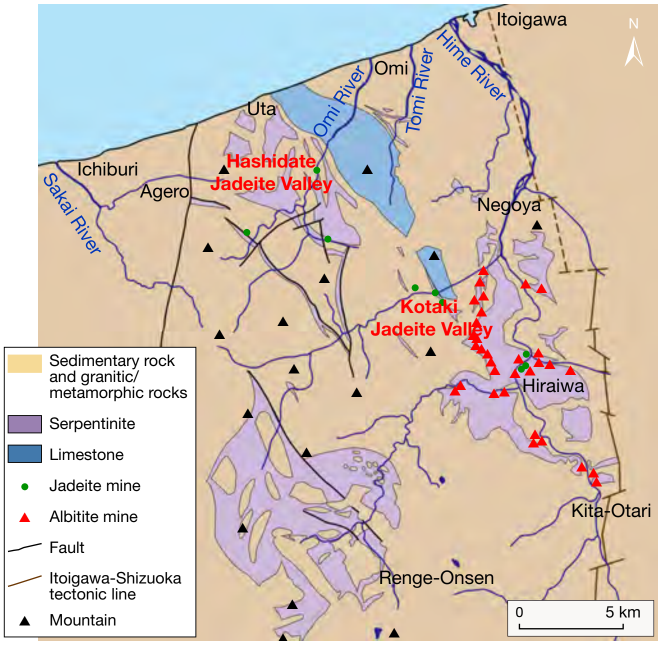

Figure 4. Jadeite from Itoigawa is found in serpentinite along a fault as blocks near the Kotaki River (upstream of the Hime River) and the Omi River. The Kotaki and Hashidate valleys are the main sources of gem-quality jadeite. White is the most common color, followed by green. Lavender, violet-blue, and blue jadeite are also found in Itoigawa-Omi. Source: Fossa Magna Museum.

nori Kawano and his colleagues at Tohoku University published a study of the samples (Kawano, 1939; Ohmori, 1939). Subsequent research led to additional discoveries in the Kotaki area, upstream of the Hime River, as well as in the Hashidate area of Itoigawa (figure 4). In 1954, some of these areas were designated as preservation sites, but jadeite is still found along these rivers or their estuaries.

Jadeite from Itoigawa, especially along the coast, is beautiful even in its rough state. Colors include white, green, violet, blue, and black. But because the sites are protected and mining is not allowed, there is little supply of this material in the market. In September 2016, Itoigawa jadeite was chosen as Japan's national stone by the Japan Association of Mineralogical Sciences.

JADEITE FROM JAPANESE LOCALITIES

Jadeite is found in high-pressure, low-temperature metamorphic belts (Essene, 1967; Chihara, 1971; Harlow and Sorensen, 2005). It is associated with kyanite, an indicator mineral of high-pressure, low-temperature metamorphism. The Japan Trench is a boundary between the Pacific plate and the Eurasia plate containing the Japanese islands, under which the cold Pacific plate subducts. This area is thought to have a high-pressure, low-temperature condition that produces jadeite. Japan has eight jadeite occurrences in all (again, see figure 2). Most of the jadeite from the Renge and Sangun belts on the western side (Itoigawa, Oosa, Oya, and Wakasa) is very pure, composed of more than 90% jadeite (including similar omphacite). Material from other parts of Japan very rarely contains more than 80% jadeite. Most contains large amounts of albite, kyanite, and analcime and no more than 50% jadeite (Yokoyama and Sameshima, 1982; Takayama, 1986; Miyazoe et al., 2009; Fukuyama et al., 2013).

Renge and Sangun Belts. The Itoigawa region is assigned to the Renge belt, a serpentinite mélange zone with various types of tectonic blocks, high-pressure and low-temperature metamorphic rocks, metamorphosed sedimentary rocks, amphibolites, and rodingites (Nakamizu et al., 1989). Gem-quality jadeite has been found only at the Kotaki and Hashidate districts in Itoigawa-Omi, occurring as boulders in the serpentinite located at the fault border between the Permian-Carboniferous limestone and Cretaceous sandstone and shale. Jadeite boulders range from one meter to several meters in size and are mostly distributed in an area several hundred meters long. Jadeite rocks in Kotaki show concentric zoning, toward the rim, of albitite (with or without quartz), white jadeite, green jadeite, soda-rich calciferous amphibole, and host serpentinite. Omi jadeite rock shows a "distinct stratiform structure," sometimes with alternating coarse and fine compact layers and often containing lavender jadeite (Chihara, 1991).

Sources other than Itoigawa in the Renge and Sangun belts (Oosa, Oya, and Wakasa) produce limited amounts of jadeite, most of it white with a few green areas. Green jadeite with high transparency has not been found in these areas. Considering that it contains similar minerals as well as zircons that are about 500 million years old (Tsutsumi et al., 2010), the material from Oosa, Oya, and Wakasa presumably formed through the same process as the Itoigawa jadeite. These fine-grained specimens cannot be differentiated microscopically from those of Itoigawa.

The Wakasa region in Tottori Prefecture of western Japan is a source of blue jadeite. Jadeite and jadeite pyroxene occur in serpentinites and metagabbros related to the Sangun regional metamorphic belt (Kanmera et al., 1980; Chihara, 1991). In this locality, jadeite rock formed as a vein in part of a serpentinite body ranging from 5 to 30 cm in diameter. The rocks are mostly weathered but still hard and compact. Most of the jadeite has a violetish blue to blue, lavender, and milky white color and is associated with albite, quartz, and chlorite. Wakasa jadeite is also known to have a blue color, but production is very limited.

Hokkaido. The northern Japanese island of Hokkaido is shown in figure 2. The Kamuikotan belt, a high-pressure metamorphic belt, extends north to south in Hokkaido. In the serpentine area of this metamorphic belt in the Asahikawa district, jadeite-bearing rocks are very rare but may locally contain more than 80% jadeite. Most of the jadeite around 10 cm in size contains less than 50% jadeite content, however. Various mineral components deprive the jadeites of their transparency, making them difficult to distinguish from surrounding green rocks of lawsonite-albite facies retrograded in greenschist facies.

In Brief

- Japan's only source of gem-quality jadeite is the Itoigawa-Omi region in Niigata Prefecture. The area belongs to a serpentinite mélange zone with high-pressure and low-temperature metamorphic rocks, amphibolites, and jadeitites.
- Some 5,500 years ago, jadeite carvings were traded throughout Japan. Since the rediscovery of the jadeite source in 1938, limited quantities have been available.
- These Japanese jadeites display a variety of colors, including white, green, lavender, violetish blue, blue, and black. White jadeite shows a very pure jadeite component, while green jadeite has a low percentage of omphacite ranging from 2% to 18% and is colored by Fe and Cr. Blue samples are enriched with Ti.
- Trace element analysis by LA-ICP-MS confirmed that lavender, violetish blue, and blue jadeite showed higher large-ion lithophile elements and higher field strength elements than green, white, and black jadeite.

Sanbagawa Belt. Two deposits of jadeite-bearing rock have been reported in the Yorii and Chichibu districts in the Kanto Mountains of Saitama Prefecture. One of the locations forms a dome with serpentine, and the maximum jadeite content there is about 50%. Another occurrence, accompanied by actinolite rocks that supposedly replaced serpentinite, is similar to the surrounding metamorphic rocks where jadeite occurs in clusters, and samples with more than 80% jadeite content are rare. The jadeite from this area is not suitable for jewelry and, like material from Hokkaido, cannot be differentiated from the surrounding metamorphic rocks. Mikkabi in Shizuoka Prefecture also produces jadeite, found as a white vein 2 to 3 cm thick in metagabbro, but it too is unsuitable for fashioning.

Kochi and Nagasaki. Rocks containing jadeite have occasionally been found within serpentinite in the city of Kochi. These include gray quartz-bearing rocks and green rocks containing pumpellyite and kyanite. Neither contains more than 60% jadeite or possesses transparency, and thus cannot be visually differentiated from common hard metamorphic rocks. In Nagasaki, rocks containing jadeite associated with serpentine have been reported. Parts of the rock contain more than 80% jadeite, but the content is often as low as 50%. Only limited amounts of the jadeite-bearing rocks have been produced.

SAMPLE DESCRIPTIONS AND ANALYTICAL METHODS

To examine the color varieties of Japanese jadeite, we collected representative samples from the field in Itoigawa and Wakasa and from the Jade Ore Museum (Hisui Genseki Kan) in Tokyo and the Fossa Magna Museum in Itoigawa (see the top table at https://www.gia.edu/gems-gemology/spring-2017-japanese-jadeite-tables). The 39 rough and cut Japanese samples consisted of white, green, dark green, lavender, violetish blue, blue, and black jadeite. They were from three different sources: the Kotaki River area (36º55'33N, 137º49'18E; 32 samples) and Hashidate (36º58'35N, 137º45'51E; five samples), both in Itoigawa, and the Wakasa region (35º32'17N, 134º44'52E; two samples).

To compare their optical features, petrographic structures, and geochemistry with samples from other parts of the world, we also tested Russian white and green jadeite from the Polar Urals (four samples); dark yellowish green and lavender jadeite from the Motagua region of Guatemala (six samples); and Burmese white, green, and lavender jadeite from Kachin State (38 samples). The samples were provided by the Jade Ore Museum (Hisui Gensekikan) and Miyuki Co., Ltd. Examples are shown in figure 5.

All 87 samples were observed by visual and microscopic means, and their refractive indices were examined by either normal reading from flat wafers or by the spot method. Specific gravity was determined

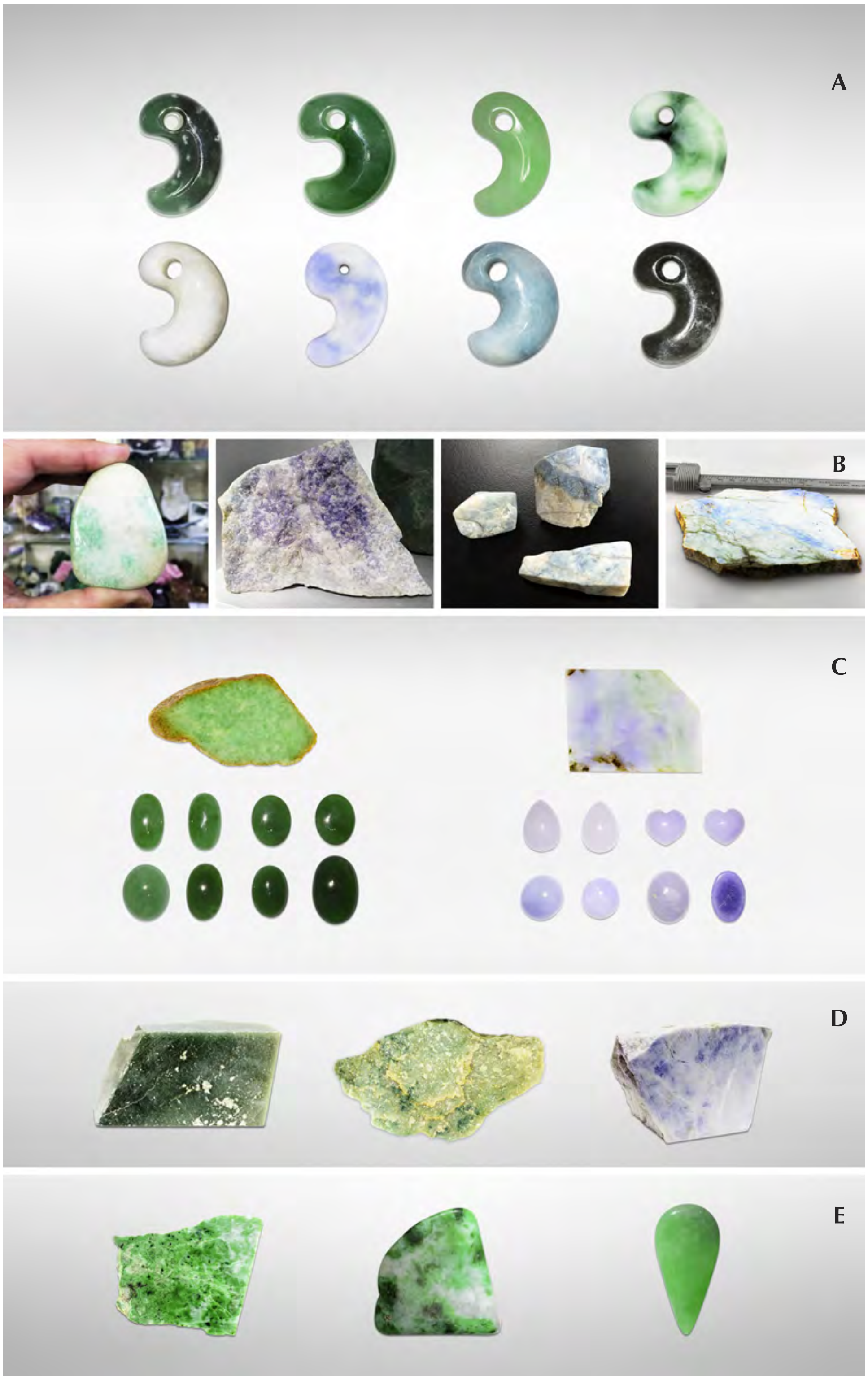

Figure 5. Representative samples from four locations. A: Magatama carvings (25.51–63.88 ct) from Itoigawa-Omi. B: Variously colored rough jadeite boulder, cobble, and pebbles from Itoigawa-Omi (15.3–622.2 g) and a polished violetish blue jadeite from the Wakasa region (458.2 g). C: Green and lavender cabochons (4.75–15.45 ct) and polished slices from Kachin, Myanmar (17.84–136.4 g). D: Rough grayish green and lavender jadeite blocks from the Motagua region of Guatemala (223–1250 g). E: A green jadeite block (304 g) and two polished translucent to opaque jadeites (139.08 and 5.93 ct) from the Polar Urals of Russia. The magatama from Itoigawa-Omi and the Russian and Guatemalan samples are courtesy of the Jade Ore Museum (Hisui Gensekikan). The Burmese jadeites are courtesy of Miyuki Co., Ltd. Photos by Masumi Saito and Ahmadjan Abduriyim.

hydrostatically for all the samples, and their absorption spectra were observed by handheld prism spectroscope. Four inclusion-bearing samples from Itoigawa and Wakasa, three from Kachin, two from Motagua, and two from the Polar Urals were cut and polished into thin sections for petrographic structure analysis. The micro-texture of these petrographic thin sections was observed using a Nikon Optiphot polarized light microscope.

To identify the inclusions and reveal the distribution of jadeite and other minerals in jadeite rock, we used a two-dimensional micro-Raman mapping spectroscope (Horiba Jobin Yvon XploRA LabRAM HR Evolution) equipped with a 532 nm Nd:YAG laser and an optical microscope (Olympus BX41) under real usage conditions. The laser beam was narrowed and focused through a 300 μm aperture and a 100× objective lens, yielding a spatial resolution of about 1 μm. Raman spectra were acquired with a single polychrome spectrometer equipped with a Si-based charge-coupled device (CCD) detector (1024 × 256 pixels). A composite spectrum in the range of 200–1800 cm^{-1} was obtained with LabSpec software, using a 600 gr/mm grating with a spectral resolution of about ±2.5 to 3.5 cm^{-1}. Before performing the measurements, we calibrated the spectrometer by the Si 520 cm^{-1} peak. Raman spectral mapping was conducted in point-by-point macro mode using XY stepping motors. It took 15 minutes to obtain a 44 × 30 mm spectral macro mapping image with a step size of 500 μm in the 200–1800 cm^{-1} range.

UV-Vis-NIR spectroscopy was performed on parallel polished wafers of green, lavender, and blue samples from Kotaki, Itoigawa; a violetish blue sample from the Wakasa region; green and lavender samples from Kachin and Motagua; and a green sample from the Polar Urals. The analyses were performed using a Hitachi U-2900 spectrophotometer at 1 nm resolution. The parallel polished plates were oriented with the main polished face perpendicular to the instrument beam, and the polarizer was not rotated. The thin sections ranged from 3.63 to 10.08 ct and from 0.86 to 3.70 mm thick.

To investigate the various colors of the jadeites, very precise quantitative chemical composition measurements were obtained by electron microprobe with wavelength-dispersive spectrometry (WDS) mode (JEOL LXA-8900) at the University of Tokyo and Waseda University. Eleven thin sections and polished thin plates from Itoigawa and Wakasa, two specimens from Motagua, and one specimen from the Polar Urals were analyzed with 15 kV accelerating voltage, using a beam current of 12 nA and beam diameter of 10 μm. Data were processed with ZAF correction software. The standards were natural albite for Al(Kα) and Na(Kα), wollastonite for Ca(Kα) and Si(Kα), orthoclase for K(Kα), chromite for Cr(Kα), Mn-olivine for Mn(Kα), and TiO_2, Fe_2O_3, MgO, and NiO for Ti(Kα), Fe(Kα), Mg(Kα), and Ni(Kα), respectively.

Trace element and rare earth element (REE) analyses were performed with LA-ICP-MS using a Thermo Scientific iCAP Q quadrupole ICP-MS with an ESI UP213 Nd-YAG laser. The laser repetition rate was 7 Hz, with an energy density of 10 J/cm^2 and a spot size of 40 μm, using a carrier gas mixture of helium and argon. It was possible to detect the signal of all isotope ratios and achieve an analytical precision of less than 10% relative standard deviation (RSD). Three to ten spots were ablated for each sample, and averaged data was calibrated. NIST SRM 610 and 612 were used as external standards. Before analysis, the samples were cleaned with acetone and aqua regia in an ultrasonic bath to eliminate surface contamination.

RESULTS AND DISCUSSION

Gemological Observations. Jadeite pebbles from Itoigawa-Omi tend to have rounded corners, resulting from erosion by fluvial processes, and a glittering whitish surface. Because of surface weathering, the rough rock does not have a brown skin. These stones are mainly white, with unevenly distributed pale green to green areas, and they feel rigid, compact, and heavy. Most of the white rocks mixed with some green were in boulder, pebble, and nodule form, transparent to semi-translucent to opaque, and finely textured, with some coarse texture in eye-visible single crystals. The largest rough specimen, found in the Hashidate district, weighed 102 tons. The author has also observed a 4.6 ton jadeite rock from the Kotaki district that is housed in the Fossa Magna Museum (figure 6, left). In this large jadeite boulder, most of the white and green parts were jadeite jade, while the fibrous black portion was composed of amphibole. Some small green areas were translucent and gemmy. Some minor faults were filled with white minerals such as prehnite, pectolite, and zeolite-group minerals that formed within fluids from the deeper part of the earth.

In lavender jade, the violet color may be dispersed irregularly over the white matrix. This color is semi-translucent to opaque, with a fine to medium texture (figure 6, center). The blue jadeite samples, found in a variety of beautiful colors, were rounded and semi-translucent to opaque, with fine to coarse texture (figure 6, right). Aggregates of minute crystals were observed through a loupe but lacked crystal form. Specimens from Itoigawa and Tottori had a spot RI of 1.65 to 1.66 and SG values ranging from 3.10 to 3.35. Green jadeite samples were inert under long-wave

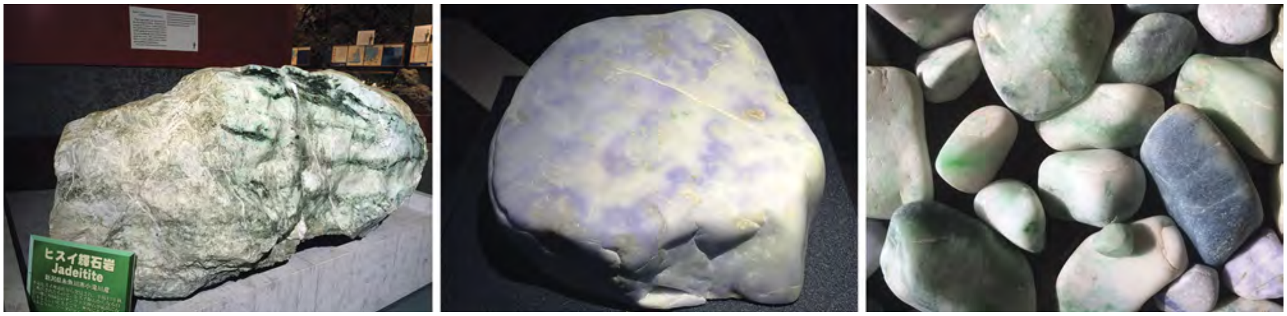

Figure 6. Left: A 4.6 ton jadeite rough boulder is displayed at the Fossa Magna Museum in Itoigawa. This eroded and rounded boulder from the Kotaki area is mostly white, with some green areas of jadeite; the fibrous structure in the black area is amphibole. Thin fault-like veins are filled with white minerals. Center: A 30 kg rounded boulder of predominantly lavender jadeite was found along the Hime River in Itoigawa. The lavender color is dispersed irregularly over the white matrix. Right: These rounded jadeite pebbles, found along the coast in Itoigawa-Omi, are approximately 2 to 15 cm long. Photos by Ahmadjan Abduriyim, courtesy of the Fossa Magna Museum and the Jade Ore Museum (Hisui Gensekikan).

(365 nm) and short-wave (254 nm) UV radiation. The lavender jadeite exhibited a stronger reddish fluorescence than Burmese lavender jadeite, which showed a weak reddish fluorescence to long-wave UV. The Japanese blue jadeite was inert to both long- and short-wave UV. The absorption spectra of all Japanese jadeite samples, measured by a handheld spectroscope, revealed weaker lines at 690, 650, and 630 nm. In addition, green jadeite from Itoigawa showed a very sharp line at 437 nm. The lavender jadeite showed weak bands at around 530 and 600 nm and a narrow band at 437 nm. The blue jadeite showed a very broad band from the yellow to red portion of the spectrum, as well as a weak narrow band at 437 nm.

The representative Guatemalan jadeite samples selected for this study were grayish and dark green, white, and violetish blue. The green rough was semitranslucent and opaque, with a fine to medium-grained texture but also somewhat coarsely grained texture in visible crystals. The "Olmec blue" rough from Guatemala was variegated violet to blue mixed with abundant white color. It was translucent to opaque, with a fine texture. Its color distribution closely resembled that of Japanese lavender and blue jade.

Jadeite from the Polar Urals occurs in different shades of green. The material usually has a more even color distribution than Japanese green jadeite, and it is highly valued. The samples from this source were semitransparent to translucent, with a fine to medium texture. Black spots of magnetite could be observed.

Petrographic Observation. In plane-polarized light, a white and green jadeite slice from Itoigawa (K-IT-JP-14; see figure 7-A1) revealed colorless, semitransparent jadeite crystals distributed in the white area, mostly as fine cryptocrystalline grains around 0.05–0.3 mm in size. Under cross-polarized light, the fine jadeite grains showed both high- and low-order interference colors, caused by the different orientation of each grain. Under plane-polarized light, we occasionally observed in matrix large pale green grains over 2 mm (figure 7-A2) that were well-formed jadeite single crystals. Their well-developed cleavages intersected at 87° angles, which is characteristic of pyroxene. This thin section of green jadeite showed a prismatic crystalloblastic texture, indicating metamorphism under nondirectional pressure. Micro-Raman spectrometry in microfolds and veinlets identified minor amounts of pectolite and prehnite as component minerals.

The thin section of lavender jadeite from Itoigawa-Omi was almost colorless under plane-polarized light (see figure 7-B1). The sample was semi-transparent to translucent and mainly composed of fine to micrograined crystals around 0.1–0.3 mm in size, showing a prismatic crystalloblastic texture. Ultramylonitic zones with radiating aggregates of fine jadeite grains randomly cutting through the matrix were observed in this sample (figure 7-B2). This texture indicates that the sample underwent lithostatic and possibly subsequent directional pressure during the metamorphic process. Prehnite and analcime, the main constituents of the veinlets that cut through the jadeite rock (figure 7-B3), were formed by hydrothermal fluids (Shoji and Kobayashi, 1988). A long prismatic vesuvianite crystal with high relief was also found as a component mineral.

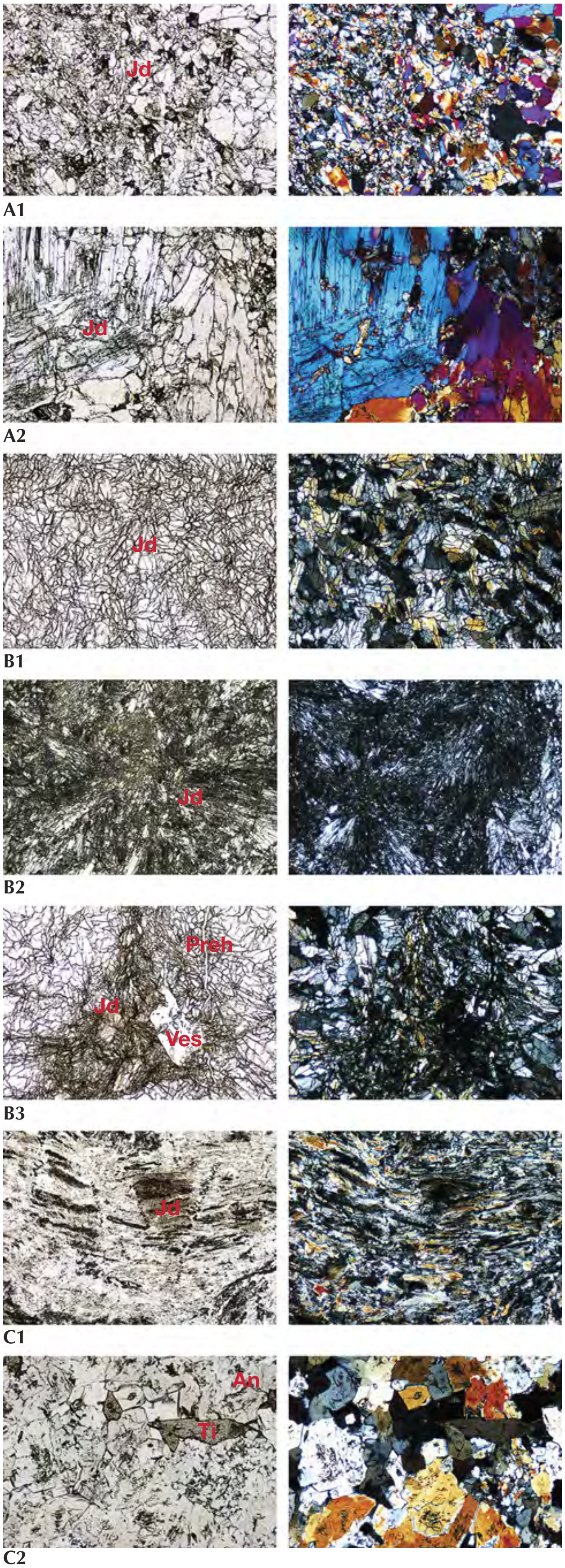

Figure 7. Petrographic microscope images of jadeite samples from Itoigawa. The left images are under plane-polarized light, the right images under cross-polarized light. Jd, Preh, Ves, An, *and* Ti *indicate jadeite, prehnite, vesuvianite, analcime, and titanite, respectively. A1: Green jadeite K-IT-JP-14 shows a prismatic-granular crystalloblastic texture, a distribution of fine colorless cryptocrystalline grains of jadeite, and a predominance of grains around 0.05–0.3 mm in size. A2: Coarse pale green grains larger than 2 mm can also be observed in the same matrix, which is a well-formed large jadeite single crystal. The prominent (110) cleavage planes intersecting at 87° are characteristic of pyroxene. B1: Lavender jadeite K-IT-JP-25 shows near-colorless fine and micro-grained jadeite crystals with a prismatic crystalloblastic texture. B2: Ultramylonitic zones with radiating aggregates of fine jadeite grains cut randomly through the center of the matrix, indicating a lithostatic pressure during the metamorphic process. B3: Dark gray prehnite and analcime, the main constituents of the veinlets that cut through this lavender jadeite, were formed by hydrothermal fluids. A high-relief prismatic vesuvianite crystal was also found as a component mineral. C1: K-IT-JP-16 is a predominantly blue specimen, translucent with fine cryptocrystalline grains. C2: Crushed preexisting minerals produce a flow structure with granoblastic and mylonitic texture. The component minerals analcime and a very minor amount of euhedral titanite grains are observed in the matrix. Photomicrographs by Ahmadjan Abduriyim.*

In the blue jadeite sample (K-IT-JP-16), the blue area was larger than the white area, and the colors gradually blended. It was translucent and granular, and the fine cryptocrystalline grains from 0.1 to 0.5 mm (figure 7-C1) showed granoblastic and mylonitic texture. In this specimen, preexisting minerals were crushed and slipped to produce a flow structure (figure 7-C2). Component minerals included analcime and titanite, as well as very minor amounts of euhedral titanite grains in the matrix that do not contribute to the blue color in this type of jadeite.

Morishita et al. (2007) proposed that jadeite from Itoigawa-Omi formed either by direct precipitation of minerals from aqueous fluids or by complete metasomatic modification of the precursor rocks by fluids. The Burmese green and lavender jadeite samples showed amphibole, albite, kosmochlor, and nepheline, while vesuvianite was rare. The Guatemalan green and lavender jadeite in this study showed grossular garnet, albite, and rutile, while the Russian green jadeite contained magnetite and analcime.

We used two-dimensional point-by-point Raman macro mapping to reveal the distribution of jadeite and other component minerals in the jadeite rocks.

Figure 8 shows a white and green/dark green sample from Itoigawa; the red, green, and blue colors correspond to the integrated intensity of jadeite, amphibole (richterite), and prehnite, respectively. This image reveals that the jadeite and amphibole grains are mixed within the matrix, while prehnite occurs in the vein. The rapid point-by-point confocal mapping technique can be performed on a whole specimen or a region of interest to examine finer details, making it possible to classify the distribution of jadeite vs. omphacite and/or amphibole.

UV-Vis Spectroscopy. *Japan*. UV-Vis absorption spectroscopy was performed on the green, violet, violetish blue, and blue jadeite wafers from the Itoigawa-Omi and Wakasa regions. Chemical analysis was carried out on similarly colored areas of the sample to confirm each chromophore's concentration.

Green portions of Itoigawa jadeite are generally colored by chromium and iron, showing a 691 nm absorption line (the Cr^{3+} "chromium line") and another absorption line that originates at around 437 nm (the Fe^{3+} "jadeite line"); see figure 9. The chromophore concentrations in the tested area, a 5 mm circle, were analyzed by LA-ICP-MS, and a concentration was averaged from three to four laser ablation spots. The green area contained relatively high Cr and Fe (280 and 810 ppma), and the isovalent chromophores Cr^{3+} and Fe^{3+} clearly contributed to the green color (Rossman, 1974; Harlow and Olds, 1987). The less significant chromophores Ti, Mn, V, and Co had lower concentrations (57, 19, 2.3, and 0.4 ppma, respectively; see the bottom table at https://www.gia.edu/gems-gemology/spring-2017-japanese-jadeite-tables).

The UV-Vis spectra of lavender jadeite from Itoigawa-Omi show features that correspond with Mn, Ti, and Fe (figure 10). A broad Mn^{3+}-related absorption band centered at 530 nm is often observed in Burmese lavender jadeite (Lu, 2012), as well as a characteristic broad band of paired Ti^{4+}-Fe^{2+} charge-transfer ions centered at 610 nm and a narrow Fe^{3+}-related 437 nm absorption band. The color-causing transition elements were analyzed in this lavender jadeite. The results showed that Ti (534 ppma average) and Fe (550 ppma average) were clearly responsible for its blue hue. Mn concentrations averaged 18 ppma and produced a weak pink or purple hue. The Japanese lavender jadeite showed a violet color, owing to the combination of minor pink and significant blue hues caused by Mn^{3+} and Ti^{4+}-Fe^{2+} absorption. Shinno and Oba (1993) discussed the substitution of Ti^{3+} at 545 nm in lavender jadeite from Itoigawa-Omi. However, the Ti^{3+} ion is very unstable in nature and is found only in meteorites and lunar samples formed in more reducing conditions (Burns, 1981). In terms of ionic radius, isovalent Ti^{3+} is noticeably larger than Al^{3+} and does not replace it in the six-fold coordinated octahedral site (figure 11). The chromophore concentrations of Ti and Fe in the violet parts reached 550 and 534 ppma, and this combination caused a noticeable blue color.

The UV-Vis spectra of blue jadeite from Itoigawa show a very broad band from 500 to 750 nm, a weak

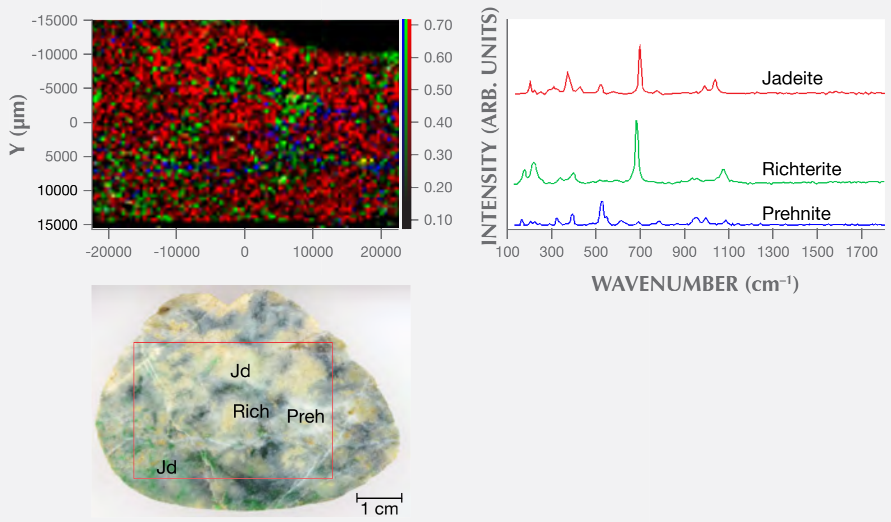

Figure 8. A two-dimensional Raman spectroscopy mapping image of a jadeite boulder from Itoigawa. The red area corresponds to the jadeite distribution, the green area to dark green richterite (amphibole group), and the blue area to the mineral prehnite, which is located at the veinlet and crosses through the stone. The mapping area is 44 × 30 mm.

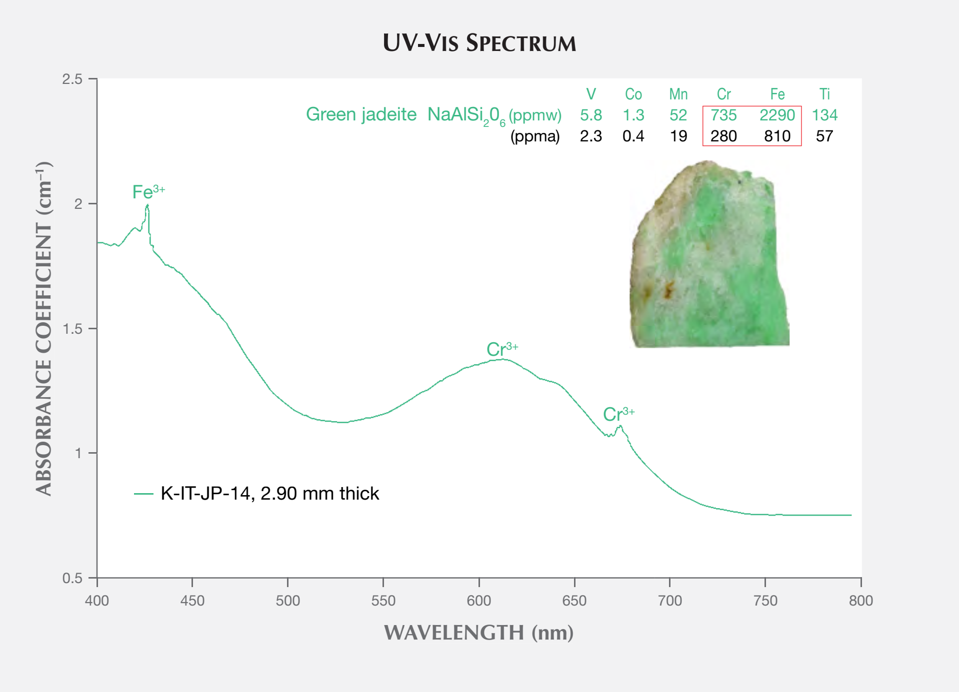

Figure 9. The UV-Vis spectrum of a green sample from Itoigawa (K-IT-JP-14) shows the features corresponding to Cr- and Fe-bearing green jadeite: the characteristic narrow 691 nm absorption, two Cr^{3+}-related weak shoulders at 650 and 630 nm, and a sharp, narrow absorption of Fe^{3+} at 437 nm. The saturated green area of the spectrum corresponds to the concentration of the chromophores Cr and Fe (280 and 810 ppma, on average).

Fe^{3+} absorption at 437 nm, and a cutoff above 350 nm (figure 12). This absorption pattern is similar to the spectra of blue sapphire and can be attributed to a charge transfer between Ti^{4+}-Fe^{2+} pairs (Ferguson and Fielding, 1971). Significant amounts of Ti (1943 ppma) and Fe (4212 ppma) produced a noticeable blue color. By comparison, Mn was too low (64 ppma) to produce a pinkish component.

The violetish blue jadeite from Wakasa in Tottori Prefecture showed a similar spectral characteristic, with lower Ti, Fe, and Mn concentrations than blue jadeite but higher concentrations than violet

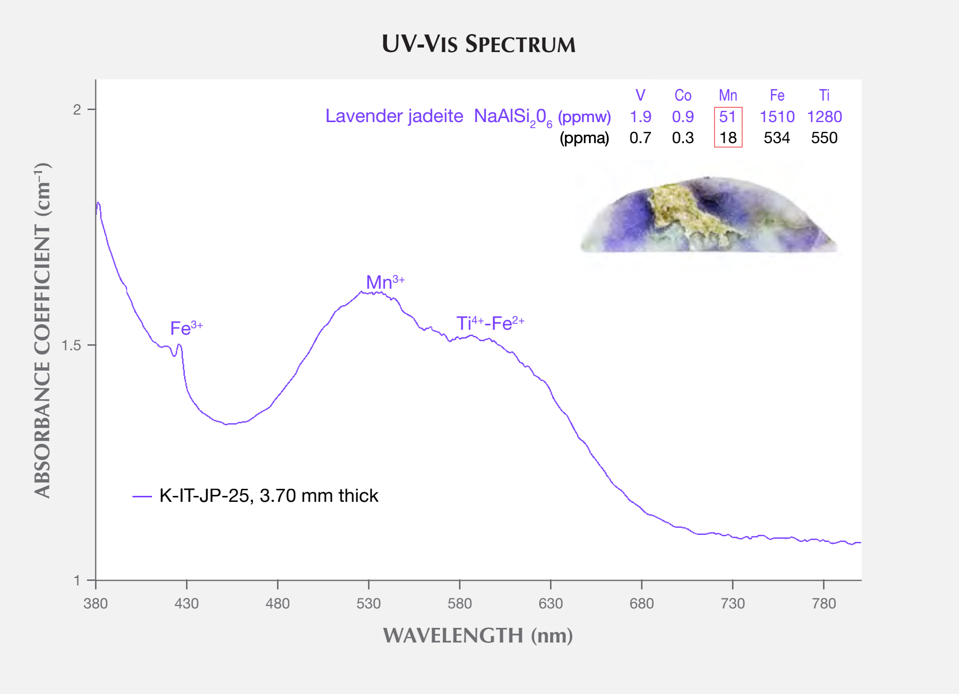

Figure 10. The UV-Vis spectrum of a lavender sample from Itoigawa-Omi (K-IT-JP-25). Two broad bands centered at 530 and 610 nm correspond to Mn and Ti-Fe charge transfer, and there is also a weak narrow band at 437 nm. The violet color reflects the chromophore combination of low Mn (18 ppma) and much higher Ti (534 ppma) and Fe (550 ppma).

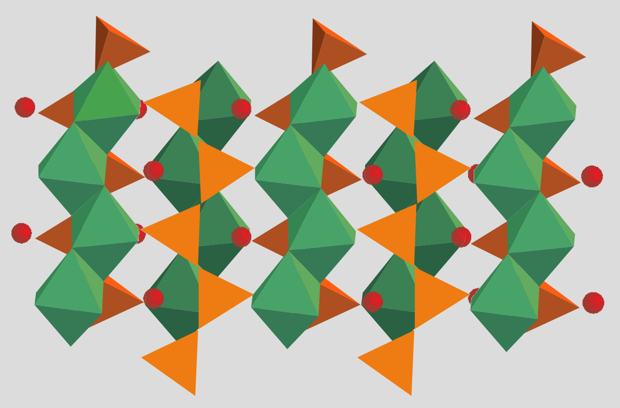

Figure 11. Illustration of the atomic arrangement of a single-chain pyroxene crystal structure, from the a-axis to b-axis direction. In the SiO_4 tetrahedrons (indicated in yellow and brown), four oxygen atoms surrounding a silicon atom are connected to form a strand, and other six-coordinate octahedron atoms (in green) are arranged so that they link the strands. Larger atoms (orange spheres) fill the spaces. Modified after Miyawaki (2004).

jadeite from Itoigawa (see the bottom table at https://www.gia.edu/gems-gemology/spring-2017-japanese-jadeite-tables).

Myanmar. The UV-Vis spectrum of the Burmese green jadeite (K-MYA-16) showed the characteristic narrow Cr^{3+}-related absorption band at 691 nm and the sharp, narrow Fe^{3+}-related absorption band at 437 nm that is very common in natural green jadeite. The Cr and Fe absorption feature generally overlapped with the spectrum of Japanese green jadeite, but the absorption intensity was much higher in Burmese jadeite due to its color saturation and transparency (figure 13A). The Burmese lavender jadeite (K-MYA-20) with a predominantly purple color component had a broad absorption centered at 570 nm, related to Mn concentration (figure 13B). The Fe and Ti concentration was much lower than in Japanese lavender jadeite and might not cause any noticeable blue component.

Guatemala. Only the characteristic Fe^{3+}-related narrow absorption band at 437 nm was found in the Guatemalan grayish green jadeite spectrum, which lacked the Cr^{3+} absorption (figure 13C). A very closely matched absorption spectrum was observed in Guatemalan lavender jadeite, which showed multiple broad bands centered at 530 and 610 nm and a weak narrow band at 437 nm (figure 13D). This absorption feature, related to Mn^{3+}, Ti^{4+}-Fe^{2+} pairs, and Fe^{3+}, generally overlapped with the bands observed in Itoigawa lavender jadeite. The concentrations of V, Cr, and Co were too low to create any noticeable color.

Russia. A highly saturated vivid green jadeite from the Polar Urals showed an Fe^{3+} band and strong multiple chromium lines in the 580–700 nm range, a

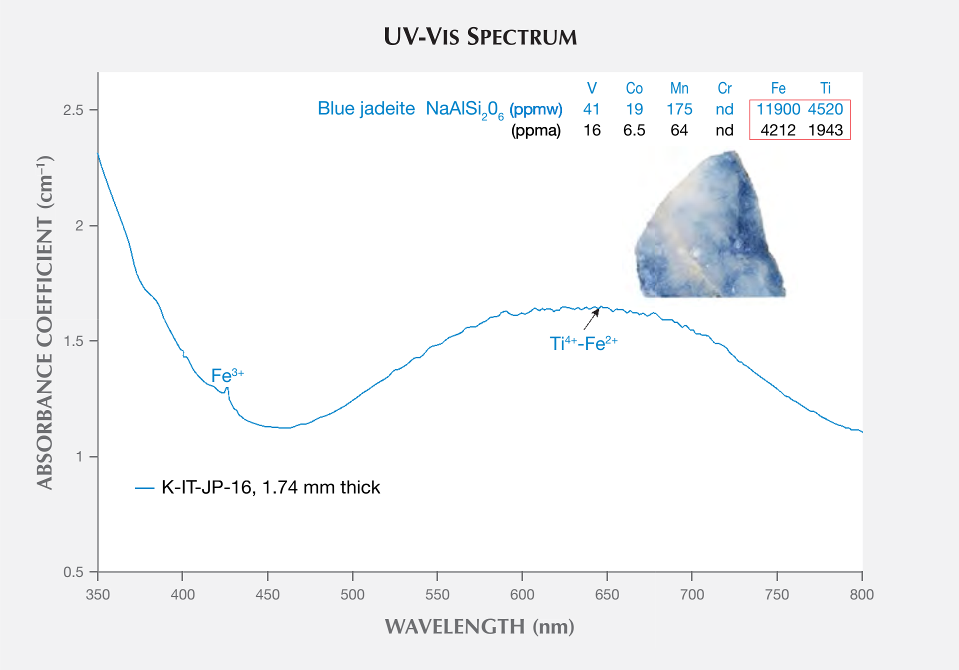

Figure 12. The UV-Vis spectrum of a blue sample from Itoigawa (K-IT-JP-16). The absorption shows a very wide broad band from 500 to 750 nm that overlaps the Mn-related broad bands at 530 and 570 nm observed in Burmese lavender jadeite. The chromophores Ti and Fe show a significant concentration at 1943 and 4212 ppma, respectively, and this jadeite's blue color could be mainly due to the Ti^{4+}-Fe^{2+} charge transfer.

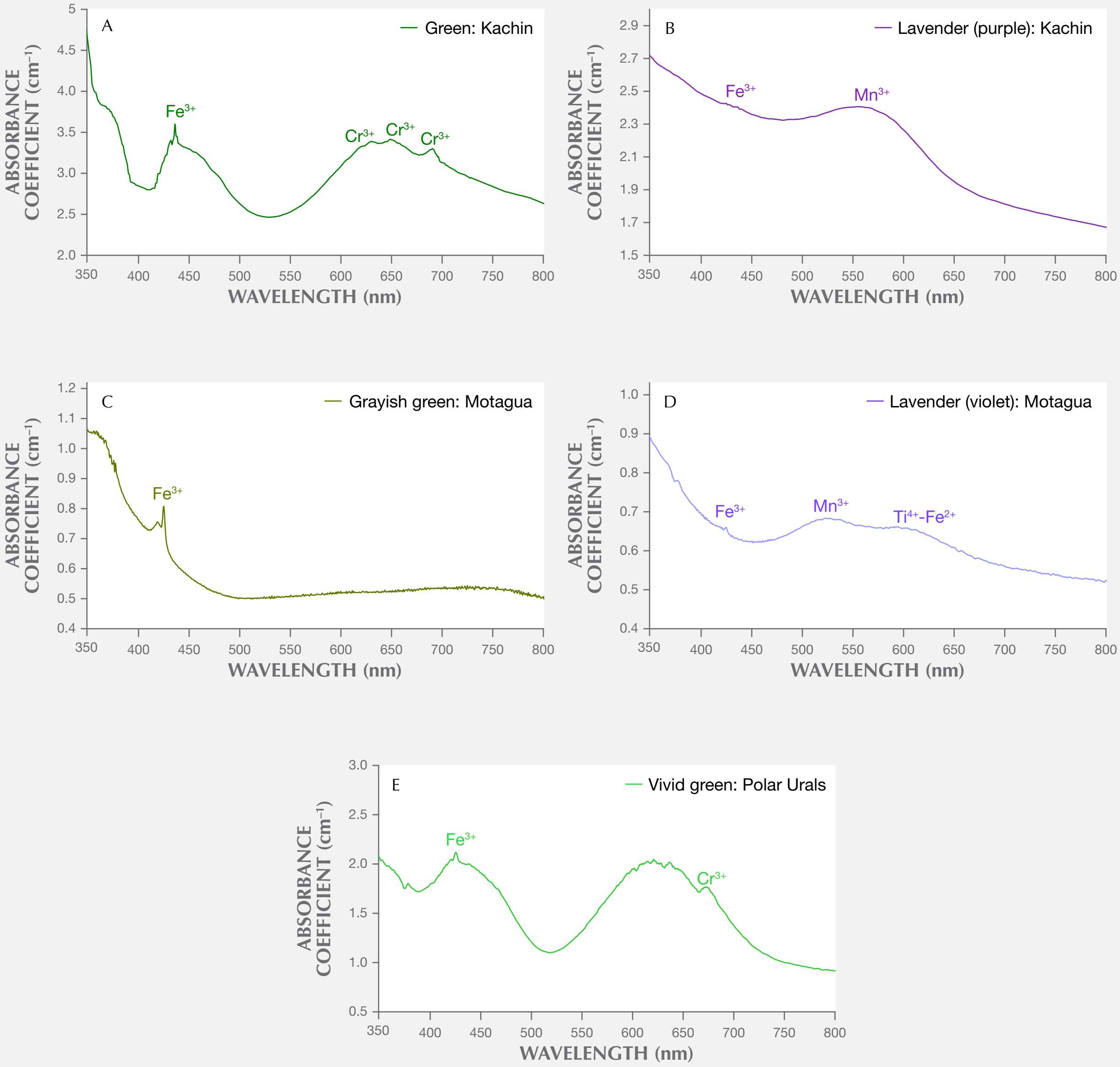

Figure 13. A: The UV-Vis spectrum of a green Burmese jadeite (K-MYA-16) shows the characteristic chromium lines at 630, 650, and 691 nm and the sharp, narrow Fe^{3+} absorption band at 437 nm that is commonly seen in natural green jadeite. The Cr^{3+}- and Fe^{3+}-related feature generally overlaps with the spectrum of Japanese green jadeite, but the absorption intensity is much higher due to its color saturation and transparency. B: Burmese lavender jadeite (K-MYA-20) showed a dominant broad absorption band centered at 570 nm, related to Mn^{3+} concentration. C: The narrow Fe^{3+} absorption band at 437 nm, often present in Guatemalan green jadeite (M-GUA-02). The absorption of Cr^{3+} is not detectable in this 2.32-mm-thick sample. D: The spectrum of Guatemalan lavender jadeite (M-GUA-03) shows multiple broad bands centered at 530 and 610 nm and a weak narrow band at 437 nm. The absorption feature related to Mn^{3+}, Ti^{4+}-Fe^{2+}, and Fe^{3+} generally overlaps with the bands observed in Itoigawa lavender jadeite. E: A vivid green Polar Ural jadeite shows an Fe^{3+} band and strong multiple chromium lines in the 580–700 nm range, a combination that typically produces a highly saturated green color. The concentration of Cr (maximum of 3042 ppma) is much higher than in Japanese green jadeite.

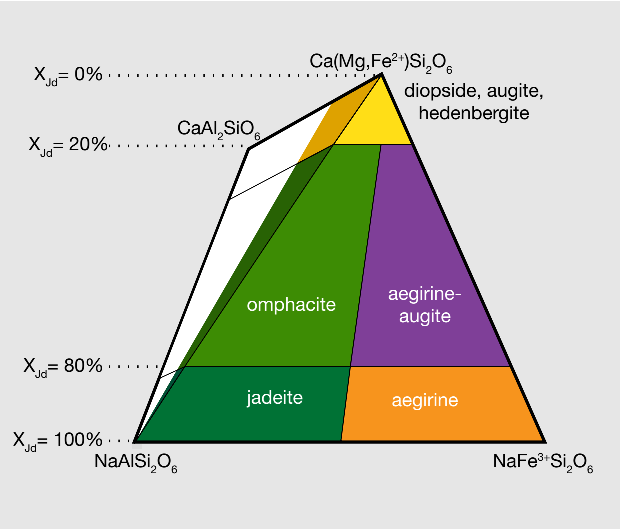

Figure 14. This classification of pyroxene based on chemical composition shows the relationship between jadeite and other pyroxenes in the main isomorphous substitution. Source: National Museum of Nature and Science, Tokyo.

combination that typically produces a highly saturated green color (figure 13E). The Cr concentration (up to 3042 ppma) was much higher than in Japanese green jadeite.

Chemical Analysis. Quantitative chemical data collected by EPMA for the samples from Japan, Guatemala, and Russia are summarized in table 1. The results are described below for each representative color: white, green, lavender, and blue (including violetish blue). X_{Jd}, $X_{(Ae+Ko)}$, and $X_{Quad\ (Dio+Aug+Hed)}$ were calculated as mol.% of Al/(Na + Ca), Fe^{3+}/(Na + Ca), and Ca/(Na + Ca), respectively (figure 14). The highest and lowest concentrations of jadeite (X_{Jd}) for 11 tested samples are listed in table 1. The 87 specimens from the four countries in this study (Japan, Myanmar, Guatemala, and Russia) were analyzed by LA-ICP-MS, with averaged data calculated based on three to ten laser ablation spots for each specimen; minimum and maximum values of each element concentration are listed in the bottom table at https://www.gia.edu/gems-gemology/spring-2017-japanese-jadeite-tables, with averaged data in parentheses.

White Jadeite. White jadeite from Itoigawa belongs to the clinopyroxene group and is close to the ideal jadeite composition (again, see table 1). All analyses (more than five spots) were close to the end member composition, up to X_{Jd} = 98 mol.%. The CaO, MgO, and FeO_{tot} contents were lower than those tested from any other jade color (0.26, 0.12, and 0.44 wt.%, respectively). Values for Cr_2O_3, MnO, K_2O, and NiO were below the detection limit of the analysis. TiO_2 (0.03 wt.%) was lower than values analyzed from violet and blue jadeite elsewhere. The white jadeite was very pure.

LA-ICP-MS analyses of the white jadeite consistently identified 19 minor and trace elements (Li, Mg, K, Ca, Sc, Ti, V, Cr, Mn, Fe, Co, Cu, Sc, Ni, Zn, Ga, Se, Sr, and Zr). Other trace elements (B, Rb, Y, Nb, Sm, Eu, Gd, Tb, Dy, Ho, Er, Tm, Yb, Lu, Hf, Ta, W, Th, and U) were above the detection limits. Although Itoigawa "white" jadeite generally had lower Mg and Ca contents (3841 and 8495 ppmw, respectively) than green, blue, and black jadeite, almost all of the detectable minor and trace element contents were higher than in white jadeite from Kachin State in Myanmar (see the bottom table at https://www.gia.edu/gems-gemology/spring-2017-japanese-jadeite-tables).

Green Jadeite. Microprobe analyses of four green jadeites revealed significant Fe content, from a minimum value of 0.22 wt.% to a maximum of 0.864 wt.%, and a slightly low Cr value of 0.01–0.57 wt.%. Values for MgO (0.16–2.83 wt.%) and CaO (0.24–4.18 wt.%) were relatively high, but the compositions fit within the jadeite range of X_{Jd} = 98.7 to 82.4 (figure 15). Samples from Itoigawa-Omi showed slight differences in major element composition between crystal aggregates and discrete single-mineral grains. This study indicates that the green jadeite is also nearly pure jadeite, though some discrete single-mineral grains showed a composition closer to omphacite within the jadeite-dominant matrix.

The 13 green specimens from Itoigawa revealed the remarkable transport of large-ion lithophile elements in subduction zones, such as Li, B, K, Sr, and Ba, as well as elements that are considered more refractory, such as rare earth elements (La, Ce, Pr, Nd, Sm, Eu, Gd, Tb, Dy, Ho, Er, Tm, Yb, and Lu) and Hf, Ta, W, Tl, Pb, Th, and U. The Mg and Ca contents were also relatively high, ranging from 2383 to 77,100 ppmw for Mg (averaged to 19,957 ppmw) and 4400 to 82,700 ppmw for Ca (averaged to 39,206 ppmw). Mg and Ca contents were much higher in the dark green areas, which indicates that the dark green omphacite component is more abundant in trace elements (except Li and Ga) than jadeite. To establish a useful chemical fingerprint diagram for separating omphacite jade from jadeite jade, we plotted two different combinations of major and minor elements. As seen in figure 16, plot-

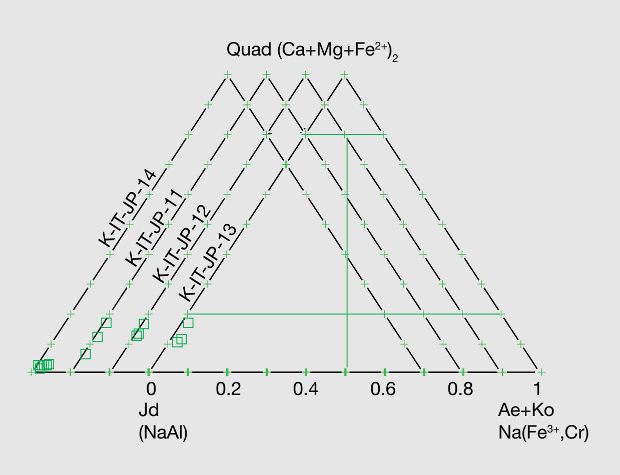

Figure 15. This ternary diagram for jadeite (Jd)-aegirine + kosmochlor (Ae + Ko)-Ca-Fe-Mg pyroxene (diopside + augite + hedenbergite) indicates the chemical concentration data of four green jadeites from Itoigawa-Omi by EPMA, based on Morimoto et al. (1988). Their compositions fit the jadeite range of X_{Jd} *= 98.7 to 82.4. Three to 12 spots were tested on the green area of each specimen.*

ting Al/Fe vs. Ca/Na clearly separates the jadeite according to chemical concentration.

By comparison, the green samples from Itoigawa-Omi showed higher Li, B, Mg, K, Ca, Ni, and Sr than green jadeite from Myanmar, while the transition metal elements Ti, V, Cr, Mn, Fe, and Co showed similar ranges. Ti and Fe were dominant in Russian and Guatemalan green jadeite. The Russian green jadeite showed the highest Cr content (up to 7940 ppmw, averaged to 2872 ppmw) of any samples.

Lavender Jadeite. EPMA performed on a violet sample from Itoigawa (K-IT-25) yielded significant TiO_2 (up to 0.362 wt.%) and FeO_{tot} (up to 0.694 wt.%), whereas MnO was relatively low (up to 0.019 wt.%). The color of the Japanese lavender jadeite likewise should correlate to the chromophores Ti^{4+}, Fe^{2+}, and Mn^{3+}. The contents of MgO (up to 0.864 wt.%) and CaO (up to 1.879 wt.%) were relatively low. The jadeite composition ranged from X_{Jd} = 98.7 to 93.3, close to pure jadeite.

LA-ICP-MS detected noticeably high amounts of Ti and Fe in all of the violet jadeite. Other metal elements such as Li, B, K, Sr, and Ba, as well as REEs, were higher than in white or green jadeite from the same geological source in Itoigawa-Omi. Lavender jadeite from Guatemala showed a similar violetish hue, and trace element concentrations revealed similarly high levels of Ti and REEs. But the transition metal ions V, Cr, and Co were below detection limits, consistent with its original light violet color (Sorensen et al., 2003). By comparison, 16 Burmese lavender samples showed appreciable Mn, explaining their dominant pinkish/purplish component. Oberhänsli et al. (2007) did not observe a Ti phase in the

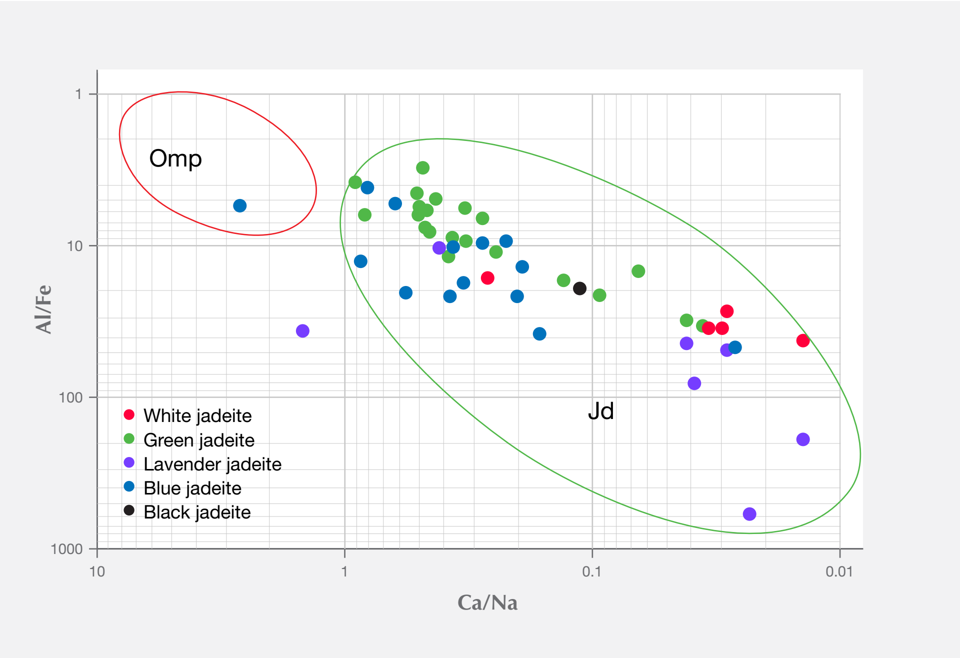

Figure 16. Chemical fingerprinting of Al/Fe vs. Ca/Na indicates the separation of jadeite (Jd) from omphacite (Omp) jade according to chemical concentration. Although the data plotted here were collected from LA-ICP-MS analysis, this type of diagram can also be adapted to EDXRF or electron microprobe data.

TABLE 1. Electron microprobe analyses of major element compositions of jadeite jade from Japan, Guatemala, and Russia.

	Itoigawa	Itoigawa		Itoigawa		Itoigawa		Itoigawa		Itoigawa	
	K-IT-JP-14 (5 spots) White	K-IT-JP-14 (12 spots) Green		K-IT-JP-11 (3 spots) Green		K-IT-JP-12 (3 spots) Green		K-IT-JP-13 (3 spots) Green		K-IT-JP-25 (6 spots) Lavender (Violet)	
Oxides (wt.%)	Averaged	Max X_{Jd}%	Min X_{Jd}%	Max X_{Jd}%	Min X_{Jd}%	Max X_{Jd}%	Min X_{Jd}%	Max X_{Jd}%	Min X_{Jd}%	Max X_{Jd}%	Min X_{Jd}%
SiO_2	58.82	60.466	58.95	58.43	57.83	59.25	58.4	59.31	57.11	59.542	59.621
TiO_2	0.03	0	0.02	0.012	0	0	0	0	0.012	0.362	0.325
Al_2O_3	24.3	24.822	24.3	22.38	20.59	21.87	20.83	21.98	21.27	24.518	22.997
Cr_2O_3	0	0.036	0.09	0.16	0.085	0.013	0.01	0.152	0.577	0.083	0.008
FeO	0.44	0.225	0.45	0.561	0.864	0.744	0.744	0.425	0.481	0.105	0.694
MnO	0	0.013	0.01	0.033	0	0.02	0.022	0.007	0.008	0.019	0
MgO	0.12	0.16	0.54	1.8	2.83	1.83	2.78	2.2	2.41	0.064	0.864
CaO	0.26	0.24	0.92	2.7	4.18	3.02	4.15	3.8	5.1	0.644	1.879
Na_2O	15.49	14.113	14.91	13.94	12.77	13.55	13.03	13.22	11.88	14.278	13.31
K_2O	0	0	0	0.01	0	0	0	0	0	0.001	0
NiO	0	0	0	0	0.032	0	0.025	0.022	0.025	0.011	0
Total	**99.46**	**100.075**	**100.2**	**100.025**	**99.181**	**100.296**	**99.992**	**101.116**	**98.873**	**99.627**	**99.895**
Cations (O=6)											
Si	2	2.026	1.991	1.989	1.994	2.009	1.996	1.999	1.975	2.001	2.02
Ti	0.001	0	0	0	0	0	0	0	0	0.008	0.008
Al	0.974	0.98	0.967	0.898	0.837	0.874	0.839	0.872	0.867	0.991	0.919
Cr	0	0.001	0.003	0.004	0.002	0	0	0.004	0.016	0	0
Fe*	0.013	0.006	0.013	0.016	0.024	0.02	0.021	0.012	0.014	0.002	0.019
Mn	0	0	0	0.001	0	0.001	0.001	0	0	0	0
Mg	0.006	0.008	0.027	0.091	0.145	0.093	0.142	0.11	0.124	0.001	0.04
Ca	0.009	0.009	0.033	0.098	0.154	0.11	0.152	0.137	0.189	0.023	0.068
Na	1.021	0.917	0.977	0.92	0.854	0.891	0.864	0.863	0.796	0.932	0.875
K	0	0	0	0	0	0	0	0	0	0.003	0.008
Ni	0	0	0	0	0.001	0	0.001	0.001	0	0	0
Total	**4.023**	**3.947**	**4.012**	**4.019**	**4.013**	**3.999**	**4.016**	**3.997**	**3.982**	**3.961**	**3.965**
End members (mol%) after Morimoto et al. (1988)											
X_{Jd}	98	98.7	95.5	88.5	82.6	88.9	83.3	86.6	82.4	98.7	93.3
$X_{(Ae+Ko)}$	1.2	0.1	1.5	2	2.3	1.7	2.1	0.4	1.6	0	0
X_{Quad}	0.8	1.2	3	9.5	15.1	10.3	14.6	13	16	1.3	6.7

high-pressure assemblage, which may contain the same accessory phases (amphibole, feldspar, and lawsonite) as jadeite from Itoigawa-Omi.

Blue Jadeite. The six blue samples from Itoigawa and the two violetish blue specimens from Wakasa had significantly high TiO_2, with maximum values of 0.649 and 0.745 wt.%, respectively. These corresponded with the intense blue area. The CaO contents were slightly higher in the light blue to blue areas (0.6% to 1.4 wt.%) than in the white areas. Violetish blue and blue areas revealed the highest concentration of Ti measured in Japanese jadeite (up to 4520 ppmw in blue jadeite from Itoigawa, and up to 3636 ppmw in violetish blue jadeite from Wakasa), as well as enriched Fe (up to 11,900 ppmw). Most of the REE contents were higher than in lavender jadeite.

Chondrite-Normalized REE and Primitive Mantle–Normalized Heavy Trace Element Pattern. To compare trace element compositions in different colors of Japanese jadeite, we studied their chondrite-normalized REE patterns and primitive mantle–normalized trace element patterns. Figures 17 and 18 show the averaged REE and heavy trace element data of white, black, green, lavender, and blue jadeite from Itoigawa-Omi, along with two violetish blue specimens from Wakasa. The REEs in Japanese jadeite tended to be more abundant in lavender, violetish blue, and blue specimens than in green, white, and black jadeite. In all colors, the light rare earth element (LREE: La, Ce, Nd, and Sm) contents tended to be higher than the heavy rare earth element (HREE: Eu, Gd, Dy, Y, Er, Yb, and Lu) contents. From this chondrite-normalized REE pattern, the lavender, violetish blue, and blue

Itoigawa		Wakasa		Matuaga		Matuaga		Polar Urals	
K-IT-JP-16 (6 spots) Blue		W-TO-JP-02 (6 spots) Violetish blue		M-GUA-03 (5 spots) Lavender (Violet)		M-GUA-02 (8 spots) Grayish green		PU-RUS-03 (11 spots) Green	
Max X_{Jd}%	Min X_{Jd}%	Max X_{Jd}%	Min X_{Jd}%	Max X_{Jd}%	Min X_{Jd}%	Max X_{Jd}%	Min X_{Jd}%	Max X_{Jd}%	Min X_{Jd}%
60.728	59.768	58.041	58.899	61.733	58.149	60.898	59.518	58.789	58.518
0.106	0.649	0.745	0.173	0.04	0.07	0.28	0.05	0.073	0.106
24.872	22.995	22.867	24.731	22.927	24.614	23.672	19.48	20.482	19.517
0.001	0.052	0	0.048	0	0.005	0	0	0.385	0.139
0.214	0.445	0.615	0.6	0	0.187	0.836	1.891	0.725	0.761
0.026	0	0.051	0.039	0	0.006	0.039	0.013	0.071	0.019
0.478	1.105	1.532	0.225	0.057	0.015	0.314	2.354	2.639	3.441
0.629	1.436	2.24	0.659	0.108	0.231	0.634	3.718	3.786	4.801
14.113	13.767	13.02	13.43	13.097	14.022	14.595	11.876	12.515	11.347
0.027	0.011	0	0.036	0.149	0.01	0	0	0.01	0.032
0.024	0.006	0	0	0	0.007	0.039	0.012	0.088	0.03
101.218	**100.234**	**99.111**	**98.84**	**98.108**	**97.316**	**101.307**	**98.912**	**99.563**	**98.711**
2.019	2.034	1.997	2.004	2.09	2.005	2.031	2.071	2.038	2.05
0.002	0.006	0.019	0.004	0.001	0.002	0.007	0.001	0.002	0.003
0.974	0.916	0.927	0.992	0.915	1	0.93	0.799	0.837	0.806
0	0.001	0	0.001	0	0.001	0	0	0.011	0.004
0.006	0.013	0.018	0.017	0	0.005	0.023	0.057	0.021	0.022
0.001	0	0.001	0.001	0	0	0.001	0	0.002	0.001
0.024	0.056	0.078	0.011	0.003	0.001	0.016	0.122	0.136	0.18
0.022	0.052	0.083	0.024	0.004	0.009	0.023	0.139	0.141	0.18
0.909	0.902	0.869	0.886	0.86	0.938	0.944	0.801	0.841	0.771
0.001	0	0	0.002	0.006	0	0	0	0	0.001
0.001	0	0	0	0	0	0.001	0	0.002	0.001
3.958	**3.981**	**3.993**	**3.944**	**3.879**	**3.962**	**3.976**	**3.99**	**4.031**	**4.019**
97.4	93.7	91.2	97.3	99.6	99.2	96.1	83.4	84	80.5
0	1	0	0.1	0	0.1	1.4	0.3	1.1	0.4
2.6	6.2	8.8	2.6	0.4	0.7	2.5	16.3	14.9	19.1

jadeite from Japan can be characterized by a high LREE/HREE ratio and a low Eu concentration relative to other REE (again, see figure 17).

Interestingly, the primitive mantle–normalized trace element patterns of all colors of Japanese jadeite showed strong positive anomalies of the large-ion lithophile elements (LILE) Sr and Ba, as well as the high field strength elements (HFSE) Zr and Nb. Green jadeite REE patterns were more depleted, but much higher than white and black jadeite, with strong positive anomalies of Sr, Zr, and Hf. This result is consistent with the conclusion by Morishita et al. (2007) that the fluid related to the formation of Itoigawa-Omi jadeite in the subduction zone was uniquely enriched in both LILE[1] and HFSE[2] brought in by the fluids in the subduction zone, and that these elements were recycled into serpentinized peridotites.

By comparison, Russian white and green jadeite revealed the highest REE and heavy trace element values in this study. Green jadeite from Japan and Myanmar showed a very close overlap, whereas the REE and heavy element contents for white samples from Myanmar were very depleted and had the lowest value.

In lavender and blue samples, Guatemalan jadeite

---

[1] LILE refers to lithophile trace elements (K, Rb, Cs, Sr, Ba, Pb, and Eu), which have an ionic radius to charge ratio that is greater than those of Ca^{2+} and Na^{+}, the largest cations common to rock-forming minerals.

[2] HFSE refers to high field strength elements (Ti, Zr, Hf, Nb, and Ta), which do not have a large ionic radius. Because of their high charge and the consequent difficulty in achieving a charge balance, they are typically incompatible.

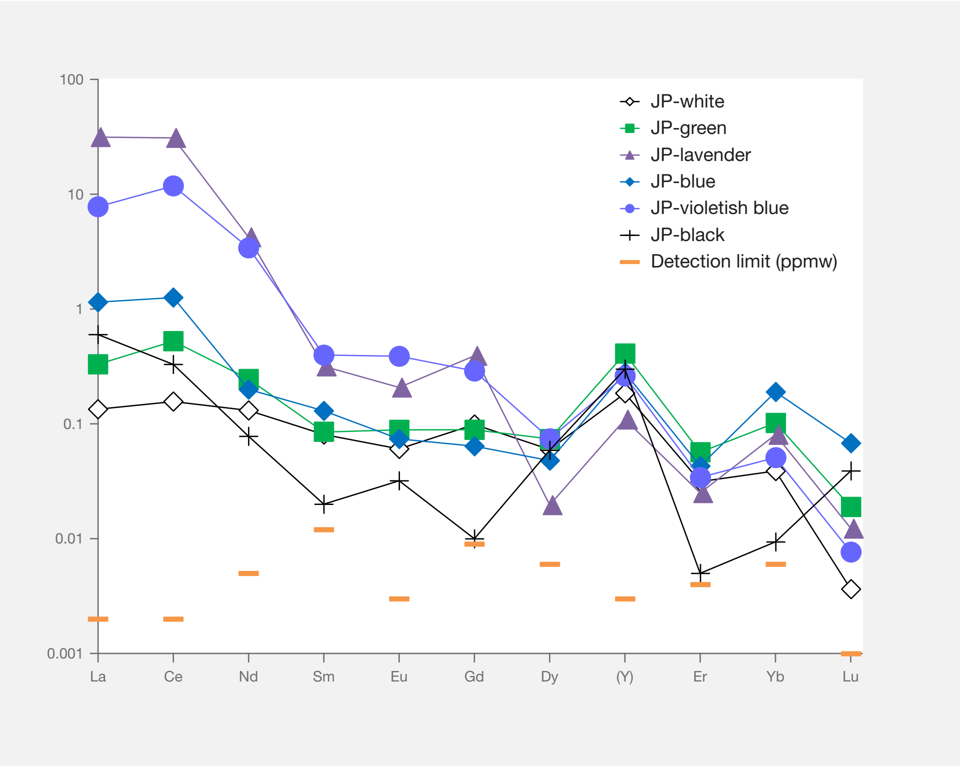

Figure 17. Chondrite-normalized rare earth element (REE) patterns are shown for each color of Japanese jadeite.

was characterized by the highest REE and heavy trace element concentrations. Japanese material showed a lower value but could be separated from Burmese lavender jadeite based on the chondrite-normalized and primitive mantle–normalized patterns.

CONCLUSIONS

Japanese jadeite from the Itoigawa-Omi region is characterized by mixtures of white with green and other colors such as lavender, blue, and black. Although jadeite mining has been prohibited there since 1954, small pebbles can be found along the rivers or estuaries. In this study, a large number of samples from Itoigawa-Omi and Wakasa were analyzed to characterize the chromophores, optical absorption features, and quantitative chemical composition of major and trace elements in each color variety. This gemological, petrographic, and chemical study also included Burmese, Guatemalan, and Russian jadeite samples for comparison. The results are summarized below.

1. Jadeite boulders and pebbles from Itoigawa-Omi tended to have rounded corners from fluvial erosion and showed a glittering whitish surface, but the rough rock did not show a weathered brown skin. The Japanese jadeite was mainly white, with unevenly distributed pale green to green and lavender to blue color.
2. Petrographic observations showed that Japanese jadeite was composed of aggregates of long, semi-euhedral prismatic crystals and granular single crystals, which combined to produce a prismatic-granular crystalloblastic texture. Pectolite, prehnite, and analcime were often present in folding, faults, and veinlets, while the minor component minerals vesuvianite and titanite were found in the matrix.
3. Quantitative analysis by electron microprobe showed that the white jadeite was close to pure jadeite ($X_{Jd} = 98$). Green jadeite was in the range of $X_{Jd} = 98–82$ and $X_{Aeg} = 2–8$, and the chromophores Fe and Cr were responsible for the green color. Lavender color was produced by a combination of higher Ti and Fe and lower Mn. In blue jadeite, the Ti^{4+}-Fe^{2+} charge-transfer played a significant role in coloration.
4. LA-ICP-MS analysis detected 19 minor and trace elements. The chondrite-normalized rare earth element and primitive mantle–normalized heavy trace element patterns of all colored jadeite showed higher light REE than heavy REE, along with positive large-ion lithophile el-

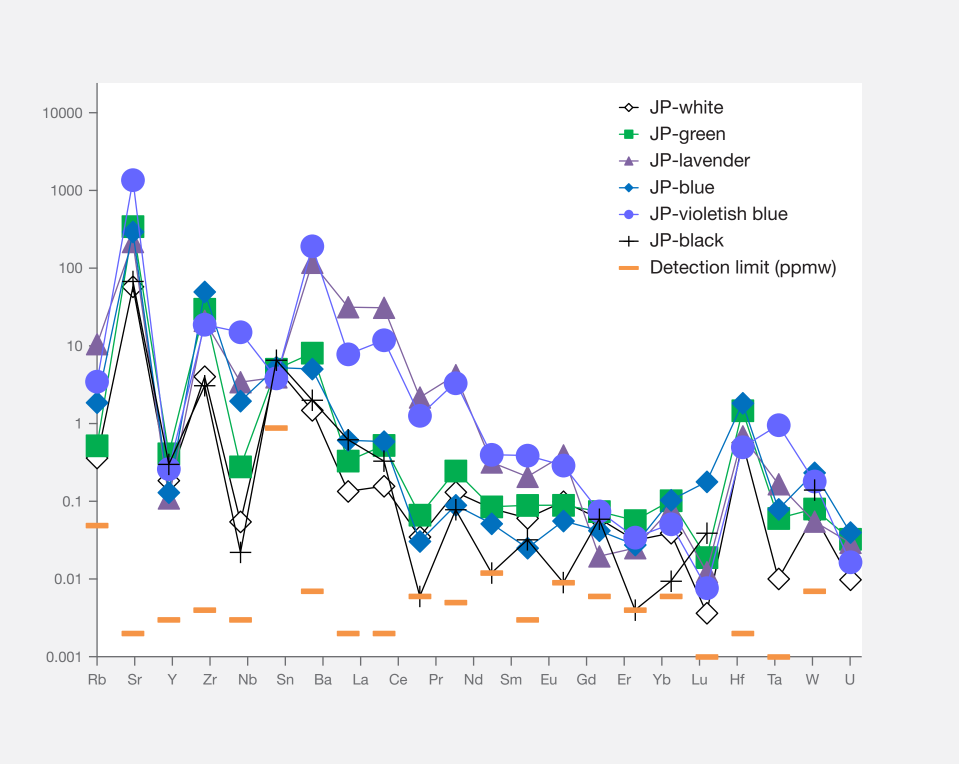

Figure 18. Primitive mantle–normalized heavy trace element patterns are shown for each color of Japanese jadeite.

ements and high field strength element anomalies. Lavender and blue (including violetish blue) jadeite had dominant REE compared to green jadeite, whereas white and black jadeite had the lowest REE contents.

Our studies confirmed that green jadeite from Itoigawa, Myanmar, and Russia have similar gemological properties such as RI and SG and absorption spectra of Cr and Fe, while Guatemalan grayish green jadeite does not contain Cr. Lavender jadeite from Japan and Guatemala showed similar color, caused by high Ti and Fe and low Mn. Investigation of thin sections revealed that Burmese jadeite contains kosmochlor, amphibole, albite, nepheline, and vesuvianite. Russian jade has the very common mineral magnetite in matrix and analcime in veinlets. Guatemalan jadeite was characterized by grossular garnet, albite, rutile, and other minerals. While Guatemalan jadeite contained abundant REEs and heavy trace elements, Burmese jade had much lower values. Japanese jadeite shows characteristic trace elements and matrix inclusion varieties that may be useful in establishing the precise country of origin.

ABOUT THE AUTHORS

Dr. Abduriyim is president of Tokyo Gem Science, LLC and director of GSTV Gemological Laboratory. He is a former senior manager and senior scientist of GIA's laboratory in Tokyo. Dr. Saruwatari and Dr. Katsurada are scientists and staff gemologists at GIA's laboratory in Tokyo.

ACKNOWLEDGMENTS

The authors thank Nobuyuki Tsurumi (The Jade Ore Museum/Hisui Gensekikan, Tokyo), Minoru Kameyama (Miyuki Co., Tokyo), and Prof. Miyajima (Fossa Magna Museum, Itoigawa) for information and specimens that made this study possible. We sincerely thank Dr. Mikouchi, associate professor at the University of Tokyo, and Prof. Ogasawara and Dr. Sakamaki at Waseda University for providing EPMA testing. We are also grateful to GIA colleagues Dr. Shoko Odake and Dr. Supharart Sangsawong, who assisted with data collection. The authors wish to thank Dr. F. Lin Sutherland, a former curator and research scientist at the Australian Museum in Sydney, for his critique of the manuscript.

REFERENCES

Barnes G.L. (1999) *The Rise of Civilization in East Asia: The Archaeology of China, Korea and Japan*. Thames and Hudson, New York.

Burns R.G. (1981) Intervalence transitions in mixed-valence minerals of iron and titanium. *Annual Review of Earth and Planetary Sciences*, Vol. 9, No. 1, pp. 345–383, http://dx.doi.org/10.1146/annurev.ea.09.050181.002021

Chihara K. (1971) Mineralogy and paragenesis of jadeites from the Omi-Kotaki area, Central Japan. *Mineralogical Society of Japan, Special Paper*, No. 1, pp. 147–156.

Chihara K. (1991) Jade in Japan. In R. Keverne, Ed., *Jade*. Van Nostrand Reinhold, New York, pp. 216–217.

Essene E.J. (1967) An occurrence of cymrite in the Franciscan formation, California. *American Mineralogist*, Vol. 52, pp. 1885–1890.

Ferguson J., Fielding P.E. (1971) The origins of the colours of yellow, green, and blue sapphires. *Chemical Physics Letters*, Vol. 10, No. 3, pp. 262–265, http://dx.doi.org/10.1016/0009-2614(71)80282-8

Foshag W.F., Leslie R. (1955) Jadeite from Manzanal, Guatemala. *American Antiquity*, Vol. 21, No. 1, pp. 81–83, http://dx.doi.org/10.2307/276111

Fukuyama M., Ogasawara M., Horie K., Lee D.C. (2013) Genesis of jadeite-quartz rocks in the Yorii area of the Kanto Mountains, Japan. *Journal of Asian Earth Sciences*, Vol. 63, pp. 206–217, http://dx.doi.org/10.1016/j.jseaes.2012.10.031

Harlow G.E., Olds E.P. (1987) Observations on terrestrial ureyite and ureyitic pyroxene. *American Mineralogist*, Vol. 72, pp. 126–136.

Harlow G.E., Sorensen S.S. (2005) Jade (nephrite and jadeitite) and serpentinite: Metasomatic connections. *International Geology Review*, Vol. 47, No. 2, pp. 113–146, http://dx.doi.org/10.2747/0020-6814.47.2.113

Kanmera K., Hashimoto M., Matsuda T. (1980) *Geology of Japan*. Vol. 15 of Iwanami Koza Chikyukagaku series. Iwanami Shoten, Tokyo, 387 pp. (in Japanese).

Kawano Y. (1939) A new occurrence of jade (jadeite) in Japan and its chemical properties. *Journal of the Japanese Association of Mineralogists, Petrologies and Economic Geologists*, No. 22, pp. 195–201 (in Japanese).

Kunugiza K., Nakamura E., Miyajima H., Goto A., Kobayashi K. (2002) Formation of jadeite-natrolite rocks in the Itoigawa-Ohmi area of the Hida marginal belt inferred from U-Pb-zircon dating. Abstract of annual meeting of the Japanese Association of Mineralogists, Petrologists and Economic Geologists in 2002, GP20 (in Japanese)

Lu R. (2012) Color origin of lavender jadeite: An alternative approach. *G&G*, Vol. 48, No. 4, pp. 273–283, http://dx.doi.org/10.5741/GEMS.48.4.273

Miyajima H., Matsubara S., Miyawaki R., Ito K. (1999) Itoigawaite, a new mineral, the Sr analogue of lawsonite, in jadeite from the Itoigawa-Ohmi district, central Japan. *Mineralogical Magazine*, Vol. 63, No. 6, pp. 909–916, http://dx.doi.org/10.1180/002646199548899

Miyajima H., Matsubara S., Miyawaki R., Yokoyama K., Hirokawa K. (2001) Rengeite, $Sr_4ZrTi_4Si_4O_{22}$, a new mineral, the Sr-Zr analogue of perrierite from Itoigawa-Ohmi district, Niigata Prefecture, central Japan. *Mineralogical Magazine*, Vol. 65, No. 1, pp. 111–120, http://dx.doi.org/10.1180/002646101550163

Miyajima H., Miyawaki R., Ito K. (2002) Matsubaraite, $Sr_4Ti_5(Si_2O_7)_2O_8$, a new mineral, the Sr-Ti analogue of perrierite in jadeitite from the Itoigawa-Ohmi district, Niigata Prefecture, Japan. *European Journal of Mineralogy*, Vol. 14, No. 6, pp. 1119–1128, http://dx.doi.org/10.1127/0935-1221/2002/0014-1119

Miyawaki R. (2004) Main minerals of jadeite jade. *Gemmology*, Vol. 35, No. 420, pp. 14–15 (in Japanese).

Miyazoe T., Nishiyama T., Uyeta K., Miyazaki K., Mori Y. (2009) Coexistence of pyroxenes jadeite, omphacite, and diopside-hedenbergite rock from a serpentinite mélange in the Kurosegawa zone of central Kyushu, Japan. *American Mineralogist*, Vol. 94, No. 1, pp. 34–40.

Morimoto N., Fabries J., Ferguson A.K., Ginzburg I.V., Ross M., Seifert F.A, Zussman J., Aoki K., Gottardi G. (1988) Nomenclature of pyroxenes. *American Mineralogist*, Vol. 73, pp. 1123–1133.

Morishita T. (2005) Occurrence and chemical composition of barian feldspar in a jadeitite from the Itoigawa-Ohmi district in the Renge high-P/T-type metamorphic belt, Japan. *Mineralogical Magazine*, Vol. 69, No. 1, pp. 39–51, http://dx.doi.org/10.1180/0026461056910237

Morishita T., Arai S., Ishida Y. (2007) Trace element compositions of jadeite (+omphacite) in jadeitites from the Itoigawa-Ohmi district, Japan: Implications for fluid processes in subduction zones. *Island Arc*, Vol. 16, No. 1, pp. 40–56, http://dx.doi.org/10.1111/j.1440-1738.2007.00557.x

Nakamizu M., Okada M., Yamazaki T., Komatsu M. (1989) Metamorphic rocks in the Omi-Renge serpentinite mélange, Hida Marginal Tectonic Belt, Central Japan. *Memoirs of the Geological Society of Japan*, Vol. 33, pp. 21–35 (in Japanese with English abstract).

Nishimura Y. (1998) Geotectonic subdivision and areal extent of the Sangun belt, inner zone of southwest Japan. *Journal of Metamorphic Geology*, Vol. 16, No. 1, pp. 129–140, http://dx.doi.org/10.1111/j.1525-1314.1998.00059.x

Oberhänsli R., Bousquet R., Moinzadeh H., Moazzen M., Arvin M. (2007) The field of stability of blue jadeite: A new occurrence of jadeitite at Sorkhan, Iran, as a case study. *Canadian Mineralogist*, Vol. 45, No. 6, pp. 1501–1509, https://doi.org/10.3749/canmin.45.6.1501

Ohmori K. (1939) Optical properties of jade (jadeite) newly occurred in Japan. *Journal of the Japanese Association of Mineralogists, Petrologists and Economic Geologists*, No. 22, pp. 201–212 (in Japanese).

Rossman G.R. (1974) Lavender jade. The optical spectrum of Fe^{3+} and $Fe^{2+}\rightarrow Fe^{3+}$ intervalence charge transfer in jadeite from Myanmar. *American Mineralogist*, No. 59, pp. 868–870.

Shibata K., Nozawa T. (1968) K-Ar age of Omi schist, Hida Mountains, Japan. *Bulletin of the Geological Survey of Japan*, No. 19, pp. 243–246.

Shinno I., Oba T. (1992) Absorption and photo-luminescence spectra of Ti^{3+} and Fe^{3+} in jadeites. *Mineralogical Journal*, Vol. 16, No. 7, pp. 378–386, http://dx.doi.org/10.2465/minerj.16.378

Shoji T., Kobayashi S. (1988) Fluid inclusions found in jadeite and stronalsite, and a comment on the jadeite-analcime boundary. *Journal of Mineralogy, Petrology and Economic Geology*, Vol. 83, No. 1, pp. 1–8, http://dx.doi.org/10.2465/ganko.83.1

Sorensen S.S., Harlow G.E., Rumble D. III. (2003) SIMS oxygen isotope analyses of jadeitite: trace element correlations, fluid compositions, and temperature estimates. *Geological Society of America Abstract with Program*, Vol. 35, No. 6, pp. 90–97.

Takayama M. (1986) Mode of occurrence and significance of jadeite in the Kamuikotan metamorphic rocks, Hokkaido, Japan. *Journal of Metamorphic Geology*, Vol. 4, No. 4, pp. 445–454, http://dx.doi.org/10.1111/j.1525-1314.1986.tb00363.x

Taube K.A. (2004) Olmec art at Dumbarton Oaks. Dumbarton Oaks Research Library and Collection, Washington, D.C.

Tsujimori T. (2002) Prograde and retrograde P-T paths of the Late Paleozoic glaucophane eclogite from the Renge metamorphic belt, Hida Mountains, southwestern Japan. *International Geology Review*, Vol. 44, No. 9, pp. 797–818, http://dx.doi.org/10.2747/0020-6814.44.9.797

Tsutsumi Y., Yokoyama K., Miyawaki R., Matsubara S., Terada K., Hidaka H. (2010) Ages of zircons in jadeitite and jadeite-bearing rocks of Japanese islands. *Bulletin of the National Museum of Nature and Science*, Vol. 36, pp. 19–30.

Umehara S. (1971) *Japan Ancient Jade Memorandum*. Yoshikawa Hirobunkan, Tokyo (in Japanese), 354 pp.

Yokoyama K., Sameshima T. (1982) Miscibility gap between jadeite and omphacite. *Mineralogical Journal*, Vol. 11, pp. 53–61, http://dx.doi.org/10.2465/minerj.11.53

ADDITIONAL READING

Abduriyim A., Kitawaki H. (2006) Determination of the origin of blue sapphire using laser ablation inductively coupled plasma mass spectrometry (LA-ICP-MS). *The Journal of Gemmology*, Vol. 30, No. 1/2, pp. 23–42.

Abduriyim A., Kitawaki H., Furuya M., Schwarz D. (2006) "Paraiba"-type copper-bearing tourmaline from Brazil, Nigeria, and Mozambique: Chemical fingerprinting by LA-ICP-MS. *G&G*, Vol. 42, No. 1, pp. 4–21, http://dx.doi.org/10.5741/GEMS.42.1.4

Blodgett T., Shen A.H. (2011) Application of discrimination analysis in gemology: Country-of-origin separation in colored stones and distinguishing HPHT-treated diamonds. *G&G*, Vol. 47, No. 2, p. 145.

Breeding C.M., Shen A.H. (2010) LA-ICP-MS analysis as a tool for separating natural and synthetic malachite. *News from Research*, Oct. 11, http://www.gia.edu/gia-news-research-nr101410

Fisher R.A. (1936) The use of multiple measurements in taxonomic problems. *Annals of Eugenics*, Vol. 7, No. 2, pp. 179–188, http://dx.doi.org/10.1111/j.1469-1809.1936.tb02137.x.

Harlow G.E., Shi G.H. (2011) An LA-ICP-MS study of lavender jadeite from Myanmar, Guatemala, and Japan. *G&G*, Vol. 47, No. 2, pp. 116–117.

Iwao S. (1953) Albitite and associated jadeite rock from Kotaki district, Japan: A study in ceramic raw material. *Bulletin of the Geological Survey of Japan*. No. 153, pp. 1–26.

Kobayashi S., Miyake H., Shoji T. (1986) A jadeite rock from Oosacho, Okayama Prefecture, southwestern Japan. *Mineralogical Journal*, Vol. 13, No. 6, pp. 314–327, http://dx.doi.org/10.2465/minerj.13.314

Luo Z.M, Yang M.X., Shen A.H. (2015) Origin determination of dolomite-related white nephrite through IB-LDA. *G&G*, Vol. 51, No. 3, pp. 300–311, http://dx.doi.org/10.5741/GEMS.51.3.300

McDonough W.F., Sun S.S. (1995) The composition of the Earth. *Chemical Geology*, Vol. 120, Nos. 3–4, pp. 223–253, http://dx.doi.org/10.1016/0009-2541(94)00140-4

Miyajima H. (2014) *Story of the Much-Valued Jadeite*. Fossa Magna Museum and Education Committee of Itoigawa, Itoigawa, 96 pp. (in Japanese).

Oba T., Nakagawa Y., Kanayama K., Watanabe T. (1992) Notes on rock-forming minerals in the Joetsu district, Niigata Prefecture, Japan: (5) Lavender jadeite from the Kotaki river. *Bulletin of Joetsu University of Education*, No. 11, pp. 367–375.

Ouyang Q. (2001) Characteristic of violet jadeite jade and its coloration mechanism. *Journal of Gems and Gemmology*, Vol. 3, No. 1, pp. 1–6 (in Chinese).

Rankin A.H., Greenwood J., Hargreaves D. (2003) Chemical fingerprinting of some East African gem rubies by laser ablation-ICP-MS. *The Journal of Gemmology*, Vol. 28, No. 8, pp. 473–482.

Saeseaw S., Pardieu V., Sangsawong S. (2014) Three-phase inclusions in emeralds and their impact on origin determination. *G&G*, Vol. 50, No. 2, pp. 114–132, http://dx.doi.org/10.5741/GEMS.50.2.114

Saminpanya S., Manning D.A.C., Droop G.T.R., Henderson C.M.B. (2003) Trace elements in Thai gem corundums. *The Journal of Gemmology*, Vol. 28, No. 7, pp. 399–415.

Shen A.H., Blodgett T., Shigley J.E. (2013) Country-of-origin determination of modern gem peridots from LA-ICP-MS trace-elements chemistry and linear discriminant analysis (LDA). *Geological Society of America Abstracts with Programs*, Vol. 45, No. 7, p. 525.

Sutherland F.L., Schwarz D., Jobbins E.A., Coenraads R.R., Webb G. (1998) Distinctive gem corundum suites from discrete basalt fields: A comparative study of Barrington, Australia, and West Pailin, Cambodia, gemfields. *The Journal of Gemmology*, Vol. 26, No. 2, pp. 65–85.

CAUSES OF IRIDESCENCE IN NATURAL QUARTZ

Xiayang Lin and Peter J. Heaney

Iris quartz specimens from geodes in the Deccan Trap basalts of west-central India have been described since 1860. These quartz crystals exhibit dominant terminal faces, and iridescence is visible on only the minor *z* {011} faces and not the major *r* {101} faces. For this study, we analyzed iris quartz crystals from India's Jalgaon District using scanning and transmission electron microscopy (SEM and TEM) and atomic force microscopy (AFM). SEM and AFM imaging revealed that the iridescent *z* faces exhibit periodic ridges with wavelengths from 400 to 700 nm, but no surface topography was apparent on the non-iridescent *r* faces. TEM examination of a section removed from a *z* face by focused ion beam (FIB) milling suggests that the ridge and valley structures were produced by preferential etching of periodic defects on the *z* faces, creating a diffraction grating. We interpret these defects as paired Brazil twin boundaries.

Iridescent solids exhibit a color change in response to variations in the lighting angle and viewing direction (figure 1). As exemplified by opal and labradorite, this phenomenon can transform an otherwise lackluster mineral into a gem, and many techniques have been developed to generate a play of light in non-iridescent stones. Applications for iridescent materials have attracted attention in diverse research fields, including photonics and computer graphics, while studies of the physics of iridescence have informed the design of cosmetics, paints, and anti-counterfeiting devices (Parker and Townley, 2007; Vigneron et al., 2007). Moreover, the functional significance of iridescence in organic structures is an active area of exploration in evolutionary and developmental biology (reviewed in Meadows et al., 2009). Here we describe the two physical mechanisms by which iridescence occurs in natural materials, and we report the results of our investigations into the cause of iridescence in naturally formed quartz crystals from India's Jalgaon District.

BACKGROUND: PHYSICS OF IRIDESCENCE

Iridescence may be caused by the interference of light either by thin films or by repetitive substructures.

Thin-Film Iridescence. Thin-film interference effects are seen when a liquid or solid is coated by a film that is nanometers to micrometers in thickness. When in-

Figure 1. Iridescence is clearly visible on the minor z face of this iris quartz from Jalgaon, India. Photomicrograph by Peter J. Heaney; field of view 4.5 mm.

See end of article for About the Authors and Acknowledgments.

GEMS & GEMOLOGY, Vol. 53, No. 1, pp. 68–81,
http://dx.doi.org/10.5741/GEMS.53.1.68

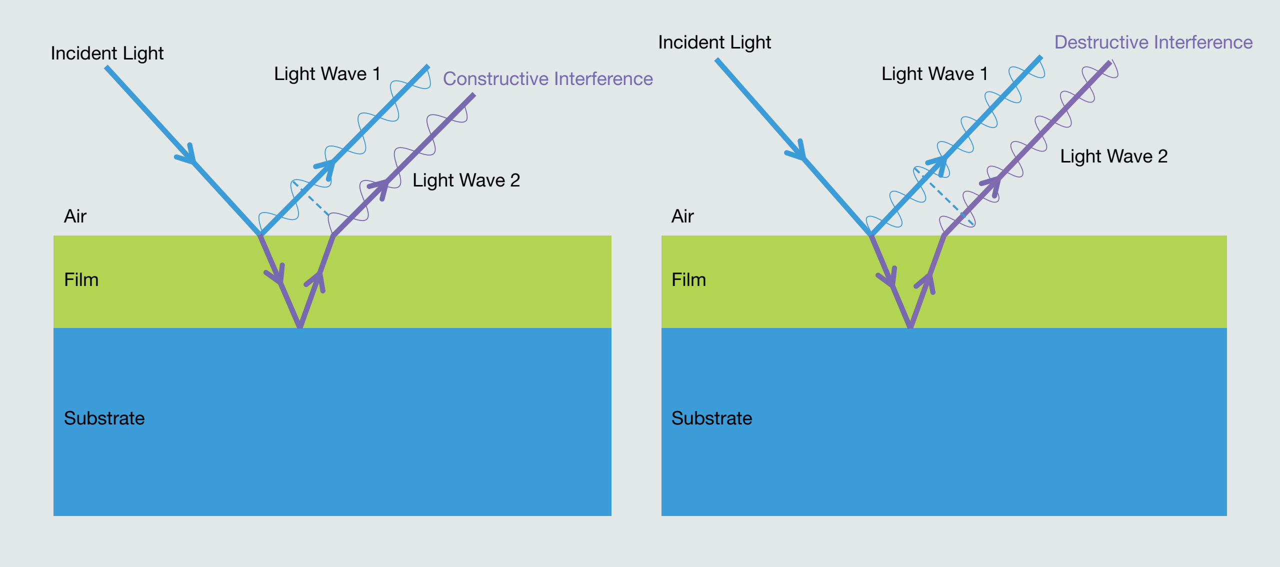

Figure 2. Light rays that reflect from the upper boundary and the lower boundary of the thin film interfere constructively or destructively and form a new wave. Left: In this illustration of constructive interference, light waves 1 and 2 are in phase. Right: With destructive interference, the two waves are out of phase.

cident light strikes the thin film's surface, a portion of the light is transmitted through the interface and the remainder is reflected. After the transmitted light impinges the lower boundary of the film, some or all of that light wave may be reflected. The two waves reflected from the thin film's upper and lower boundaries interfere with each other to produce a new light wave (figure 2). If, after its extended travel path and possible phase shift, the ray that reflects off the thin film/substrate boundary (ray 2 in figure 2, left) is exactly in phase with the wave that reflects only from the thin film surface (ray 1 in figure 2, left), the two reflected waves will constructively interfere and combine into a light wave with high intensity; otherwise, the emergent waves interfere destructively and are canceled (figure 2, right). If the source is monochromatic, the interference pattern generated by the reflected light waves will appear as bright and dark bands as a function of the viewing angle.

In Brief

- Iridescent quartz from India has been known since the mid-19th century.
- In this study, microscopic investigation of the iridescent z {011} faces of two quartz samples revealed periodic ridges, which created diffraction gratings.
- The ridge-and-valley structures were produced by the preferential etching of parallel defects. These defects are interpreted as paired Brazil twin boundaries.

When the incident light is polychromatic, only one wavelength will be reinforced by constructive interference for a given reflection angle. As a result, thin-film interference is selective for specific wavelengths depending on the angle. Longer wavelengths interfere at steeper angles according to Bragg's law, and thus a full rainbow spectrum is evident when the film is viewed from a perspective that samples a range of reflection angles. In addition, the colors associated with the iridescence depend on the thickness of the thin film and on the relative refractive indices (RIs) of the film and substrate. Refractive indices play a role because reflected light waves experience a phase shift of 180° when the RI of the thin film is lower than that of the substrate. Examples of minerals showing thin-film iridescence include bornite (Buckley and Woods, 1983; Vaughan et al., 1987) and fire obsidian (Ma et al., 2001, 2007). Likewise, many fractures in minerals, filled or unfilled, can display iridescence because of thin-film effects.

Iridescence from Diffraction Gratings. The dispersion of light can also be induced by interference effects that arise from natural diffraction gratings within or on the surfaces of minerals. The interaction of light with the diffraction grating can be purely reflective from surface grooves (figure 3), or it can be

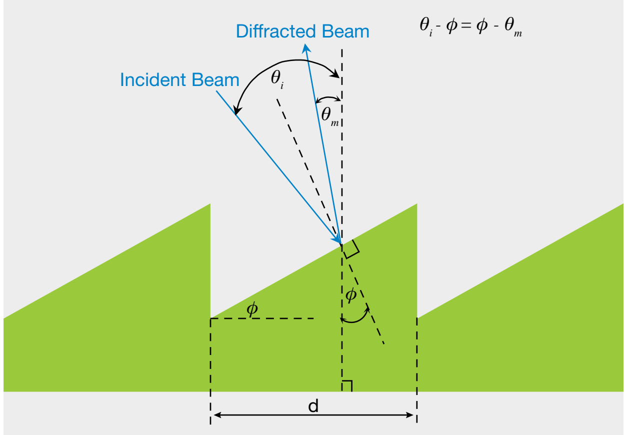

Figure 3. Schematic representation of a reflective diffraction grating. Iridescence occurs when diffracted beams interfere constructively, as in figure 2, left. The dashed lines indicate the incident normals to the grooves and base of the diffraction grating.

transmissive through transparent modular substrutures with periodic variations in refractive indices (Kinoshita et al., 2008). When light reflects from a blazed surface grating, as shown schematically in figure 3, waves that reflect from adjacent grooves will constructively interfere only when the emergent waves are in phase. When the reflected waves are out of phase, destructive interference ensues. The criterion for constructive interference is met when the difference in the distances traveled by light waves scattered from adjacent grooves is equal to an integral number of wavelengths.

In the construction shown in figure 3, the mathematical equation that governs diffraction from blazed gratings is dependent on the steepness of the blaze angle between the inclined surface and the grating plane (labeled ϕ in figure 3), the distance between grooves (d in figure 3), and the angles (θ_i and θ_m) that the incident and reflected waves make with respect to the normals to the grating plane (Laufer, 1996). The condition for constructive interference is mathematically expressed as

$$\sin(2\phi - \theta_i) - \sin\theta_i = m\lambda/d$$

where m is an integer that represents the so-called diffraction order. For a given angle θ_i, only a single wavelength of light satisfies this equation for first-order diffraction (where $m = 1$). Thus, as the incident light angle changes, the diffracted wavelength also changes, generating iridescence. The equations that govern the conditions for transmissive diffraction through repetitive substructures, as with iris agate, differ slightly from those that describe reflective iridescence, but they similarly define the conditions for constructive interference of emergent light waves (Kinoshita et al., 2008).

Mineralogical iridescence produced by intrinsic diffraction gratings is of particular interest because the substructures that create the gratings often yield insights into crystal growth processes. These in turn may allow geologists to quantify aspects of a mineral's crystallization history, suggesting new pathways toward the self-assembly of hierarchically ordered structures. Four well-known examples of iridescence produced by repetitive transparent substructures are precious opal (Sanders, 1964; Darragh et al., 1966; Gaillou et al., 2008; Rondeau et al., 2010), labradorite (Nissen, 1971; McConnell, 1974; Cliff et al., 1976; Miura and Tomisako, 1978), moonstone (Akizuki and Sugawara, 1970), and iris agate (Taijing and Sunagawa, 1994; Heaney and Davis, 1995).

IRIDESCENT QUARTZ

Naturally iridescent quartz has been recognized for more than a century and is known by many names: iris quartz, rainbow quartz, schiller quartz, anandalite, and adularescent quartz. Petrov and Tanaka (2011) published online the only detailed review of the history of iridescent quartz. Although there is some ambiguity regarding the source locality for this material, most of the iridescent quartz on the market comes from India's Deccan Traps in an area west of Burhanpur in Madhya Pradesh State, near the border with Maharashtra State. Indeed, the first known reference to iridescent quartz is the 1860 donation of an iris quartz cluster to the British Museum of Natural History by an engineer who worked on the construction of the Central India Railway. Iridescent quartz has also been reported from Washington State (USA), Uruguay, Brazil, Germany, Turkey, and Morocco (Gübelin and Koivula, 2005; Petrov and Tanaka, 2011; Renfro and Koivula, 2011).

The iris quartz in the British Museum (number 55795) is described by vom Rath (1873) and Scharff (1875), and their descriptions precisely match the characteristics of the specimens examined in the present study (figure 4). These samples occur as clusters of euhedral quartz crystals that evidently filled gaseous vugs (open spaces) within the Deccan Trap

Figure 4. Iridescent quartz from Jalgaon, India, was used in this study. Photo by Xiayang Lin.

basalts. At the base of these clusters is a rind of chalcedony, 0.2–0.4 cm thick, that abruptly transitions to quartz crystals, as is characteristic of many agate geodes. The quartz crystals exhibit strongly expressed terminal faces, and iridescence is visible only on the smaller *z* {011} faces and in zones closely surrounding them (figure 5), but not on the dominant *r* {101} faces. The spectral colors vary from red to blue depending on the angle of incident light and the viewing direction. Etch pits are commonly located on both the *z* and *r* faces, and iridescence is particularly strong within the etch pits on the *z* faces. Some crystals are broken, however, and rainbow colors are not visible in broken portions of otherwise iridescent *z* faces. The prismatic *m* {100} faces are poorly developed in these crystals. All of the single quartz crystals observed on this sample measure about 0.5–1 cm in length.

Until about 2009, one Japanese company controlled the market for iridescent quartz, importing several tons of material. Since that time, production from India has exceeded the importer's capacity and the market has opened internationally (Petrov and Tanaka, 2011). Much of this quartz is of relatively low quality, but a small brilliant piece exhibiting strong colors can easily cost up to $2,000. In light of the growing market for iridescent quartz, specimens have been produced artificially through the deposition of thin films of various metals (as with "aurora quartz"). As a result, gem buyers have become skeptical of the authenticity of iridescent quartz from India. Nevertheless, Petrov and Tanaka (2011) reported that the Japanese gemologist Koichi Iida (Japanese Saitama Jewelry Institute) examined Indian iris quartz and confirmed that the iridescence is nat-

Figure 5. The quartz crystals exhibit strongly expressed terminal faces, and iridescence is only visible on smaller z *{011} faces and not on* r *{101} faces. The sample measures approximately 5.0 × 4.0 × 3.5 cm. Photo by Xiayang Lin.*

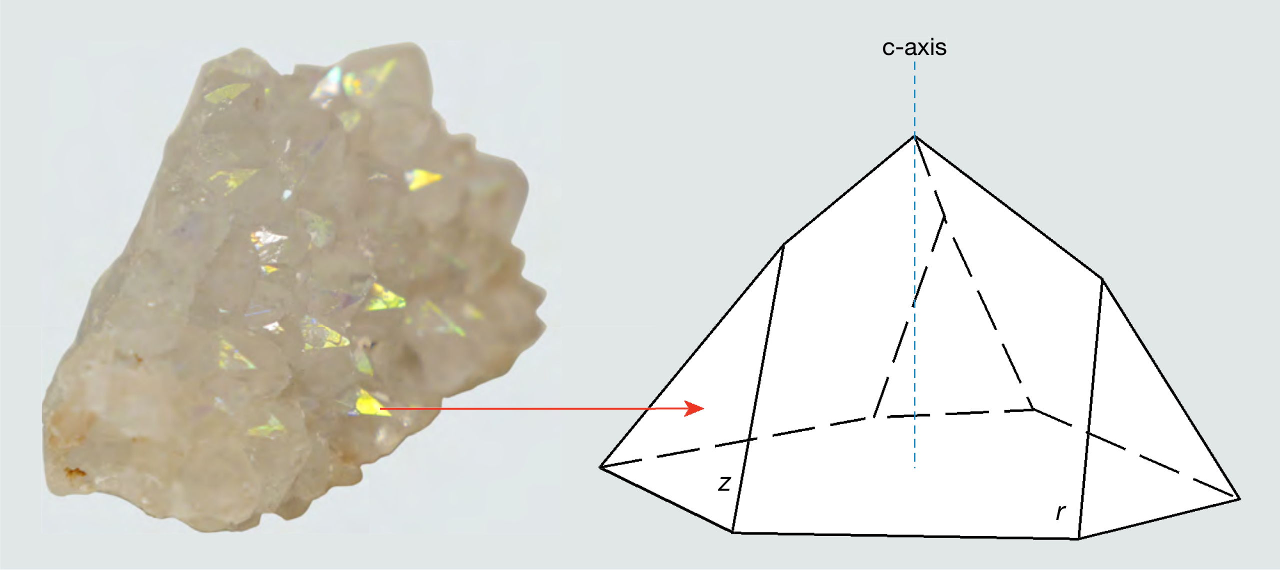

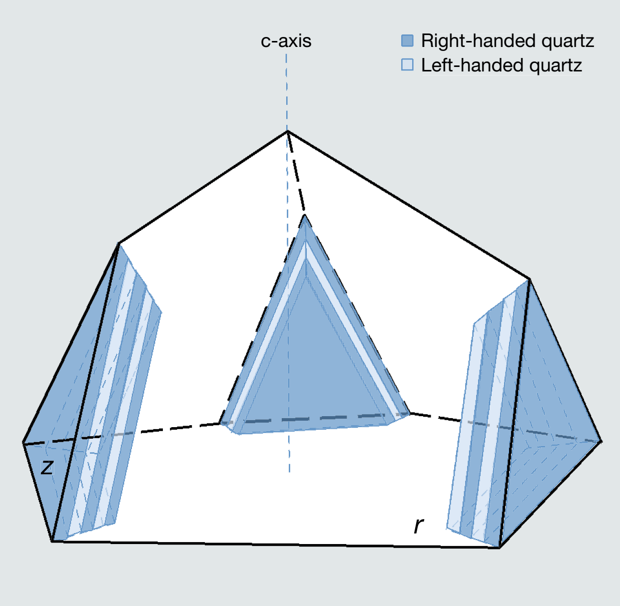

Figure 6. A schematic representation of C.V. Raman's model for lamellar Brazil twinning in iridescent quartz.

ural. In light of the historical record for this material, the natural origin of iridescent quartz from the Deccan Traps of India seems irrefutable.

C.V. Raman, the 1930 Nobel Laureate in physics, published the only scientific analysis of iridescent quartz we are aware of. Raman (1950) obtained specimens from a jeweler in Bombay and examined them using reflections of polarized light and visible light spectroscopy. He argued that the iridescence is not the result of a superficial film coating the quartz surface, as he observed the effect outside an iridescent face due to reflection within the crystal. Rather, he attributed the iridescence to "a layer of material which lies below the surface of the crystal and forms an integral part of its structure. The observations indicate the thickness of the layer to be of the order of a quarter of a millimeter."

Based on his spectroscopic study, Raman concluded that the iridescence is caused by "a stratified medium consisting of a great many parallel layers of extreme thinness," and he estimated that each layer was 0.34 μm thick (figure 6). He further hypothesized that the striations are regularly spaced polysynthetic Brazil twins oriented parallel to the minor rhombohedral *z* faces. Polysynthetic Brazil twins consist of alternating layers of right- and left-handed quartz, and they are particularly common in amethyst (Schlössin and Lang, 1965; McLaren et al., 1967; McLaren and Pitkethly, 1982; Baran et al., 1987; Schmetzer, 1987; Taijing and Sunagawa, 1990). Raman puzzled over the absence of iridescence in Brazil-twinned amethyst and recognized that the mere change in handedness at the twin boundary was insufficient to generate a schiller interference effect, as is seen in labradorite, since the RIs of Brazil twins are identical. Consequently, he speculated that the twin boundaries in the Indian iris quartz were associated with "extremely thin layers of impurity material."

Raman was unable to confirm his deductions regarding the role that Brazil twins play in generating iris effects in quartz. Even though Brazil twin boundaries occur parallel to the {101} and {011} rhombohedral planes of quartz, studies of amethyst have determined that a specific Brazil twin boundary is never oriented parallel to a rhombohedral face with the same indices—in other words, the (101) face of quartz is not underlain by Brazil twin boundaries parallel to (101) (Balakirev et al., 1975). This observation contradicts Raman's model of lamellar twin boundaries parallel to the iridescent crystal faces (figure 6). In the absence of a follow-up to Raman's work, many members of the gem community have presumed that iridescence in these quartz crystals arises from a thin film of opal coating the surface (based on our discussions with collectors).

Using more sophisticated analytical techniques than Raman had at his disposal, we sought to determine the cause of iridescence in quartz crystals from the Deccan Traps. For our investigation, we employed a combination of scanning electron microscopy (SEM), atomic force microscopy (AFM), focused ion beam (FIB) milling, and transmission electron microscopy (TEM).

MATERIALS AND METHODS

Specimens. We purchased two specimens of iris quartz clusters from Georges Claeys (Geonic Mineralen Collectie, Mariakerke, Belgium) at the 2014 Tucson Gem and Mineral Show. Figures 4 and 5 show the same specimen from different angles. Mr. Claeys reported that he obtained the specimens from a dealer who collected them from the Jalgaon District of India. The physical properties of the two specimens precisely match the descriptions of other iris quartz clusters from this locality, and we feel confident of its provenance.

Scanning Electron Microscopy and Energy Dispersive Spectroscopy. All analytical testing was performed at Pennsylvania State University's Materials Characterization Laboratory. For the first stage of our study, we

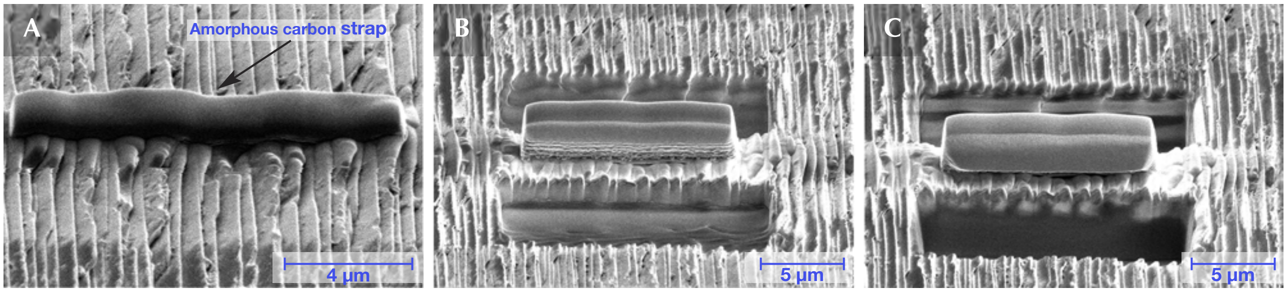

Figure 7. SEM images of the iridescent surface during the focused ion beam (FIB) milling process. The foil was extracted from a z {011} face and oriented perpendicular to the ridges that compose the diffraction grating. An amorphous carbon strap was deposited to protect the surface texture (A), and trenches were excavated in front of and behind the strap to generate the foil (B and C).

used an FEI Quanta 200 environmental scanning electron microscope to map the surface topography of both iridescent and non-iridescent pyramidal faces of iris quartz. Selected quartz crystals were pried from the cluster, cleaned in methanol, and attached to a standard scanning electron microscope aluminum mounting stub with double-sided carbon tape. Because quartz is not conductive and was not coated by carbon, SEM images were taken at low vacuum with an accelerating voltage of 20 kV. An Oxford Instruments INCA x-act (Model 51-ADD0001) EDS detector on the microscope was used for surface chemical analysis. EDS data were analyzed using Oxford Instruments' AZtec nanoanalysis software (version 2.4). We used three different accelerating voltages (20, 10, and 5 kv) to acquire spectra for the same sites.

Atomic Force Microscopy. We next employed AFM to construct high-resolution three-dimensional topographic maps of the pyramidal faces. By rastering a probe across the sample's surface, AFM can reveal surface structure at the nanoscale. We removed two quartz single crystals from the cluster and oriented one iridescent face and one non-iridescent face parallel to the flat stage in the AFM. A PeakForce Tapping model with ScanAsyst was used for these surface measurements. The peak force set point ranged from 2.5 to 7.5 nN for AFM imaging, and the scan rate was 1 to 0.5 Hz. The AFM probe used in these analyses was a Bruker ScanAsyst-Air probe, which has a silicon tip on a nitride lever. The front angle of the tip was 15°, and the back angle was 25°. The data were collected as line scans with 512 points per line, with 256 lines collected in total. NanoScope Analysis software (version 1.50) was used to process the AFM data, and the average distance between two adjacent ridges was calculated through a fast Fourier transform (FFT) algorithm using MATLAB (MathWorks, Inc).

Focused Ion Beam Milling and Transmission Electron Microscopy. To ascertain any relationship between iridescent behavior and Brazil twinning, we prepared an electron-transparent mineral section, or foil, for TEM using focused ion beam lift-out (Heaney et al., 2001). Focused ion beam milling was performed with an FEI Helios NanoLab 660 FIB. A single quartz crystal was removed from a cluster and coated with conductive carbon paint to avoid charging. After the sample was mounted within the FIB, an amorphous carbon strap was deposited over the area of extraction to protect the foil and preserve the surface structure during the milling process (figure 7). A Ga+ ion beam was used to excavate the material on both sides of the foil. The initial Ga beam voltage of 30 kV was reduced to 5 kV and then 2 kV for the final thinning. Beam currents operated at 0.23 nA for the amorphous carbon deposition, 21 nA and 9.3 nA for intermediate milling stages, and finally 2.5 nA for milling prior to foil lift-out.

Next, the foil was soldered to a glass probe tip and deposited onto a V-shaped TEM half-grid post. Milling the sample on the grid began with a 30 kV ion beam with the stage tilted to 53.5°. As an angle of 52° is normal to the ion beam, this yielded an over-tilt of 1.5°. The over-tilt was increased to 3.5° for 5 kV milling, and finally to 5.0° for 2 kV milling. The thickness of the final foil was less than 100 nm to allow electron transparency, and the area of the quartz foil was approximately 7 µm × 4.5 µm. The entire milling and extraction process was monitored by secondary electron imaging. The milled sample was loaded in a

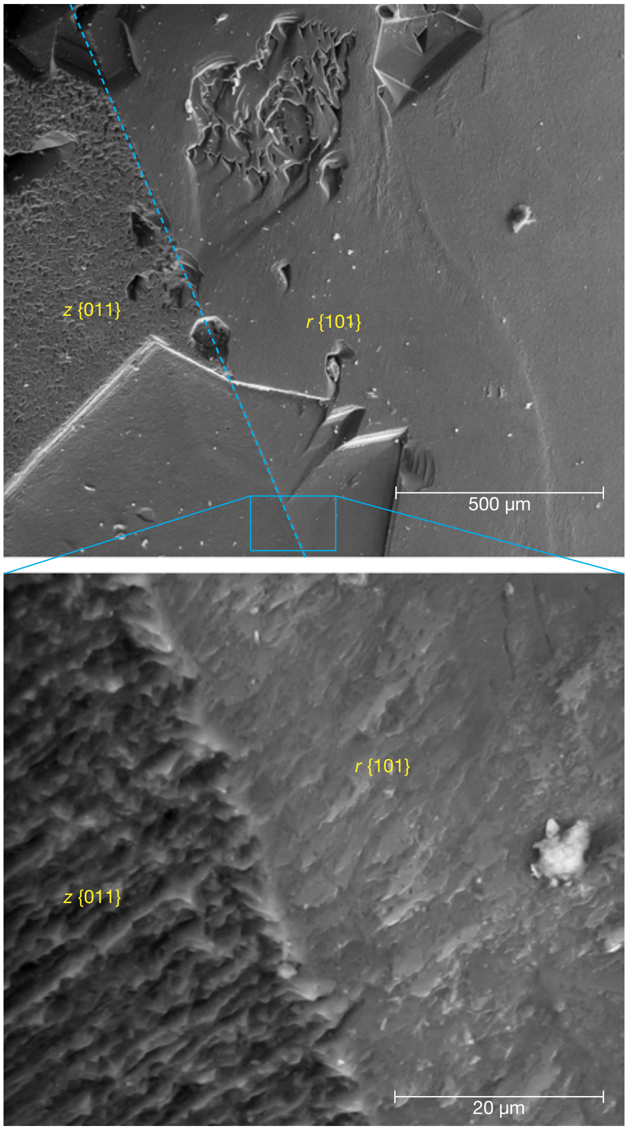

Figure 8. SEM images of the iridescent z *{011} face and the non-iridescent* r *{101} faces. Top: A lower-magnification view reveals the prevalence of etch pits on both faces. The dashed line separates the* z *and* r *faces. Bottom: A higher-magnification image within an etch pit clearly shows the parallel ridge-and-valley topography of the* z *face and the absence of ridges on the* r *face.*

Philips double-tilt holder with a Be stage and examined using a Philips 420 TEM at 120 kV.

RESULTS

Surface Morphology and Composition. Topographic differences between the iridescent *z* and the non-iridescent *r* faces were apparent in SEM images of the crystals (figure 8). In particular, a high-magnification backscattered electron (BSE) image of an apparent etch pit across both faces revealed that the iridescent *z* face features parallel ridge-and-valley structures (figure 8, bottom), whereas the non-iridescent face was relatively flat and smooth. The SEM images suggested that the average distances between adjacent ridges fell below a micron, but AFM analysis (see below) allowed for more rigorous quantification. Although the striations were more pronounced in the apparent etch pits, an examination of the unetched surfaces of the *z* faces also revealed a substructure that consisted of alternating lamellae (figure 9).

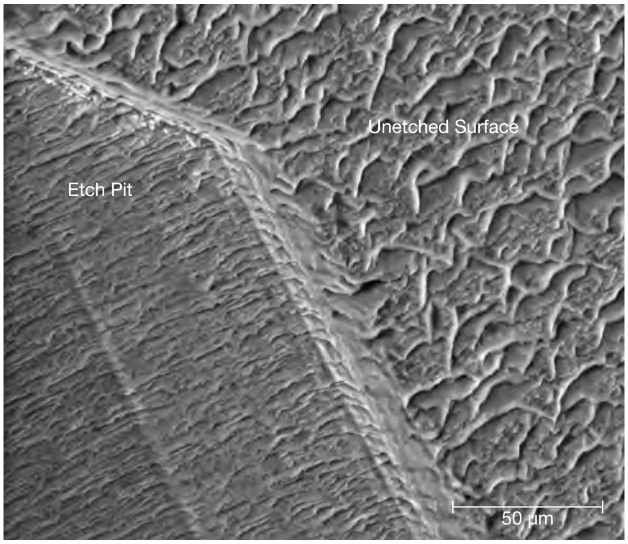

Figure 9. An SEM image of an iridescent z *face that shows the boundary of an etch pit and an unetched surface. The striations are continuous across the boundary.*

Compositional analyses on the iridescent faces obtained by EDS offered little evidence of a thin-film coating that might be responsible for the iridescence (figure 10). Trace amounts of Na, Al, and Ca were detected, but these elements were present in equal amounts on the iridescent and non-iridescent faces. Al commonly substitutes for Si in natural quartz (Heaney, 1994).

AFM confirmed the existence of distinctly periodic ridge-and-valley structures on the iridescent *z* faces and the absence of such surface modulations on the non-iridescent *r* faces (figure 11). The ridges were oriented parallel to the edge between the *m* and *z* faces. We calculated an average distance between adjacent ridges by processing the AFM images through

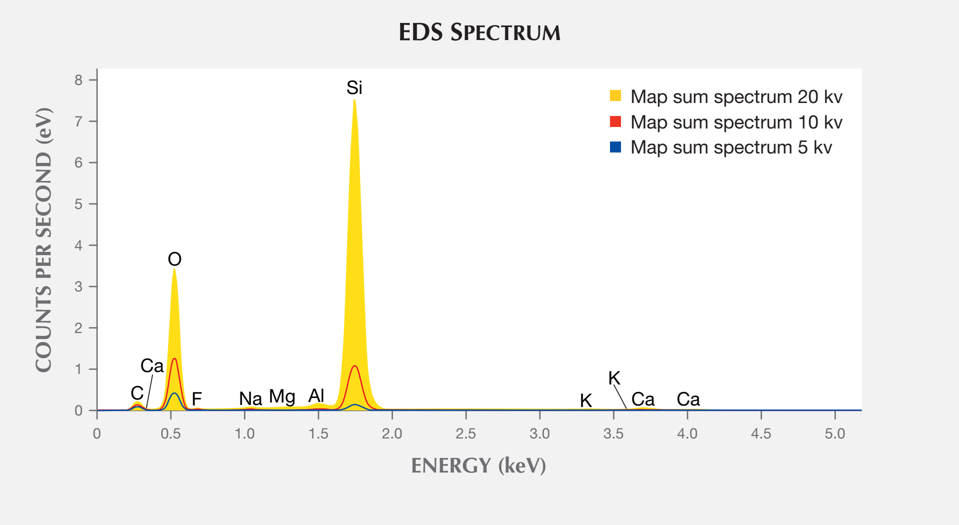

Figure 10. An EDS spectrum of an iridescent face. Data were collected at 20 kv (yellow), 10 kv (red), and 5 kv (blue). Higher-voltage spectra reflect chemical composition at greater depths.

an FFT algorithm using MATLAB. As the ridge shapes were not identical from top to bottom, we sliced the images into 256 cross sections from the top down (figures 12A and 12B), performing FFT on each section (figure 12C), and stacked the 256 FFT results to extract the most dominant frequency of ridge oscillation. The results of our FFT calculations are shown in figure 13. The first few high-amplitude peaks were caused by signal leakage in the FFT and

Figure 11. Atomic force microscopy (AFM) images show the difference in topography between an iridescent and a non-iridescent face. The height varies from 500 to –500 nm on an iridescent face, and the valley-and-ridge structure can be clearly observed. Non-iridescent faces have a much narrower height range. The bright spots are dirt on the surface, and the black holes are pits.

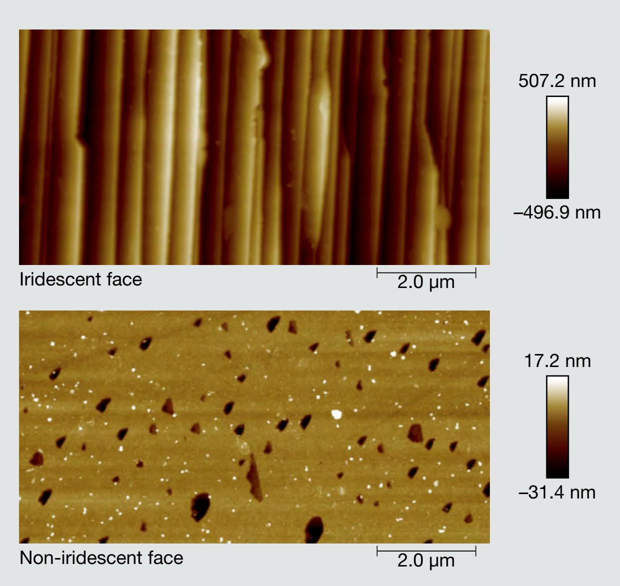

Figure 12. Fast Fourier transform (FFT) analysis of the spatial variation for an iridescent face as determined by AFM. A: An AFM image of an iridescent face. This image provided 256 cross sections from top to bottom for FFT analysis. B: The variation in topography for the cross section indicated by the blue line in A. C: An FFT spectrum of B to calculate the most dominant frequency of the ridge oscillation.

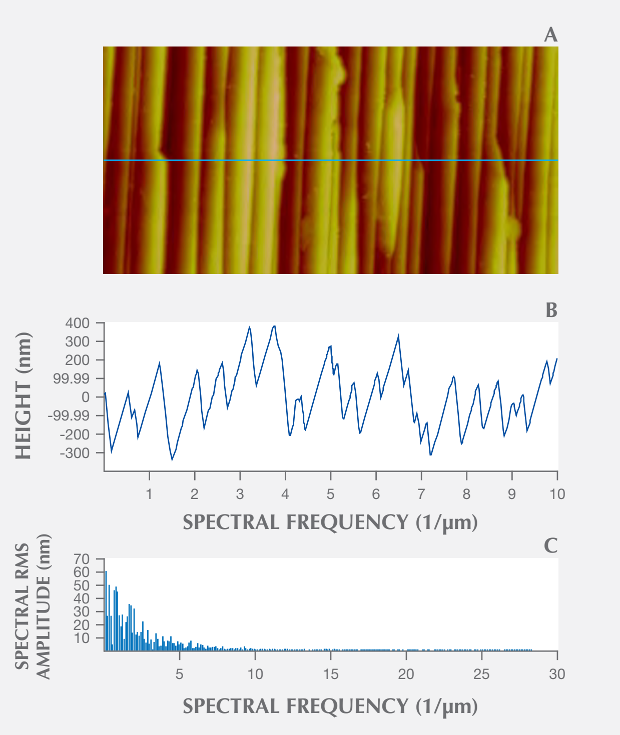

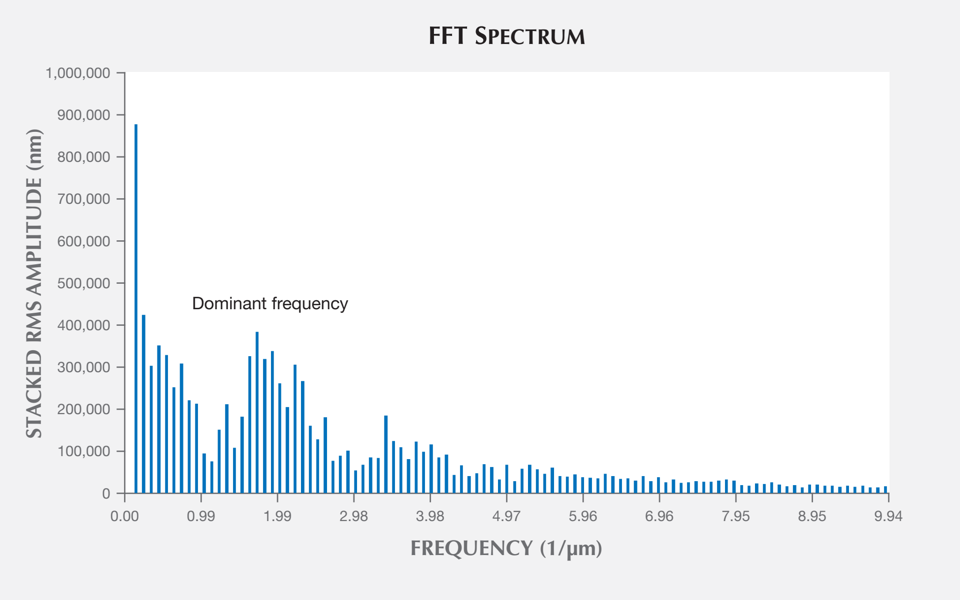

Figure 13. The final FFT spectrum for the iridescent face in figure 12A. The low-frequency peaks are caused by "signal leakage" and should be ignored. The most dominant frequencies that represent the typical distances between two adjacent ridges on the z faces are in the 1.59–2.29 µm^{-1} range. Therefore, the wavelength of the oscillation is on the order of 437 to 629 nm.

should be ignored. The most dominant frequencies that reflect the wavelengths of the surface modulations ranged from 1.59 to 2.29 µm^{-1}. Therefore, the real-space wavelength of the oscillation was on the order of 437 to 629 nm. These distances fall within the range of visible-light wavelengths, explaining the effectiveness of the substructure as a diffraction grating for visible light. These values are impressively close to Raman's 1950 estimate of 0.34 µm (340 nm) for the periodicity of the iris quartz striations.

Figure 14. This brightfield TEM image of the FIB section was extracted from an iridescent face perpendicular to the surface striations, which appear as the jagged surface near the top of this cross-sectional foil beneath the carbon cap. The lighter striations indicated by arrows are artifacts of FIB milling.

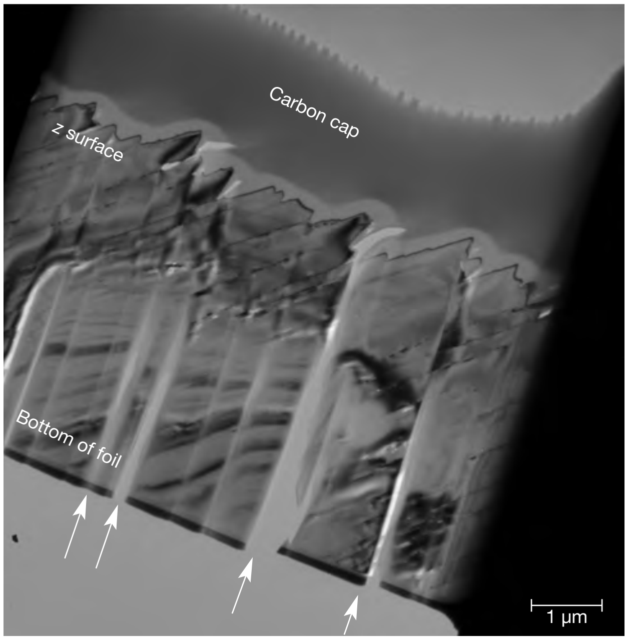

TEM Characterization. Using FIB milling, we extracted a thin foil from an iridescent *z* face; the foil was oriented perpendicular to the grooved surface striations (figure 7). Brightfield TEM imaging of the foil revealed the surface valley-and-ridge structure documented by SEM and AFM very clearly beneath the protective carbon cap (figure 14). Two varieties of defect structures associated with the surface ridges are evident in these images. First, corridors of missing material can be observed oriented normal to the ridged surface of the foil (arrowed in figure 14). As striking as these features are, they are not meaningful, because they were produced artificially during the sample preparation process. It is commonly observed that when solids with uneven surfaces are sputter milled by the focused ion beam technique, the Ga ions are channeled by the valley structures downward into the specimen during milling (Volkert and Minor, 2007). As a result, the section is selectively scoured along distinct channels, leading to the uneven excavation of material in parallel rows. This undesirable artifact creates an appearance of parallel slats within the foil.

The second set of visible defect features is structurally more significant. A higher-magnification

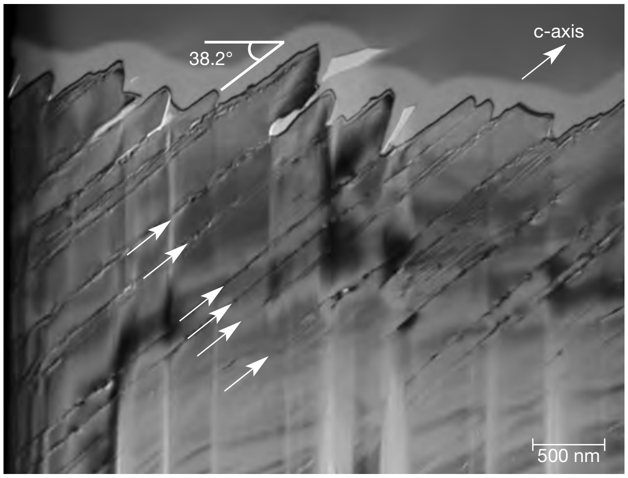

Figure 15. At higher magnification, planar defects oriented at 38.2° from the surface of the z *face are apparent in this TEM image (arrows). The valleys on the* z *face coincide with the intersection of these defects with the surface. We hypothesize that the defects were preferentially etched and are responsible for the surface grooving that gives rise to the diffraction-based iridescence.*

image of the foil (figure 15) shows that the slopes of the surface ridges are inclined ~38° from the top surface of the foil, which corresponds to the *z* (011) plane of the original crystal. Parallel line defects extend from the inclined ridges at the top of the foil through to the bottom of the section (arrowed in figure 15). We interpret these defects as traces of defect planes oriented parallel to the *m* (010) face of the quartz crystal. The calculated angle between *m* (010) and *z* (011) for quartz is 38.2°, consistent with the inclination observed in figure 15. The defects generally run parallel to each other, but in places near the surface they create vein-like networks. Micropores measuring tens of nanometers in diameter can also be seen as material gaps along the defects.

DISCUSSION

Cause of Iridescence. Our SEM and AFM images revealed that the *z* faces of iris quartz are marked by a topographic valley-and-ridge structure with remarkably regular intervals. The ridges were inclined from the *z* (011) surface at an angle of 38°, and the distance from the top to the bottom of the grooving ranged from approximately 100 to 600 nm. Fourier analysis of the AFM images placed the periodicity within the range of visible light, between 437 and 629 nm. That magnitude is consistent with the spacing between the inclined planar defects observed in brightfield TEM images. Electron diffraction patterns from the foil revealed only quartz, with no evidence of an opaline phase.

Consequently, it seems clear that the iridescence observed on the *z* faces of quartz from the Deccan Traps of India is caused by a combination of the surface grooving with an effective blaze angle of 38.2° and an underlying lamellar structure, which together create a diffraction grating for visible light. The absence of either opal or compositional impurities definitively rules out iridescence by a thin-film effect, *sensu stricto*. In addition, our observation contradicts Raman's 1950 model for iridescence insofar as the planar lamellae we observed were oriented parallel to *m* {010} rather than *z* {011}. On the other hand, we did find some support for Raman's interpretation that diffraction arises from a surface layer of the quartz crystals. After noting that broken *z* surfaces were not iridescent, we polished iridescent faces with a diamond polishing compound (8 µm grit) to see whether the iridescence could be eliminated by abrasion. In fact, the iridescence at first intensified and then disappeared. Although our study could not quantitatively constrain the depth of the diffracting layer, we estimate the thickness of the stratified medium as less than 500 µm but greater than the 5 µm depth of our FIB TEM foil, consistent with Raman's estimate of 250 µm.

Origin of the Periodic Substructure. We pose two models for the existence of the repetitive structures that create the diffraction grating. One possibility is that the lamellae observed in figure 15 represent subdivided growth faces of quartz. Quartz is known to grow with "artichoke" or "cathedral" morphologies (figure 16) that involve the emergence of split, layered crystals from the rhombohedral faces of a parent crystal. The cause of the phenomenon is not known, but it may result from the poisoning of growth faces by impurities, leading to the division of the rhombohedral faces into multiple members, whose c-axes point roughly in the same direction.

Although we initially favored this genetic mechanism, we have subsequently grown skeptical of it. The artichoke morphology has been described for macroscopic crystals with layered outgrowths that are several millimeters in thickness. We know of no analogue for the nanoscale periodicity displayed by the iris quartz crystals from the Jalgaon District. Moreover, it is not clear to us how an undulating surface topography might emerge on the *z* faces and not the *r* faces of quartz during crystal growth. If the quartz druses grew in response to pulses of silica-rich fluids into the basaltic cavities of the Deccan Traps, then periodic growth behavior might be attributed to pulsing of the fluids, but episodic infusions of fluids would seem more likely to produce growth layers stacked normal to the *z* and *r* faces, which was not observed.

The second and more plausible explanation attributes the observed microstructures to polysynthetic Brazil twinning, as Raman (1950) originally speculated, but with a few departures from his original model. Whereas Raman proposed that Brazil twins were stacked parallel to the *z* faces and contained impurities at the twin boundaries, we argue that the Brazil twin boundaries occur as pairs, that they are oriented parallel to *m* {010}, and that diffraction of light occurs at the twin boundaries as the result of etching by aqueous fluids along the boundaries.

We base this interpretation on the observation that when one traces the planar defects along the FIB TEM foil from the surface of the crystal toward the interior, the slightly curved and wandering defect traces grade into strictly flat planar defects. Those defect planes occur as paired boundaries separated by ~30 nm (figure 17). Bragg thickness contours crossed these boundaries without interruption, and diffraction patterns that include these regions appeared as single-crystal patterns. Consequently, we found no evidence that these intergrowths represent exsolution lamellae or intergrowths of another phase, and we conclude that they are paired twin boundaries. The two most common twins in quartz are the Dauphiné and the Brazil twins, and it is notoriously difficult to distinguish between these by diffraction methods (Heaney, 1994).

McLaren and Phakey (1965, 1966) demonstrated that interference fringes can be observed in brightfield and darkfield TEM images across Brazil twin boundaries. We examined a TEM foil from a Brazilian amethyst (Smithsonian National Museum of Natural History, USNM #R1453) to confirm the appearance of these fringes under the imaging conditions we applied to the Indian iris quartz, and the fringes were immediately apparent. We saw no such fringes during our examination of the parallel defect planes in the iris quartz from Jalgaon. That might weigh against an interpretation of these features as Brazil twins, but we are unaware of Dauphiné twins occurring as polysynthetic, nanoscale intergrowths except when crystals are heated to the transition tempera-

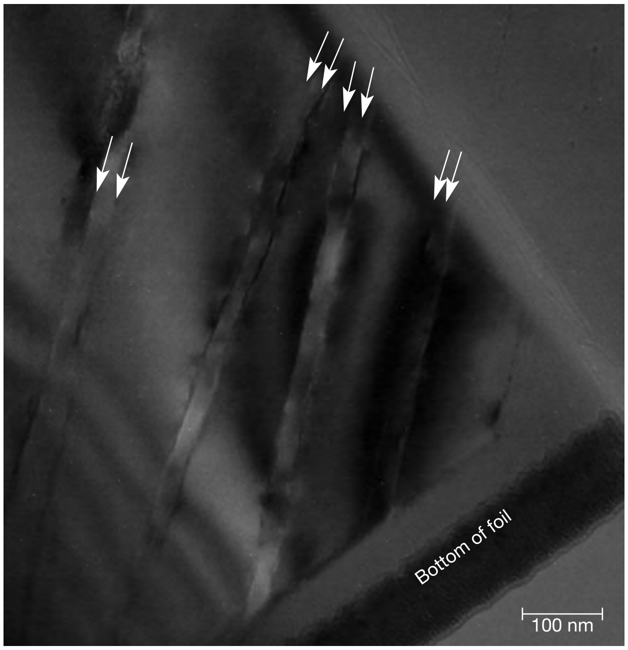

Figure 17. In this TEM image, paired twin boundaries (see arrows) are visible in the lower portion of the crystalline quartz foil.

Figure 16. Schematic cross section of an “artichoke” quartz crystal.

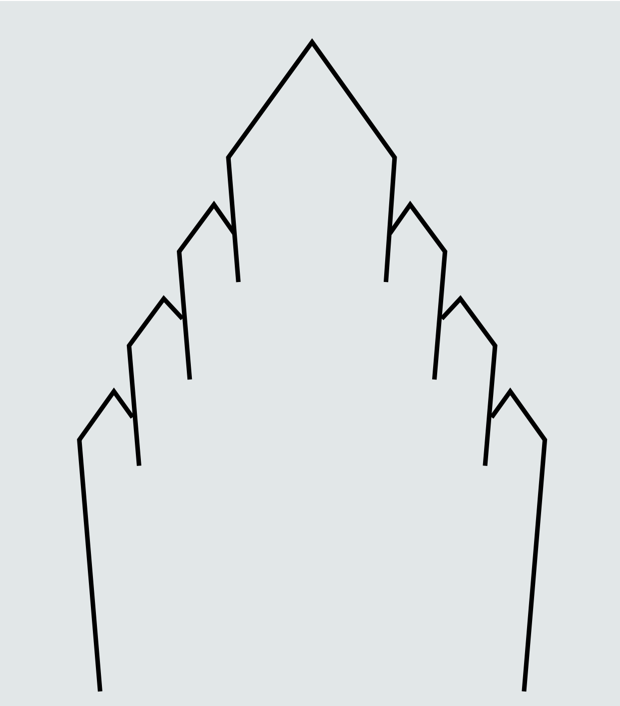

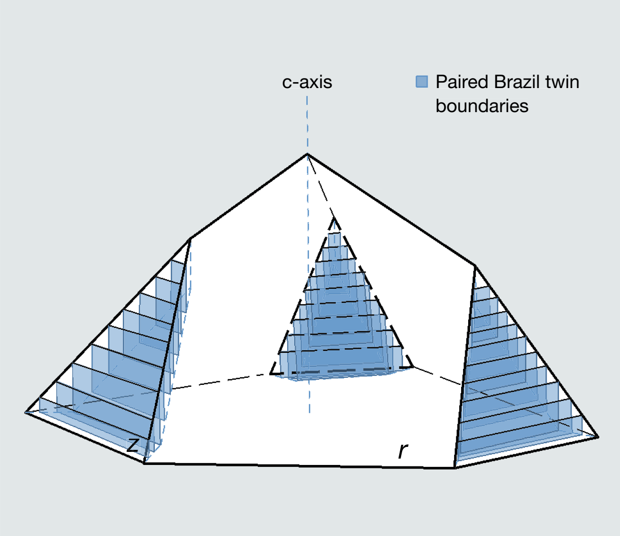

Figure 18. Our model for iridescence in quartz. Paired Brazil twin lamellae oriented parallel to m *{010} intersect the* z *{011} faces and were preferentially etched by aqueous fluids to create a surface grating.*

ture between low and high quartz (573°C; van Tendeloo et al., 1976). Moreover, interference fringes are *not* expected at Brazil twin boundaries when the TEM section of quartz is oriented exactly perpendicular to the twin boundary—the electron beam from one twin member does not interfere with that of the other, as happens when the twin walls are oblique to the surface of the TEM foil.

McLaren (1967) reported an absence of telltale Brazil twin fringes in his TEM analysis of quartz crystals exposed to a shear deformation parallel to (001). Deformation generated paired Brazil twin boundaries approximately 30 nm apart, and these boundary pairs were themselves separated by hundreds of nanometers. Brightfield images from TEM foils cut normal to the twins exhibited no fringe interference. The defect structures described by McLaren (1967) are virtually identical to those we characterized for the Indian iris quartz. Although we do not suggest that the quartz druses from the Deccan Traps were exposed to deformational shear, we speculate that another process (possibly incorporation of Al or rapid growth rates) may have generated periodic paired Brazil twin boundaries oriented parallel to *m* {010}.

It is well known that twin boundaries in minerals are vulnerable to preferential weathering (e.g., Cornell et al., 1974; Wilson and McHardy, 1980; Cornell and Giovanoli, 1988). The paired Brazil twin boundaries in iris quartz is proposed by us to represent strained regions that were particularly susceptible to dissolution, and we suggest that post-growth episodes of etching by invasive fluids preferentially altered the paired Brazil twin boundaries where they intersected the surface *z* faces, sculpting the valley-and-ridge topography we observed. Moreover, the channeling of these fluids along the twin boundaries within the crystal resulted in dissolution and recrystallization of the twin boundaries, producing both fluid-filled nanopores and the vein-like defect surfaces observed near the top of our TEM foil.

Consequently, we interpret the diffraction effect as a result of surface etching and subsurface alteration by post-depositional fluids. The iridescence thus represents a combined effect of reflective interference from the grooved surface and transmissive interference at the weathered twin boundaries just below the surface (figure 17). When the etched surface layer is removed, as on the naturally fragmented and the artificially polished *z* faces, then the iridescence disappears. Thus, the depth of the iridescence effect traces the reach of aqueous alteration, not the interior extent of the twinning. In turn, this observation explains why iris quartz crystals occur globally yet remain elusive to collectors. Many quartz crystals—particularly amethysts—are extensively twinned according to the Brazil law and contain periodic defects separated by distances close to the wavelengths of visible light. But it is only when these crystals have experienced a subsequent stage of dissolution, with differential etching along the defect planes (figure 18), that they will transform to iris quartz.

In "To the Rainbow," the Scottish poet Joanna Baillie (1762–1851) lamented the fate of natural wonders when their magic is reduced to empirical hypotheses:

> *When science from creation's face*
> *Enchantment's veil withdraws,*
> *What lovely visions yield their place*
> *To cold material laws!*

As C.V. Raman understood, the search for an explanation of rainbows in gem materials is not simply an exercise to recast a beautiful phenomenon as a mathematical equation. Gem rainbows can appear when crystal structures invisible to the unaided eye are arrayed in repetitive patterns that will diffract light. Thus, modern scientific analysis withdraws enchantment's veil only to yield new enchantments.

ABOUT THE AUTHORS

Ms. Lin received her M.S. in geosciences at Pennsylvania State University in 2015 and is working with the Rapaport Diamond Corporation. Dr. Heaney is a professor in the Department of Geosciences at Pennsylvania State University.

ACKNOWLEDGMENTS

This research was made possible through funding from the National Science Foundation (NSF-EAR11-47728). SEM, FIB, and AFM work were performed at Pennsylvania State University's Materials Characterization Laboratory with the assistance of Dr. Trevor Clark, Julie Anderson, Joshua Maier, and Timothy Tighe. Special thanks are due to Drs. James Kubicki, Maureen Feineman, Jeffrey Post, Long-Qing Chen, Yi Wang, and Mr. Phil Kong for their useful suggestions.

REFERENCES

Akizuki M., Sugawara H. (1970) The lamellar structure in moonstone and anorthoclase from Korea. *Contributions to Mineralogy and Petrology*, Vol. 29, No. 1, pp. 28–32, http://dx.doi.org/10.1007/BF00387996

Balakirev V.G., Tsinober L.I., Tsyganov E.M. (1975) Electron-microscope study of Brazilian twins in synthetic amethysts. *Kristallografiya*, Vol. 19, No. 4, pp. 517–520.

Baran Z., Godwod K., Warminski T. (1987) X-ray study of Brazil twins in natural amethyst. *Physica Status Solidi (a)*, Vol. 404, No. 4, pp. 9–24, http://dx.doi.org/10.1002/pssa.2211010102

Buckley A.N., Woods R. (1983) X-ray photoelectron spectroscopic investigation of the tarnishing of bornite. *Australian Journal of Chemistry*, Vol. 36, No. 9, pp. 1793–1804, http://dx.doi.org/10.1071/CH9831793

Cliff G., Champness P.E., Nissen H.U., Lorimer G.W. (1976) Analytical electron microscopy of exsolution lamellae in plagioclase feldspars. In H.-R. Wenk, Ed., *Electron Microscopy in Mineralogy*. Springer, Berlin, Heidelberg, pp. 258–265.

Cornell R.M., Giovanoli R. (1988) Acid dissolution of akaganéite and lepidocrocite: The effect on crystal morphology. *Clays and Clay Minerals*, Vol. 36, No.5, pp. 385–390.

Cornell R.M., Posner A.M., Quirk J.P. (1974) Crystal morphology and the dissolution of goethite. *Journal of Inorganic and Nuclear Chemistry*, Vol. 36, No. 9, pp. 1937–1946, http://dx.doi.org/10.1016/0022-1902(74)80705-0

Darragh P.J., Gaskin A.J., Terrell B.C., Sanders J.V. (1966) Origin of precious opal. *Nature*, Vol. 209, pp. 13–16, http://dx.doi.org/10.1038/209013a0

Gaillou E., Fritsch E., Aguilar-Reyes B., Rondeau B., Post J., Barreau A., Ostrooumov M. (2008) Common gem opal: An investigation of micro- to nano-structure. *American Mineralogist*, Vol. 93, No. 11–12, pp. 1865–1873, http://dx.doi.org/10.2138/am.2008.2518

Gübelin E.J., Koivula J.I. (2005) *Photoatlas of Inclusions in Gemstones*. Opinio Verlag, Basel, Switzerland, Vol. 2.

Heaney P.J. (1994) Structure and chemistry of the low-pressure silica polymorphs. *Reviews in Mineralogy and Geochemistry*, Vol. 29, No. 1, pp. 1–40.

Heaney P.J., Davis A.M. (1995) Observation and origin of self-organized textures in agates. *Science*, Vol. 269, No. 5230, pp. 1562–1565, http://dx.doi.org/10.1126/science.269.5230.1562

Heaney P.J., Vicenzi E.P., Giannuzzi L.A., Livi K.J.T. (2001) Focused ion beam milling: A method of site-specific sample extraction for microanalysis of Earth and planetary materials. *American Mineralogist*, Vol. 86, No. 9, pp. 1094–1099, http://dx.doi.org/10.2138/am-2001-8-917

Kinoshita S., Yoshioka S., Miyazaki J. (2008) Physics of structural colors. *Reports on Progress in Physics*, Vol. 71, No. 7, pp. 076401, http://dx.doi.org/10.1088/0034-4885/71/7/076401

Laufer G. (1996) *Introduction to Optics and Lasers in Engineering*. Cambridge University Press, Cambridge, England.

Ma C., Gresh J., Rossman G.R., Ulmer G.C., Vicenzi E.P. (2001) Micro-analytical study of the optical properties of rainbow and sheen obsidians. *The Canadian Mineralogist*, Vol. 39, No. 1, pp. 57–71, http://dx.doi.org/10.2113/gscanmin.39.1.57

Ma C., Rossman G.R., Miller J.A. (2007) The origin of color in "fire" obsidian. *The Canadian Mineralogist*, Vol. 45, No. 3, pp. 551–557, http://dx.doi.org/10.2113/gscanmin.45.3.551

McConnell J.D.C. (1974) Electron-optical study of the fine structure of a schiller labradorite. In W.S. MacKenzie and J. Zussman, Eds., *Feldspars*. Manchester University Press.

McLaren A.C., Phakey P.P. (1965) A transmission electron microscope study of amethyst and citrine. *Australian Journal of Physics*, Vol. 18, No. 2, pp. 135–142, http://dx.doi.org/10.1071/PH650135

McLaren A.C., Phakey P.P. (1966) Electron microscope study of Brazil twin boundaries in amethyst quartz. *Physica Status Solidi (b)*, Vol. 13, No. 2, pp. 413–422, http://dx.doi.org/10.1002/pssb.19660130213

McLaren A.C., Pitkethly D.R. (1982) The twinning microstructure and growth of amethyst quartz. *Physics and Chemistry of Minerals*, Vol. 8, No. 3, pp. 128–135, http://dx.doi.org/10.1007/BF00311283

McLaren A.C., Retchford J.A., Griggs D.T., Christie J.M. (1967) Transmission electron microscope study of Brazil twins and dislacations[*sic*] experimentally produced in natural quartz. *Physica Status Solidi (b)*, Vol. 19, No. 2, pp. 631–644, http://dx.doi.org/10.1002/pssb.19670190216

Meadows M.G., Butler M.W., Morehouse N.I., Taylor L.A., Toomey M.B., McGraw K.J., Rutowski R.L. (2009) Iridescence: views from many angles. *Journal of The Royal Society Interface*, Vol. 6, Suppl. 2, pp. S107–S113, http://dx.doi.org/10.1098/rsif.2009.0013.focus

Miura Y., Tomisako T. (1978) Ion microprobe mass analysis of exsolution lamellae in labradorite feldspar. *American Mineralogist*, Vol. 63, No. 5–6, pp. 584–590.

Nissen H.-U. (1971) End member compositions of the labradorite exsolution. *Naturwissenschaften*, Vol. 58, No. 9, pp. 454–454, http://dx.doi.org/10.1007/BF00624619

Parker A.R., Townley H.E. (2007) Biomimetics of photonic nanostructures. *Nature Nanotechnology*, Vol. 2, No. 6, 347–353, http://dx.doi.org/10.1038/nnano.2007.152

Petrov A., Tanaka Y. (2011) Iris quartz. Mindat.org, www.mindat.org/article.php/1335/Iris+Quartz

Raman C.V. (1950) Crystals of quartz with iridescent faces. *Proceedings of the Indian Academy of Sciences, Section A*, Vol. 31, No. 5, pp. 275–279.

Renfro N., Koivula J.I. (2011) Gem News International: Spectral interference in quartz from India. *G&G*, Vol. 47, No. 1, pp. 58–59.

Rondeau B., Fritsch E., Mazzero F., Gauthier J.-P., Cenki-Tok B., Bekele E., Gaillou E. (2010) Play-of-color opal from Wegel Tena, Wollo Province, Ethiopia. *G&G*, Vol. 46, No. 2, pp. 90–105, http://dx.doi.org/10.5741/GEMS.46.2.90

Sanders J.V. (1964) Colour of precious opal. *Nature*, No. 204, pp. 1151–1153, http://dx.doi.org/10.1038/2041151a0

Scharff F. (1875) *Neues Jahrbuch für Mineralogie, Geologie, Paläontologie*, Stuttgart, Germany, E. Schweizerbart'sche Verlagshandlung (in German).

Schlössin H.H., Lang A.R. (1965) A study of repeated twinning, lattice imperfections and impurity distribution in amethyst. *Philosophical Magazine*, Vol. 12, No. 116, pp. 283–296, http://dx.doi.org/10.1080/14786436508218871

Schmetzer K. (1987) Microscopic observation of twinning microstructure in natural amethyst. *Neues Jahrbuch fur Mineralogie-Monatshefte*, Vol. 1, pp. 8–15.

Taijing L., Sunagawa I. (1990) Structure of Brazil twin boundaries in amethyst showing Brewster fringes. *Physics and Chemistry of Minerals*, Vol. 17, No. 3, pp. 207–211, http://dx.doi.org/10.1007/BF00201451

Taijing L., Sunagawa I. (1994) Texture formation of agate in geode. *Mineralogical Journal*, Vol. 17, No. 2, pp. 53–76, http://dx.doi.org/10.2465/minerj.17.53

van Tendeloo G., van Landuyt J., Amelinckx S. (1976) The α→β phase transition in quartz and $AlPO_4$ as studied by electron microscopy and diffraction. *Physica Status Solidi (a)*, Vol. 33, No. 2, pp. 723–735, http://dx.doi.org/10.1002/pssa.2210330233

Vaughan D.J., Tossell J.A., Stanley C.J. (1987) The surface properties of bornite. *Mineralogical Magazine*, Vol. 51, No. 360, pp. 285–293, http://dx.doi.org/10.1180/minmag.1987.051.360.11

Vigneron J.P., Pasteels J.M., Windsor D.M., Vértesy Z., Rassart M., Seldrum T., Dumont J., Deparis O., Lousse V., Biró L.P., Ertz D., Welch V. (2007) Switchable reflector in the Panamanian tortoise beetle *Charidotella egregia* (Chrysomelidae: Cassidinae). *Physical Review Series E*, Vol. 76, No. 3, p. 031907, http://dx.doi.org/10.1103/PhysRevE.76.031907

Volkert C.A., Minor A.M. (2007) Focused ion beam microscopy and micromachining. *MRS Bulletin*, Vol. 32, No. 05, pp. 389–399, http://dx.doi.org/10.1557/mrs2007.62

vom Rath G.(1873) Mineralogische Mittheillungen von Gerhard vom Rath. *Annalen der Physik und Chemie*, Vol. 6, No. 3, pp. 337–386 cited in A. Petrov and Y. Tanaka (2011) Iris quartz. Mindat.org, www.mindat.org/article.php/1335/Iris+Quartz

Wilson M.J., McHardy W.J. (1980) Experimental etching of a microcline perthite and implications regarding natural weathering. *Journal of Microscopy*, Vol. 120, No. 3, pp. 291–302, http://dx.doi.org/10.1111/j.1365-2818.1980.tb04149.x

CHARACTERISTICS OF GEM-QUALITY BY-PRODUCT SYNTHETIC ZINCITE

Ji Zhang, Yujie Gao, and Guanghai Shi

Gem-quality synthetic zincite from Poland, an industrial by-product of zinc oxide processing, has been available in the market since the early 1980s. In this investigation, conventional gemological methods, spectroscopic techniques, and advanced analytical testing were carried out on 10 rough and faceted samples. The chromophore manganese (Mn), which is significant in natural zincite and can reach 1 wt.% MnO, appears to be negligible in by-product crystals. These crystals also appear to have low to insignificant levels of other potential chromophores such as iron and copper. Inclusions matching previously reported oval and "tadpole-like" inclusions in Polish synthetic zincite were observed and tested by Raman and IR spectroscopy. These inclusions were identified as carbon-bearing material, possibly belonging to soot and/or gases captured during the growth of the synthetic zincite host.

Zincite (ZnO) was discovered in 1810 (Dunn, 1995; Welch, 2008) and mined from marble-hosted Zn-Fe-Mn skarn-type deposits (Hague et al., 1956; Webster, 1983) at the Franklin and Sterling Hill mines of Sussex County, New Jersey. These mines are still considered the only locality for gem-quality natural zincite (Dunn, 1995; Peck et al., 2009; Wilson, 2013). The natural zincites were always aggregates, both massive and small (Nowak et al., 2007). Only a few large gem-quality crystals displaying strong luster and a beautiful bright red color have been faceted (Welch, 2008). Some collectors seek the stone for its rarity and attractive appearance, although a relatively low hardness (4 on the Mohs scale) limits its use in jewelry (Henderson, 1945; Nowak et al., 2007; Wilson, 2013).

Zincite is also an important semiconductor material, doped by impurity elements to enhance its physical properties in applications such as photodetectors (Soci et al., 2007), LED lights (Dong et al., 2007), laser diodes (Liang et al., 2010), transparent transistors, and substrates (Gahtar et al., 2013). The wide-ranging industrial applications of ZnO have driven crystal growth efforts. Zincite crystals have been synthesized in labs through vapor deposition (Pasko et al., 1976), hydrothermal methods (Karipidis et al., 2008), and pressurized melt growth methods (Nause and Nemeth, 2005). Yet there have been no reports of any effort to pursue synthetic gem crystal growth. Crystals grown by vapor deposition often appear one-dimensional, needle-like, or columnar due to rapid growth along the c-axis (Pasko et al., 1976). Hydrothermal crystals display a two-dimensional plate-like appearance because of the seed orientation (Kortounova et al., 2001; Karipidis et al., 2008), and pressurized melt growth normally produces round boules (Nause and Nemeth, 2005).

During the 1980s, a new form of synthetic zincite emerged from an unnamed foundry in Poland's Lower Silesia Province (Crowningshield, 1985; Kammerling and Johnson, 1995). This material grew as an industrial by-product in the chimney vents of industrial kilns producing zinc oxide powder, through a process similar to chemical vapor deposition (Nowak et al., 2007). We will refer to it as "by-product zincite" hereafter. These crystals possess better transparency and brighter color than natural zincite. By-product zincites were sold in the jewelry market

In Brief

- The colors of by-product synthetic zincite from the foundry in Lower Silesia, Poland, may be related to the material's structure.
- Raman spectroscopy may be useful in distinguishing the Polish specimens from natural zincite.
- Oval and "tadpole-like" inclusions in the by-product synthetic zincite were identified by Raman as carbon-bearing material, possibly from soot captured during the growth process.

See end of article for About the Authors and Acknowledgments.

Gems & Gemology, Vol. 53, No. 1, pp. 82–89,
http://dx.doi.org/10.5741/GEMS.53.1.82

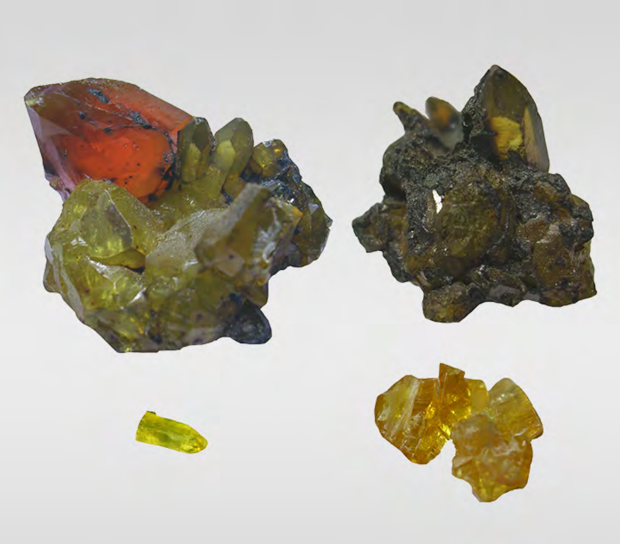

Figure 1. Most of the by-product synthetic zincites in this study had a reddish orange to yellow color; one sample (ZnO-G) was yellowish green. Top row, left to right: samples ZnO-LC (13.85 g) and ZnO-SC (6.34 g). Bottom row, left to right: samples ZnO-G (0.06 g) and zin-7 (1.12 g). Composite photo by Ji Zhang.

from the early 1980s until the 2000s, but now they can only be acquired from existing stocks (Kammerling and Johnson, 1995; Nowak et al., 2007).

The properties and formation processes of by-product synthetic zincite crystals from the Olawa foundry in Lower Silesia have previously been studied (e.g., Crowningshield, 1985; Kammerling and Johnson, 1995; Nowak et al., 2007). Insights into their color and the nature of their unusual oval or "tadpole-like" inclusions (Nowak et al., 2007) have remained elusive. In this investigation, rough by-product zincite crystal samples from the foundry in Lower Silesia were chosen for standard gemological observations, elemental analysis by X-ray fluorescence (XRF) and inductively coupled plasma–mass spectrometry (ICP-MS), and spectroscopic analysis in order to find the characteristics that distinguish them from natural material, identify their inclusion features, and provide an explanation for the cause of color.

MATERIALS AND METHODS

Figure 1 shows four of the 10 rough by-product zincite crystal samples (0.34–13.85 g) that were analyzed. Two were faceted by author YG (labeled Zincite-L and Zincite-S). Sample zin-10 is a group of five unprocessed rough fragments from a yellow crystal; the remainder of this crystal is the faceted sample Zincite-S. All rough samples were purchased at the Warsaw Mineral Show in September 2010; the seller claimed they were produced at an undisclosed foundry in Lower Silesia, Poland.

Standard gemological testing, visible spectroscopy, and Fourier-transform infrared (FTIR) spectroscopy were performed at the School of Gemology,

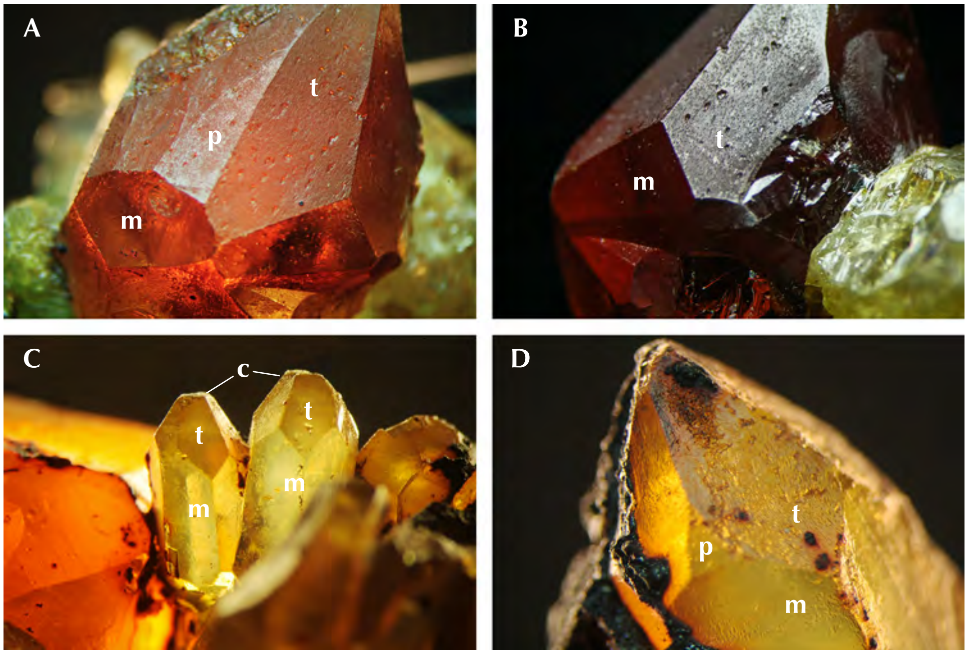

Figure 2. The main crystal faces of the by-product zincite: hexagonal prism m, hexagonal pyramids t and p, single face c, and contact twins along the (0001) direction. These features follow the wurtzite structure of zincite (Zhao et al., 2006). A: sample ZnO-LC, field of view 12.5 mm. B: sample ZnO-LC in another direction, field of view 13.0 mm. C: sample ZnO-SC, field of view 3.5 mm. D: sample ZnO-SC, field of view 4.5 mm. Photomicrographs by Ji Zhang.

China University of Geosciences in Beijing (CUGB). Visible spectra of samples Zincite-L, Zincite-S, and ZnO-G were recorded using a LabTech UV-Vis spectrophotometer in the 400–700 nm range with a sampling interval of 1 nm at a rate of 600 nm/min. Mid-infrared (4000–400 cm^{-1}) spectra of rough sample zin-10 were obtained with a Bruker Tensor 27 FTIR spectrophotometer, operating in absorption and reflectance modes with a resolution of 4 cm^{-1} and 50 scans per sample at room temperature using the KBr pellet method (100 mg KBr and 1.0 mg sample).

XRF results for nine samples (ZnO-LC, Zincite-L, Zincite-S, zin-10, ZnO-G, zin-fs, zin-fc, zin-7, and zin-8) were tested at the Shanghai laboratory of the National Gemstone Testing Center (NGTC), using a Shimadzu EDX-7000 from ^{11}Na to ^{92}U with a 3 mm collimator and a two-minute testing time.

ICP-MS of five samples (ZnO-LC, Zincite-L, Zincite-S, three specimens of the zin-10 group, and ZnO-G) was conducted at Key Laboratory of Submarine Geosciences of the Second Institute of Oceanography, State Oceanic Administration in Hangzhou, using an Elan DRC-e ICP-MS with the U.S. Geological Survey (USGS) standard BHVO-2 measured to monitor accuracy. Small quantities of the five samples were ground into a powder and sieved to obtain a 200 mesh size. Aqueous solutions of the powders were created by dilution of solutions of the powders created using first aqua regia in a Teflon bomb with heating followed by $HClO_4$ and HNO_3 in a Teflon bomb with heating. The unit of ICP-MS results was ppmw; detection limits for all elements were lower than 4 ppmw.

Raman spectroscopy was performed at the Chinese Academy of Geological Sciences (CAGS) in Beijing. Six samples (Zincite-L, Zincite-S, ZnO-LC, ZnO-SC, zin-fs, and zin-fc) were analyzed using a Renishaw 2000 laser Raman microspectroscopy system with an argon-ion laser (514.5 nm excitation), 20 mW power, minimum spot size of 1 µm, and spectral resolution of 1–2 cm^{-1}. The oval inclusion in Zincite-S and another unidentified inclusion belonging to zin-fc were also analyzed *in situ* by Raman spectroscopy.

We compared our results with the Raman spectra and chemical data of two previously tested natural red zincite samples (R050419 and R050492) from the RRUFF database (http://rruff.info). Sample R050419 is a deep red crystal from the Sterling Hill mine, and sample R050492 is a massive deep red crystal from the Franklin mine. No natural zincite was examined in this study due to the difficulty of obtaining such material.

TABLE 1. Chemical composition of potential chromophore elements of by-product synthetic zincite tested by ICP-MS (in ppmw).

	ZnO-LC (orange-red)	Zincite-L (reddish orange)	Zincite-S (yellow)	zin-10 (yellow)	ZnO-G (yellowish green)
Ti	8.3	10.8	5.8	0.0	0.8
V	0.2	1.4	5.2	1.4	0.7
Cr	1.6	3.8	7.7	11.0	2.3
Mn	1.8	1.6	4.3	7.5	1.5
Fe	63.3	51.0	104.9	86.2	38.3
Co	0.7	0.7	1.9	0.6	0.7
Ni	9.2	6.1	19.7	6.1	10.8
Cu	16.1	6.8	29.1	6.9	9.3
Cd	bdl	bdl	bdl	bdl	bdl

Sample detection limits (ppmw) were Ti (0.336), V (0.058), Cr (0.245), Mn (0.014), Fe (3.383), Co (0.007), Ni (0.023), Cu (0.020), and Cd (0.021).bdl = below detection limit

RESULTS AND DISCUSSION

Crystallography and Gemological Properties. The by-product crystals exhibited a hexagonal prismatic and pyramid appearance, consisting of hexagonal prism *m* $\{10\bar{1}0\}$, hexagonal pyramids *t* $\{11\bar{2}4\}$ and *p* $\{10\bar{1}1\}$, and single face *c* {0001} (figure 2), with contact twinning along (0001) following wurtzite structure (Zhao et al., 2006). The samples' colors ranged from reddish orange to yellow to greenish yellow, and all of them were transparent, with a subadamantine to vitreous luster (figures 1 and 3). Their RIs were over the limit of the refractometer (RI = 1.78). With a handheld

Figure 3. The 36.54 ct reddish orange Zincite-L (left) and the 2.87 ct yellow Zincite-S (right) were faceted from the by-product zincite rough. Photo by Yujie Gao.

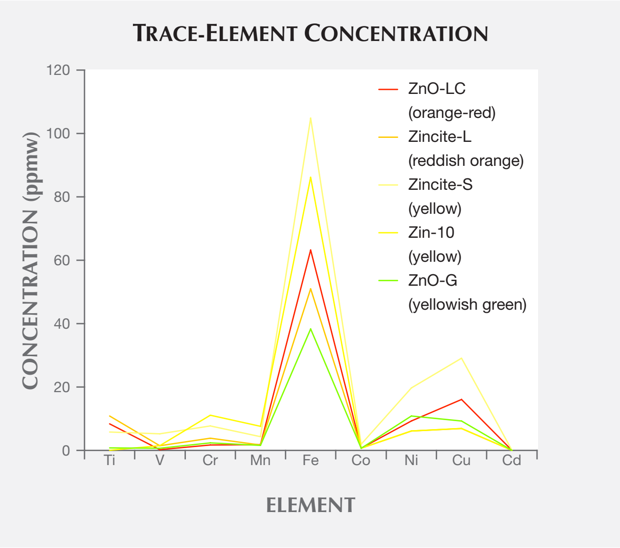

Figure 4. The nine potential chromophore elements of five by-product zincite samples were tested by ICP-MS. In all five samples, Fe content was higher than the other eight elements; the concentrations of each of the non-iron elements are lower than 30 ppm.

spectroscope, absorption bands were only seen in the blue to violet regions. The samples' specific gravity, measured hydrostatically, ranged from 5.66 to 5.70. These properties were consistent with previous reports (Crowningshield, 1985; Kammerling and Johnson, 1995; Nowak et al., 2007).

Figure 5. The visible spectrum of reddish orange by-product sample Zincite-L showed that it absorbed light in the green to violet region, from 550 to 400 nm.

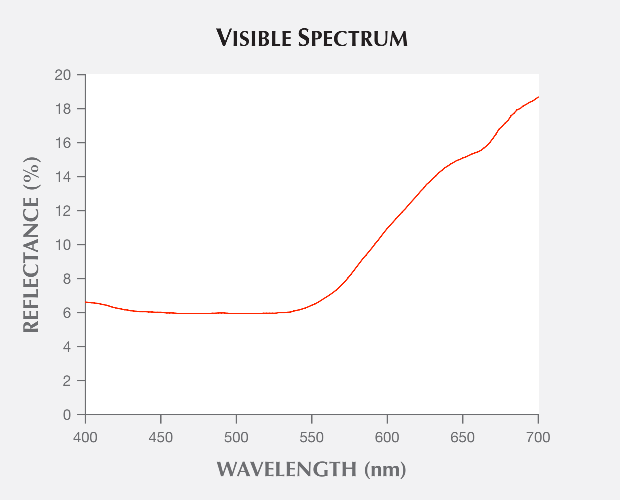

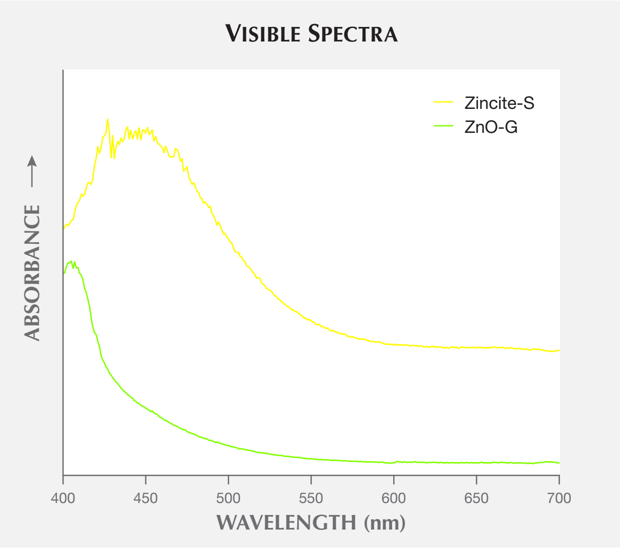

Figure 6. The visible spectra showed that yellow by-product samples Zincite-S and ZnO-G also absorbed light in the blue to violet regions.

Chemical Composition. XRF testing suggested that the samples were composed of almost pure zinc and oxygen. To investigate the potential chromophores of by-product zincite, the powders of five samples were tested by ICP-MS. The results showed that Mn levels were negligible, ranging from 1.53 to 7.55 ppm with a mean of 3.38 ppm, corresponding to previous reports (Kammerling and Johnson, 1995; Nowak et al., 2007). These levels were all dramatically lower than Mn contents in natural material (approximately 1 wt.% MnO; see Webster, 1983; http://ruff.info). Iron contents in by-product samples were relatively high among nine potential chromophores, ranging from 38.31 to 104.92 ppmw with a mean of 68.74 ppm; the contents of other elements were lower than 30 ppmw (table 1; figure 4).

Visible Spectra and Cause of Color. The visible spectrum of reddish orange Zincite-L displayed a wide absorption band from 550 to 400 nm, covering the green to violet regions (figure 5). Yellow Zincite-S revealed a broad absorption band between 480 and 420 nm in the blue to violet region, while yellowish green ZnO-G absorbed only violet light from 450 to 400 nm (figure 6).

There is no clear relationship between the material's color and its chemical composition, and the contents of potential chromophore elements were low, although the yellow samples had relatively

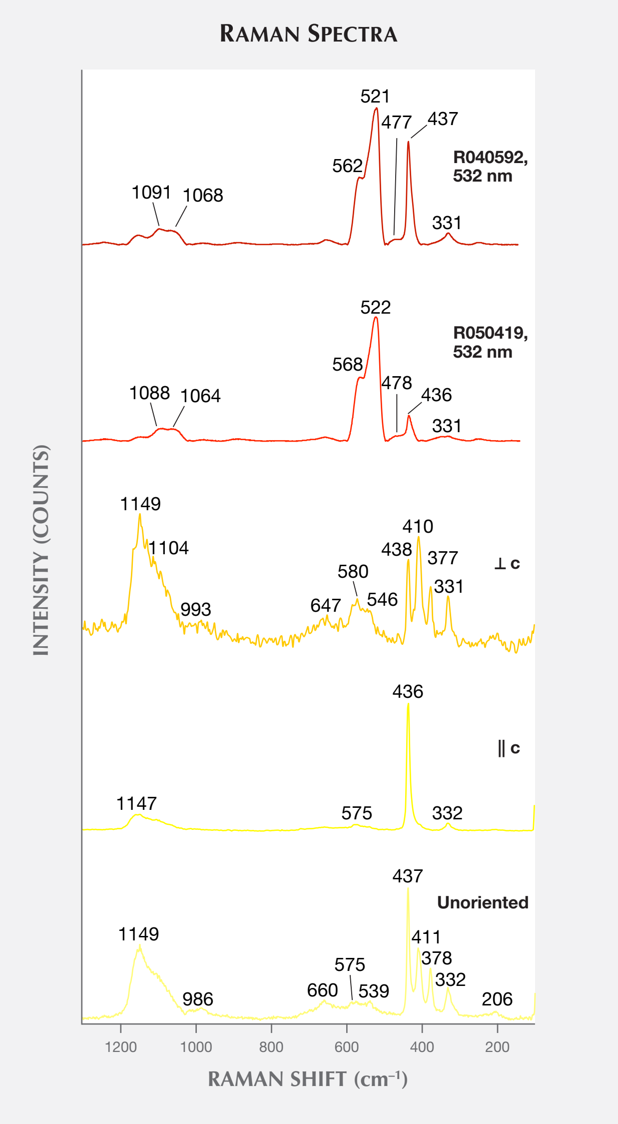

Figure 7. These Raman spectra of zincite, from top to bottom, belong to natural samples R050492 and R050419 from the RRUFF database (both unoriented) and three by-product samples from this study: Zincite-L (⊥c-axis), Zincite-L (|| c-axis), and Zincite-S (unoriented). Spectra are vertically shifted for clarity.

higher Fe contents than orange to red or yellowish green samples (again, see table 1 and figure 4). The cause of various colors observed may be related to structure rather than chemical composition. These structural factors include increasing amounts of band gap absorption from defect states (Kammerling and Johnson, 1995), lattice defects with electron donors such as neutral zinc atoms (Nowak et al., 2007), and either oxygen deficit or zinc excess within zincite (Mikami et al., 2005; Karipidis et al., 2008).

Raman Spectra. Raman spectra were obtained from sample Zincite-L with its c-axis oriented parallel and perpendicular to the laser beam, together with five other samples (Zincite-S, ZnO-LC, ZnO-SC, zin-fs, and zin-fc) whose c-axes were randomly oriented with respect to the laser. In addition, the spectra from two natural samples, taken from the RRUFF database, were analyzed. The unoriented Raman spectra were similar, so one representative spectrum of Zincite-S was chosen (figure 7). The Raman peaks of zincite were divided into three groups:

(1) Shared peaks in natural and by-product zincite spectra at approximately 331 and 437 cm^{-1}

(2) Unique peaks in natural zincite spectra at about 477, 522, 568, 1065, and 1090 cm^{-1}

(3) Unique peaks in by-product synthetic spectra at approximately 379, 410, 540, 580, 660, and 1150 cm^{-1}

The latter two groups of peaks could serve to distinguish by-product zincite from natural zincite using Raman spectroscopy.

Oval Inclusion. Nowak et al. (2007) reported unusual oval and "tadpole-like inclusions" in Polish by-product synthetic zincite; in this study, two similar inclusions were observed and tested. The first oval inclusion, belonging to sample Zincite-S (figure 8), showed Raman peaks at 2938, 2923, 2882, 2854, 1613, 1546, 1507, 1442, and 1098 cm^{-1}, which indicated some carbon-bearing material stretching modes (figure 9). The second inclusion, located at the cleavage plane of sample zin-fc (the figure was not obtained successfully due to the rough cleavage surface), displayed Raman peaks at 2929, 2882, 2850, 1613, 1580, 1430, 1392, 1346, 1296, and 1204 cm^{-1} (figure 10).

Combined with the C-H stretching mode indicated by the IR spectra of rough sample zin-10 (figure 11) and excluding the shellac used in the cutting process (whose Raman peaks are not a match), it is suggested that there are some carbon-bearing materials that make up the oval inclusions in the by-product synthetic zincite. Although the origin of the oval inclusion was not clear, possible sources include (1) a group of carbon-bearing gases such as CH_4 and CO_2 in the crystal formation atmosphere; and (2) the complex fuel ashes (carbon-bearing soot) produced by the smelting process (Nowak et al., 2007). On one hand, Raman spectra of individual gases (Dickinson and Rasetti, 1929) have one or two peaks near the peaks of the oval inclusion, such as the 1285 cm^{-1} peak of CO_2 and the 2914 and 3022 cm^{-1}

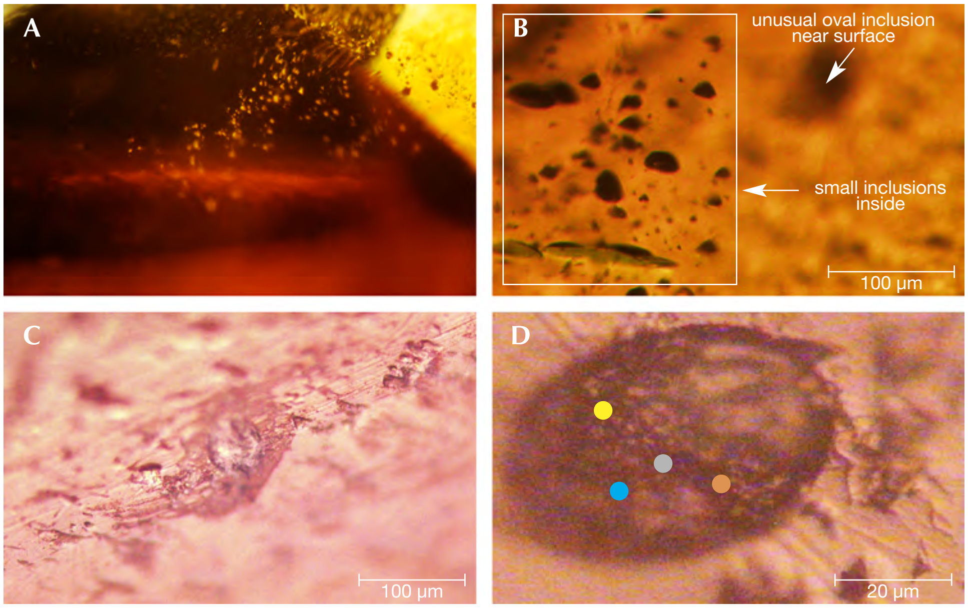

Figure 8. A: Small inclusions were observed in the pavilion of Zincite-S; field of view 2.5 mm. B: When the internal features of Zincite-S were examined with magnification, the inclusions shown in figure 8A came into focus, but the oval inclusion near the surface was blurred. C: The round dot in the middle is the same oval inclusion as in figure B, shown in reflected light. D: This oval inclusion in Zincite-S was also observed and photographed in situ *when Raman spectroscopy was performed. The colored dots represent analysis spots. Photomicrographs by Yujie Gao.*

peaks of CH_4. On the other hand, some peaks in the oval inclusion's spectra are the same as or similar to the peaks in Raman spectra of soot (e.g., Ramya et al., 2013; Kim et al., 2005; Sadezky et al., 2005). These are at 1580 cm^{-1} (same as the G band of soot), 1346 cm^{-1} (near the 1350 cm^{-1} D1 band), 1507 cm^{-1} (near the 1500 cm^{-1} D3 band), 2800–2900 cm^{-1} (near the 2700, 2900, and 3100 cm^{-1} Lorentz-shaped

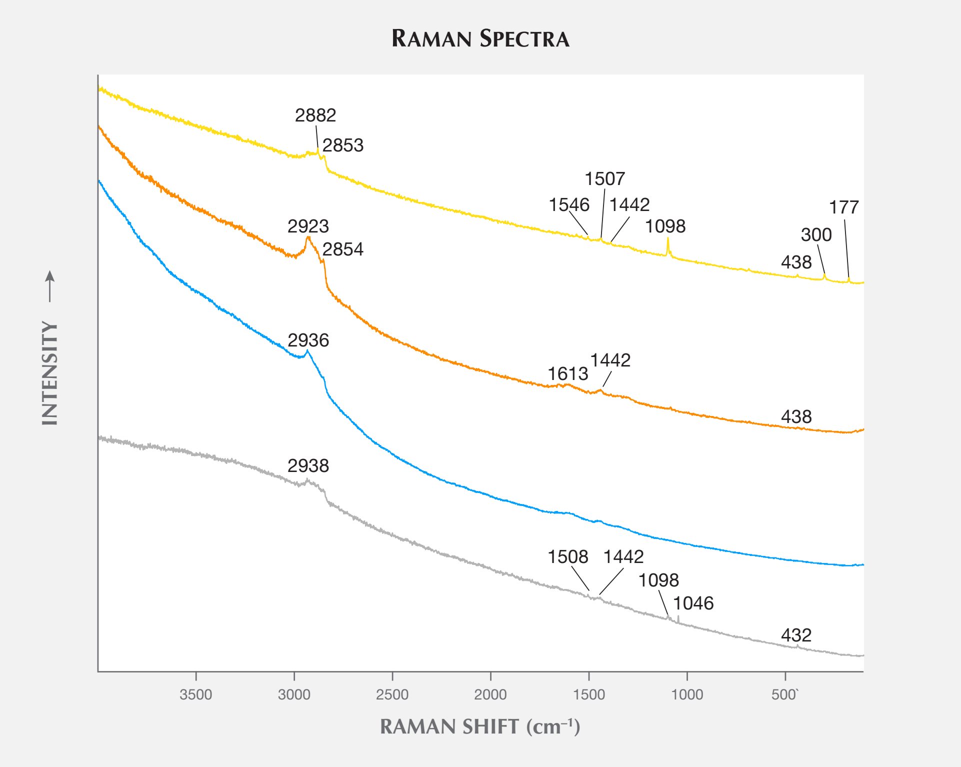

Figure 9. Raman spectra of the unusual oval inclusion in sample Zincite-S showed peaks at 2938, 2923, 2882, 2854, 1613, 1546, 1507, 1442, and 1098 cm^{-1}. These peaks indicated some carbon-bearing material stretching modes. The colors of the traces correspond to the analysis spots shown in figure 8D. Spectra are vertically shifted for clarity.

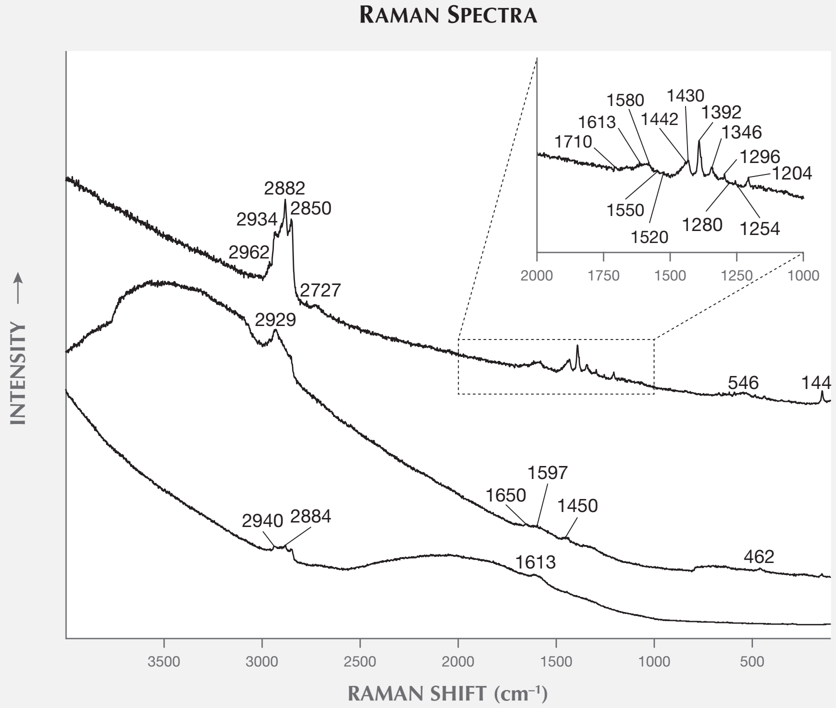

Figure 10. Raman spectra of the inclusion located on the cleavage plane of sample zin-fc showed peaks at 2929, 2882, 2850, 1613, 1580, 1430, 1392, 1346, 1296, and 1204 cm^{-1}. Spectra are vertically shifted for clarity.

bands), 1613 cm^{-1} (near 1620 cm^{-1}), and 1204 cm^{-1} (near 1200 cm^{-1}).

The Raman peaks of the oval inclusion more closely matched peaks of carbon-bearing soot than those of individual organic gases. Thus, the Raman results might be contributed mainly by soot and supported by some individual gases.

Figure 11. In the IR spectrum of rough sample zin-10, the peak at 438 cm^{-1} belongs to the zincite crystal, while a series of bands at 2850 and 2920 cm^{-1} indicate the C-H stretching mode of some possible carbon-bearing materials.

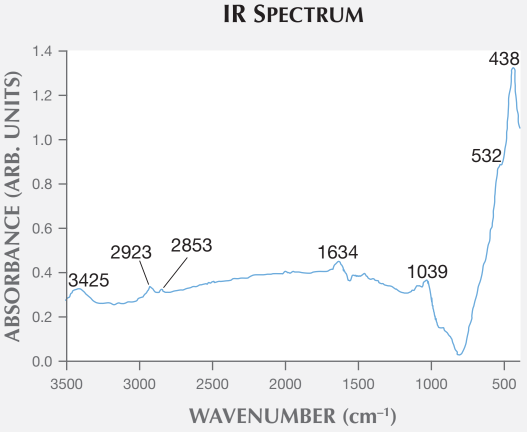

The oval inclusions reported by Nowak et al. (2007) and in this paper were quite different from the fluid inclusions, liquid film negative crystals, growth tubes, and cloud inclusions in natural zincite (Kawano, 2008). Although lab-grown synthetic zincite has not been reported for gemstone use, the oval inclusion composed of carbon-bearing materials (possibly soot and/or gases) might not occur in lab-grown zincite because of the accurately controlled original materials and reaction processes (Pasko et al., 1976; Nause and Nemeth, 2005; Karipidis et al., 2008).

CONCLUSIONS

The by-product synthetic zincite has much less manganese than natural zincite, and the causes of color of by-product synthetic and natural zincite crystals appear to be different. Besides Mn, the contents of other potential chromophores are also at levels low enough to indicate that the various colors of the by-product material may be affected by structure-related factors. Oval inclusions consistent with a previous report on by-product synthetic zincite were observed, and testing suggested they were soot and/or gases captured during the growth of host by-product synthetic zincite.

ABOUT THE AUTHORS

Mr. Zhang, a postgraduate student at the State Key Laboratory of Geological Processes and Mineral Resources at China University of Geosciences in Beijing at the time of this study, is currently a teaching assistant at the School of Gemology, Shanghai Jian Qiao University. Mr. Gao, a postgraduate student at the School of Gemology, China University of Geosciences in Beijing at the time of this study, is an assistant appraiser at National Gems & Artworks Appraisal Company Limited of Shenzhen. Dr. Shi (shigh@cugb.edu.cn) is a professor of gemology and mineralogy at the State Key Laboratory of Geological Processes and Mineral Resources at China University of Geosciences in Beijing.

ACKNOWLEDGMENTS

The authors would like to thank Prof. Pu Wang and Drs. Yingxin Liu, Mingyue He, Xiaoyan Yu,Ye Yuan, and Xuemei He at CUGB, along with Prof. Wenyi Xue at CAGS, for their help in analysis and discussions. Dr. Jie Li and Dr. Jihao Zhu at Key Laboratory of Submarine Geosciences of the Second Institute of Oceanography, State Oceanic Administration in Hangzhou, China, are thanked for their help with ICP-MS testing. Ms. Ling Du at the Shanghai laboratory of the NGTC is thanked for her assistance with XRF testing. The thoughtful and constructive comments by reviewers and editors are gratefully acknowledged. This research was partially supported by Grant No. 41373055 from the National Science Foundation of China.

REFERENCES

Crowningshield G.R. (1985) Gem Trade Lab Notes: Synthetic zincite. *G&G*, Vol. 21, No. 4, pp. 237–238.

Dickinson R.G., Dillon R.T., Rasetti F. (1929) Raman spectra of polyatomic gases. *Physical Review*, Vol. 34, No. 4, pp. 582–589, http://dx.doi.org/10.1103/PhysRev.34.582

Dong C.K., Han W.S., Kong B.H., Cho H.K., Hong C.H. (2007) Fabrication of the hybrid ZnO LED structure grown on p-type GaN by metal organic chemical vapor deposition. *Physica B: Condensed Matter*, Vols. 401–402, No. 4, pp. 386–390, http://dx.doi.org/10.1016/j.physb.2007.08.194

Dunn P.J. (1995) *Franklin and Sterling Hill, New Jersey: The World's Most Magnificent Mineral Deposits*. The Franklin-Ogdensburg Mineralogical Society.

Gahtar A., Benramache S., Benhaoua B., Chabane F. (2013) Preparation of transparent conducting ZnO:Al films on glass substrates by ultrasonic spray technique. *Journal of Semiconductors*, Vol. 34, No. 7, pp. 26–30.

Hague J.M., Baum J.L., Herrmann L.A., Pickering R.J. (1956) Geology and structure of the Franklin-Sterling area, New Jersey. *Bulletin of the Geological Society of America*, Vol. 67, No. 4, pp. 435–474, http://dx.doi.org/10.1130/0016-7606(1956)67%5B435:GASOTF%5D2.0.CO;2

Henderson E.P. (1945) Zincite. *G&G*, Vol. 5, No. 3, pp. 251–256.

Kammerling R.C., Johnson M.L. (1995) An examination of "serendipitous" synthetic zincite. *Journal of Gemmology*, Vol. 24, No. 8, pp. 563–568.

Karipidis T.K., Maltsev V.V., Volkova E.A., Chukichev M.V., Leonyuk N.I. (2008) Thermal stability of zincite single crystals. *Crystallography Reports*, Vol. 53, No. 2, pp. 326–330, http://dx.doi.org/10.1134/S1063774508020247

Kawano J. (2008) Research Lab. Report: Natural zincite GAAJ-ZENHOKYO Laboratory 2008.7.11, http://grjapan.ddo.jp/gaaj_report/2008/2008_07en.html

Kim U.J., Furtado C.A., Liu X., Chen G., Eklund P.C. (2005) Raman and IR spectroscopy of chemically processed single-walled carbon nanotubes. *Journal of the American Chemical Society*, Vol. 127, No. 44, pp. 15437–15445, http://dx.doi.org/10.1021/ja052951o

Kortounova E.V., Lyutin V.I., Dubovskaya V.D., Chvanski P.P. (2001) The growth of zinc oxide crystals with impurities. *High Pressure Research*, Vol. 20, No. 1–6, pp. 175–183, http://dx.doi.org/10.1080/08957950108206165

Liang H.K., Yu S.F., Yang H.Y. (2010) Directional and controllable edge-emitting ZnO ultraviolet random laser diodes. *Applied Physics Letters*, Vol. 96, No. 10, pp. 101116–101116-3, http://dx.doi.org/10.1063/1.3356221

Mikami M., Eto T., Wang J., Masa Y., Isshiki M. (2005) Growth of zinc oxide by chemical vapor transport. *Journal of Crystal Growth*, Vol. 276, No. 3–4, pp. 389–392, http://dx.doi.org/10.1016/j.jcrysgro.2004.11.431

Nause J., Nemeth B. (2005) Pressurized melt growth of ZnO boules. *Semiconductor Science and Technology*, Vol. 20, No. 4, pp. S45–S48, http://dx.doi.org/10.1088/0268-1242/20/4/005

Nowak J.W., Braithwaite R.S.W., Nowak J., Ostojski K., Krystek M., Buchowiecki W. (2007) Formation of large synthetic zincite (ZnO) crystals during production of zinc white. *Journal of Gemmology*, Vol. 30, No. 5/6, pp. 257–267.

Pasko P.G., Kidyarov B.I., Avdienko K.I. (1976) Influence of the vapor phase composition and reagent flow on the growth mechanism and morphology of ZnO crystals. *Journal of Crystal Growth*, Vol. 33, No. 2, pp. 298–302, http://dx.doi.org/10.1016/0022-0248(76)90056-7

Peck W.H., Volkert R.A., Mansur A.T., Doverspike B.A. (2009) Stable isotope and petrologic evidence for the origin of regional marble-hosted magnetite deposits and the zinc deposits at Franklin and Sterling Hill, New Jersey highlands, United States. *Economic Geology*, Vol. 104, No. 7, pp. 1037–1054, http://dx.doi.org/10.2113/econgeo.104.7.1037

Ramya K., John J., Manoj B. (2013) Raman spectroscopy investigation of camphor soot: Spectral analysis and structural information. *International Journal of Electrochemical Science*, Vol. 8, pp. 9421–9428.

Sadezky A., Muckenhuber H., Grothe H., Niessner R., Pöschl U. (2005) Raman microspectroscopy of soot and related carbonaceous materials: spectral analysis and structural information. *Carbon*, Vol. 43, No. 8, pp. 1731–1742, http://dx.doi.org/10.1016/j.carbon.2005.02.018

Soci C., Zhang A., Xiang B., Dayeh S.A., Aplin D.P.R., Park J., Bao X.Y., Lo Y.H., Wang D. (2007) ZnO nanowire UV photodetectors with high internal gain. *Nano Letters*, Vol. 7, No. 4, pp. 1003–1009, http://dx.doi.org/10.1021/nl070111x

Webster R. (1983) *Gems: Their Sources, Descriptions and Identification*, 4th ed. Revised by B.W. Anderson, Butterworth-Heinemann Ltd., London.

Welch F.S. (2008) Identification of 1850s brown zinc paint made with franklinite and zincite at the U.S. Capitol. *APT Bulletin*, Vol. 39, No. 1, pp. 17–30, http://dx.doi.org/10.2307/25433934

Wilson W.E. (2013) The best zincite specimens from Franklin, New Jersey. *The Mineralogical Record*, Vol. 44, No. 5, pp. 509–534.

Zhao J., Jin Z.G., Li T., Liu X.X. (2006) Preparation and characterization of ZnO nanorods from NaOH solutions with assisted electrical field. *Applied Surface Science*, Vol. 252, No. 23, pp. 8287–8294, http://dx.doi.org/10.1016/j.apsusc.2005.10.050

G&G Lab Notes

Editors
Thomas M. Moses | Shane F. McClure

Three Faceted COLLECTOR SPECIMENS

Three stones recently submitted to GIA (figure 1) were found to be rare mineral species that had not previously been examined at the Carlsbad laboratory. Standard gemological testing and Raman analysis identified these specimens as wagnerite, thaumasite, and strontianite.

Figure 1. Left to right: 0.60 ct golden yellow wagnerite, 1.72 ct colorless thaumasite, and 1.41 ct pale yellow strontianite.

A 0.60 ct transparent golden yellow pear brilliant cut with vitreous luster was identified as the phosphate monoclinic crystal wagnerite, $(Mg,Fe^{2+})_2(PO_4)F$. Though uncommon, wagnerite occurs in various geologic settings, such as granitic pegmatites, gneisses, eclogites, and hydrothermal environments (P. Korbel and M. Novak, *The Complete Mineral Encyclopedia*, Gramercy, Lisse, the Netherlands, 2003). It had a specific gravity (SG) of 3.15, a refractive index (RI) of 1.568–1.580, and a biaxial positive optic nature. Wagnerite is a relatively soft and brittle mineral with a Mohs hardness of 5.0–5.5. The stone was inert under both long-wave and short-wave UV radiation. Multiphase fluid inclusions, fingerprints, graining, and color zoning features were observed with magnification.

The largest stone, a 1.72 ct transparent colorless octagonal step cut, had a relatively low SG of 1.90, an RI of 1.470–1.515, and a biaxial negative optic nature. It was inert to long-wave and short-wave UV. These properties, along with Raman testing, led to its identification as thaumasite, a silicate mineral with the chemical formula $Ca_3(SO_4)[Si(OH)_6](CO_3)\cdot 12H_2O$ belonging to the hexagonal crystal system. Magnification revealed strong doubling, spectacular radiating fibrous inclusions, reflective films, tiny crystal inclusions, and strong hexagonal angular graining. Thaumasite has a vitreous luster and a brittle nature due to its low hardness of 3.5 on the Mohs scale. Thaumasite occurs in geothermal waters or seawaters reacting with basalt and tuffs, or in areas of contact metamorphism (J.W. Anthony et al., *Handbook of Mineralogy: Volume II: Silica, Silicates: Part 2*, Mineral Data Publishing, Tucson, Arizona, 1995, p. 790).

The last stone we observed was a transparent pale yellow octagonal step cut with vitreous luster. It proved to be strontianite, $SrCO_3$, an orthorhombic carbonate mineral member of the aragonite group with a Mohs hardness of 3.5. The 1.41 ct specimen was highly birefringent, with an RI of 1.511–1.661, an SG of 3.76, and a biaxial negative optic nature. It fluoresced red under long-wave UV but displayed a weak whitish reaction under short-wave UV. The stone exhibited strong doubling and fluid inclusions under magnification. Raman spectroscopy confirmed its identity. Strontianite occurs together with calcite and zeolites in hydrothermal, low-temperature veins and in cavities of volcanic rocks (Korbel and Novak, 2003).

Wagnerite, thaumasite, and strontianite are rarely seen as faceted gems due to their softness and brittleness. These collector specimens were the first of their kind to be submitted to

Editors' note: All items were written by staff members of GIA laboratories.

Gems & Gemology, Vol. 53, No. 1, pp. 90–101.

GIA's Carlsbad laboratory for testing. Although challenging to identify without advanced testing techniques, they bring excitement to gemologists searching for unusual faceted gems.

Jonathan Muyal and Nicole Ahline

Unusual Dark Orangy Red CORDIERITE

The New York lab recently examined the transparent dark orangy red cordierite shown in figure 2. Cordierite, a magnesium aluminum cyclosilicate with the formula $Mg_2Al_4Si_5O_{18}$, is better known by its gemological name of iolite, which comes from the Greek *ios* (violet). The term is reserved for the violet through slightly violetish blue gem-quality variety of cordierite. Iolite's typical colors have been compared to blue sapphires and tanzanites. These colors are thought to come from the charge transfer between Fe^{2+} and Fe^{3+} ions.

The stone's RI ranged from 1.515 to 1.547, with a birefringence of 0.037. This refractive index is much lower than what is listed in the literature for iolite, and we believe the discrepancy is due to the stone's lower Fe content. SG was measured as 2.56. The stone showed strong trichroism ranging from orangy red to dark brown to purple. There was no fluorescence observed with exposure to long- and short-wave UV. Raman spectroscopy using 514 nm laser excitation conclusively identified the stone as cordierite (figure 3) with a strong match to the cordierite spectra in the RRUFF database (http://rruff.info).

Figure 2. This 8.13 ct cordierite had an unusual dark orangy red color.

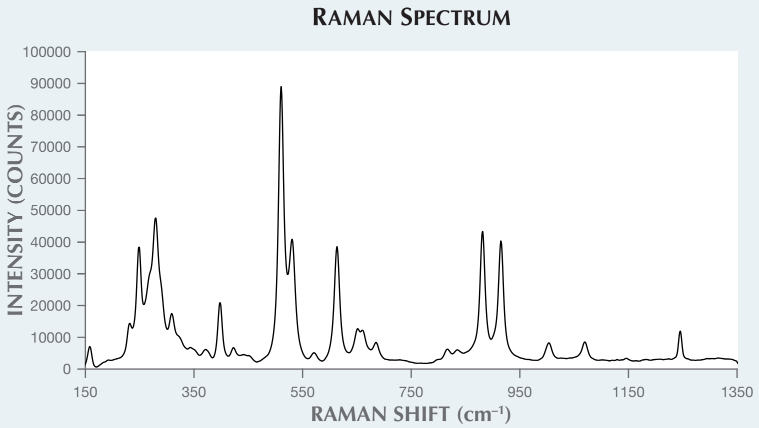

Figure 3. Raman spectroscopy identified the orangy red stone as a cordierite.

Microscopic examination with fiber-optic illumination revealed fingerprints, rows of flaky whitish inclusions, and large fractures throughout the stone that had been filled with an unknown clarity-enhancing material (figure 4). The larger surface-reaching fractures in the stone appeared to have a "heat wave" appearance (figure 4B), that could be characteristic of the clarity-enhancing material. Cordierite, which is structurally similar to beryl, will easily develop fractures and is commonly clarity enhanced with oil-based fluids. Both cordierite and beryl are structurally similar in that they are cyclosilicates,

Figure 4. Various inclusions within the dark orangy red cordierite. Numerous partially enhanced fractures are visible (B), along with low visibility on the surface (D). Field of view 4.77 mm (A), 14.48 mm (B), 3.57 mm (C), and 3.57 mm (D).

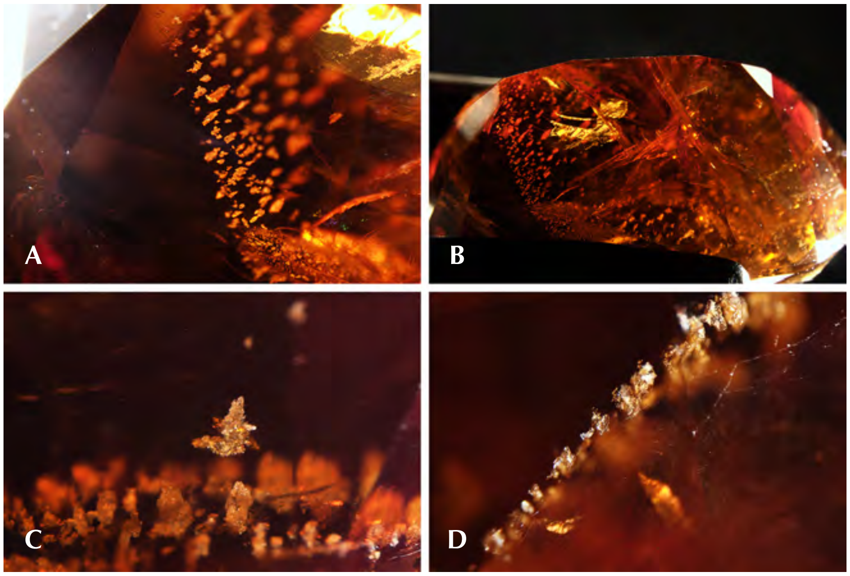

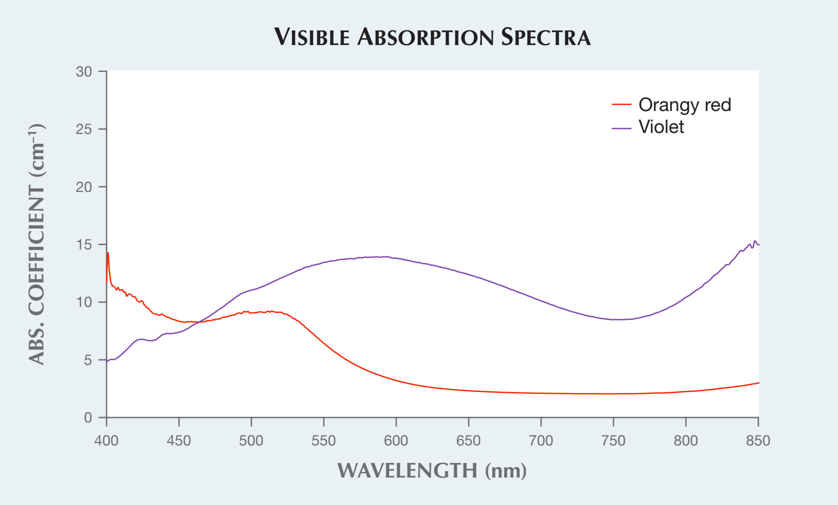

Figure 5. In these visible absorption spectra, notice the large window between 600 and 800 nm for the orangy red cordierite sample and the absorption band centered at 580 nm for the GIA reference spectrum of violet iolite.

containing linked six-member rings of tetrahedra that result in channels within the crystal structure. These channels are capable of trapping water along with cations such as from the alkali and alkaline earth metals. The high water content within the stone was represented by the strong overtone bands seen in the Fourier-transform infrared (FTIR) spectrum, with very similar features to that of hydrothermal natural beryl spectra. Laser ablation–inductively coupled plasma–mass spectrometry (LA-ICP-MS) detected trace levels of alkali and alkaline metals.

A similar red cordierite, examined in December 2015, was said to be from the Iakora district of Fianarantsoa Province in southeast Madagascar (Spring 2016 GNI, pp. 97–98). The visible absorption spectrum we observed was similar to the one described by Fritsch et al. (figure 5). The spectrum had a decrease in absorption in the 400–500 nm region and low absorption between 600 and 800 nm, resulting in a transmittance window in the orange to red region that produced the color of the stone. These regions of low absorption are characteristic of the trichroic color components noted in the stone. We compared this visible spectrum to a GIA reference spectrum of ordinary iolite. The violet color of iolite is produced by a strong absorption band centered at approximately 580 nm, resulting from intervalence charge transfer to either valence state of Fe cations that might have occupied the divalent and trivalent sites in the crystal structure (substituting for Mg and Al, respectively; see M. O'Donoghue, *Gemstones*, Chapman and Hall Ltd., London, 1988, p. 77). Although the red cordierite contained a considerable amount of iron, this charge transfer did not appear to be taking place. The potential causes of the color are still unknown but can be linked to manganese (up to 486 ppmw in the orangy red sample and 248 ppmw in the violet sample) or iron, both of which were detected by LA-ICP-MS. This orangy red cordierite appeared to have roughly half as much iron as a saturated violet iolite (approximately 25,000 and 40,000 ppmw, respectively). No other transition metals varied significantly between the orangy red and violet samples. Regardless of the origin of color for the orangy red cordierite, naming this variety "iolite" could be misleading according to the definition of the term.

This is the first time GIA has encountered a cordierite of this color.

Augusto Castillo and Akhil Sehgal

Cape DIAMOND with Yellow Phosphorescence

Phosphorescence in a cape diamond is very rare, especially after exposure to long-wave UV light. The New York laboratory recently examined a cape diamond exhibiting yellow phosphorescence after exposure to a long-wave UV source. The 0.75 ct Faint yellow-green round brilliant is shown in figure 6.

Cape absorption peaks were observed at 415 and 477 nm, along with a GR1 peak (figure 7, left). The IR spectrum confirmed that this was a type Ia diamond, with nitrogen aggregates detected in the one-phonon region. Hydrogen-related peaks were also detected at 1405, 2785, 3107, 3237, 4169, and 4496 cm^{-1}. Brown radiation stains were found on the girdle. The diamond contained contacted partially graphitized omphacite crystals with cuboctahedral morphology (figure 7, right). Strong blue fluorescence and medium yellow phosphorescence were observed under a desktop long-wave UV light source. Under short-wave UV, medium yellow fluorescence was noted but phosphorescence was absent. DiamondView imaging (<225 nm excitation) also showed greenish blue fluorescence but no phosphorescence. Fiber-optic illumination revealed the blue "transmission" luminescence that occurs when a

Figure 6. This yellow-green 0.75 ct cape diamond displayed yellow phosphorescence to long-wave UV light.

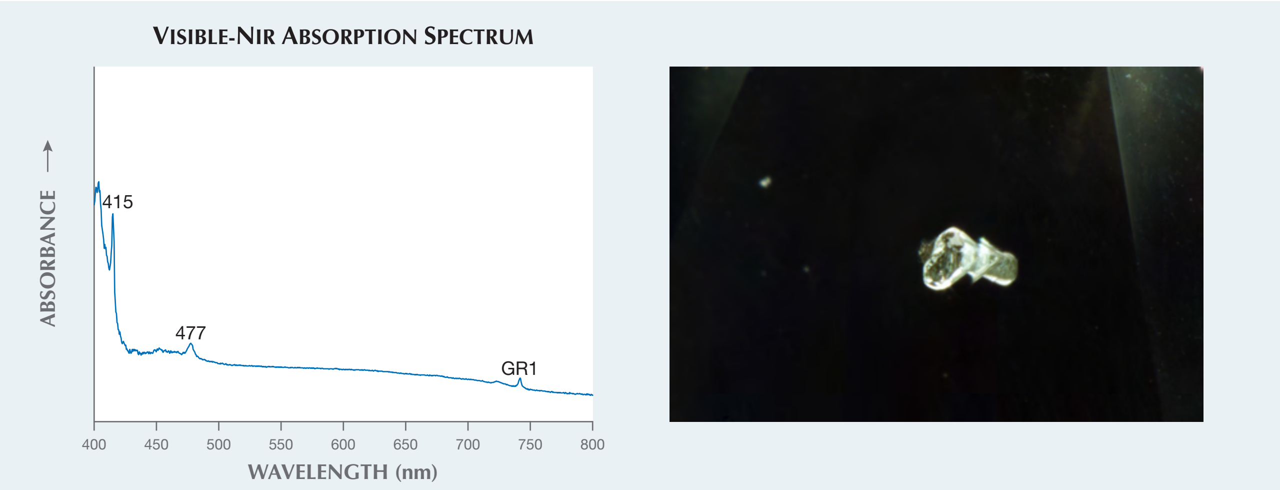

Figure 7. The diamond displayed "cape" absorption peaks at 415 and 477 nm along with a GR1 peak (left). It contained contact crystal inclusions of green omphacite (right; field of view 1.41 mm).

strong light travels through a diamond. The UV-Vis spectrum of such diamonds shows an absorption peak at 415 nm and a luminescence peak at the lower energy end of the peak. Such is the case with this stone.

Nearly 30 years ago, a bicolor diamond with a near-colorless central portion and light yellow tips was reported in *G&G* (Winter 1989 Lab Notes, p. 237). It showed very weak chalky yellow phosphorescence for approximately 10 seconds after the long-wave UV lamp was turned off. This yellow phosphorescence was observed throughout the stone regardless of its bicolor nature. Its central colorless region exhibited weak cape lines and strong blue transmission, similar to the green diamond in this note. Unlike our sample, the bicolor diamond also showed very weak yellow phosphorescence to short-wave UV. A chameleon diamond may display strong yellow phosphorescence to a long-wave UV light source (Summer 1992 Lab Notes, p. 124; Spring 2000 Lab Notes, pp. 60–61). Our sample was not a chameleon diamond, however.

Greenish yellow phosphorescence in a chameleon diamond has been systematically measured using a spectrometer (see S. Eaton-Magaña et al., "Fluorescence spectra of colored diamonds using a rapid, mobile spectrometer," Winter 2007 *G&G*, pp. 332–351). The peak maximum recorded for the chameleon diamond was 557 nm. We used an Ocean Optics USB2000 charge-coupled device (CCD) spectrometer similar to the one described in Eaton-Magaña et al. (2007), but with a different UV source. In place of a deuterium source, we used

Figure 8. Phosphorescence spectra (left) show a peak maximum at 570 nm, which is responsible for the cape diamond's yellow phosphorescence. Shown on the right is the phosphorescence decay curve at 570 nm.

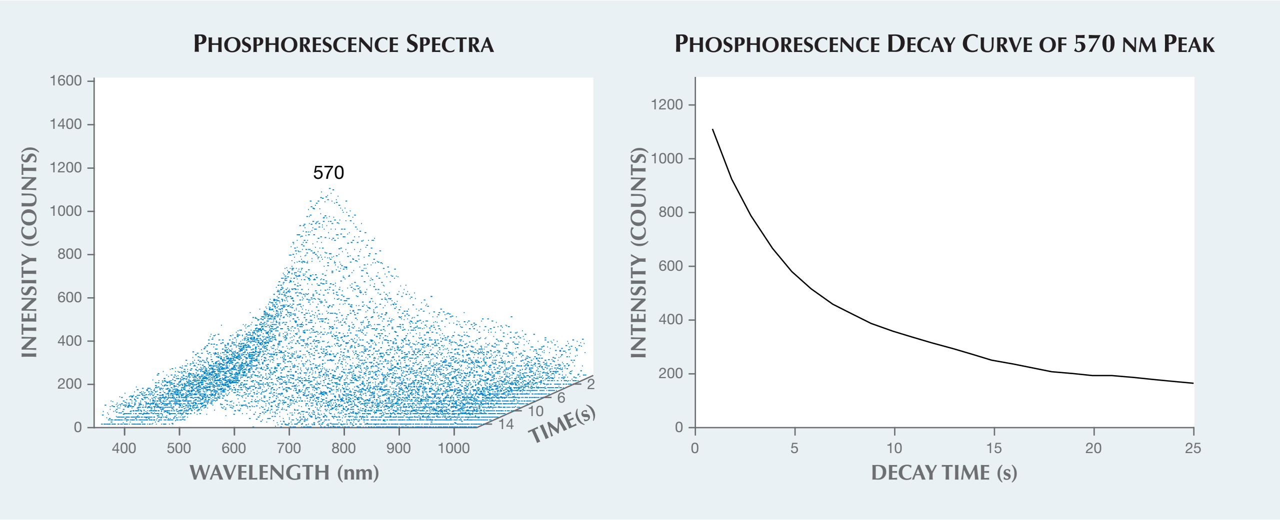

GIA's new LED desktop long-wave UV (365 nm excitation) light source. A broad peak at approximately 570 nm, which is responsible for the yellow phosphorescence, was observed in the emission spectra (figure 8, left). The phosphorescence decay curve at 570 nm, representing the rate of decreasing intensity with time, is plotted in figure 8 (right). Half-life is defined as the time required for the initial peak intensity to decrease to one-half its original value (again, see Eaton-Magaña et al., 2007). The half-life value measured for our sample was 5.0 seconds.

Yellow phosphorescence is a very rare feature in cape diamonds. The defect responsible for this optical feature remains unknown.

Kyaw Soe Moe, Jon Neal, and Paul Johnson

Pink SAPPHIRE Filled with Bismuth-Based Glass

Recently, GIA's Bangkok laboratory received a 2.77 ct light pink sapphire (figure 9) for an identification report. The sample was a semi-transparent cabochon with natural inclusion features: silk needles and particles, twinned planes, and thin films. Also observed throughout the stone were numerous gas bubbles of various shapes and sizes that were trapped along surface-reaching fractures and cavities (figure 10). These indicate the presence of glass filling. However, no flash effect was evident in the filled fractures. The stone's RI of 1.76 and UV fluorescence reaction (medium red to long-wave and weak red to short-wave) were consistent with corundum. Its SG of 3.87 was lower than that of corundum and possibly a result of the filler. Due to the sapphire's very light color, its visible-range absorption spectrum was difficult to observe.

Figure 9. This 2.77 ct light pink sapphire cabochon was treated with a bismuth-based glass filling.

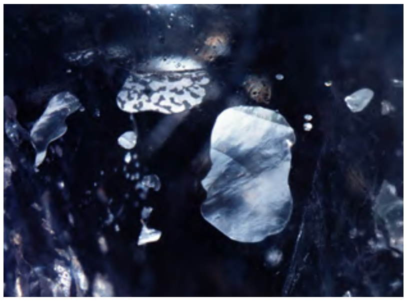

Figure 10. With the aid of fiber-optic illumination, magnification revealed these trapped gas bubbles of various shapes and sizes in the light pink sapphire. Field of view 2.00 mm.

Qualitative chemical analysis using energy-dispersive X-ray fluorescence (EDXRF) spectroscopy showed the presence of bismuth in addition to the expected Al, Cr, Fe, and Ga. No lead was detected in the sample, even with the aid of the thick palladium filter. The chemical composition of the filler indicated that the stone had undergone fracture filling using bismuth-based glass ("Ruby treatments – revisited, with Mozambique's perspective," *Lab Information Circular*, Gem Testing Laboratory, Vol. 63, December 2011). Due to the large difference in refractive indices between the bismuth-based glass filled area and the surrounding corundum, this treatment was easier to visually detect than lead-glass filling (figure 11).

Figure 11. Under reflected illumination, the pink sapphire's large cavity filling was readily visible with the unaided eye. Field of view 2.70 mm.

Fracture filling with lead glass and non-lead glass has been widely used in low-grade ruby (S.F. McClure et al., "Identification and durability of lead glass–filled rubies," Spring 2006 *G&G*, pp. 22–34). Pink sapphires such as this 2.77 ct stone are less commonly encountered in the laboratory for examination and identification.

Ratima Suthiyuth

First Observation of H4 Defect in CVD SYNTHETIC DIAMOND

Diamond consists of a relatively simple lattice of carbon atoms wherein only a few impurities can substitute into the structure. Despite the apparent simplicity, the diversity of defects that can exist in the diamond lattice is astounding. Nitrogen is the most abundant impurity in diamond; one of the defects commonly seen in natural diamonds, the H4 defect, consists of four nitrogen atoms and two vacancies. It is strongly associated with B-aggregated nitrogen impurities, which consist of four nitrogen atoms surrounding a single vacancy. H4 is created through a fairly straightforward formation mechanism where a single vacancy is trapped adjacent to a B-aggregate of nitrogen. H4 is often seen in irradiated and annealed diamonds with suitable amounts of B-form nitrogen, and is a mature aggregate of nitrogen that is very difficult to achieve in synthetic diamond growth or even post-growth treatment.

We were very surprised to observe an H4 peak at 496 nm in a pink synthetic diamond grown by chemical vapor deposition (CVD) that was recently submitted to GIA's Carlsbad laboratory for a synthetic colored diamond grading report. This 0.26 ct

Figure 12. This 0.26 ct pink synthetic diamond contains the first H4 defect GIA has observed in a CVD synthetic diamond.

round brilliant (figure 12) was type Ib (single substitutional nitrogen impurities) with a very low total nitrogen content and no detectable A or B form nitrogen. FTIR spectroscopy also showed a peak at 3107 cm^{-1}, indicating the presence of a defect consisting of three nitrogen atoms surrounding a vacancy along with a hydrogen atom.

In addition to the observation of the H4 defect (figure 13, left), the synthetic nature of the sample was revealed by the 737 nm SiV$^-$ defect in the photoluminescence (PL) spectrum (figure 13, right). The presence of (subtle) growth layers in the DiamondView fluorescence images provided further confirmation. This diamond was grown using gas that was doped with nitrogen, allowing its incorporation into the diamond lattice as single substitutional nitrogen. The pink color was produced by NV$^-$ centers created during post-growth irradiation and annealing treatment. Nitrogen aggregation from single substitutional nitrogen to the more complex B-form nitrogen requires very high temperatures and pressures: 2500°C and 9.5 GPa for several hours (I. Dobrinets et al., *HPHT-Treated Diamonds: Diamonds Forever*, Springer Science & Business Media, 2013, p. 41) and generally requires a high starting concentration of nitrogen. This CVD synthetic diamond had low total nitrogen content and was grown under vacuum and likely irradiated and annealed at atmospheric pressure, making the occurrence of H4 even more puzzling. It is possible that the H4 was created during the irradiation and annealing process, but among the many samples GIA has examined, this was the first observation of this defect in a CVD synthetic diamond.

Troy Ardon and
Christopher M. Breeding

HPHT Synthetic Diamond Melee Without Si or Ni Defects

Near-colorless synthetic diamond melee grown using the high-pressure, high-temperature (HPHT) method have created significant concern in the industry, and various screening methods have been developed to take into account their most reliable distinguishing features. In general, the specimens described in previous Lab Notes (e.g. Summer 2015, pp. 183–184) were very small round faceted goods ranging between 0.005 and 0.01 ct.

Figure 14. These four near-colorless round brilliant melee were identified as HPHT synthetic diamonds lacking the typical Si- and Ni-related defects.

Recently GIA's Bangkok laboratory received four loose near-colorless round brilliants for quality assurance service (figure 14). They weighed between 0.07 and 0.09 ct, slightly more than previously submitted melee. All were identified as type IIb HPHT-grown material using FTIR spectrometry. Their most interesting feature was the absence of silicon- or nickel-related emission peaks when analyzed

Figure 13. Photoluminescence spectra of the pink CVD synthetic diamond showed the occurrence of an H4 defect (left) as well as a SiV$^-$ defect (right).

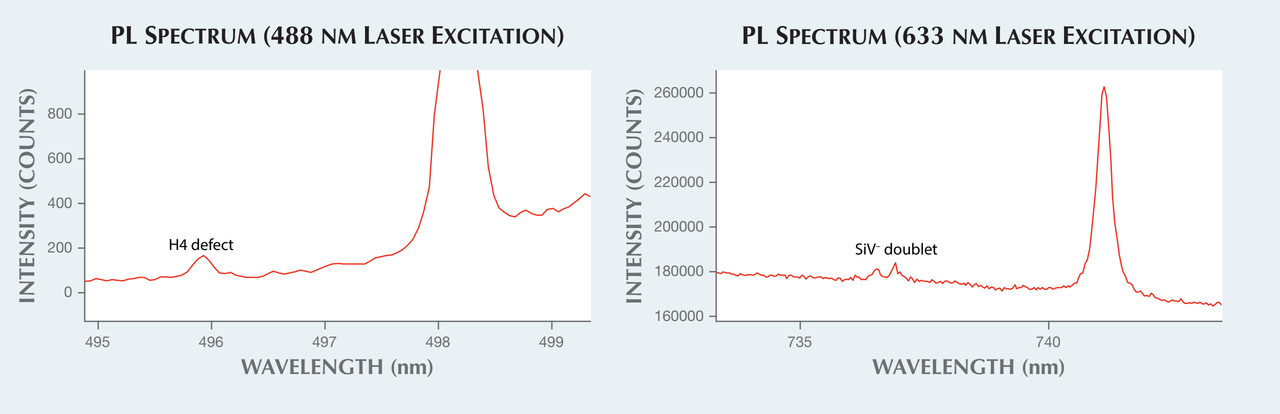

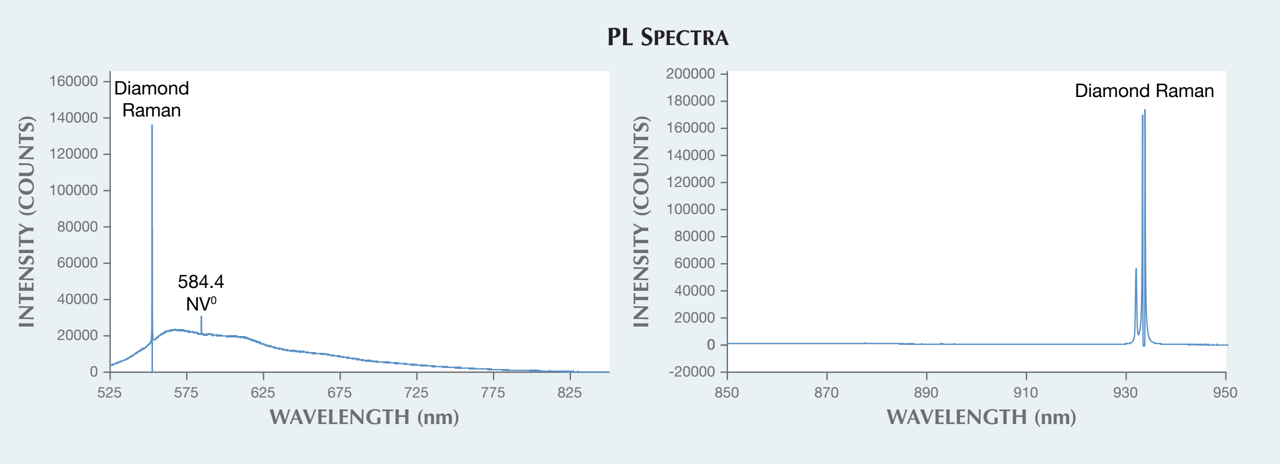

Figure 15. The PL spectra features observed at liquid nitrogen temperature lacked the 736.6/736.9 nm emission doublet related to the SiV^- defect (left, 514 laser excitation) and the Ni-related defect doublet at 883/884 nm (right, 830 nm laser excitation).

at liquid nitrogen temperature by PL spectroscopy (figure 15). The spectra typically observed in HPHT synthetic diamonds show an emission doublet related to the negatively charged silicon split-vacancy defect SiV^- at 736.6/736.9 nm and an associated Ni-related defect at 883.0/884.7 nm (Summer 2015 Lab Notes, pp. 183–185).

The growth patterns observed in the DiamondView were an identifying feature that did remain the same. The characteristic angular growth patterns and blue-green fluorescence, together with an associated green phosphorescence, still provide important evidence that aid in the separation of natural and synthetic diamonds (figure 16). Examination with a gemological microscope revealed metallic and rod-like inclusions (figure 17) that also assisted in identifying these melee as synthetic diamonds.

The study of these four melee-size HPHT synthetic diamonds revealed atypical PL spectra. However, other means of identification (inclusions, growth patterns as seen via the DiamondView, and their phosphorescence reactions) still played an important role in their identification. It is interesting to note that HPHT synthetic melee diamonds being submitted to GIA for identification are getting larger, indicating the continuous improvement of synthetic technology.

Piradee Siritheerakul and Wuyi Wang

Figure 16. These DiamondView fluorescence and phosphorescence images of a 0.081 ct sample show growth patterns characteristic of HPHT synthetic diamond.

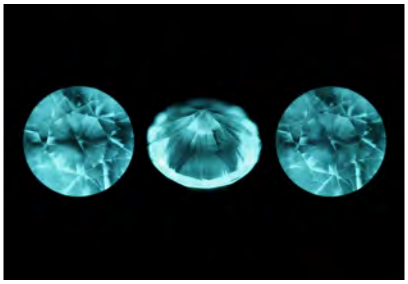

Figure 17. Darkfield illumination reveals rod-like inclusions in a 0.087 ct HPHT-grown melee diamond.

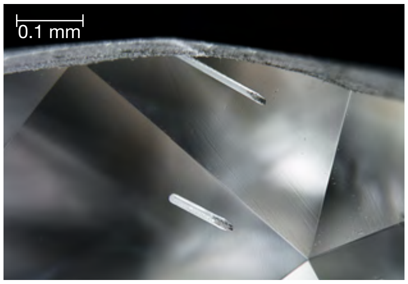

HPHT Synthetic Diamond with Intense Green Color

HPHT-grown synthetic diamonds are predominantly colorless, yellow, and blue, depending on the control of impurities during growth. Other colors are very rare. In this study, we report on an intensely colored green HPHT synthetic diamond identified in the New York laboratory.

This square-cut synthetic diamond, which weighed 0.42 ct and measured 4.42 × 4.34 mm with a depth of 2.59 mm, was graded as Fancy Deep green (figure 18). Initial observation revealed strong color zoning with narrow, colorless growth sectors on the pavilion that were visible without magnification. An abundance of small metallic inclusions observed under magnification (figure 19) caused the sample to exhibit magnetism. Magnetism is a common but not diagnostic feature in HPHT synthetic diamonds. Natural diamonds may also exhibit magnetism, though only in extremely rare cases (G.R. Rossman and J.L. Kirschvink, "Magnetic properties of gem-quality synthetic diamonds," Fall 1984 *G&G*, pp. 163–166).

Upon further examination, the diamond was determined to be type IIb (containing the impurity boron), as seen from its mid-FTIR absorption spectrum (figure 20). The concentration of uncompensated boron in this diamond was 0.013 ± 0.003 ppma.

Figure 18. This 0.42 ct green HPHT synthetic diamond displayed strong growth sectors that were observed without magnification.

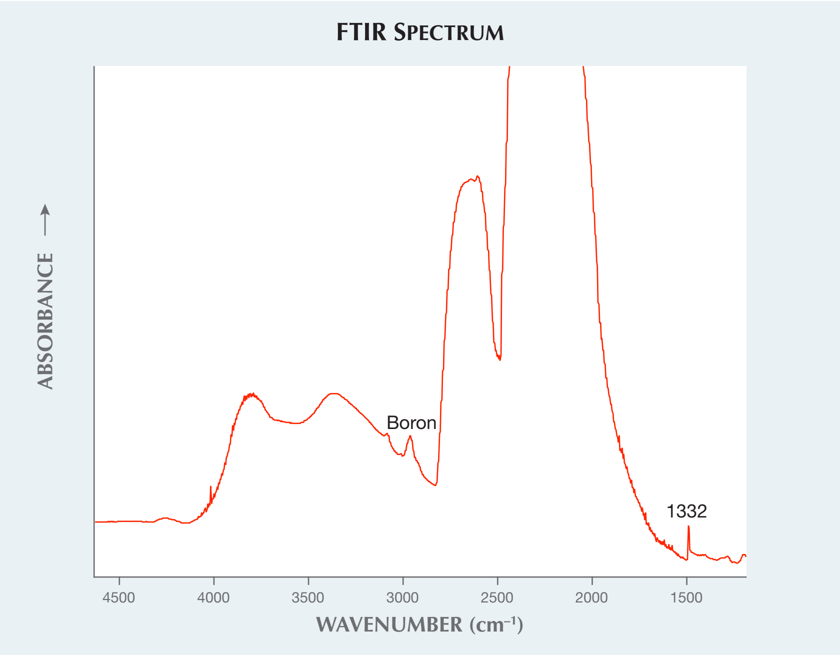

Figure 20. The green synthetic diamond's mid-FTIR spectrum, which determined that the material was type IIb, showed an uncompensated boron concentration at ~0.013 ppma.

This amount, though detectable, did not contribute to the green color. Many synthetic diamonds grown by New Diamond Technology (NDT) in Russia reportedly also contain this level of boron impurity, as it is incorporated during the growth process (B. Deljanin et al., "NDT breaking the 10 carat barrier," *Contributions to Gemology*, No. 15, 2015). DiamondView imaging revealed the typical hourglass growth structure of HPHT synthetic diamonds (figure 21), along with extremely strong phosphorescence for which the presence of boron might be responsible. Noted in the FTIR spectrum was an absorption feature related to nitrogen impurity, a relatively strong peak at 1332 cm^{-1} caused by N$^+$. It is unusual to see such features in today's synthetic diamonds. A UV-Vis-NIR absorption spectrum showed strong nickel-related absorption, with a band observed at ~685 nm (figure 22). This center, due to a Ni$^+$ interstitial vacancy, creates a "transparent" window at approximately 555–585 nm, resulting in an observed green color. This diamond was most likely HPHT treated post-growth to activate the Ni$^+$ and cause this intense absorption. It is very rare to see HPHT synthetic diamond with an intense green color attributed to a nickel-related impurity.

In addition to boron and nickel, this synthetic diamond also contained the SiV$^-$ impurity in its crystal lattice. Recent studies have shown that while this impurity is common in CVD-grown diamonds, it may also be observed in HPHT-grown diamonds (U.F.S. D'Haenens-Johansson et al., "Near-colorless HPHT synthetic diamonds from AOTC Group," Spring 2014 *G&G*, pp. 30–45). The distribution of Si and Ni impurities were mapped using Raman mapping techniques, and the results proved consistent with previous studies of near-colorless HPHT-grown diamonds also observed in the trade (P. Johnson et al., "Discovery and distribution of the [Si-

Figure 19. The green synthetic diamond displayed strong magnetism, caused by abundant metallic inclusions. Field of view ~1.4 mm.

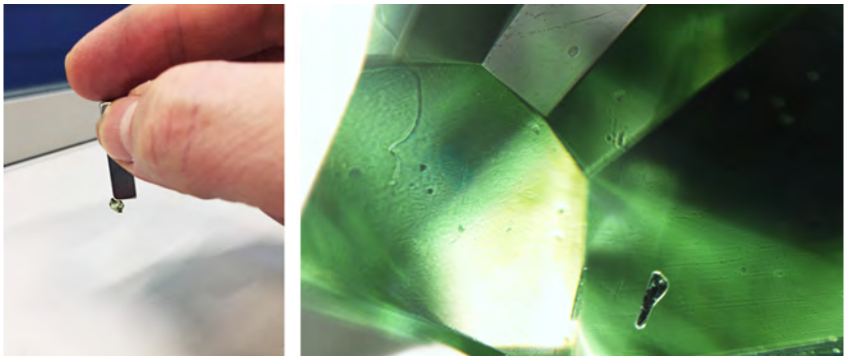

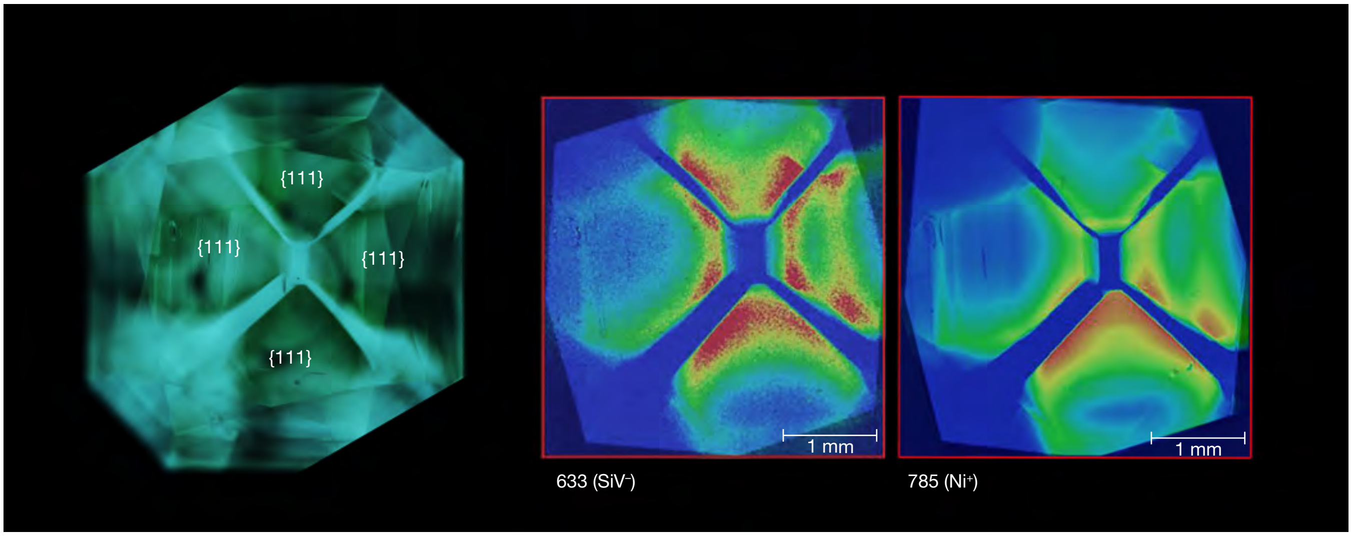

Figure 21. An oriented DiamondView image (left) and 633 and 785 nm PL maps (right) show the SiV$^-$ and Ni$^+$ defects confined to the {111} growth sectors.

V]- defect in HPHT-grown gem-quality diamonds," 2015 GSA Annual Meeting, paper No. 300-12), with both the Ni$^+$ and SiV$^-$ confined to the {111} growth sectors. Typically observed in HPHT-grown diamonds, these {111} sectors are the most developed and dominate the diamond crystal's morphology. The SiV$^-$ center does not contribute to the color of these synthetic diamonds, and it is either intentionally or unintentionally incorporated during crystal growth (again, see figure 21).

These spectroscopic and gemological features, with the exception of the green color resulting from nickel, were consistent with typical HPHT synthetic diamond. This is the first instance in which nickel has been reported to contribute to the deep green color of a synthetic diamond. This finding could indicate a new development in growth technology and a new material making its way into the diamond trade. This example was submitted as an undisclosed synthetic diamond and was subsequently issued an identification report.

Figure 22. The HPHT synthetic diamond's UV-Vis-NIR spectrum displayed a very intense Ni-related absorption.

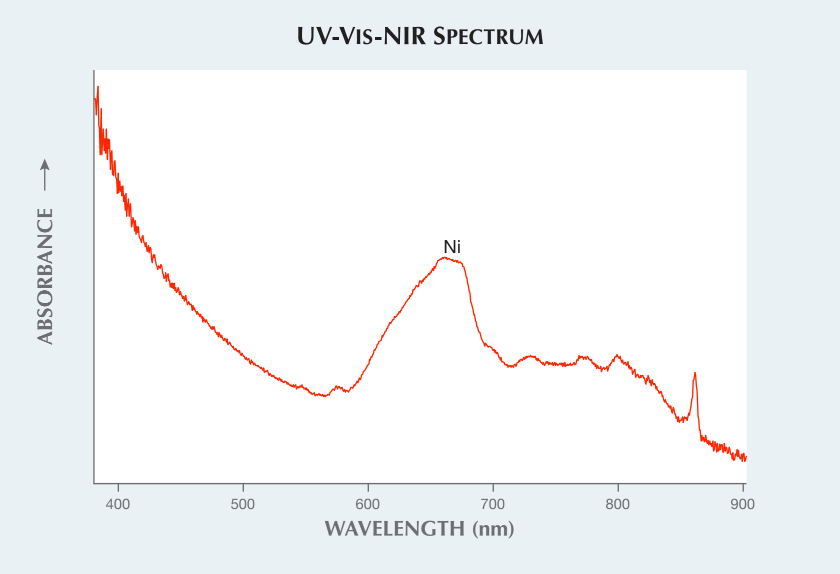

Developments in synthetic diamond growth technologies (both CVD and HPHT) continue to emphasize the need for careful observation and testing techniques to identify the new types of materials encountered in the gem trade today.

Paul Johnson and Elina Myagkaya

Multi-Elemental Diffused and Melt-Grown SYNTHETIC SAPPHIRE

GIA's Carlsbad laboratory examined a 4.21 ct faceted blue oval. Standard gemological testing determined that the stone was uniaxial negative and had an RI of $n_\varepsilon = 1.759$ and $n_\omega = 1.769$, with a corresponding birefringence of 0.010. Hydrostatic SG was measured as 4.00. The stone was inert to long-wave UV and showed medium chalky blue color to short-wave UV. These

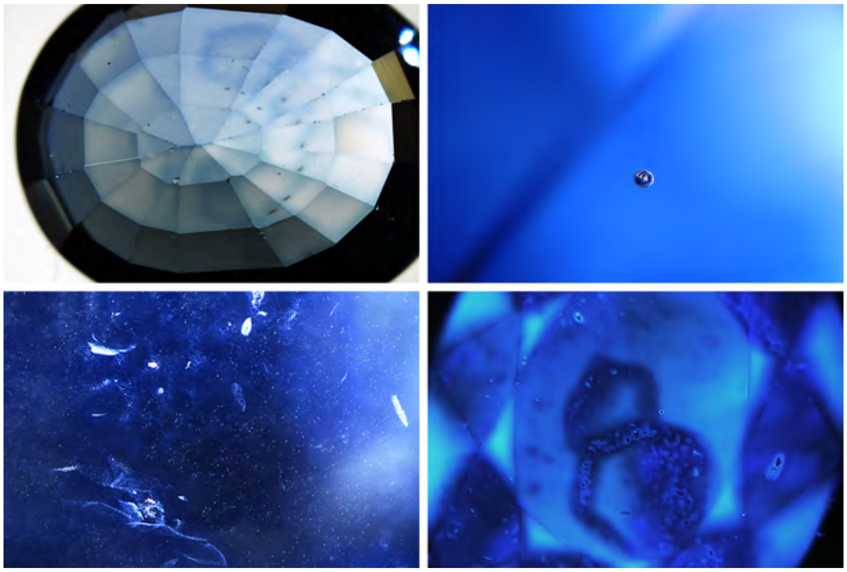

Figure 23. Top left: Color concentration was seen along the pavilion facet junctions of the synthetic sapphire, and blue halos were shown on the table facet. Top right: A spherical gas bubble was observed. Bottom left: Numerous clouds were visible throughout the stone. Some formed fingerprint-like patterns. Bottom right: Under the DiamondView's short-wave UV radiation, blue fluorescence was absent where there were concentrations of the diffusion color in the stone. Fields of view: 9.61 mm (top left), 1.25 mm (top right), 2.9 mm (bottom left), and 8.58 mm (bottom right).

properties were consistent with heated sapphire, either natural or synthetic. Under magnification and diffused transmitted lighting, a blue color concentration was observed along the facet junctions on both the pavilion and crown facets, along with a few large blue halos on the table facet (figure 23, top left), which indicated that the stone had been titanium diffused (R.E. Kane et al., "The identification of blue diffusion-treated sapphire," Summer 1990 *G&G*, pp. 115–133; Summer 2015 GNI, pp. 203–205). Under darkfield lighting, individual large spherical gas bubbles were present (figure 23, top right). Numerous clouds observed throughout much of the stone could have easily been mistaken for natural clouds. Some of them grouped to form natural-looking fingerprint-like inclusions (figure 23, bottom left). The stone's internal characteristics indicated a melt-grown synthetic origin. However, when immersing in methylene iodide under crossed polarizers and viewing down the optic axis, no Plato lines were observed (see W. Plato, "Oriented lines in synthetic corundum," Fall 1952 *G&G*, pp. 223–224). The absence of Plato lines does not rule out flame-fusion growth. The heat from diffusion treatment can reduce the visibility of Plato lines (S. Elen and E. Fritsch, "The separation of natural from synthetic colorless sapphire," Spring 1999 *G&G*, pp. 30–41). More advanced testing is needed to reveal all the physical and chemical properties of this unique stone.

Under the short-wave radiation (a 20-nm-wide band centered at 225 nm) in a DiamondView device, the stone displayed a strong chalky blue fluorescence. Hughes and Emmett (2005) concluded that the chalky blue fluorescence was due to isolated Ti^{4+} ions, or Ti-Al vacancy pairs. The strength of the chalky fluorescence depends on the growth temperature and Ti^{4+} concentration relative to other impurities. In melt-grown corundum, the high growth temperature allows Ti^{4+} to pair with Al vacancies more easily than other charge compensating ions; this creates the chalky fluorescence. In contrast, Pairing of Ti^{4+} with other ions (usually Fe^{2+} or Mg^{2+}) and the presence of Fe^{3+} ions prevent fluorescence. That could explain why the chalky fluorescence was not present where the blue diffusion color was concentrated (R. Hughes and J. Emmett, "Heat seeker: UV fluorescence as a gemological tool," 2005, www.ruby-sapphire.com/heat_seeker_uv_fluorescence.htm).

LA-ICP-MS analysis was performed on the girdle of the stone. Three laser ablation spots were drilled six times down into the stone. The concentration vs. depth profile is shown in figure 24. From the surface of the stone to around 180 μm depth, the Be concentration decreased from 76.8 to 13.9 ppma, Mg from 7.8 to 0.8 ppma, Ti from 580 to 391 ppma, Fe from 390 to 83.4 ppma, and Ga from 6.12 to 1.36 ppma. The results confirmed diffusion treatment, not only by Ti and Fe but also by Be, Mg, and Ga. The presence of Mo provided some indication of synthetic origin. In a GIA identification report, the stone was described as titanium and beryllium diffused. It is the first time GIA has examined a multi-elemental diffused and melt-grown synthetic sapphire.

Ziyin Sun, Jonathan Muyal, and Nicole Ahline

TOURMALINE

Paraíba Tourmaline with Unusual Coating

Paraíba tourmaline, named after the Brazilian state where it was discovered in the late 1980s, is a precious copper-bearing tourmaline variety (e.g., J.E. Shigley et al., "An update on 'Paraíba' tourmaline from Brazil," Winter 2001 *G&G*, pp. 260–276). Treatments such as heating and clarity enhancement have been described (e.g., S.F. McClure et al., "Gemstone enhancement and its detection in the

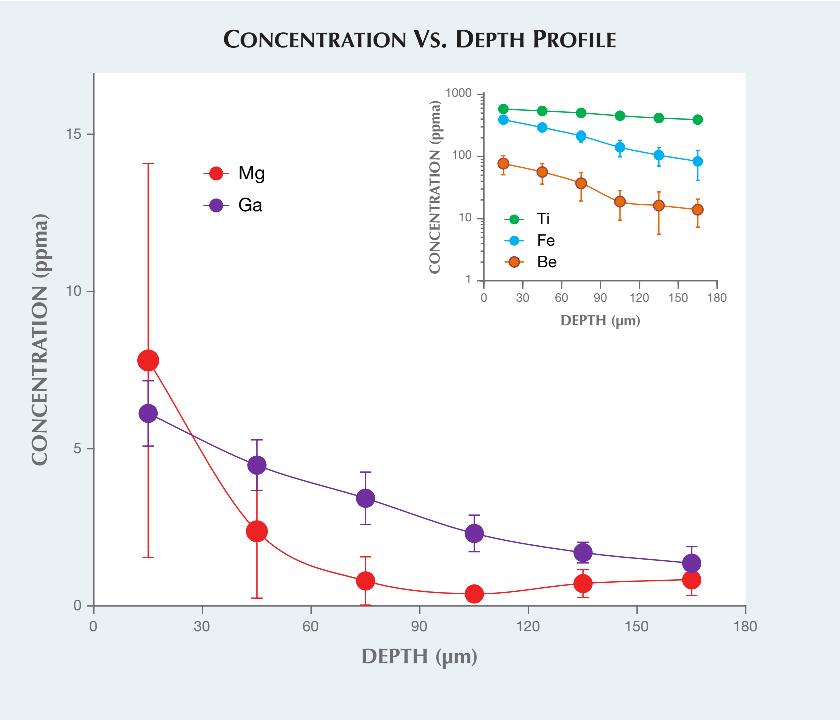

Figure 24. The synthetic sapphire's concentration vs. depth profile revealed that concentrations of Be, Mg, Ti, Fe, and Ga decreased significantly when the laser ablation spots went deeper into the stone.

2000s," Fall 2010 *G&G*, pp. 218–240), but coating has never been reported.

A Paraíba tourmaline ring with an unusual coating was recently submitted to GIA's Tokyo laboratory for identification and origin service (figure 25). Standard gemological properties revealed an RI of 1.640–1.620, consistent with tourmaline. The stone showed medium to strong dichroism displaying greenish blue and light blue colors. Natural inclusions such as trichites and fingerprints were observed. We identified the stone as tourmaline using Raman spectroscopy. EDXRF and UV-Vis spectroscopy were performed to confirm the presence of copper within the material, as well as the material's cause of color.

Viewed face-up with the unaided eye, the stone appeared normal. However, the coated surface looked different under reflected lighting and darkfield illumination (figure 26, left). A brassy, uneven submetallic luster was observed under reflected light, while whitish features in the submetallic luster area (figure 26, right) appeared under darkfield illumination. Coatings typically show signs of wear due to their low durability. This is often seen at the facet junctions. This coating did not show signs of wear and could not be removed using a standard ink pen eraser.

LA-ICP-MS chemical analyses detected elements such as B, Li, and Na, indicating elbaite tourmaline. However, strong early (near-surface) peaks of elements Pt, W, and Mo, which are not normally contained in natural tourmaline, were detected. We determined that this chemistry difference probably resulted from the submetallic surface coating. As with Pt- and Pt-related coatings, it is possible that the coating was used to improve abrasion resistance (e.g., K. Schmetzer, "Surface treatment of gemstones, especially topaz – an update of recent patent literature," *Journal of Gemmology*, Vol. 31, No. 1, 2008, pp. 7–13)

Figure 25. The Paraíba tourmaline in this ring had an unusual submetallic surface coating.

Figure 26. Left: An uneven submetallic coating with an irregular pattern is revealed with reflected light. The white dashed box represents the area shown in the right photo. Field of view 3.33 mm. Right: Under brightfield illumination, a part of the left table facet shows whitish surface structures surrounding the metallic luster domains. Field of view 1.31 mm.

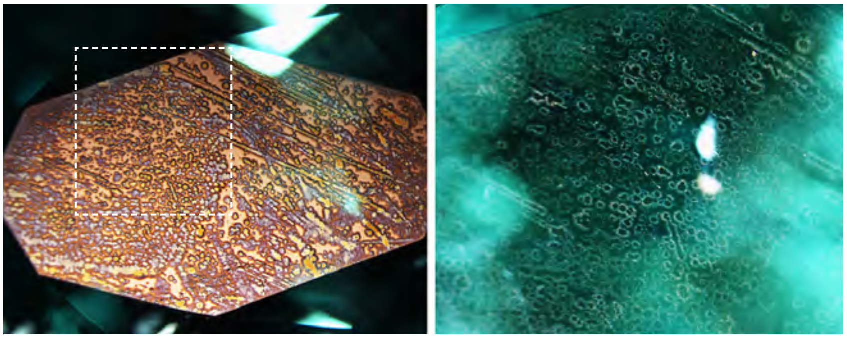

or to assist with scanning electron microscopy (SEM) observation (e.g., I. Stokroos et al., "A comparative study of thin coatings of Au/Pd, Pt and Cr produced by magnetron supporting for FE-SEM," *Journal of Microscopy*, Vol. 189, No. 1, 1998, pp. 79–89).

The reason for applying this coating is unknown. This is the first time GIA's laboratory has observed coated Paraíba tourmaline.

Kazuko Saruwatari and
Philip G. York

RUBELLITE with Incredibly Strong "Pink Sleeves"

GIA's Hong Kong laboratory recently examined a purplish red cabochon-cut rubellite tourmaline. Standard gemological tests yielded a spot RI of 1.64 and SG of 3.06, which are consistent with tourmaline. Magnification revealed strong doubling, fluid inclusions, and parallel growth tubes, all typical of tourmaline. What made this specimen unusual were its localized zones of strong pink coloration surrounding surface-reaching growth tubes and fractures (figure 27, left). Bleeding of pink color from the growth tubes into the body of the stone was best observed looking down the length of the growth tubes (figure 27, right); the pink color gradually faded away into the surrounding tourmaline host. This type of zoning has come to be known as "pink sleeves."

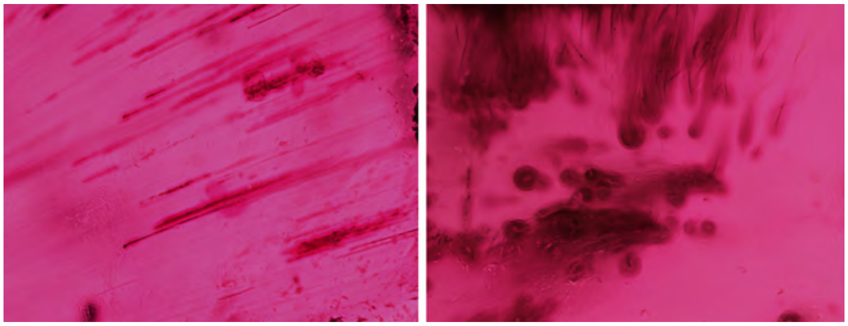
Figure 27. Left: Surface-reaching growth tubes and fractures associated with strong pink sleeves, whose color became weaker as they penetrated the stone's interior; field of view 2.83 mm. Right: Looking down the length of the growth tubes, bleeding of pink color was observed; field of view 1.13 mm.

It is different from dye concentrations, which would only be located inside the surface-reaching growth tubes and fractures.

Radiation-induced pink sleeves surrounding surface-reaching growth tubes and fractures have been reported in Paraíba tourmalines from Mozambique. The formation is believed to be due to a radioactive solution entering the growth tubes and fractures by capillary action, and the presence of pink sleeves proves that the stone has not undergone heat treatment. (J.I. Koivula et al., "Solution-generated pink color surrounding growth tubes and cracks in blue to blue-green copper-bearing tourmalines from Mozambique," Spring 2009 *G&G*, pp. 44–47). To the best of our knowledge, the incredibly strong pink sleeves seen in this rubellite have not been previously reported in either Paraíba or rubellite tourmaline.

Xiaodan Jia and Mei Mei Sit

PHOTO CREDITS:
Robison McMurtry—1, 12; Jian Xin (Jae) Liao—2, 18; Augusto Castillo—4; Sood Oil (Judy) Chia—6; Kyaw Soe Moe—7 (right); Nuttapol Kitdee—9, 14; Charuwan Khowpong—10, 11, 16, 17; Ungkhana Atikarnsakul—17; Paul Johnson—19, 21; Jonathan Muyal—23; Nicole Ahline—23; Masumi Saito—25; Kazuko Saruwatari—26; Xiaodan Jia—27.

G&G Micro-World

Editor
Nathan Renfro

Contributing Editors
Elise A. Skalwold and John I. Koivula

Ametrine Optical Dishes: Windows into the Effects of Crystal Structure

During exploration of a gem's interior, it is important to understand how crystal structure affects the incorporation and orientation of inclusions, how an inclusion can affect its host, how interpretation of observations can depend on point of view, and the nature of light as it passes through a crystal—host or inclusion. As proposed earlier in this column (Spring 2016, p. 81), polished inclusion study blocks are ideal for showcasing, studying, and reviewing basic concepts relating to the micro-world. Here we take a look at light and crystal structure.

Of all the varieties of quartz, ametrine is perhaps the most fascinating to observe. While its stunning color zoning makes it a popular designer gemstone, it also encompasses several optical properties unique to different quartz varieties that can all be explored in one specimen. Almost unrecognizable as quartz, ametrine crystals are deeply etched (figure 1, left) and have abundant healed fractures. The only clues to the trigonal symmetry typical of quartz are occasional rhombohedral faces and, very rarely, an enigmatic flat termination manifesting a three-armed figure (figure 1, right). Only when a basal section is made by cutting a slice perpendicular to the c-axis is the improbable yet beautiful combination of citrine and amethyst revealed.

About the banner: In this scene, pyrite inclusions have dissolved, leaving behind hematite and goethite, both of which react dramatically to polarized light. Photomicrograph by John Koivula; field of view 10 mm.

Editors' note: Interested contributors should contact Nathan Renfro at nrenfro@gia.edu and Jennifer-Lynn Archuleta at jennifer.archuleta@gia.edu for submission information.

GEMS & GEMOLOGY, VOL. 53, NO. 1, pp. 102–108.

Figure 1. Left: An 85 × 25 mm ametrine crystal from Bolivia's Anahí mine exhibits the deeply etched prism faces typical of this quartz variety. Right: The crystal's termination, viewed in the direction of its c-axis, displays a rare "Y"-shaped manifestation of the crystal's trigonal symmetry. Slices made perpendicular to this direction will reveal this symmetry with alternating amethyst and citrine sectors. Since the optic axis parallels the c-axis located at the intersection of the "Y" arms, all paths of light found across this termination face will be along the optic axis. Photos by Elise A. Skalwold.

Beauty and function are married in an ametrine study block oriented so that the view through its two largest faces is directly along the optic axis of a crystal, as seen in figure 1. The innovation of adding a set of concave dishes for sampling each color zone, as well as the borders between them, reveals truly remarkable optical phenomena (figures 2 and 3). These optical dishes allow the viewer to see light passing

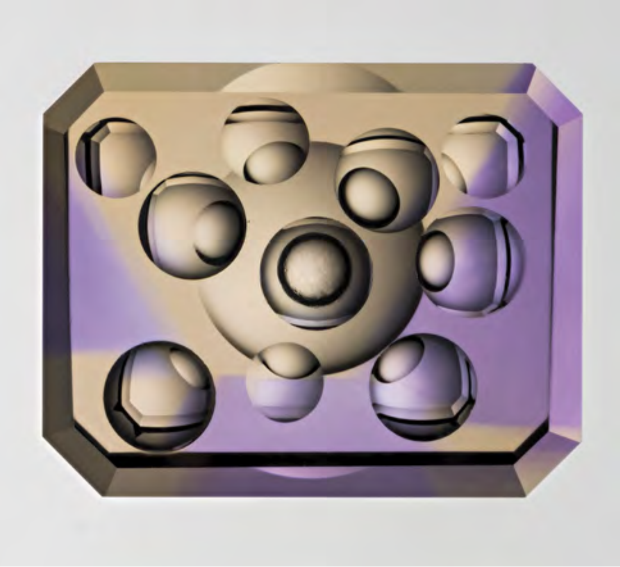

Figure 2. An ametrine study block with concave dishes cut and polished into its surface, including one on the opposite side. Viewed in transmitted light along the optic axis direction (i.e., all paths parallel to the c-axis), as in figure 1 (right), the trigonal symmetry of the crystal defines the citrine and amethyst sectoral zoning and allows observation of the effects of the optic axis on light. This specimen was fashioned by Nathan Renfro. Photo by Kevin Schumacher.

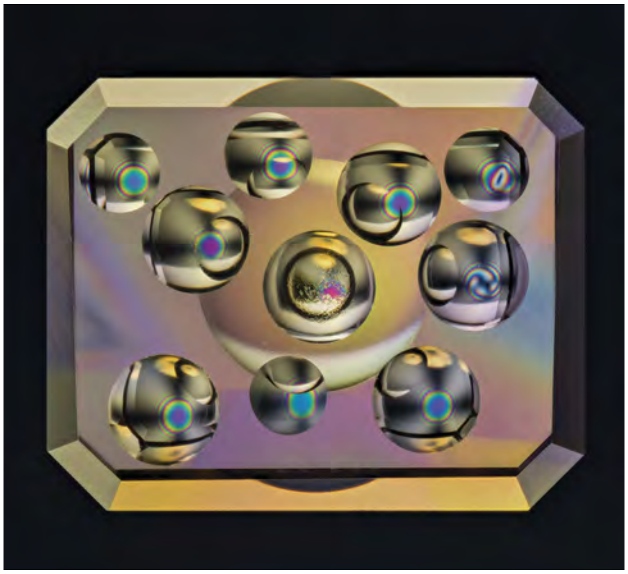

Figure 3. Placing the study block between crossed polarizing filters in transmitted light results in a variety of bull's-eye optic figures that form in the divergent light produced by the concave dishes. The citrine sectors under the minor rhombohedral faces (z) are free of twinning and show a classic bull's-eye optic figure with varying colors due to slightly different thicknesses. The amethyst sectors display an Airy's spiral (middle row, right dish) produced by the alternating layers of left- and right-handed quartz of the Brazil-law twinning that formed under the crystal's major rhombohedral faces (r); broadly angled colors in these latter areas are also indicative of this twinning. The dish on the upper right is a distorted figure on the border of the sectors. Photo by Kevin Schumacher.

through the specimen in many directions, as does the strain-free glass sphere familiar to gemologists for use with a polariscope (figure 4). When viewed between crossed polarizing filters, these dishes dramatically display the different uniaxial optic figures unique to quartz, which vary depending on thickness and placement in the sectors: the classic "bull's-eye" optic figure seen in the untwinned citrine sectors, an Airy's spiral in the amethyst sectors, and a distorted figure produced in a border region. All of these observed phenomena are produced by optical activity (i.e., the rotatory dispersion of light as it travels along the optic axis direction within the quartz crystal). By analyzing these figures, we can determine handedness and the effects of thickness, while observations of the amethyst's Brazil-law twinning may help distinguish natural versus synthetic origin.

For an in-depth analysis of the phenomenon of optical activity and the origin of quartz's optic figure, see E.A. Skalwold and W.A. Bassett, *Quartz: A Bull's Eye on Optical Activity*, Mineralogical Society of America, 2016, www.minsocam.org/msa/OpenAccess_publications/Skalwold/Quartz_Bullseye_on_Optical_Activity.pdf.

Elise A. Skalwold and William A. Bassett
Ithaca, New York

Figure 4. Left: A section through part of the study block. The dish serves as a concave (negative) lens that causes the light rays to diverge. Right: A gemologist's strain-free glass sphere is used to observe an interference figure. Although the rays first converge at the base of the sphere, they ultimately diverge just like the rays in the figure on the left. Illustration by William A. Bassett.

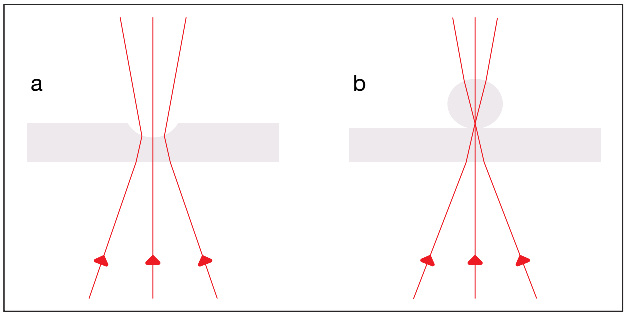

Figure 5. This 6.92 mm bastnäsite-(Ce) from Pakistan contains numerous straight and curving acicular inclusions of astrophyllite. Photo by Kevin Schumacher.

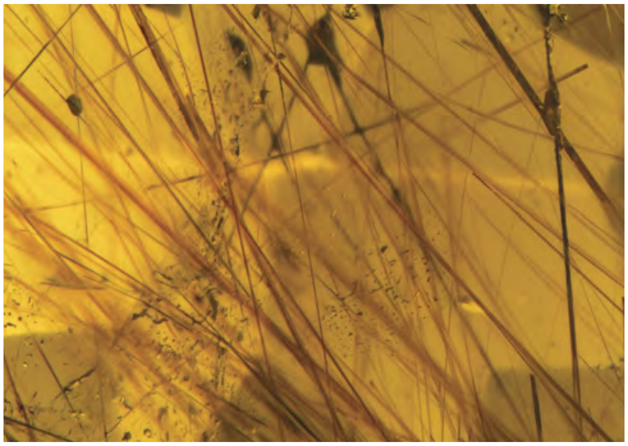

Figure 6. Magnification affords a more detailed view of the bastnäsite-(Ce) inclusions. Photomicrograph by Nathan Renfro; field of view 2.85 mm.

Astrophyllite in Bastnäsite-(Ce)

Pakistan's Zagi Mountains are known as a source for both astrophyllite and bastnäsite-(Ce). The two minerals often grow together, with bastnäsite-(Ce) overgrowing stalks and fibers of astrophyllite; the latter is then sometimes incorporated as inclusions in the bastnäsite-(Ce). We refer to these types of inclusions as "protogenetic."

The author recently had the opportunity to examine the brownish orange bastnäsite-(Ce) seen in figure 5. The 1.40 ct oval modified brilliant, provided by Luciana Barbosa (Gemological Center, Asheville, North Carolina), hosted an abundance of eye-visible inclusions of astrophyllite (figure 6), both straight and curved, that were identified by Raman analysis. Some of the included fibers and stalks appear to have been partially altered or coated with iron compounds.

John I. Koivula
GIA, Carlsbad

Flashes and Flames in Ethiopian Opal

The relatively new source for precious opal located in Ethiopia's Wollo Province produces material with vibrant play-of-color and occasionally with interesting inclusions.

Figure 7. This 2.68 ct opal displayed play-of-color when viewed face-up (left) and flame-like chatoyancy on its slightly domed base (right). A more pronounced dome might have had the effect of sharpening the sheen into a cat's eye. Photos by Kevin Schumacher.

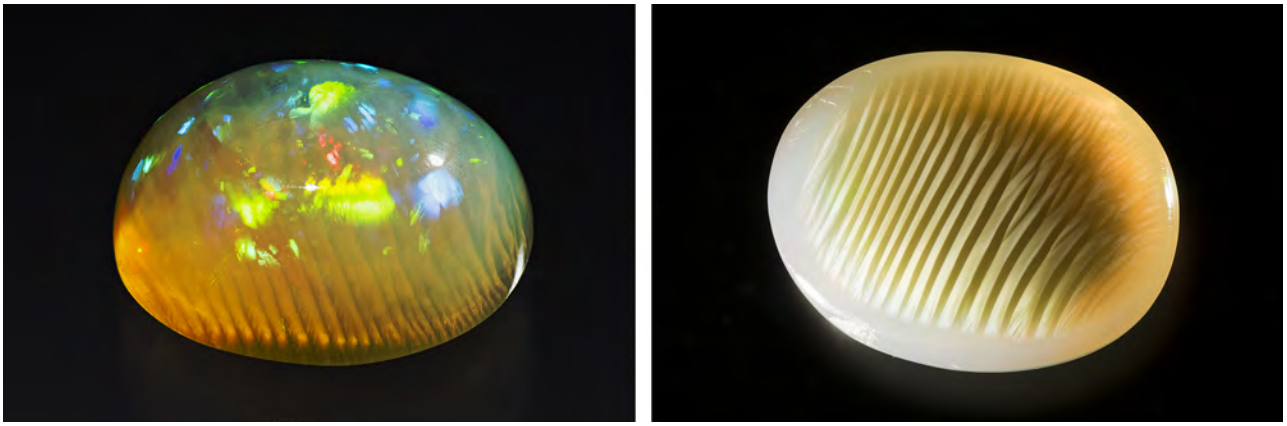

A recently examined 2.68 ct cabochon contained a scattering of octahedral metal sulfide inclusions (relatively common in Ethiopian opal) along with an unusual combination of optical phenomena: play-of-color and chatoyancy. Face-up, the stone showed the typical flashes of colors one would expect in precious opal (figure 7, left). However, the back of this cabochon contained an interesting structure that produced a sheen-like chatoyancy over its slightly rounded surface (figure 7, right). This chatoyant zone was strikingly similar to the flame structure seen in some non-nacreous pearls, which is produced by an intricate structure of aragonite crystal laths (figure 8). In the case of this opal, the flame-like structure's cause remains an enigma, though it could be due to the structural influence of a pre-existing fibrous mineral replaced by opal. Unfortunately, Raman analysis was unable to detect any presence of another mineral phase in the chatoyant area, so the exact cause of chatoyancy is still unknown.

Chatoyancy is not unheard of in opal, though it is quite rare in precious material. Cat's-eye common opal from Tanzania owes its optical effect to arrays of parallel needles, while the asterism and chatoyancy unique to the precious opal of Spencer, Idaho, are due to the arrangement of the same silica micro-spherules responsible for its play-of-color. At least one cat's-eye precious opal was observed to even "wink" at the viewer when viewed with opposing lighting (Summer 2003 Lab Notes, p. 148). This Ethiopian opal cabochon joins the rarefied group of chatoyant precious opal with its unusual phenomenal display of flashes and flames.

Nathan D. Renfro
GIA, Carlsbad

Elise A. Skalwold

Figure 8. The fibrous nature of the opal's unusual chatoyant zone is clearly revealed, along with the numerous minute octahedral black metal sulfide crystals that are a common inclusion in opal from Wollo. Oblique fiber-optic illumination. Photomicrograph by Nathan Renfro; field of view 2.73 mm.

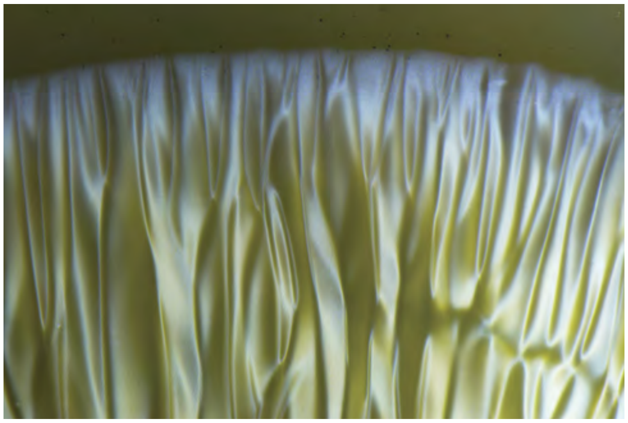

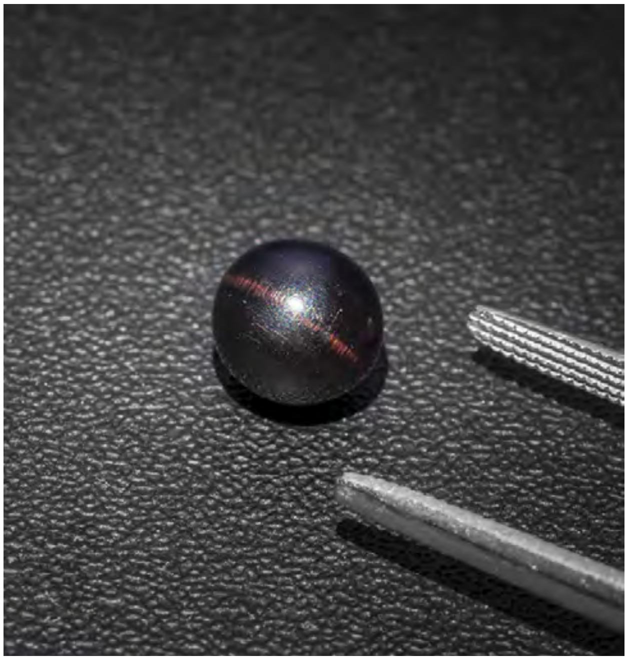

Figure 9. With fiber-optic illumination, a sharp, bright pink chatoyant band extends across the surface of a 1.89 ct dark brown button-shaped imitation pearl perpendicular to its internal fibrous structure. Photo by Robert Weldon/GIA.

Imitation Cat's-Eye Pen "Pearls"

Chatoyancy is an optical phenomenon commonly seen in gemstones that have an abundance of parallel solid or hollow long acicular inclusions in which an eye-like band is produced when viewed in strong light. Fine cat's-eye gemstones of various mineral species are prized; however, natural chatoyancy in pen pearls would be an extraordinary occurrence. During a recent study on reportedly non-nacreous pearls from the Dr. Eduard J. Gübelin Collection, the author found three dark brown button-shaped samples stated to be from a *Pinna* species mollusk. All three samples displayed an attractive cat's-eye effect when illuminated under a fiber-optic light or any single white light (figure 9). In each specimen, the chatoyant band manifested as a single bright pink line extending across the surface in a direction perpendicular to the internal fibrous structure.

Evidence of human manipulation includes fine linear features present in random directions across cellular structures; these are proof of work carried out during the fashioning of the samples into cabochons. Microscopic examination revealed the fibrous structure as numerous well-formed, minute parallel acicular crystals. Infrared spectroscopy subsequently confirmed the crystals to be calcite. The calcite was arranged in a vertical columnar orientation rather than in a radial and concentric structure characteristic of non-nacreous *Pinna* (pen) pearls, which led to further doubts concerning the "pearl" identity of the samples.

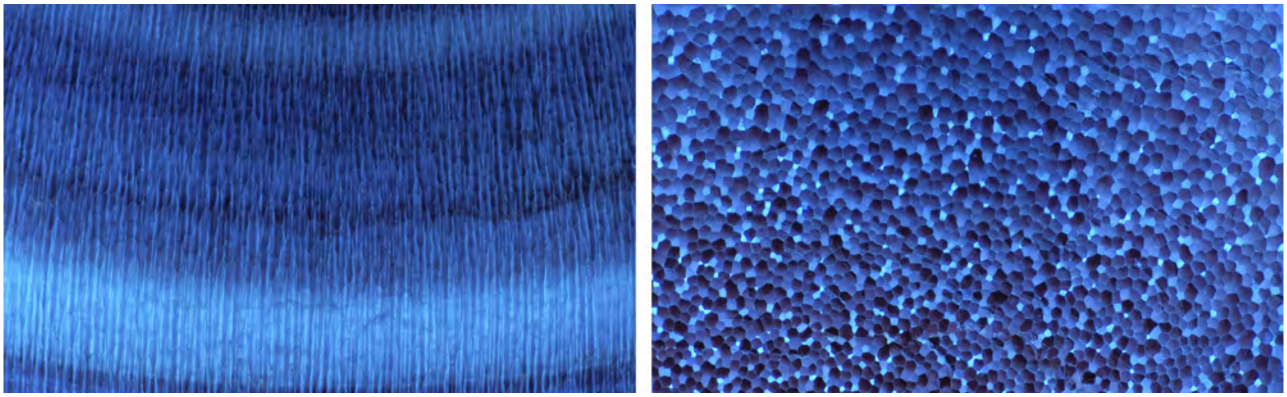

Figure 10. Fluorescence images reveal banded features, typical of shell, at right angles to the vertical columnar structure of the calcite crystals (left). A mosaic pattern (right) is apparent looking down the hexagonal cross-section of the calcite columns. Photomicrographs by Artitaya Homkrajae; fields of view 2.88 mm and 1.44 mm, respectively.

Microradiography of all three samples revealed tight internal structures. The obvious radial structures that would be expected in pen pearls were not observed (N. Sturman et al., "Observations on pearls reportedly from the Pinnidae family (pen pearls)," Fall 2014 *G&G*, pp. 202–215). Based on its external and internal features, this material was almost certainly the same type of imitation pearl previously reported in *G&G* (Winter 2011 GNI, pp. 330–332).

Fluorescence images taken of one specimen using a polarizing microscope and an ultraviolet excitation filter with a wavelength range of 330–380 nm (figure 10, left) reveal a prominent banded structure at right angles to the calcite columns. When viewed at right angles to their lengths under the same conditions, the long, thin calcite crystals reveal a hexagonal cross-section, creating a striking mosaic or cellular pattern (figure 10, right). The cells varied in form, and their approximate diameters ranged from 15.50 to 38.00 microns.

These samples were appealing for the magnificent kaleidoscopic colors that were seen using fiber-optic illumination (figure 11). The semitranslucent to translucent nature of the crystals allowed light to pass through and produce vibrant, colorful scenes owing to the interference of the light rays that were reflected and refracted when interacting with the crystals. As one can see, exploration of the micro-world is not only important to forensics—it can also be quite beautiful.

Artitaya Homkrajae
GIA, Carlsbad

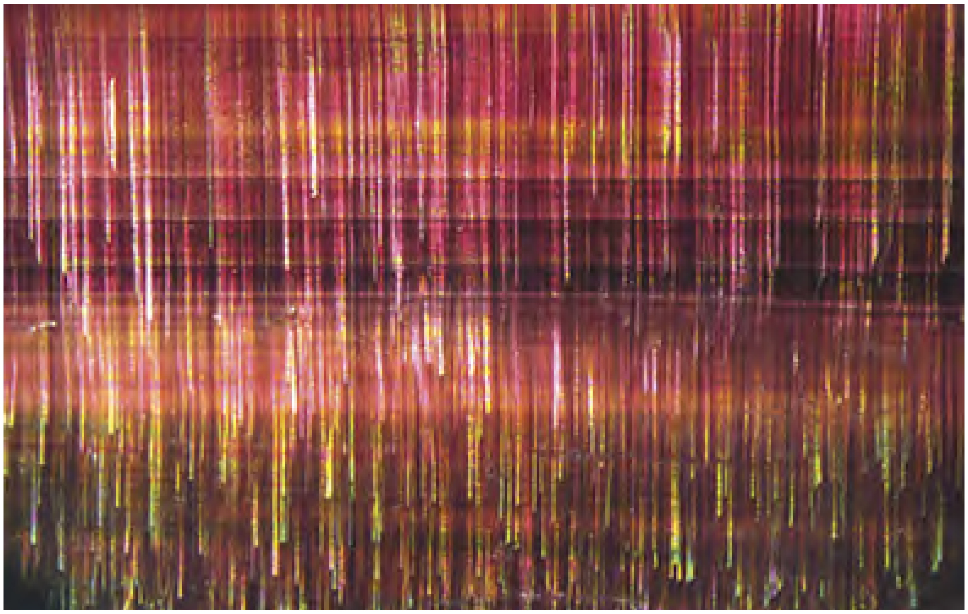

Figure 11. Under fiber-optic light, magnificent reflective kaleidoscopic colors of pink, yellow, and green are revealed from the well-formed acicular calcite crystals after mineral oil is applied to the sample's surface. Photomicrograph by Artitaya Homkrajae; field of view 3.57 mm.

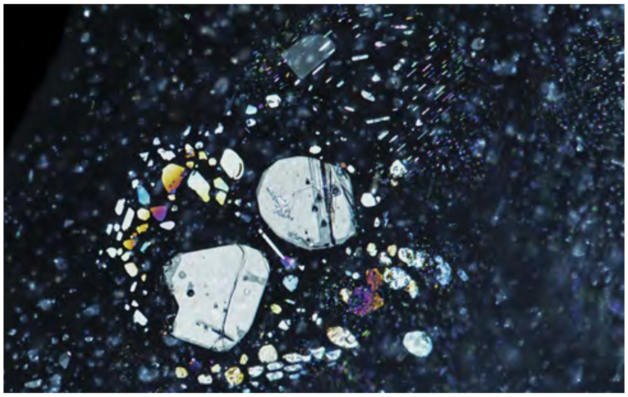

Figure 12. A beautiful iridescent rosette pattern made up of flattened negative crystals appears around the primary negative crystals when illuminated by oblique fiber-optic lighting. Photomicrograph by Victoria Raynaud; field of view 1.07 mm.

Figure 13. These two large primary fluid inclusions containing a black solid phase are associated with fingerprints that have a variable orientation. The photo was taken along the c-axis in darkfield illumination. Photomicrograph by Victoria Raynaud; field of view 1.07 mm.

Negative Crystals in Sapphires

Negative crystals, or cavities within a crystal, and fluid inclusions occur in almost every mineral. They are generally too small to notice without high magnification, but these modest features hold great beauty and scientific value. These microscopic features are valuable to understanding the growth of continents, the rise of mountains, and the formation of gems. The following photos show beautiful examples of such inclusions in sapphires from the Baw Mar mining area in Mogok, Myanmar. Some of these fluid inclusions are arranged in a "rosette" pattern consisting of a large flattened negative crystal surrounded by smaller ones. This structure is always seen perpendicular to the c-axis (figure 12). The larger primary inclusions like those seen in figure 13 are characterized by their high relief and may display triangular growth markings as well as beautiful iridescence under oblique fiber-optic illumination. Other negative crystals associated with healed fissures are observed in random orientation. The smaller, more delicate fluid inclusions in these structures have a smoother outline, while the fingerprints themselves are often associated with the primary negative crystals.

The multiphase inclusion in figure 14 contains a gas, a liquid, and at least one solid. When the specimen was gently heated by the microscope's well light, the gas and the liquid homogenized. Raman spectroscopy identified the gas phase as pure CO_2 and the opaque solid as marcasite. Using the same method, we also identified diaspore fibers, seen as faint lines in the inclusions, and a miniscule siderite crystal. Although fluid inclusions are common in most blue sapphires, the examples from Baw Mar reveal these fascinating inclusions in an appealing way.

Figure 14. Left: A large fluid inclusion containing a CO_2 gas bubble and a marcasite crystal. The primary inclusion is surrounded by smaller inclusions that make up a healed fissure. Right: When the sample was gently heated, the gas bubble disappeared as the gas and liquid homogenized. The sample is illuminated using diffused backlighting. Photomicrographs by Victoria Raynaud; field of view 1.20 mm.

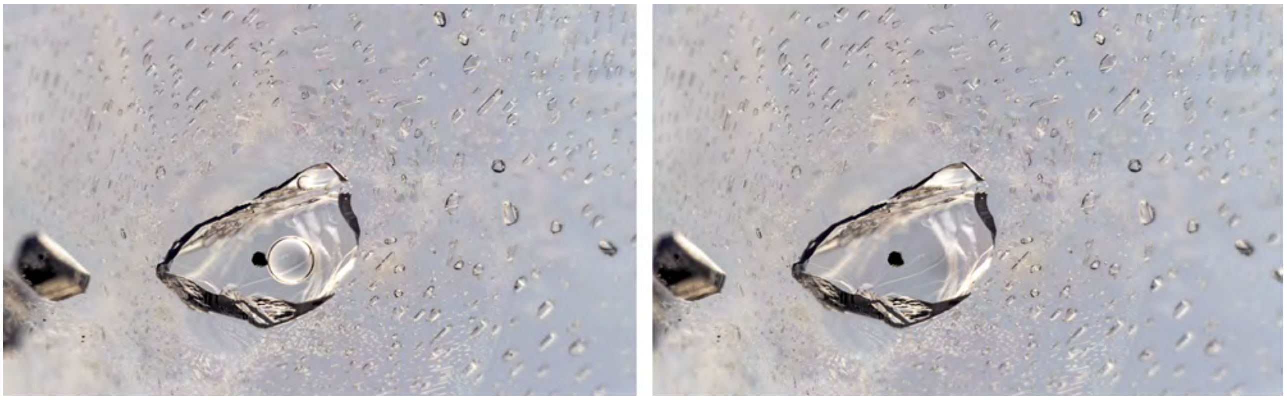

Figure 15. The interior of this 5.10 ct Sri Lankan topaz is dominated by a dramatic inclusion scene. Photo by Kevin Schumacher.

These photos were taken as part of a research project to document the blue sapphires from the Baw Mar mine. The complete report of this study can be found at https://www.gia.edu/gia-news-research/blue-sapphires-baw-mar-mine-mogok-myanmar.

Victoria Raynaud and Wim Vertriest
GIA, Bangkok

Quarterly Crystal: Mystery in Topaz

Occasionally we run into an inclusion identification problem we just can't solve. Such was the case with the 5.10 ct topaz from Elahera, Sri Lanka, shown in figure 15. This transparent colorless crystal, acquired from Kusum S. Naotunne (Colombo, Sri Lanka), hosts a prominent translucent light green crystal and a flowery cluster of hexagonal opaque silvery black plates (figure 16). The bodycolor and characteristic form of the green inclusion suggest fluorite; this was confirmed by laser Raman micro-spectrometry.

Analysis of the opaque black plates was a more difficult matter. GIA's Carlsbad lab staff employed Raman to identify the plates, but the inclusion was too deep to get any signal other than the spectral lines of the topaz host. Energy-dispersive X-ray fluorescence (EDXRF) was attempted to pick up any hints of the plates' chemical composition, but useful information continued to elude such efforts. It became clear that destructive analysis would be needed to clearly identify the black plates. Since this was an inclusion combination, we decided that this topaz should be preserved unaltered for future exploration. Surely one day technological advances will allow the identification of this mystery inclusion, but for now it is enough to enjoy the aesthetics of such a beautiful included crystal and the fascinating exploration of its inner world.

John I. Koivula

Figure 16. While the light green crystal was identified as fluorite by Raman analysis, the opaque platy inclusions were too deep to be identified. Photomicrograph by Nathan Renfro; field of view 5.87 mm.

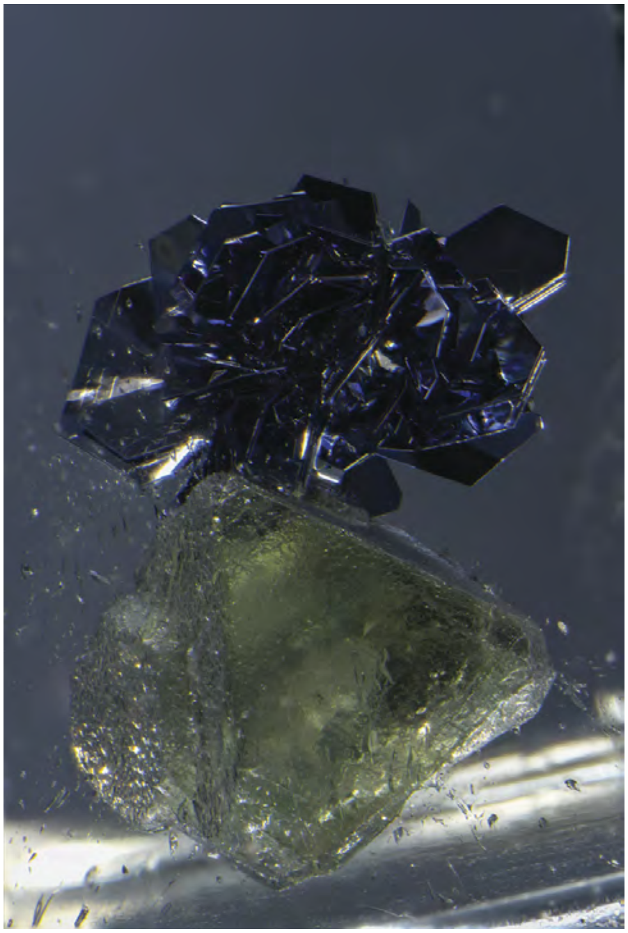

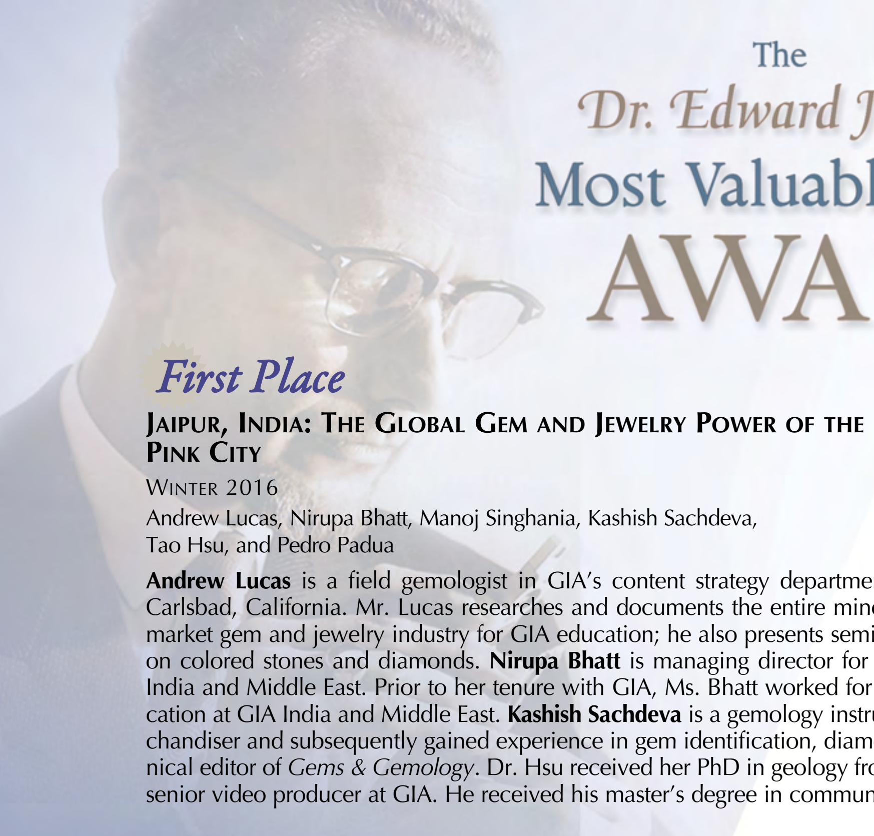

The
Dr. Edward J. Gübelin
Most Valuable Article
AWARD

Most Valuable Article

First Place

JAIPUR, INDIA: THE GLOBAL GEM AND JEWELRY POWER OF THE PINK CITY

WINTER 2016

Andrew Lucas, Nirupa Bhatt, Manoj Singhania, Kashish Sachdeva,
Tao Hsu, and Pedro Padua


Andrew Lucas


Nirupa Bhatt


Manoj Singhania

Andrew Lucas is a field gemologist in GIA's content strategy department in Carlsbad, California. Mr. Lucas researches and documents the entire mine-to-market gem and jewelry industry for GIA education; he also presents seminars on colored stones and diamonds. **Nirupa Bhatt** is managing director for GIA India and Middle East. Prior to her tenure with GIA, Ms. Bhatt worked for Rio Tinto for 20 years. **Manoj Singhania** is director of education at GIA India and Middle East. **Kashish Sachdeva** is a gemology instructor at GIA India. Mr. Sachdeva began his career as a merchandiser and subsequently gained experience in gem identification, diamond grading, and gemstone treatments. **Tao Hsu** is the technical editor of *Gems & Gemology*. Dr. Hsu received her PhD in geology from the University of Southern California. **Pedro Padua** is the senior video producer at GIA. He received his master's degree in communications from Loyola Marymount University.

Second Place

AN INTRODUCTION TO PHOTOLUMINESCENCE SPECTROSCOPY FOR DIAMOND AND ITS APPLICATIONS IN GEMOLOGY

SPRING 2016

Sally Eaton-Magaña and Christopher M. Breeding


Sally Eaton-Magaña


Christopher M. Breeding

Sally Eaton-Magaña is a research scientist at GIA in Carlsbad, where she investigates the physics of natural, treated, and synthetic diamonds. Dr. Eaton-Magaña received her PhD in chemical engineering from Case Western Reserve University. **Christopher M. Breeding** is a senior research scientist and manager at GIA in Carlsbad, where he investigates origin of color in diamond and other gems. Dr. Breeding, who is a co-editor of *G&G*'s Gem News International section, holds a PhD in geology from Yale University.

Third Place

INCLUSIONS IN NATURAL, SYNTHETIC, AND TREATED EMERALD

WINTER 2016

Nathan D. Renfro, John I. Koivula, Jonathan Muyal, Shane F. McClure,
Kevin Schumacher, and James E. Shigley


Nathan Renfro


John I. Koivula


Jonathan Muyal

Nathan Renfro is the analytical manager of the gem identification department and analytical microscopist in the inclusion research department at GIA in Carlsbad. **John I. Koivula** is the analytical microscopist at GIA in Carlsbad. He is the co-author of the three-volume *Photoatlas of Inclusions in Gemstones* and the author of *MicroWorld of Diamonds*. **Jonathan Muyal** is a staff gemologist GIA in Carlsbad, where he also serves as the librarian for the research reference stone collection. Mr. Muyal specializes in photomicrography of inclusions in gem materials. **Shane McClure** is director of identification services at GIA in Carlsbad. He is well known for his many articles and lectures on gem identification. He is also co-editor of *G&G*'s Lab Notes section. **Kevin Schumacher** serves on the *G&G* production staff as a photographer, videographer, and image specialist. He has 37 years of professional photography experience, the past 11 with GIA. **James E. Shigley** is distinguished research fellow at GIA in Carlsbad. He is the author of numerous articles on diamonds and colored gemstones. Dr. Shigley holds a PhD from Stanford University.

Thank you to all the readers who voted. In addition to our winning authors, we congratulate Sandra Wen of Wuhan, China, whose name was randomly drawn from the entries to win a one-year subscription to *G&G*.

Take the 2017 GEMS & GEMOLOGY CHALLENGE

The following 25 questions are from the four 2016 issues of *G&G*. Refer to the articles in those issues to find the single best answer for each question.

Mark your choice on the response card provided in this issue or visit gia.edu/gems-gemology to take the Challenge online. Entries must be received no later than **Friday, August 11, 2017**. All entries will be acknowledged with an e-mail, so please remember to include your name and e-mail address (and write clearly).

Score 75% or better, and you will receive a certificate of completion (PDF file). Earn a perfect score, and your name also will be listed in the Fall 2017 issue of *Gems & Gemology*.

1. Which statement about pink CVD synthetic diamonds is usually true?
   - A. They demonstrate no fluorescence to long-wave UV light.
   - B. They show weak red fluorescence to long-wave UV light.
   - C. They show blue fluorescence to long-wave UV light.
   - D. They start out as light brown CVD material.

2. Which statement about ruby mining in northern Mozambique is true?
   - A. Montepuez Ruby Mining plans to incorporate more automation in the sorting process.
   - B. Activity is slowing down.
   - C. The highest-quality rubies are coming from Napula.
   - D. *Garimpeiros* will play a more significant role as the existing deposits are further developed.

3. In general, rough diamonds from the Diavik mine demonstrate
   - A. cubic morphology and near colorless to yellow colors.
   - B. dodecahedral morphology and brown color.
   - C. octahedral morphology and D–Z color.
   - D. octahedral morphology accompanied by complete or partial coatings.

4. CVD synthetic diamond can usually be separated from HPHT synthetics by
   - A. diamond type.
   - B. viewing strain patterns in crossed polarizers.
   - C. IR absorption spectroscopy.
   - D. the absence of a SiV^- doublet.

5. What risk does an opal cutter take when trying to maximize play-of color from a piece of rough?
   - A. Viewing the color bars from the side may give a false sense of the play-of-color present at the top of the bar.
   - B. Color bars may vary in thickness or even disappear within a stone.
   - C. Sand may be embedded in the silica gel, resulting in blemishes and disrupting the potential for a smooth top surface.
   - D. All of the above.

6. Flux residues were found in synthetic emeralds donated by Richard Nacken to the Deutsches Museum. This find indicates what is true about these samples?
   - A. None of them were grown hydrothermally.
   - B. All of them contain both molybdenum and vanadium.
   - C. Only gold crucibles were used.
   - D. Only synthetic emerald seeds were used.

7. Diavik diamonds
   - A. are among the oldest diamonds formed.
   - B. can be overgrown with a thin diamond coating of a much younger age.
   - C. are found beneath Lac de Gras.
   - D. all of the above

8. The Sutara Placer is significant because
   - A. it is a new source of facet-grade sapphire.
   - B. it produces trapiche and trapiche-type sapphire.
   - C. it is one of only two known gem-bearing sapphire placer deposits in Russia.
   - D. its sapphire's color range is rivaled only by Yogo sapphire from Montana.

9. Which statement about Colombian emeralds is true?
   - A. The oxidation of organic matter released the elements Be, Cr, and V, which were incorporated into the growing emeralds.
   - B. The emeralds formed at 330°C from hot evaporitic brines.
   - C. The emeralds' fluid inclusions generally contain doubly refractive crystals.
   - D. A and B

10. Which statement about the zero-phonon line (ZPL) in photoluminescence spectroscopy is false?
    - A. With increasing temperatures, the ZPL emission decreases.
    - B. The ZPL photon emission re-

sults when only phonons are involved.
C. At room temperature, it is hard to distinguish the ZPL from other emission features.
D. The wavelength of a given ZPL is exact.

11. The Fabergé hardstone figures of the Cossack guards Pustynnikov and Kudinov can be distinguished by all of the following features except
A. the color of their kiver bags and belts.
B. the gems used for their eyes.
C. the inscription on the bottom of their boots.
D. Kudinov's Gold Badge of Office.

12. In 1943, Richard Nacken filed a patent application for a method that would influence synthetic crystal growth for technical applications. What did the patent cover?
A. A hydrothermal process for synthetic emerald growth.
B. A hydrothermal process for primarily synthetic quartz growth.
C. A hydrothermal process for primarily synthetic sapphire growth.
D. An autoclave for growing quartz and emerald from flux.

13. Which statement about variscite is false?
A. It was used in Neolithic jewelry.
B. The main source today is central Tajikistan.
C. Its phosphate component comes from guano decomposition.
D. Relative concentrations of iron and chromium are the main color contributors.

14. In peridot, cleavage separations that result from the presence of a small solid inclusion paired with a fluid-filled negative crystal are called ___________ inclusions.
A. fingerprint
B. tension halo
C. lily pad
D. three-phase

15. Which exceptionally rare B- and Si-containing orthorhombic gem material with an SG of about 3.0 shows a B-O-Si bending vibration at a Raman shift of 612 nm?
A. Danburite
B. Grandidierite
C. Variscite
D. Tourmaline

16. Val Malenco serpentine is
A. composed of lizardite, antigorite, and chrysotile.
B. composed of lizardite and similar to that from China.
C. composed of antigorite and similar to that from Korea.
D. distinguished from Chinese and Korean material by RI and SG.

17. Which of the following is a difference between natural and non-bead-cultured (NBC) pearls?
A. NBC pearls do not contain beads.
B. NBC pearls only form in a graft location.
C. Only hatchery-raised mollusks can produce NBC pearls.
D. There is no difference.

18. Which statement regarding the blue color in blue zircon is true?
A. It is the natural color of zircon.
B. It is stable to long-wave UV exposure.
C. It can be altered and restored.
D. It is assumed to result from the treatment of yellow material.

19. Some companies preforming emerald rough in Jaipur maximize the weight yield of finished stones by
A. using hand-controlled jam pegs.
B. using high-tech equipment and computerized cutting.
C. outsourcing material to ensure they get the best cutters.
D. using traditional bow-powered laps.

20. Which statement regarding the materials used by Fabergé to construct the hardstone Cossack figures is false?
A. All the materials are natural.
B. All gemstones are from the Russian Empire.
C. Individual gem pieces were joined with animal hide glue.
D. The preferred carving material was nephrite.

21. How does phosphorescence differ from fluorescence?
A. Phosphorescence is a form of thermoluminescence and fluorescence is a form of photoluminescence.
B. Phosphorescence occurs after the excitation light source is turned off and fluorescence occurs while it is turned on.
C. Fluorescence lasts longer than phosphorescence.
D. Fluorescence is delayed luminescence; phosphorescence is not.

22. What gem-quality minerals contain BO_3 and SiO_4 groups, have an SG of approximately 3.0, and are found in Madagascar?
A. Grandidierite and tourmaline
B. Danburite and tourmaline
C. Danburite and grandidierite
D. None of the above

23. Ballerina Pearl Co. treats pearls from *P. margaritifera* to achieve a pistachio color. Which statement about their color is true?
A. It is altered by acetone.
B. It is enhanced by isopropanol.
C. It results primarily from dyeing.
D. None of the above are true.

24. What percentage of the gold refined by Hoover and Strong comes from recycled material?
A. 80%
B. 20%
C. 100%
D. 50%

25. Finding chrysoberyl and sapphire together associated with host rocks of volcanic origin such as basalts is related to
A. pegmatitic activity, which is common.
B. high-grade metamorphism, which is somewhat rare.
C. tertiary volcanic host rocks, which is very rare.
D. none of the above.

G&G

Gem News International

Contributing Editors
Emmanuel Fritsch, *University of Nantes, CNRS, Team 6502, Institut des Matériaux Jean Rouxel (IMN), Nantes, France* (fritsch@cnrs-imn.fr)
Gagan Choudhary, *Gem Testing Laboratory, Jaipur, India* (gagan@gjepcindia.com)
Christopher M. Breeding, *GIA, Carlsbad* (christopher.breeding@gia.edu)

TUCSON 2017

The 2017 Tucson gem and mineral shows drew eager buyers from all over the globe. Although many dealers reported lower traffic this year, most were content with the volume of business and noted that buyers were "serious."

As in previous years, we identified some strong trends:

- Demand for special one-of-a-kind pieces in both pearls and colored gemstones
- Continuing investment by multinational companies in colored gemstone mining and distribution
- A growing focus on ethically sourced gemstones and beneficiation
- Strong demand for high-end gems and a softening of demand for commercial goods
- Continuing importance of the secondary market in the U.S. for exceptional pieces
- Innovative partnerships emerging between individual colored gemstone mines, designer cutters, and television merchandisers

This year's big story was the emergence of Ethiopia as a potentially major source of gem-quality emerald. These new gems resemble other schist-hosted emeralds, especially those from Brazil and Zambia. Although most of the material is less saturated and included, dealers are excited that the new source also produces fine gem-grade crystals of exceptional size, color, and clarity.

Dealers also talked about the October 2016 removal of U.S. sanctions on Myanmar, legalizing the import of Burmese jadeite and rubies. According to Edward Boehm of RareSource, the lifting of the ban was widely welcomed, but Myanmar government reforms of the gem mining sector have some way to go. Conditions on the ground are much improved, however. Boehm told us new production might take some time to appear, which would impact prices and selection of available goods in the short term.

Large multinational companies have significantly impacted colored gemstone mining and distribution over the last decade. Gemfields' Kagem and Montepuez mines supply approximately one-third of global emerald and 70% of global ruby production, respectively. At this year's show we were able to interview Gemfields CEO Ian Harebottle for his perspective on the company's operations and its 2013 merger with luxury brand Fabergé.

Representing another publicly traded company intending to mine ruby in Mozambique, Christiaan Jordaan of Mustang Resources LLC told us about Mustang's initial 2016 bulk sampling and exploration activities. The company hopes to become an important supplier of commercial and gem-quality ruby.

Marcello Ribeiro of Belmont Group updated us on developments at the company's Belmont and Canaan emerald mines at Itabira, Brazil. He emphasized the importance of sound mine planning through fieldwork and trace-element analysis of potential emerald host rocks.

David Bindra of B&B Fine Gems confirmed the importance of the secondary market for exceptional gems, which are in very high demand. He noted less consumption of commercial to mid-grade material.

A partnership between Morocco's Geostone Group and U.S. gem carver Glenn Lehrer illustrates another interesting development. Production from Geostone's Moroccan amethyst mine is cut to Lehrer's high standards in an Indian factory, featuring a branded designer cut with high weight retention. The resulting faceted stones—and finished amethyst jewelry—are sold directly to consumers through television merchandising. The approach helps

Editors' note: Interested contributors should send information and illustrations to Stuart Overlin at soverlin@gia.edu or GIA, The Robert Mouawad Campus, 5345 Armada Drive, Carlsbad, CA 92008.

Gems & Gemology, Vol. 53, No. 1, pp. 112–142.

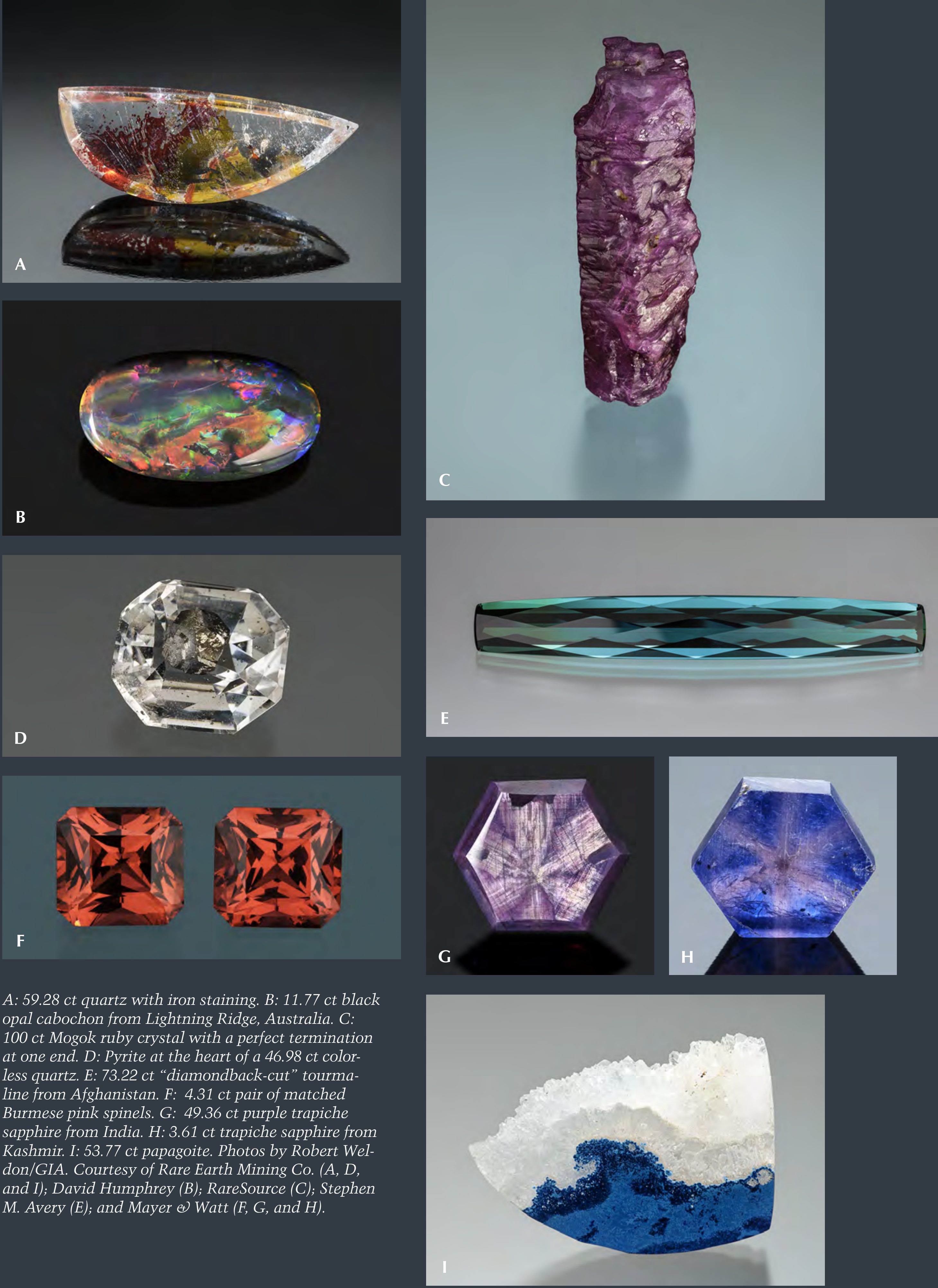

A: 59.28 ct quartz with iron staining. B: 11.77 ct black opal cabochon from Lightning Ridge, Australia. C: 100 ct Mogok ruby crystal with a perfect termination at one end. D: Pyrite at the heart of a 46.98 ct colorless quartz. E: 73.22 ct "diamondback-cut" tourmaline from Afghanistan. F: 4.31 ct pair of matched Burmese pink spinels. G: 49.36 ct purple trapiche sapphire from India. H: 3.61 ct trapiche sapphire from Kashmir. I: 53.77 ct papagoite. Photos by Robert Weldon/GIA. Courtesy of Rare Earth Mining Co. (A, D, and I); David Humphrey (B); RareSource (C); Stephen M. Avery (E); and Mayer & Watt (F, G, and H).

build a niche for Moroccan amethyst and brings the benefits of scale to designer cutting, which is usually associated with unique pieces.

Eternity Emerald's Arthur Groom shared his rough emerald buying expertise with us, especially his years of experience negotiating with miners in Afghanistan's Panjshir Valley. He noted that the quality of Afghan emerald is not realized in the West because large, fine crystals are often damaged by improper blasting and extraction techniques.

Potentate Mining's Warren Boyd showed us sapphire production from Montana's Rock Creek alluvial deposits, including a remarkable 12.61 ct blue sapphire cut from a 6.37 g rough crystal. Although most of the production has greenish or brownish pastel colors, it reacts well to heat treatment. Boyd told us bright natural colors are in high demand. He showed several suites of fancy sapphires cut by his client, Americut. Montana's alluvial sapphire deposits will be the subject of an upcoming *G&G* field report.

The trend toward ethical, sustainable business practices and transparent supply chains is exemplified by Sheahan Stephen of Sheahan Stephen Sapphires, Inc. His company documents and guarantees the integrity of the gems it sells from the mine, through treatment and cutting and directly to the customer.

Nigeria is an under-documented source of fine rubellite and indicolite tourmaline and predominantly blue basalt-hosted sapphire. For this reason, we especially welcomed talking to Zoe Michelou, who represented a Nigerian mining company. She updated us on production of these gemstones from that country's Oyo, Kwara, and Taraba states.

Gem paintings, which GIA has documented in Vietnam and Mogok, made their first appearance at Tucson. Wanlaya Suwannapirom's Than Thong Arts booth featured an array of art-inspired handmade portraits and miniatures. The technique converts otherwise unusable natural gem fragments into valuable art objects and wearable art such as pendants and pins.

Gem artist Alexander Kreis showed us a spectacular 27.20 ct freeform tanzanite complemented by a custom ring mount made by his mother Sonja, a master goldsmith. They related the importance of the story behind a jewelry piece for their clients—how details of the stone's cut and the ring's design represent the toil and effort of the Tanzanian miners and imbue the piece with added significance.

Fran Mastoloni provided a cultured pearl market update, explaining how careful selection and matching of the different cultured pearl types into a range of varied necklaces help him cater to the market's desire for distinctive "fashion-forward" yet flexible jewelry.

Dealer Bill Vance of Vance Gems exhibited rare gem-quality magnesio-axinites from just one location in Merelani, Tanzania. This material displayed remarkable fluorescence, and we hope to report further on its chemistry in the near future.

We were delighted to find a Southwest-inspired Starship Enterprise, handmade by David Freedland of David R. Freedland Jr. Designs in sterling silver. This quirky blend of science fiction and traditional inlay work is one of the show's unexpected finds.

Finally, no survey of the Tucson shows would be complete without Paula Crevoshay's one-of-a-kind designs. This year, she showcased a bracelet featuring five large freeform fire opals, a swallowtail butterfly pin with yellow and black diamonds, an elephant pin with mother-of-pearl tusks, and a stunning cuff bracelet featuring a spectacular boulder opal centerpiece.

Duncan Pay, Andy Lucas, Tao Hsu,
Eric Welch, and Albert Salvato
GIA, Carlsbad

A new discovery of emeralds from Ethiopia. In recent years Ethiopia has gained considerable attention in the gem trade for large amounts of high-quality opal from an area near Wegel Tena (B. Rondeau et al., 2010, "Play-of-color opal from Wegel Tena, Wollo Province, Ethiopia," Summer 2010 *G&G*, pp. 90–105). Apart from opal, emeralds have been sporadically mined, near Dubuluk, for more than a decade. This deposit is located about 80 km from the Kenyan border. Gemfields has been exploring this deposit since July 2015 (Fall 2012 GNI, pp. 219–220).

A new deposit of high-quality emeralds (see figure 1) has been found in the rural villages of Kenticha and Dermi, in the Seba Boru district (figure 2). In November 2016, author MN and business partner Daniel Kifle visited the local trading town of Shakiso, where Ethiopian gem merchants gather to legally buy and sell emeralds that are mined several kilometers away. Shakiso is located about 160 km north of the Dubuluk emerald deposit. The mining area is divided into a few "associations." Each consists of a manager and several members who control the actual mining and distribution of the emerald rough. After the rough has been sorted, it makes its way first through Shakiso before

Figure 1. This suite of untreated emeralds is from a new find in Ethiopia's Seba Boru district. The largest faceted stone weighs 10.64 ct. The largest rough crystal weighs 63.12 g. Photo by Robison McMurtry, courtesy of Michael Nemeth Inc.

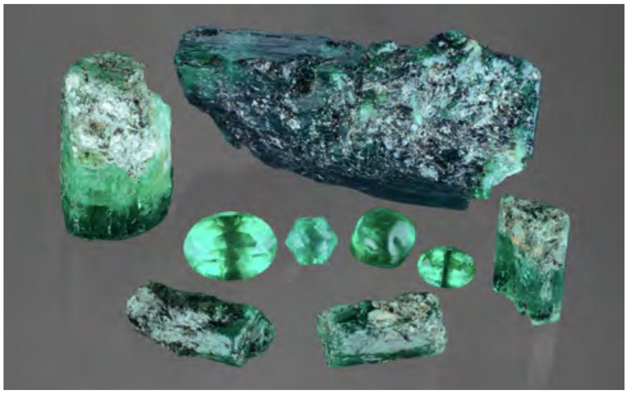

Figure 2. The new deposit of Ethiopian emerald is located near the town of Shakiso, about 12 hours from Addis Ababa.

being sold to dealers in the capital city of Addis Ababa, about a 12-hour drive from the mining area.

According to Tewoldebran Abay, the mineral marketing director of the Ministry of Mines, Petroleum and Natural Gas, more than 100 kilograms of emerald rough have been produced to date. Mining still is done the traditional way using hand tools, without heavy machinery.

Figure 3. Author Michael Nemeth sorts through parcels of gem-quality rough emeralds from the open market in Shakiso. Rough crystals can weigh more than 20 g, with reports of some weighing almost 100 g. Photo by Michael Nemeth.

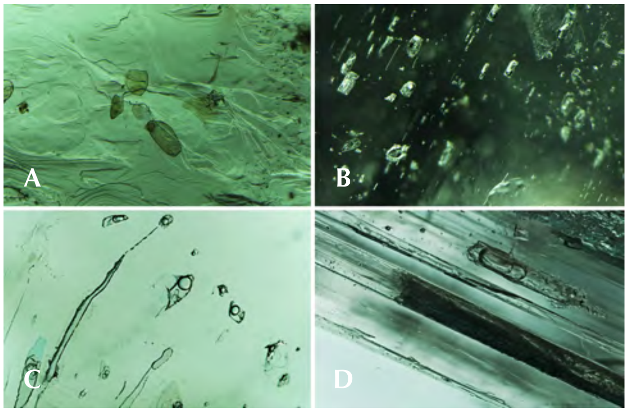

Figure 4. Microscopic observation of the Ethiopian emeralds revealed (A) biotite crystals; (B) blocky multiphase inclusions; (C) multiphase inclusions containing a liquid, gas, and multiple daughter crystals seen parallel to the c-axis; and (D) a multiphase fluid inclusion showing liquid and gaseous CO_2 phases and an immiscible aqueous liquid (parallel to this inclusion are several growth tubes). Photomicrographs by Nathan Renfro (A and B) and Victoria Raynaud (C and D). Field of view 2.04 mm (A), 1.79 mm (B), 1.07 mm (C) and 1.03 mm (D).

Samples from the new deposit, acquired from multiple independent sources, were examined at GIA's Carlsbad and Bangkok laboratories. Even though most of the material is commercial grade, lighter in saturation, and moderately to heavily included, fine gem-grade crystals of exceptional size, color, and clarity (see figures 1 and 3) are obtainable and can produce stones that do not require clarity enhancement. Many of the rough crystals were completely covered in dark biotite crystals, but had an extremely pleasant green color when examined with transmitted light. However, these Ethiopian crystals often do not yield large clean stones because their interior is riddled with dense, dark biotite mica crystals. Some show a double termination, but most are broken and heavily included on one end. Usually only one end of the crystal is clean enough to yield faceted gems. The matrix minerals attached to some of the emeralds were identified as dark brown to black biotite flakes, quartz, and kaolinite.

These emeralds are very similar in appearance to other schist-hosted emeralds—in particular, those from Brazil and Zambia. Among the faceted and rough samples examined, blocky multiphase inclusions and irregular biotite crystals were the most common microscopic features observed (figure 4). Otherwise, the gemological properties were very consistent with emeralds, including an average specific gravity of 2.73 and a refractive index of 1.581–1.589. These emeralds were generally inert to long- and short-wave UV exposure due to their moderately high iron content, which is typical of schist-hosted emeralds. UV-Vis-NIR spectroscopy results (figure 5) were consistent with emeralds colored by chromium and vanadium. The Fourier transfer infrared (FTIR) spectrum was consistent with beryl, as expected, but did not reveal any other diagnostic features.

Quantitative trace element chemical analysis was performed with a Thermo Scientific iCap Q inductively coupled plasma–quadrupole mass spectrometer combined

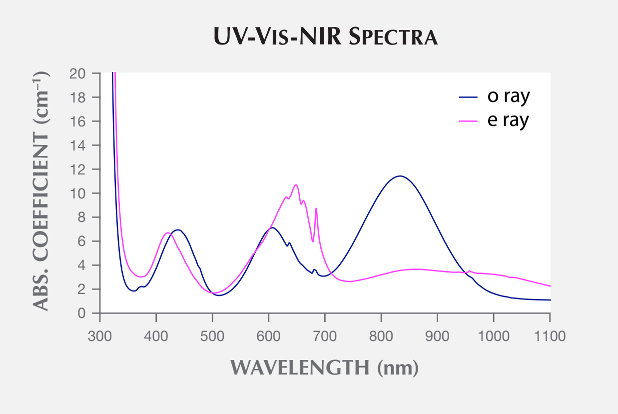

Figure 5. The characteristic UV-Vis-NIR spectra of the new emerald production from Ethiopia.

with a New Wave Research UP-213 laser ablation unit. The analyses were compared to data from other known sources using GIA reference samples, including Zambian and Brazilian schist-hosted emeralds. Based on the results, it was possible to separate the new find of Ethiopian emeralds from other sources by comparing trace alkali metals and some transition metals (figure 6).

Due to heightened tensions and fear of price instability, most of the mine area was temporarily closed by a joint effort of the mining associations and the local government from early November through December 2016. It has been reopened, but now all dealers, including Ethiopian dealers, need written permission to enter the Shakiso area for buying. The law is vigorously enforced, and penalties are severe.

This exciting discovery in Ethiopia will provide a new source of large, high-quality emeralds for the gem and jewelry trade. So far, this deposit appear to be quite promising, as significant production was seen in the recent gem shows in Tucson, Bangkok, and Hong Kong. Only time will tell how significant this deposit will be.

Nathan Renfro and Ziyin Sun
GIA, Carlsbad

Michael Nemeth
MLN Gems, San Diego, California

Wim Vertriest, Victoria Raynaud, and
Vararut Weeramonkhonlert
GIA, Bangkok

Fine gems and update from Myanmar. At the AGTA GemFair, Edward Boehm (RareSource, Chattanooga, Tennessee) showed us a succession of top-quality gems. Boehm is a geologist, gemologist, and accomplished gem dealer who works with rare and higher-end gems. He noted that the price of spinel from Myanmar has increased dramatically, with recent prices at the source more than double those of previous years. He explained that spinel has gained favor in Myanmar, which is reflected by the higher prices at this year's show.

Boehm noted that a growing appreciation for spinel from all sources is driving higher market prices. As an example,

Figure 6. LA-ICP-QMS quantitative trace-element composition analysis of alkali and some transition metals (measured in ppmw) proved useful in separating this new deposit of Ethiopian emeralds from Brazilian and Zambian schist-hosted deposits.

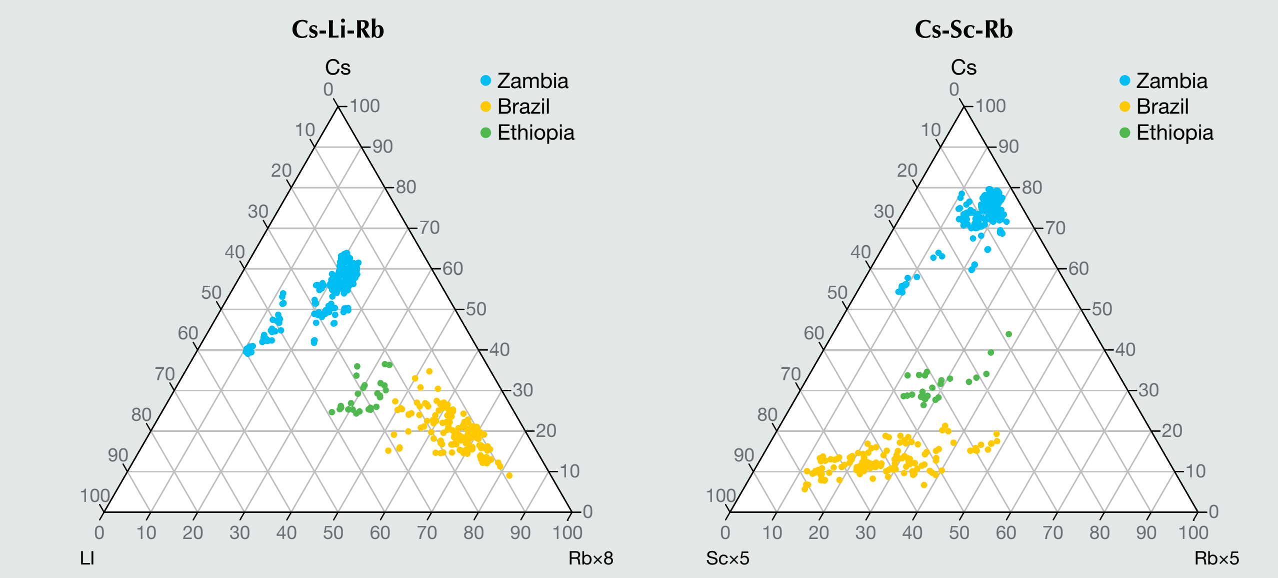

Figure 7. Suites combining blue-to-violet pastel colored spinels with red to rose-colored gems of similar tone. The blue gems range from 3.63 to 8.30 ct and the pink to red examples from 3.16 to 5.70 ct. Photo by Albert Salvato; courtesy of RareSource.

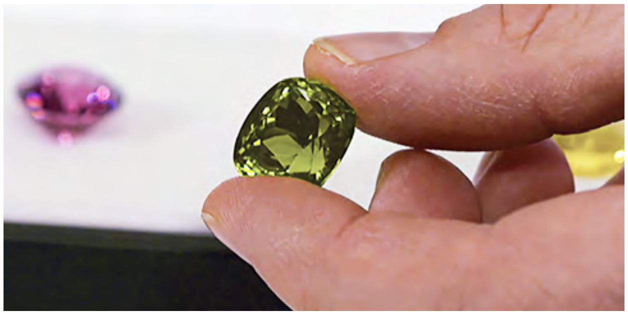

Figure 8. This cushion-cut 20.41 ct Burmese peridot shows a softer appearance due to a multitude of tiny inclusions. Photo by Albert Salvato; courtesy of RareSource.

he showed us a beautiful oval 21.56 ct Sri Lankan pink spinel cut to make the most of the gem's high clarity and moderate dispersion. The size, clarity, and brightness are reminiscent of Tajik spinel. He compared this bright lilac pink Sri Lankan spinel with a strong orangy red square cushion-cut 9.82 ct Burmese gem, which he described as having a "flame" color. The per-carat price of the flame-colored Burmese stone is almost double that of the Sri Lankan spinel—$12,000 per carat wholesale versus $7,000 per ct. A strong red "flame" color makes the price jump significantly. If the stone were above 10 ct, Boehm added, the price would further jump to around $15,000 per carat.

Pastel blue to violet spinels are also selling well for Boehm. Designers like to mix these delicate blues with pinks or "rose" colors of similar tone and saturation to produce very attractive suites and sets. The pinks help to highlight the violet or purple in the pale blues, he added. The bluish violet examples he showed us hailed from Sri Lanka and wholesaled for $1,200–$1,500 per ct (figure 7). Complementary rose-colored gems came from a variety of sources—including Vietnam, Sri Lanka, and Myanmar—and ranged from $1,000 to $1,800 per ct.

Boehm explained that the most sought-after color is the "electric" haüyne blue, which comes from Luc Yen, Vietnam, and is only sporadically available in small sizes. He added that the light-toned, gray-to-violet blue colors are more available than in the past—partly because there's more demand so more people are bringing it to market.

Like Burmese spinel, Burmese peridot is currently in vogue. Boehm showed us a fine 20.41 ct cushion-cut gem (figure 8). The presence of a multitude of tiny inclusions lend it a softness and reduce extinction. By comparison, fine Pakistani peridot—which is also available in large sizes—has a more "crystalline" appearance and deeper color, but shows more extinction. He explained that the price of Burmese peridot has recently gone up sharply. A top gem like the one in figure 8, which would formerly have been in the $250–$350 per carat range, is now wholesaling for $450–500 carat and even up to $600 per carat. He cautioned buyers to check whether a stone shows doubling in the pavilion in the face-up position, which is considered less desirable. Buyers want to ensure the stone is oriented in such a way that doubling isn't visible through the table.

Next, he showed us a rich green, 4.81 ct cushion-cut demantoid garnet from Russia, which contained a golden-colored horsetail inclusion. Such a gem would wholesale for $15,000 per ct, he said. According to Boehm, gems of such pure green color rarely come out of the ground—they are typically heated to this color. This treatment has been going on for 10–15 years, he explained. Despite this treatment, the demantoid is still an exceptional stone.

Boehm explained that judicious heating converts a yellowish green gem to a vibrant green but removes some of the stone's characteristic fire, making it an almost "electric" green color. He prefers a balance of color and fire, acknowledging that the gem's inherent fire—flashes of red and blue coming off a green bodycolor—is part of its unique appeal. In today's market, any demantoid over 2 ct is extremely rare, so this gem's size of almost 5 ct makes it very desirable.

The demantoid was from new production rather than the secondary market, Boehm explained. He added that there is still newly mined supply and treaters are perfecting heating techniques to make gems much more vivid, although not all respond like this one.

Finally, he showed us a striking 31.79 ct Sri Lankan pear-shaped sapphire with *padparadscha* color—a delicate pink flushed with a bloom of orange (figure 9). He explained that the gem had been recut three times to perfect its shape and proportions. The objective of recutting the original old-style cut was to close the window on the pavilion, but any further work would affect the brilliance and might even lose the cherished pinkish orange color. He added that when cutting padparadscha sapphire, it is very hard to keep that balance of pink and orange, because sometimes the orange might be in just one portion of the stone, which could easily be removed accidentally. A gem of this size is enormous for a padparadscha, he noted, and the wholesale asking price would be in the neighborhood of $30,000–$35,000 per ct.

Boehm noted that on October 7, 2016, President Barack

Figure 9. This 31.79 ct Sri Lankan padparadscha *sapphire shows the cherished combination of a pink bodycolor suffused with orange. Photo by Albert Salvato; courtesy of RareSource.*

Obama signed an executive order lifting U.S. sanctions on Myanmar, allowing Burmese jadeite and rubies, and any jewelry containing them, to be imported into the United States. The sanctions had been imposed in 1997 (see https://www.treasury.gov/resource-center/sanctions/Programs/pages/burma.aspx).

Boehm felt fortunate to be in Mogok (figure 10) when the ban was lifted and was able to celebrate with many of the local miners and brokers. He hoped the change would significantly improve the supply of Mogok gems but anticipated that any increase in gems reaching the U.S. from this source would likely take some time. Most if not all Mogok mining licenses have been suspended as the Burmese parliament and ministries work together to rewrite mining laws in Mogok and the jade mining areas in Pagan. These laws have been in place for more than 100 years and have changed little.

Figure 10. In October 2016, an AGTA delegation visited gem markets and mines around the world-famous locale of Mogok. Their mission was to report back on conditions within the local gem and mining industry after the new government took office. Photo by James E. Shigley.

When Aung San Suu Kyi's National League of Democracy party won a majority of seats in parliament during the November 2015 election, it was able to effect change with a special focus on the environment. The new administration's objective is to make reclamation integral to obtaining a mining or prospecting license, so that when mining finishes, the licensee will be obligated to return the land to its original condition. The government wants to ensure these laws are enforced and that environmental and ethical standards conform to Western expectations for the gem mining sector. The aim is for the new mining laws to meet the internationally accepted standards outlined by the Organization for Economic Cooperation and Development (OECD), a group of 34 democratic countries that develop economic and social policy to support free market economies. These principles are laid out in the policy paper *OECD Due Diligence Guidance for Responsible Supply Chains of Minerals from Conflict-Affected and High-Risk Areas* (http://dx.doi.org/10.1787/9789264252479-en). For more information on corporate social responsibilities and ethical colored stone supply chains, please see J. Archuleta, "The color of responsibility: Ethical issues and solutions in colored gemstones," Summer 2016 *G&G*, pp. 144–160).

Boehm mentioned the recent AGTA October 2016 delegation (figure 11) to Myanmar that visited the cities of Yangon, Nay Pyi Taw, Mandalay, and Mogok. Along with other U.S. trade and industry bodies, AGTA is seeking to reestablish responsible gemstone trade between the two countries. This is only possible because of the political and economic progress Myanmar has made in the past six years, but it also depends on Myanmar's gemstone sector meeting international standards such as OECD's guidelines.

The delegation, which included GIA researcher Dr. James Shigley and representatives from Jewelers of America, met with a cross section of stakeholders, including the U.S. ambassador, ministers and representatives of the Myanmar government, international and local organizations, trade associations, gem dealers and traders, and mine owners. They visited a number of gem markets and mines, including the Baw Maw mine (figure 12) and the Taung ruby and sapphire mine.

According to Boehm, the delegation was an impartial group sent to look at the situation "on the ground" in Myanmar, particularly in Mogok. He explained that it was an "eye-opening" experience and although conditions were much better than the group anticipated, there was room for improvement. The delegation made a series of observations that were set out in their white paper, *Step by Step – Myanmar Gem Sector Emerges from Isolation and U.S. Sanctions*, which is available from AGTA's website at http://agta.org/info/docs/burmawhitepaper2016.pdf

Figure 11. The October 2016 AGTA delegation at Mogok's Taung ruby and sapphire mine. Edward Boehm and GIA's Dr. Jim Shigley are at left. Photo courtesy of James E. Shigley.

Boehm indicated that Mogok was still beholden on the U.S. gem industry's ongoing efforts to ensure that Myanmar's government follows through with its promise to manage the gem sector properly and that the Burmese people benefit from the gems. He cautioned that a lot of mining licenses remain suspended. Therefore it's very unlikely that U.S. businesses will see much production until these are reinstated, possibly in late 2017. He forecasts that the U.S. trade at large will have to wait at least another year before production appears in earnest. At that point, he expects many more U.S. buyers will travel to Mogok and competition for scarce goods will drive prices up, but at least the goods can be legally imported into the U.S. once more.

He reported that because of the government's suspension of mining licenses, Mogok's mines are currently closed again after a brief reopening. Boehm suspects several reasons for caution on the part of the authorities. Firstly, it would be very tempting for miners to produce as much material as possible now that dealers from the U.S. can legally buy gems in Mogok, so the government wants to buy time to regulate mining ethically to make sure the Burmese people are protected (figure 13). Secondly, they want to prevent large foreign investors from taking over the mining sector. Finally, there are some security issues with traveling the new road leading into Mogok at night, which the authorities want to correct before mining licenses are reinstated. Boehm considers these good signs that demonstrate the Myanmar government's commitment to security and corporate social responsibility for the good of its citizens.

Duncan Pay

Figure 12. Workers sorting heavy mineral concentrate from the Baw Mar mine near Mogok. Photo by James E. Shigley.

Conversation with Gemfields. UK-based Gemfields is widely considered the largest producer and distributor of responsibly sourced colored gemstones. This year in Tuc-

Figure 13. During the AGTA trip, delegates watched villagers searching for peridot in the waste tailings of the Pyaung Gaung mine near Mogok. Photo by James E. Shigley.

Figure 14. The massive open-pit Kagem emerald mine in Zambia is perhaps the largest colored gemstone mining operation in the world. Photo by Andrew Lucas, courtesy of Gemfields.

son, we had an exclusive interview with CEO Ian Harebottle to get his insights on the company and the colored gemstone industry overall.

Unlike the diamond industry, almost every segment of the colored stone trade has traditionally lacked scale and systematic practices. Gemfields has dramatically changed this dynamic in some of the most influential colored stone categories. The company is actively working on three mining operations: the Kagem emerald mine (figure 14) and the Kariba amethyst mine in Zambia, and the Montepuez ruby mine in Mozambique. Among the three, Kagem and Montepuez are world-class operations, supplying about one-third of the global emerald production and 70% of ruby production. Before, both stone types experienced fluctuating supply and chronic shortages. Gemfields is very optimistic about the expected supply from Kagem and Montepuez, based on scientific field surveys and detailed geophysical and geochemical studies.

To stabilize supply for the global market, Gemfields requires the mines to reserve one year's production in case yield declines significantly. Based on the authors' research, many Gemfields clients appreciate the standards set by the company on emerald and ruby mining and distribution. The consistent supply and well-tuned rough grading systems grant buyers more time to focus on faceting, jewelry making, and sales. This practice also has a positive influence on other mining companies that aim to meet the same standards.

In 2013, Gemfields purchased the iconic luxury brand Fabergé. Harebottle explained that the deal does not reflect an interest in vertical integration but in creativity and uniqueness in the market, an area where Fabergé has a rich heritage (figure 15). Therefore, he hopes that the brand can be a platform of magnificent jewelry designs, igniting the passion for colored gemstones in the younger generation. According to Gemfields, Fabergé's sales orders jumped 95% during the second quarter of fiscal year 2017.

When it comes to corporate social responsibility, Gemfields sets a good example across its mining locations through successful joint ventures and community programs. The Kagem emerald mine is one of the only mining companies that has paid federal taxes in the past 15 years in Zambia. The Montepuez ruby mine was named Mozambique's most transparent tax payer and the most important job generator in its province. Harebottle described the different challenges the company has faced and will be facing in the future. Since the sites are usually located in areas

Figure 15. The merger of Gemfields and Fabergé should continue to inspire one-of-a-kind colored gemstone pieces. Photo courtesy of Fabergé.

that lack robust mining regulations or laws and some countries have a very long mining history, the company often applies different strategies to localize itself. To champion responsibility and sustainability on location, a foreign company such as Gemfields needs to make the local people feel confident about their future, and this is fueled by job opportunities.

Since its founding less than 10 years ago, Gemfields has always sought to rekindle the passion for colored gemstones. Harebottle likes to compare the company's role in colored stones with that of De Beers in the diamond sector, especially when the latter heavily promoted diamonds. He also feels that colored gemstones should have a stronger position in the luxury goods market. With this mission under way, and active exploration for new production sites in Colombia and Ethiopia, more accomplishments are expected from this major colored gem supplier.

Andrew Lucas and Tao Hsu

Figure 16. The washing process used by Mustang Resources is different from most jigs used for colored stone mining. Photo courtesy of Mustang Resources.

New ruby miner in Mozambique. Mustang Resources LLC, a publicly listed Australian company, is developing a ruby mining operation in northern Mozambique. With the success of the colored stone mining giant Gemfields, Mozambique has secured its position in today's global ruby market. Mustang's concession is located about 8 km northwest of Gemfields' Montepuez ruby mine. Both properties are located on the ruby mineralization belt in the Montepuez Complex, where ideal physical and chemical conditions favored the formation of gem-quality ruby. In between the two concessions there are some designated ruby-bearing areas where individual small-scale miners can legally work.

While the geology of the Mustang operation is generally similar to that of the Gemfields concession, the bulk sampling strategy and washing process are slightly different (figure 16). Currently, the miners focus on exploring and sampling the secondary deposits. They open pits of 20 × 5 meters or 20 × 7 meters and immediately refill the first pit before opening the adjacent ones; this way, no large pit is left open on the surface of the mining area. Mustang has been using scrubbers instead of log washers to break the clay bodies in the ore. A new customized scrubber system will soon be in place to optimize this process. Unlike the jig system applied by many colored gemstone mining operations around the world, the team uses a giant rotary pan to concentrate the heavy minerals, including ruby, through the centrifugal forces generated during rotation.

Since the team from Mustang started to develop the project in early 2016, the exploration, bulk sampling and ruby recovery have made significant progress. Christiaan Jordaan, the managing director of Mustang's Montepuez ruby project, informed the authors that the washing plant had been successfully relocated and tuned to operate efficiently and that grading into parcels had begun (figure 17). The team has test marketed these rubies in the United States, where some large, significant stones will be cut by well-known cutters. Mustang will also test the ruby market in Asia and other parts of the world. Jordaan reassured the authors that Mustang will focus on improving quality of life in the mining community and promoting their ruby as an ethically mined product. Since the beginning of this ruby mining project, the company has hired and trained 70 local employees to work together with foreign experts.

Andrew Lucas and Tao Hsu

New emerald production from Belmont. The Belmont mine in Brazil has been a key emerald supplier in the global market for the past 40 years. It is one of the very few companies that can guarantee a complete mine-to-market chain

Figure 17. Taking a cue from Gemfields, Mustang Resources grades rough rubies into specific quality and size parcels. Photo by Andrew Lucas and Tao Hsu, courtesy of Mustang Resources.

of custody for the emeralds it produces. As open-pit mining became more expensive over the past decade, underground mining gradually generated a larger share of production at Belmont. Today, all mining activity at the original open pit is underground. Open-pit mining will continue in the two pits to the north of the original site. General manager Marcelo Ribeiro revealed some exciting news about the Canaan mine, about 2 km away from the original pit, and expansion plans for the sorting and cutting facilities.

Belmont acquired interest in the Canaan mine through a partnership with its original owners. Exploration and underground mining infrastructure are still ongoing at this site. Although the operation just started about a year ago, Ribeiro and his team have learned a lot about this deposit through field studies and chemical analysis. The interesting finding is that there is plenty of beryllium in this area, which makes the survey of chromium concentration critical to locating the mining targets. This is the exact opposite of the situation at the original Belmont site, where beryllium is the critical factor.

According to Ribeiro, two geological events were responsible for emerald crystallization in the area. The original Belmont mine is mainly influenced by the first event, Canaan by the second. Based on research, the second event was much stronger at the Canaan mine, destroying most of the crystals formed during the first event. The second-generation emeralds have a lower chromium concentration, and therefore lighter green colors, but they are often larger and cleaner than those from the Belmont mine (figure 18). The new production is sometimes slightly yellowish or bluish. Ribeiro is very excited about the Canaan production, which allows the company to provide a greater selection to its clientele.

Belmont currently cuts 50% of the Canaan production by value. All medium- to high-quality stones are cut onsite to add more value. To increase the capacity of the operation and make mining cheaper for long-term sustainability, the company plans to add two more optical sorters and further expand the cutting facility. Belmont will also keep promoting its mine-to-market product and better communicate with younger buyers to make them feel proud of their emerald purchases.

Figure 18. Second-generation stones from Brazil's Canaan mine are often cleaner and lighter in color than those from the first geological event. Photo by Eric Welch/GIA.

Andrew Lucas and Tao Hsu

Importance of the secondary market for fine gems. At the AGTA show, Dave Bindra (B&B Fine Gems, Los Angeles) showed us some exceptional items he recently sourced from the secondary market. These are previously sold goods recirculated back into the market by the former owners or their heirs.

Bindra also updated us on his perception of U.S. traders' reaction the withdrawal of sanctions against Myanmar (Burma) and what that means for U.S. dealers like him. According to Bindra, most U.S. dealers greeted lifting of the trade embargo with enthusiasm as they can legally import and trade Burmese rubies again. Prior to this they were limited to trading items that had come into the country "preban." Bindra doesn't expect prices to come down; rather, he projects they will strengthen as American demand and consumption of Burmese goods grows. He noted that during the ban, some consumers and certain major brands stopped consuming rubies altogether, basically because they weren't open to consuming rubies from sources like Mozambique, which has become a prolific source of commercial-to-fine grade gems. Now that the ban is lifted, Bindra hopes many of these companies will start buying and selling Burmese rubies again. The main issue now is the very limited supply coming out, but he says there's definitely a strong market for fine-quality stones.

Bindra highlighted some exceptional pieces at his booth to illustrate the importance of the secondary market for his inventory. The company also procures gem materials from currently active mining areas, but the secondary market is important for larger, more important stones, which are scarce as a percentage of new production. As an example, he shows us a fine, oval-cut, 55.52 ct copper-bearing tourmaline from Mozambique (figure 19). He notes this particular stone came out of the original 2007 production from Nampula Province, northeastern Mozambique, near the village of in Mavuco (see B.M. Laurs et al., "Copper-bearing (Paraíba-type) tourmaline from Mozambique," Spring 2008 *G&G*, pp. 4–30).

B&B actually sold this stone about seven years ago, and was lucky to reacquire it when the opportunity arose in 2016. Bindra considers this fortunate as there is no production from this deposit today and it would be impossible for them to find an item like this, other than the secondary market.

Another example he cites is a beautiful 5.06 ct trillion-cut benitoite (figure 20). This gem—a barium titanium silicate—is typically colorless to blue, and is noteworthy for its high refractive indices, moderate birefringence, and strong dispersion. It comes from just one mine, located in

Figure 19. This exceptional oval-cut, 55.52 ct copper-bearing tourmaline from Mozambique was previously sold by B&B. They recently reacquired it through the secondary market. Photo by Eric Welch; courtesy of B&B Fine Gems.

San Benito County, California (see B.M. Laurs et al., "Benitoite from the New Idria District, San Benito County, California," Fall 1997 *G&G*, pp. 166–187). The benitoite mine has been closed for years. Bindra describes this 5 ct as an "astronomical size for this deposit"—the typical size range of commercially available finished gems from this mine was between 0.30 and 1.70 ct. He noted that this gem was a prized possession of an original mine owner.

Bindra also showed us a couple more recirculated pieces: a fine 15.06 ct double-sided black opal cabochon (figure 21) with broad flashes of play-of-color from Australia's Lightning Ridge and a 19 ct antique-cut Brazilian Imperial topaz. This last stone was old, unheated material from Ouro Preto. The stone came out of an old collection and was a little over 20 ct. They were able to recut it with minimal loss of weight to significantly improve luster and brilliance. Bindra told us these gems underscore the importance of the secondary market for his inventory. While it doesn't supply the day-to-day production B&B needs, it does produce truly exceptional items from time to time. He noted that fine colored gemstones always retain their value, which is why B&B is often able to reacquire items over a period of time. He always keeps this in mind whenever selling rare, esoteric gemstones.

Next, Bindra showed us one of the most exceptional stones he's had in years: a 10.22 ct cushion-cut Brazilian alexandrite. He adds that B&B has trouble fulfilling orders for 6 mm (approximately 1.00 ct) round alexandrite with current Brazilian production, so finding a 10 ct size is really an anomaly. According to Bindra, it came out of an old collection in Japan, where it sat in a safe for 20 years. He said he "couldn't write the check fast enough" to get it into B&B's inventory. In this case, there was no need for repolishing. The gem is unusual not just for its size and the quality of its color change, but also because of its brilliance. He notes that Brazilian alexandrite of this rich blue-green to reddish purple color tend to be "over dark" and lack life. This stone was faceted with a typical Portuguese pavilion, which confers considerable brilliance. Due to these factors, Bindra adds, the wholesale value of a truly fine gemstone like this is well over $55,000 per carat.

Finally Bindra shows us a 20-ct-plus star sapphire with a sharp six-rayed star, strong blue bodycolor, exceptional translucency, and a well-proportioned, high-domed cabochon shape. It's another piece that's "come out of recirculation," says Bindra. He suspects the current marketplace scarcity of fine blue star sapphires is due to a newly discovered heating process, leading to a lot of fine-color examples being recut into faceted gems. He cites an example of a 23 ct star sapphire, which might be heated and refashioned into a top-gem royal blue color faceted stone in the 10–15 ct range. For some people, that's more desirable, so stars are becoming rarer. Not every stone can be heated and improved, as they might break due to the unforeseen way inclusions react to the heat.

Bindra sees strong demand from the top one percent of consumers. He notes that exceptional gemstones are in very high demand, as more than ever people find value in

Figure 20. This fine-quality 5.06 ct trillion-cut gem is exceptionally large for benitoite. Photo by Robert Weldon/GIA; courtesy of B&B Fine Gems.

Figure 21. This 15.06 ct double-sided black opal cabochon from Lightning Ridge was another recirculated gem offered by B&B. Photo by Eric Welch; courtesy of B&B Fine Gems.

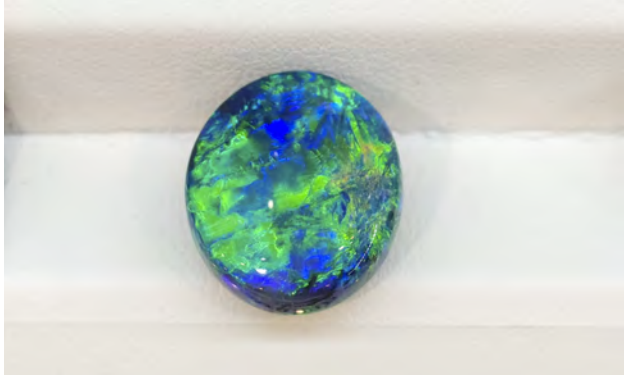

hard assets—fine art, classic automobiles, fine wine, high-end watches, important diamonds—and colored gemstones are "in that same conversation." Bindra professes some skepticism about the middle of the market, where commercial to mid-grade material is not moving as well. At the top end of the market, high-end colored gemstones are difficult to find because of competition from overseas—from new markets, from new capital—especially in Southeast Asia, where there is a cultural affinity for consuming fine colored gemstones.

Duncan Pay

Cultured pearl market update. At the 2017 AGTA show, Fran Mastoloni (Mastoloni Pearls, New York City) provided a cultured pearl market update. Mastoloni is a 30-year veteran of the Tucson show and well positioned to place the ups and downs of demand in context. There is a real desire for cultured pearls, he says, but people have moved away from the traditional white necklace. Partly this is because cultured pearl sources have become much more diverse in recent years, with French Polynesia, Australia, the Philippines, Indonesia, and China contributing a diverse array of cultured pearl types, shapes, sizes, and colors (figure 22).

Figure 22. The range of necklaces at Mastoloni's AGTA booth included innovative blends of different cultured pearl types. Photo by Eric Welch; courtesy of Mastoloni Pearls.

Mastoloni's clients are seeking—and selecting—something different. "They all want a unique necklace," he says. And since the second quarter of 2016, he's seen demand pick up considerably. Most clients don't want to spend a fortune, but they do want the piece they choose to be unique and individual. His job is to create cultured pearl necklaces that meet their needs.

To demonstrate, Mastoloni showed us his "Fantasy" necklace: a standard-length strand combining South Sea and Tahitian cultured pearls with lighter gold ones from Indonesia. This blends a repeating pattern of large (up to 16 mm) eye-catching, semi-baroque pearls with smaller examples—down to 8 mm—to create a large, mixed look. The use of light and dark pearls also confers the ability to use the piece on a variety of clothing colors for day or night use, he added, so it's very versatile. He added that products must also appeal to female self-purchasers, so the retail price point—less than $2,000 per strand—is an important consideration. This is a very important—if not the most important—market segment for him today.

Mastoloni showed us another successful cultured pearl line for the company, which he dubbed the "Cocktail" necklace (figure 23). It combines Philippine gold pearls, white Australian South Sea, and lighter Tahitian pearls to create a long necklace that can be draped twice. Again, every necklace is individual, so that a customer can "key into" an individual pearl—maybe a large South Sea or Tahitian—and identify that necklace as unique. Examples like these, he explained, transform the concept of what a cultured pearl necklace might be.

Customers are similarly drawn to baroque pearls for their uniqueness. Mastoloni used a variation of the "Cocktail" necklace to illustrate the point, this time with baroque pearls ranging from 16–17 mm plus down to 9 mm. The organic shapes bring texture and movement to the piece and "make it fun."

The next necklace he showed us blended 9 mm baroque white South Sea "keshi" pearls with 14 mm dark Tahitian round cultured pearls, creating two transitions: from light to dark and from organic shapes to regular, round ones (figure 24). A customer might own all three of these necklaces, he said, and use them for different occasions.

Also popular are variations on the wave necklace, which blends a uniform strand of round white Japanese akoya cultured pearls with "waves" of graduated silvery black Tahitian cultured pearls that swell and pinch out against the white of the akoyas. The mix of the different cultured pearl types working together is what makes these

Figure 23. The "Cocktail" necklace features a combination of differently sized round cultured pearls: darker Tahitian, golden Philippine, and white Australian South Sea. Photo by Eric Welch; courtesy of Mastoloni Pearls.

designs so successful. They're the kind of "fashion-forward" pieces that stylish but price-conscious consumers pick out, he says.

Of course, sourcing pearls for all these necklaces is always a challenge for Mastoloni. One of his key considerations is maintaining standards. For the "Cocktail" necklaces he has to source pearls of the same tone, color saturation, and luster. You just can't throw pearls together and expect them to look good, he explains. It requires an understanding of the product along with consistency in both quality and look—as well as an enormous amount of pearls.

Mastoloni asked us to look at professional women of power on television, who frequently wear significant pearl necklaces. Their choice might be a necklace combining different pearl colors, or a uniform one with large round white South Sea or Tahitian cultured pearls. Fine pearls can be worn in the boardroom or at social gatherings—they show that the wearer "has arrived." No other jewelry is as versatile.

Mastoloni noted that the supply of Tahitian cultured pearls has changed. Although there looks to be a good variety of subtle colors, he's not seeing the same wide range of colors as 10–15 years ago. This appears to be because the culturing process is improving and there is more control over color consistency. This is better from the point of view of investors, because consistent colored pearls are easier to match and sell. As a result, those investing in pearl cultivation find it easier to recoup their expenses.

Next, he showed us single pearls and collection pieces, starting with a 23.3 × 28.6 mm Australian baroque South Sea pearl that was solid and unblemished on all its surfaces. Single pearls like this one are unique items that a person can make their signature piece—something they wear every day.

Figure 24. This necklace features 14 mm round Tahitian cultured pearls in the front and 9 mm South Sea "keshi." Photo by Eric Welch; courtesy of Mastoloni Pearls.

Figure 25. A pair of 15 × 18.5 mm light pistachio Tahitian cultured pearls, A matching-color drop shape measuring 16 × 22.7 mm makes up a trio. Photo by Eric Welch; courtesy of Mastoloni Pearls.

Pairs, such as the 15.0 × 18.5 mm Tahitian cultured pearls seen in figure 25, are also perfect for unique pieces. Their light pistachio color is one of the colors Mastoloni used to love but can no longer easily obtain. Serendipitously, he found a matching-color larger drop shape measuring 16.0 × 22.7 mm to make up a trio (again, see figure 25). According to Mastoloni, the right designer could make an incredible piece out of these.

His next piece was a 16 × 23 mm Tahitian drop pearl with a unusual shape and excellent luster. It was a near-perfect teardrop with a very attractive slightly asymmetrical tip, shaped almost like a drop of water. It begs attention, he explains, a pearl like this could be the center of attention in a one-of-a-kind necklace. Mastoloni confirmed that such teardrop-shaped pearls are now difficult to find in Tahitian production. As pearl culturing techniques improve, drop pearls are nowhere near as desirable—or as profitable to produce—as spherical ones. Pearl farmers are more concerned with return on investment, so they are really striving to produce more round pearls. As pearl culturing methods improve, consequently, it becomes harder and harder to find nice teardrops—producers make a lot of less attractive, misshapen examples which bring down the value of the harvest.

Finally, Mastoloni showed us a top-quality pair of 15.3 mm round golden pearls. He noted that golden pearls—which are generally produced from the gold-lipped oyster in the Philippines and Indonesia—are still a good business, with much stronger demand in Asia than in the U.S., although the market probably peaked about a year ago. He notes that there might be a little oversupply in Asian markets, but he expects it to be temporary. As far as quality is concerned, Mastoloni's advice is to look for a pearl that has a good "gold" color—he always likens it to a "ring color"—"you don't want yellow and you don't want green, but it's got to have a richer gold to it," he says. Indonesia is always going to have a steady supply of pearls, because cultivation takes place over such a large area, he says but cautions that there's so much champagne and creamy greenish yellow production that he cannot use. He notes that their supply is getting better, but it's not quite there yet. In his opinion, cultivators in the Philippines are excellent at producing gold pearls, as their waters and their oysters are better suited for these products. Indonesia will continue to produce all colors, and Australian pearl farmers will concentrate on white, while those in Tahiti focus on the different shades and nuances of black pearls.

Duncan Pay

Moroccan amethyst: Mining and marketing. Characteristic "hourglass" color zoning (figure 26) and striking red hematite "finger" inclusions help distinguish Moroccan amethyst. Although amethyst is readily available on the market, the material from Boudi in southern Morocco stands out. While Moroccan amethyst has been featured in *G&G* previously (F. Troilo et al., "Amethyst from Boudi, Morocco," Spring 2015, pp. 32–40), we gathered some fresh insights on the mine and the marketing strategy for this material from Alaeddine Rafei, who directs grading and sales for Geostone Group in Morocco.

Figure 26. These amethyst crystals from Morocco show the strong zoning characteristic of stones from this location. Photo by Eric Welch/GIA, courtesy of Geostone Group.

About 40 years ago, a group of nomads were stuck in a storm in the Anti-Atlas mountain range of southern Morocco. The next morning, they found purple crystals on the washed ground. The nomads kept bringing the crystals to tourist shops in the villages nearby. Seven years ago, a geologist and a cofounder of Geostone Group finally had the stones analyzed by GIA and confirmed that they are amethyst. Mining started in 2011–2012 and has continued on a small scale since then. From 2011 to 2015, the miners mainly used hand tools to remove the earth and extract the crystals. As the wall has gotten pushed further back, excavators have been used since 2015 to move earth. The miners are still hand picking crystals out of the removed earth.

Rough amethyst crystals are transported to the company's warehouse in Casablanca for washing and grading. Washing is done with water and acid. Rafei explained the four grades of Moroccan amethyst. The topmost grade consists of double-terminated single crystals, which are extremely rare. Rafei explained that only 1% of the production is gem quality (figure 27), of which only 2% are the double-terminated crystals. Next come the AAA grade, which refers to the deep purple stones, and the slightly less purple AA grade. The AA grade is the most common on the market. The fourth grade is a category called Rose du Maroc. Amethysts falling to this grade have an even lighter purple color than AA stones.

Marketing these amethysts is an even greater challenge. As people can imagine, the rough amethyst market is very competitive, since there are many sources in different countries. In 2013, when Geostone's founders brought their Moroccan amethysts to Tucson to test the market, they went home deflated by the feedback. Large colored stone cutting companies see little value in these amethysts. Luckily, the founders got connected with world-renowned gem carver Glenn Lehrer, who became their marketing advisor and took Moroccan amethyst in a completely different direction. Lehrer saw the unique features in these stones and applied his cutting styles and award-wining patented cuts to show off their beauty. The special cuts also better use the rough. The yield of Moroccan amethysts at a normal cutting factory is only about 8%. When Lehrer's special cuts are applied, the yield was increase to an average of 20% for top-quality stones. He also introduced these amethysts to Gems TV. Instead of selling the rough to gem cutters, the company now offers faceted stones and finished amethyst jewelry directly to consumers through multiple TV programs in different countries.

As a result, Moroccan amethyst is not just another amethyst. It is now a brand and trademark of Geostone Group. The mine-to-market story is sold with the gems. The story even landed Moroccan amethyst in the Rio Grande catalog. In return, the company is actively involved in community building in the mining area. It only hires

Figure 27. Morocco produces deep purple amethyst with red hematite "finger" inclusions that can cause red flashes of color. Photo by Eric Welch/GIA, courtesy of Geostone Group.

local Berbers to work in the mine, offering them a good salary and health care. During the past several years, Geostone Group has kept production quite stable and limited mining crew sizes to around 20 people. Wells, roads, electricity, and designated vehicles for schoolchildren and villagers are all provided using profits from the amethyst mine. In 2016, Geostone Group received an award from the Moroccan government to highlight its contributions to social responsibility and gem mining in Morocco.

Andrew Lucas and Tao Hsu

Emerald dealing in Afghanistan. Dealing rough gemstones is never easy. This is true even for gemstones dealers with decades of experience such as Arthur Groom of Eternity Emerald (Ridgewood, New Jersey). Groom has traveled all over the world to purchase emerald rough, and his current focus is Afghanistan. In Tucson, he demonstrated to us the art of rough purchasing and the critical decisions that must be made during this process.

Groom started by opening a parcel of about 260 g of rough emerald (figure 28), which he valued at a minimum of $600,000. He recounted the decisions he had to make in the field in Afghanistan when buying this parcel from miners. Just as with individual colored gemstones, the first thing buyers need to look at is the color of the whole parcel. Tip number one: Always spread out the stones after you get the first impression of the parcel. This is important, because colors always look better when stones are clustered together; spreading out the stones helps the buyer see the appearance of individual stones and better sort them into several groups. Next, do a quick estimation of the percentage of each group relative to the whole parcel. For example, a parcel may contain about 20% lighter-colored emeralds.

Since evaluation is the most critical step in rough purchasing, there are several aspects buyers must pay extra attention to when estimating the value of a certain piece or group. The color, the model (shape) of the crystal, and the clarity features are the three key observations that determine your decision. When looking at color, it is especially important to consider the crystal's core. This is essential for Afghan emeralds, because many of them have a lighter core (figure 29). Stones like these will lose color after faceting, which demands extra planning and often results in a higher weight loss. For emeralds, darker rough is more likely to maintain its color after cutting. The lighter rough tends to lose color, especially when cut into melee.

The rough dealer must visualize how the finished stone can be placed inside the rough based on the model, as it dictates the final yield of the rough. Groom demonstrated the types of emerald that achieve high weight retention and others that do not. There is a large quantity of pencil-shaped rough coming from the mountains of Afghanistan, material once regarded as waste by some miners and buyers. Groom said that with today's technology, these stones can be cut into melee that command on average $500–$1500 per carat. Old Soviet ammunition from the war three decades ago is still used to blast the emerald-bearing rocks due to the shortage of mining dynamite in Afghanistan. This is a problem for emerald mining, since many larger stones are broken during the blasting. The broken crystals also limit the weight retention. For instance, a perfectly preserved rough crystal can reach a yield of 60%, compared to only 10–15% for a broken one.

Figure 28. This 260 g rough emerald parcel was used to demonstrate the methodology in grading and negotiating the purchase of rough gemstones in the field. Photo by Eric Welch/GIA.

The "Four Cs" of colored gemstones are generally the same as for diamonds; however, a fifth "C" is crucial for emeralds. This is clarity enhancement, a common practice in the emerald trade. Imperfections are removed by cutting them out or treating fissures to lower their visibility. In the case of emerald, the latter is more common if higher weight retention and better proportions are desired. The buyer must find the emerald's fractures and make a decision on the possibility of enhancing them and leaving them in the stone. The essence of rough evaluation is to comprehensively consider all the factors and find the balance between them. Mastering the process requires years of

Figure 29. Upon close examination of this emerald crystal, sorted out of a large parcel during a buying trip to Afghanistan, Arthur Groom found the crystal core to be much lighter in color. Photo by Andrew Lucas.

Figure 30. Buying rough emerald in the field under less than ideal conditions, like a miner's office in Kabul, requires discipline and a systematic approach. Photo by Andrew Lucas.

practice and familiarity with both the rough and the finished stone markets.

After evaluation comes the art of negotiation. If the buyer is enthusiastic about purchasing the parcel, the negotiation takes off from there. Based on Groom's experience, buyers need to stay cool and offer reasonable prices to get what they want. The key takeaway here is that as a buyer, you need to know the value of the parcel and show the miners that you know what you are doing. Ridiculously low offers should be avoided, since that would immediately cast doubts on your capability and reputation. Once both sides realize that a fair deal is going to happen, the "sweet spot" for the price can be reached quickly.

Dealing with gemstones is ultimately about dealing with people. Afghan emerald miners (figure 30) are a very strong-willed group. They always come together to sell their stones. These miners do not owe banks money, so there is no pressure for them to sell the goods. In this situation, winning their trust is the key to motivating them to bring in more stones that fit the buyers' needs. Groom reminded us that respecting the locals and bringing value and benefit to them will guarantee good business and long-lasting friendship.

Andrew Lucas and Tao Hsu

Magnificent sapphires from Montana's Rock Creek mine. Potentate Mining marketing director Warren Boyd presented two magnificent sapphires (figure 31) and a suite of fancy sapphires extracted from the company's Rock Creek operation in Montana in 2016. He also updated the authors on this past mining season.

The larger of the two stones is the 12.61 ct blue sapphire, one of the largest of its kind from Montana. It was faceted from a 6.37 g rough that had been heated. The rough showed strong blue color before heating but had a core with heavy silk inclusions. Heating dissolved the silk and enhanced the blue color. The 7.9 ct orange oval is the largest of this color ever recovered from Montana, to Boyd's knowledge. This stone was faceted from a 5.2 g rough of pale greenish color with a dark brownish core. While the rough was of very low transparency, the results of heating were better than expected. The heated rough showed a royal blue rim surrounding a bright orange core. Both stones were faceted by Jeff Hapeman (Earth's Treasury, Westtown, Pennsylvania).

Most of the Rock Creek sapphire is small, and larger stones with spectacular colors are very rare. Because the bulk of the production comes out of the ground with greenish pastel colors, natural stones with bright colors are also very valuable. Boyd and his clients from Americut showed us a suite of natural fancy sapphires (figure 32) recovered in 2016. The company had produced sapphire rough from its Rock Creek deposit for two consecutive mining seasons and gradually built up a large inventory. Potentate is not planning to increase production but to keep it stable in the near future. The company installed a new water clarifier in its washing plant at Eureka Gulch, which recycles the water used in ore washing. The company will keep its focus on building inventory and bridging the gap between supply and demand.

Andrew Lucas and Tao Hsu

Magnesio-axinite from Merelani, Tanzania. Colored gemstone dealer Bill Vance (Vance Gems, Newark, Delaware) showed us some transparent examples of magnesio-axinite, a rare magnesium-dominant member of the axinite group of minerals. Axinite has a general formula of $H(CaFe^{2+}MnMg)_3(Al_2BSi_4O_{16})$. Gem-quality magnesio-axinite—also known as axinite-(Mg)—is transparent to

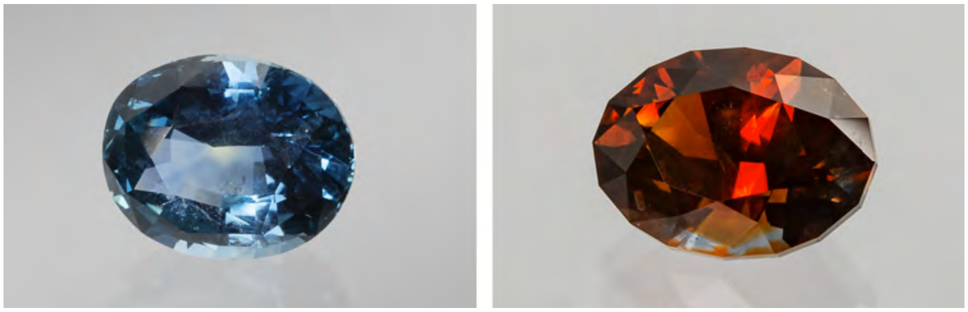

Figure 31. This 12.61 ct blue sapphire and 7.90 ct orange sapphire recently mined by Potentate show that large material still comes out of Rock Creek, Montana. Photo by Eric Welch/GIA, courtesy of Potentate Mining.

Figure 32. As displayed by these rough and cut sapphires, Potentate's sapphire production includes a wide variety of colors. Photo by Eric Welch/GIA, courtesy of Potentate Mining.

translucent, with pale blue to pale violet, light brown to light pink, or yellow to golden yellow or orange color (figure 33, left). More intensely colored bluish violet to purple magnesio-axinite tends to have a higher RI (1.659–1.681) than lighter-colored pink, purple, or yellow material (1.652–1.668). Magnesio-axinite has a birefringence of 0.010–0.016, strong dispersion, and a Mohs hardness of 5.5. Stones with a blue color component display pale blue to pale violet and pale gray pleochroic colors. Fluorescence is one of the material's most striking properties—the gem shows a dull red under short-wave ultraviolet light and a vibrant "merthiolate flame color" red under long-wave UV (figure 33, right). We intend to report on the chemistry of this interesting material at a future date.

Vance said he's attempting to name the gem "vanceite." Besides the fluorescence, pink to blue-violet stones display a color shift: If you view it under a fluorescent light, you're going to see a blue stone, he says, under incandescent, it's more of a pinkish color. Yellows don't show a color shift.

Because of the material's color shift and strong fluorescence, Vance believes it appeals to a wide audience. According to Vance, these examples come from a very limited occurrence in the Karo pit "D" block, Merelani Hills, Tanzania, where the chemistry and formation conditions were just right, and new material is very hard to get. It comes from the same rocks as green garnet, tanzanite, and chrome tourmaline. He remarked that while cutting of magnesio-axinite is straightforward, the biggest problem is getting clean pieces to cut as almost all have inclusions. In terms of size, he said, anything over four carats is a "monster."

Vance also showed us a heart-shaped 10.46 ct Tanzanian "Merelani mint" garnet. He noted that it displayed a very strong response to both long-wave and short-wave ultraviolet light (figure 34). Although such vanadium-bearing grossular garnet can come from Kenya or Tanzania, most of the Kenyan material displays no long-wave UV reaction. According to Vance, a strong long-wave UV reaction from a green grossular garnet is strong evidence of a Tanzanian stone from D block. Vance explained that supply of this material is now dwindling. In the beginning, prices ranged from $400–$500 per carat up to $800 per carat. Today's prices for equivalent material are in the range of $2,500 per carat. For a particularly fine example over six carats, prices might be as high as $10,000 per carat. Demand is really strong, especially in China.

Duncan Pay

Figure 33. Left: A suite of eight magnesio-axinite faceted gems and one rough stone. Clockwise from top right:1.21 g orange-yellow rough, 2.72 ct. yellow-orange pear shape, 1.14 ct bicolor marquise, 1.51 ct pair of pale pinkish blue princess-cut stones, 1.43 ct pink-blue oval, 1.83 ct light pink to light blue triangle, and at center in the pendant, a 4.22 ct. oval pink-blue gem. Right: The same magnesio-axinite gems under long-wave ultraviolet fluorescent lighting. Photos by Eric Welch; courtesy of Vance Gems.

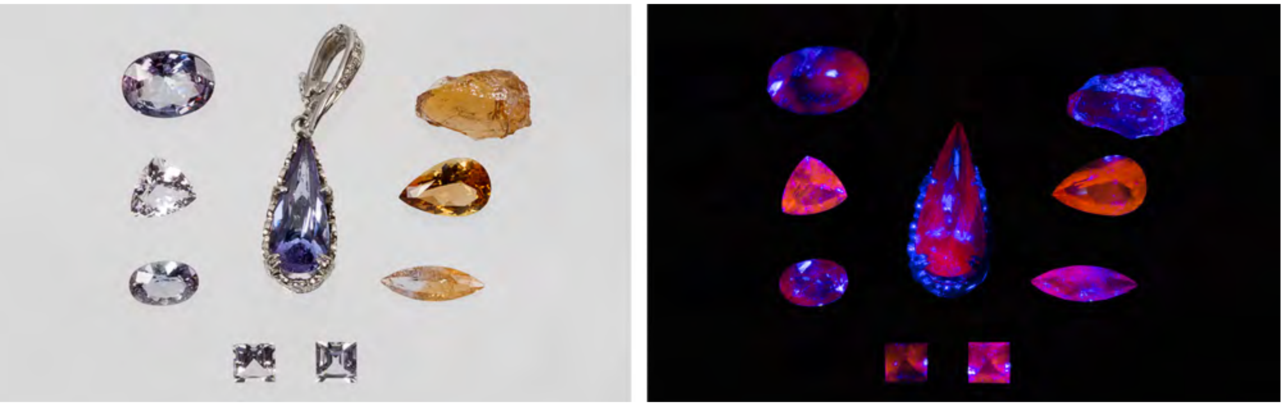

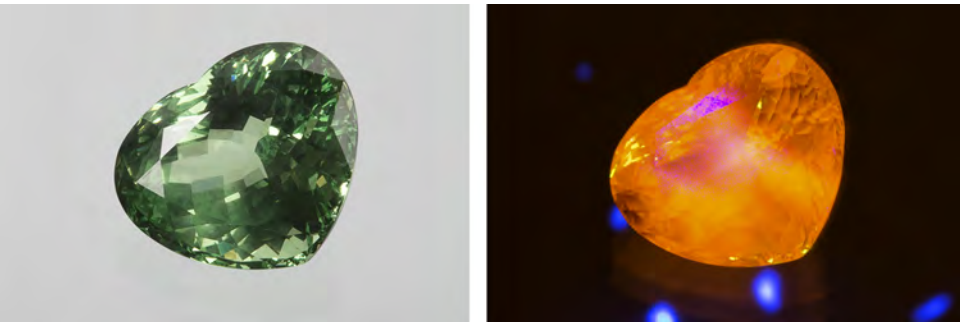

Figure 34. Left: A 10.46 ct heart-shaped green grossular garnet of the color known as "Merelani mint" in the trade. Right: The same grossular garnet displays a strong orange reaction to long-wave ultraviolet light. Photo by Eric Welch; courtesy of Vance Gems.

Ethical and sustainable vertical integration in the sapphire market. When the recession of 2008 struck, Sheahan Stephen (Sheahan Stephen Sapphires, Inc., San Francisco, California) had been dealing in Sri Lankan gemstones for two years. He saw his monthly cash flow drop to a third of what it had been when he first started traveling to Sri Lanka to buy stones for resale in the United States. During the recession he decided to borrow money and become vertically integrated. Stephen created a transparent supply chain and an ethical supply model by becoming directly involved in mining. His new business also included heat treatment, cutting, and sales.

Sustainable practices tie directly into Stephen's beliefs in how businesses should strive to operate. He sees lack of sustainability as a major cause of many of society's problems. He works with his customers in what he calls "customized" vertical integration. He fills specific orders for his customers directly from mines and brings the sapphires to market in a controlled manner, meaning they are always in his hands or an employee's hands until they reach the final customer. Stephen guarantees the entire supply chain and strives to provide full documentation, including the mine the sapphires (figure 35) came from and the name of the treater and the cutter.

He focuses on education and training in Sri Lanka to obtain the quality and traceability his customers expect. Training and complete trust in his Sri Lankan staff allow him to buy stones unseen that will fill his customers' specifications. Stephen also believes in providing education and other assistance for his employees' families in Sri Lanka.

Stephen finds that customers today want more information about their jewelry. They want to know where a piece came from, who was involved in manufacturing it and bringing it to market, and the corporate social responsibility practices of the company involved. With many of his customers today willing to pay 30% more for documented ethical sapphires and sapphire jewelry, he focuses on growing his sales with sustainability-minded clients. At the same time, he strives to be close to other wholesalers in his pricing to stay competitive and grow his business.

A major part of his business investment is the time he spends growing relationships with miners and cutters in Sri Lanka that can take years. That is an essential element of developing a sustainable business model for artisanal mining. Stephen hopes that building long-term relationships with his employees and suppliers in Sri Lanka and perfecting the processes throughout the supply chain will allow for slow but sustainable business growth. His vision is to take this model to other gem mining countries, especially in Africa, where he is currently working in Madagascar.

Tao Hsu and Andrew Lucas

Exceptional freeform tanzanite and Oregon sunstone rings. At the Gem and Jewelry Exchange (GJX), we caught up with gem artist Alexander Kreis (Sonja Kreis Unique Jewelry, Niederworresbach, Germany). As we've noted in previous Tucson reports, theirs is a family business: father Stefan buying the rough, mother Sonja designing the jewelry, and Alexander cutting the gems. Alexander and Sonja showed us a new ring (figure 36) set with a spectacular 27.20 ct vivid blue freeform tanzanite (figure 37). He explained that he had recently traveled to East Africa seeking a singular piece of gem rough to inspire an exceptional jewelry piece. He found his inspiration in Tanzania with a 65 ct rough tanzanite of remarkable color and clarity.

Even with such a top-quality piece, Alexander cautioned that success is never guaranteed. Unlike baseball—where you get three chances—with cutting, it's "one strike and

Figure 35. Untreated yellow sapphires such as this 12.18 ct gem command a premium in the marketplace, especially when a transparent chain of custody and sustainable mining practices can be documented for the customer. Photo by Eric Welch/GIA, courtesy of Sheahan Stephen Sapphires.

you're out!" He added that the gem can never be its best if the cutter misjudges and makes it too flat. For this one-of-a-kind rough, classic cutting styles such as oval or cushion shapes might be counterproductive if too much weight is lost getting proportions right or if the deep blue color is lost.

For Alexander, cutting is an "intuitive adventure" in which it might take months to place the first facet. The finished stone is a nonsymmetrical shield shape with a mixture of large and small facets that catch the light and create a strong sense of movement. According to him, cutting a freeform allows more reflections so that the gem will exhibit maximum sparkle and display the best possible color from the rough.

The facet dimensions govern the size of the reflections from the gem's surface, and a series of grooves on the base of the gem running at right angles to the facets on the top create sharp angles, heightening the sense of movement and drama (figure 38). For Alexander, this represents not just the movement of the earth, but also the volume of material the workers had to shift to recover the gems.

He reminded us that mining in Merelani is a challenge, taking place at depths of up to 3,900 ft (1,189 meters). Miners can only work for short periods due to temperatures reaching 122°F (50°C), and they must take regular breaks in designated cooling areas.

As a goldsmith and jewelry designer, Sonja follows a 500-year family tradition. She explained that it's not just attributes like size, shape, and color that drive the design of a jewelry piece to complement the stone. She normally starts thinking about the jewelry design when Alexander completes the stone, noting that it can change substantially from the rough crystal to the finished piece.

When Sonja saw the finished cut tanzanite, still wet from the wheel, she held it and examined it from every angle in front of a mirror to get a feeling for the gem and for the best type of jewelry mounting to accompany it. It's not just the size and shape that influences the gem, she noted, but the story behind it, too. This aspect is increasingly important for clients who like to buy into the romance and unique attributes of a jewelry piece. In this case, the rose gold on the mounting represents the heat the miners endure to recover the gems at depth in the mine, while the white gold cradling the tanzanite stands for the designated cooling areas where the workers have a chance to recover. The diamonds along the edges of the center gem symbolize the many stones that have been moved out of the way to reach the tanzanite. The branching metalwork in the galleries at each end of the mounting represents the air that must be pressed into the mine depths to sustain the miners. The little trail of melee diamonds around the curve of the ring's shank adds a final touch of elegance to a significant piece with a large center stone.

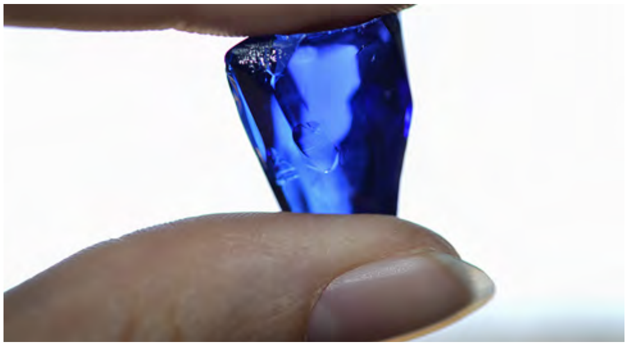

Figure 37. The gem was cut from a 13 g rough tanzanite of remarkable color and clarity. Photo courtesy of Sonja Kreis Unique Jewelry.

Figure 36. This ring is set with a spectacular 27.20 ct vivid blue freeform tanzanite. Photo courtesy of Sonja Kreis Unique Jewelry.

Figure 38. Angled grooves on the base of the 27.20 ct freeform tanzanite create a dramatic sense of movement. Photo courtesy of Sonja Kreis Unique Jewelry.

Sonja also shared with us a striking ring centered on a 28.21 ct freeform Oregon sunstone from the Dust Devil mine (figure 39). The organic outline of the mounting complements the smooth contours of the gem, which rests in an 18K rose gold "cup." The cup is highly polished to reflect light back through the gem and amplify its rich orange color. The gem itself is shot through with an array of glittering copper particles that catch the light and add to the piece's allure.

Duncan Pay

Figure 39. A 28.21 ct freeform Oregon sunstone from the Dust Devil mine is the centerpiece of this ring. Photo courtesy of Sonja Kreis Unique Jewelry.

Gem paintings from Thailand. The 2017 GJX show hosted a new vendor that manufactures and sells gem paintings, merchandise not typically seen in international gem and jewelry shows. Only a handful of companies around the globe are active in this market segment. Than Thong Arts operates its own factory in northern Thailand. Owner Wanlaya Suwannapirom is from a family that has been in the jewelry industry for over 70 years. She started her gem painting business more than a decade ago and gradually became the industry leader, with both international and domestic clientele (figure 40).

These paintings are handmade by highly skilled artisans in Thailand, using natural uncut gem fragments sourced from all over the world. The fragments come from either mining operations or cutting factories. The paintings' bright colors are generated by colored gem fragments, while the background and skin tones are created by dyed quartz or calcite powder. Artists also use extremely thin 24K gold leaf to color human hair and other details (figure 41). Unlike many other gem paintings, the gemstones are not glued to paper or canvas but attached to the glass and then framed.

The process includes several steps: sketching the painting on paper, a reverse transfer to glass, gluing the gem fragments and the dyed quartz or calcite powder, drying the glue, and framing the artwork. The middle steps are the most critical for the quality of the final product. The fragments are sorted into different sizes. Painters need to follow the order to apply the coarser grains first and then gradually go down to smaller sizes to fill the holes in between the fragments. This step continues until no space left between any fragments and the motif is completely colored by gems. Another challenge is to accurately and naturally reflect the human skin tone (again, see figure 41). To achieve this, painters grind quartz or calcite into very fine powder and dye them to slightly different tones for a very gradational transition of skin tone.

To cater to a wide range of customers, paintings are produced in many sizes and framed in various ways (figure 42). Besides wall and desk decor, the paintings are framed in jewelry boxes and wearable jewelry. According to Suwannapirom, smaller paintings require more attention to detail. In addition, crystal glass that contains a higher concentration of lead is used on the wearables to give them a glossier look than the pyrolytic glass used for decor. Therefore, the price range of the jewelry is similar to some of the larger desk decor pieces.

Customized gem paintings based on photos can also be specially created. At the booth, we saw some photo-based portraits made by Suwannapirom and her team. Some

Figure 40. While her family had been involved in different sectors of the gem industry for more than 70 years, Wanlaya Suwannapirom found a passion for gem paintings such as the one in this pendant. Photo by Albert Salvato/GIA, courtesy of Than Thong Arts.

Figure 41. By dyeing ground quartz or calcite in slightly different tones, a realistic gradation of skin tones can be achieved. Here, 24K gold leaf is used to create a beautiful hair color for the mother. Photo by Eric Welch/GIA.

Figure 42. Than Thong Arts' gem paintings are offered in a variety of sizes, frames, and styles. Photo by Tao Hsu/GIA.

prominent figures have hired her to produce their portrait in gems, including the kings of Saudi Arabia and Thailand. The finished products look very accurate and natural. The gems in the paintings offered at the show came with a certificate of authenticity issued by a Thai gemological lab.

Andrew Lucas and Tao Hsu

New designs from Paula Crevoshay. Paula Crevoshay came to Tucson some new designs that once again showcase her unique talent.

The "Queen Thai" bracelet (figure 43) contains five large freeform fire opals. Accompanying the opal are micropavé brilliant tsavorite accents and blue zircons connecting the bracelet sections. Four of the fire opals are from Mexico, and one is from Brazil. Crevoshay pointed out that the four Mexican fire opals have better transparency, while the Brazilian one has a more saturated orange color. All of them show some green and blue play-of-color, which complements the tsavorite and blue zircon accents. In return, the strong blue and green color of highly refractive tsavorite and zircon accentuates the opals' play-of-color. The intense orange color of the Brazilian fire opal forms a dramatic contrast with the Mexican stones and adds another layer to draw viewers' attention. The mounting of the bracelet follows the profile of the freeform opals, giving the jewelry its own personality.

Crevoshay expressed her love of nature in two new pieces from the collection. The "Swallowtail" butterfly (figure 44, left) combines yellow diamond, black diamond, blue Yogo sapphire, yellow sapphire, and red spinel. She informed us that this swallowtail is modeled specifically

Figure 43. In the "Queen Thai" bracelet, the contrast in orange color between the more intense Brazilian fire opal (left) and the Mexican fire opals leads the eye directly to the Brazilian stone. All of the opals are complemented by the green tsavorite. Photo by Eric Welch/GIA, courtesy of Paula Crevoshay.

after those found in Montana, a state whose natural beauty and sapphires she admires. She noted that she always tries to find an excuse to involve Montana sapphire in her artworks. The various stones are mounted over a large surface area, which allows them to optically interact with each other. The colors of the stones accurately reproduce the colors on the wings of these butterflies. When people move the piece in their hands, it vividly reflects the whimsical look of the real butterfly. The elephant head in figure 44 (right) evokes Crevoshay's memories of visiting an elephant orphanage in Sri Lanka. Captured in this pendant is the extinct East African forest elephant, which is smaller and less aggressive than most other species. A special texture was generated on the gold to depict the elephant's skin. A sapphire and spinel headdress shows the royalty of this creature. The eyes are tsavorite, while the tasks are carved mother-of-pearl.

Last but not least is the cuff bracelet featuring a large Australian boulder opal accented with sapphire (figure 45). To Crevoshay, "all opals are created by Monet," since each is a striking blend of colors. The play-of-color pattern of this opal reminds viewer of a spectacular cityscape at night. There is a subtle red linear play-of-color across the middle of this piece. This long marquise-shaped boulder opal has blue as its deepest play-of-color, and Crevoshay selected the blue sapphire to go with it. According to color theory, blue is a color that recedes. The blue sapphire and the blue play-of-color seem to dominate the cuff bracelet but then recede to the background to allow the other colors such as the green and the red to take center stage.

Andrew Lucas and Tao Hsu

Figure 45. The blue play-of-color from the boulder opal and the blue color from the sapphires dominate one's initial impression of the cuff bracelet. Photo by Eric Welch/GIA, courtesy of Paula Crevoshay.

Tourmaline and sapphire from Nigeria. Zoe Michelou, marketing manager for a Nigerian mining company, gave an update in Tucson on the production of gemstones, particularly tourmaline. She primarily handles sales and marketing of rubellite from Oyo State, where there are around 350 pits. There are usually 10 to 15 miners per pit. The miners descend 10 to 20 meters by ladder to the bottom of a pit, and then the pegmatites are blasted and tunneled before extraction. Some tunnels are linked for better air circulation. Pits can be very close together, although some larger open-pit operations have excavators in the pits and carts to remove the ore. Rubellite is concentrated in pockets within the pegmatites. There are plans to increase mechanization, and new pockets are being discovered.

Miners are paid a salary and provided with food and tools, as well as a bonus based on the value of the production. Sometimes miners can recover one ton of rubellite from a large pocket. Large single crystals can easily reach 18 kg. The rubellite is kept in a safe and then transported to the city of Ibadan for grading every two to three weeks, depending on production. Currently there are three to four quality categories. Most of the material is now shipped to Bangkok for final grading and sale. A new facility is planned to per-

Figure 44. Left: The yellow diamond, black diamond, blue Yogo sapphire, yellow sapphire, and red spinel in this swallowtail brooch create a stunning color combination. Right: This brooch was inspired by a visit to an elephant orphanage in Sri Lanka, which adds an extra touch of humanity to the piece. Photos by Eric Welch/GIA, courtesy of Paula Crevoshay.

form the final grading in Nigeria, with training of locals to create parcels for international clientele. Many of the rubellite crystals sent to Bangkok weigh 1 kg or more.

There is also an alluvial deposit where rubellite pebbles can be recovered without moving too much earth. In Kwara State there is important production of indicolite and green tourmaline, including some pink and bicolor. Most of the mining is still near the surface, with a few deeper pits. The first production of indicolite tourmaline sent to Bangkok had crystals of 2–34 grams ranging from commercial to very high quality.

Currently, the Nigerian is focused on selling rough rubellite (figure 46) through the Bangkok office and trade shows to the international market, especially in East Asia. The clients are mainly rough dealers and manufacturers from China, Hong Kong, and Thailand. This year, the company will start a training program for grading at the mining site in Nigeria. In the future, rough will be sorted and graded prior to shipment to Bangkok.

The interests Michelou represents just bought 180 square kilometers of land in the Mambilla Plateau area of Taraba State for sapphire mining. Nigeria has produced large quantities of fine-quality basalt-related sapphires. Extraction will start in the spring, with sales expected by the end of 2017 or beginning of 2018. They will only sell rough sapphires in Bangkok. Both primary and secondary deposits will be mined, with an initial focus on the secondary deposits. The washing plant will be able to handle 50 tons of ore per hour. Good-quality material weighing 3 to 5 grams is already being recovered. Security will be tight, and dealers from the Cameroon side of the border currently buying from unlicensed miners will be restricted from the commercial mining area. Transparent supply from the mine to Bangkok is an important part of the marketing strategy. The company is working out its grading system for rough sapphires.

The company primarily sells rough but also sells some cut stones to manufacturing jewelers in Europe and the United States. Michelou sees an increase in manufacturing jewelers buying rough, including tourmaline and sapphire, and having it cut instead of just purchasing finished stones. By doing so they can guarantee mine-to-market custodianship and meet strict supply chain compliance regulations.

Andrew Lucas and Tao Hsu

Figure 46. High-quality rubellite rough is highly sought after in the Asian market. Photo by Eric Welch/GIA, courtesy of Zoe Michelou.

"Boldly go" with a Southwest-inspired Starship Enterprise. At the Pueblo (Riverpark Inn) show, David Freedland (David R. Freedland Jr. Designs, Tucson) showed us some unusual pieces that stood out at his booth. Normally, you expect Southwest-style jewelry to embrace nature or Native American influences for pieces featuring detailed inlays of Arizona turquoise and other materials. Although Freedland had these in abundance, what really caught our eye was this handmade, sterling-silver rendition of the Starship Enterprise from the cult science fiction television series *Star Trek*. The piece measures 6.5 cm in length and stands 4.5 cm high. It rests on a sterling silver stand inlaid with Arizona turquoise (figure 48).

The iconic starship's saucer section is also inlaid with Arizona turquoise and a concentric band of purple spiny oyster centered on a lab-grown white opal representing the bridge. Other oval lab-grown opal cabochons grace the ends of the engine nacelles, and a turquoise cabochon represents the ship's shuttle bay. The starship portion has a loop and can be detached and worn as a pendant, if desired. Freedland also has another handmade starship available: the "Reliant" from the 1982 motion picture *Star Trek II: The Wrath of Khan* along with an array of cyberpunk—or steampunk—ray guns that are redolent of classic U.S. science fiction films of the 1950s.

Freedland told us there's no other reason behind the considerable time and effort required to hand fabricate these unique pieces except that he's always liked the idea

Figure 47. A sampling of Nigerian indicolites after fashioning. Photo by Eric Welch/GIA, courtesy of Zoe Michelou.

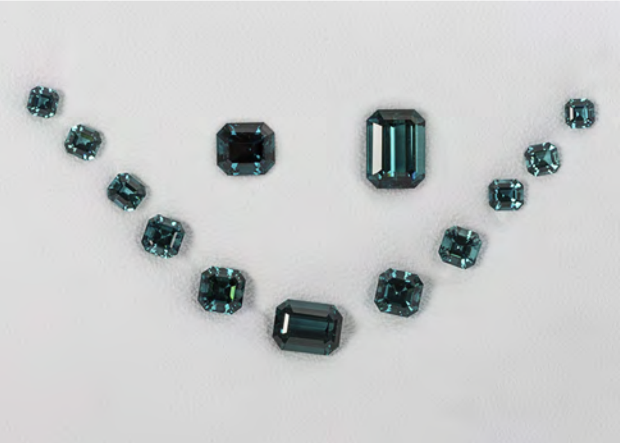

Figure 48. This handmade piece fuses Southwestern style and its characteristic inlay techniques with a science fiction icon: the Starship Enterprise from Star Trek. *Photo by Kevin Schumacher; courtesy David R. Freedland Jr. Designs.*

of space and the unknown—"what's out there," as he says. And he thought they would be a lot of fun to make. We hope these designs live long and prosper.

Duncan Pay

Golden rutilated quartz artisanal mining community. At the January 2017 Jewelry Industry Summit held in Tucson, Brian and Kendra Cook (Nature's Geometry) discussed their efforts to promote sustainable mining in Brazil's Bahia State. In cooperation with 2,500 miners from the region, the Cooks are developing a collective in Remedios, Novo Horizonte (figure 49). Plans to brand the region's unique golden rutilated quartz will be supported by a warehouse and cutting facilities, as well as a visitor center. To provide food security for the population, the Cooks also intend to bring organic community farming to the area.

Brian Cook first visited the remote site, located in Chapada Diamantina bordering the Atlantic Rain Forest and the Serrado and Caatinga ecological communities, in 1983 as a geology student. The trip from Salvador, Bahia's capital, took 2½ days, and he was shown an example of golden rutilated quartz (figure 50), which was relatively rare on the gem market at the time. He later became an exporter of the quartz and helped raise its profile. The Cooks have since become landowners in Remedios, and their property includes a successful golden rutilated quartz mine. Over the years they have visited with their children from their home in Salvador (now a ten-hour journey thanks to improved infrastructure) and become trusted members of the community.

The Cooks have already helped locals formalize their land and mining rights, and now they are turning their attention to other initiatives. Their agenda includes mine safety, certificates of origin to ensure transparency and consumer satisfaction, and teaching cutting and polishing gemstones. They especially seek to empower local women, who already sell rough gems at the local markets, through lapidary and beadmaking training. The community's proximity to the Atlantic Rain Forest makes it an ideal location for ecotourism, a concept that can be combined with gemological study and buying expeditions.

Figure 49. The remote Brazilian mining community of Remedios is the site of the Bahia golden rutilated quartz mines. The town is developing a sustainable collective of artisanal miners. Photo by Brian Cook.

Figure 50. A local miner holds up an example of the golden rutilated quartz found in the Remedios area. Photo by Robert Weldon/GIA.

Brian and Kendra Cook are seeking investors and corporate sponsorship for their community. Learn more about their work at bahiainitiative.com.

Jennifer-Lynn Archuleta
GIA, Carlsbad

Jewelry Industry Summit. The second Jewelry Industry Summit was held in Tucson, Arizona, January 29–30. The meeting was a continuation of the first summit, held in New York in March 2016, though new initiatives emerged from the Tucson gathering.

Opening remarks by Doug Hucker and Jeff Bilgore (AGTA) were followed by three speakers from outside the gem and jewelry industry. Lisa Manley (Sustainability Strategy and Cone Communications, Boston) discussed exploring a company's strengths, opportunities, and aspirations, calling sustainability "a team sport." Thea Polancic (Conscious Capitalism, Chicago) spoke on imagining the industry's future, citing specific companies that have used their leverage in their industries to make a difference in the world. Bob Mitchell (Electronic Industry Citizenship Coalition, Washington DC) presented on pinpointing possibilities for successful and sustainable business practices.

The majority of the summit was focused on committee updates from the first meeting and creating new initiatives to be worked on. Carried over from 2016:

- Brian Cook (Nature's Geometry, Tucson) is developing a model community for golden rutile miners in Bahia State, Brazil. A construction site has been chosen, and negotiations with the municipal government for lapidary equipment have begun. See p. 136 for more information.
- The education committee, headed by Christina Miller (College Corner, Ohio) is creating a glossary that can help members of the industry and consumers understand the language of sustainability, ethical sourcing, and responsible practices.
- The chain of custody and due diligence committee drafted guidelines for suppliers seeking responsible sources.
- The harmonization team is charged with establishing best practices among the existing standards across industries. Under the lead of Mark Hanna (Richline, Providence, Rhode Island) and Richard Nehls (LA Rocks, Los Angeles), the team has collaborated with other organizations to learn from their challenges and successes.
- #ResponsibleJewelryStories, the marketing arm of the summit, is led by Cleo Zancope Gnatek (Jane Taylor Jewelry, New York), Dana Bronfman (Dana Bronfman Fine Jewelry, New York), and Cecilia Gardner (New York). This team has created a website to share stories of responsible sourcing, ethical practices, and sustainability. Industry members interested in sharing their stories on this topic should contact responsiblejewelrystories@gmail.com.
- Members of the sales associate and consumer education team, led by Kevin Reilly (Platinum Guild International, New York), have developed an outline for training purposes and a proposal for content providers and potential sponsors.
- The sustainability in jewelry committee, headed by Mike Pace (New York), has distributed a survey about perceptions of sustainability to 800 fine jewelry buyers who identify as "millennials."
- The team working to fight silicosis and industrial diseases among gemstone cutters, led by Eric Braunwart (Columbia Gem House, Portland, Oregon), is creating pilot programs with three NGOs as well as the AGTA.

Among the new initiatives proposed at the summit were an effort to find a safe, affordable alternative for mercury in gold mining; a development index to measure the positive and negative effects of the gem and jewelry industry on a nation's economy; and a plan to build an agro-geo-ecotourism movement in Thailand.

The location and dates of the next Jewelry Industry Summit will be announced later in 2017.

Jennifer-Lynn Archuleta

REGULAR FEATURES

COLORED STONES AND ORGANIC MATERIALS

Pyrope-spessartine color-change garnet with a high grossular component. During the 2016 Tucson Gem and Mineral Show, Jeff Aylor provided several transparent rough garnets, reportedly from Sri Lanka, to GIA for scientific examination. We noticed that the rough garnets showed obvious color change from yellow-green under daylight equivalent lighting to orange under incandescent illumination. Three rough garnets were polished into wafers and analyzed to fully understand the chemistry and color behavior of the material.

Standard gemological testing of three garnet wafers revealed an RI from 1.76 to 1.77; hydrostatic SG ranged from 3.93 to 4.00. Fluorescence was inert to long-wave and short-wave UV light. The stones did not show any pleochroism when utilizing the dichroscope. Using a handheld spectroscope, absorption lines in the blue and violet section, and very weak absorption bands at 520 and 573 nm, were observed. Microscopic examination showed intersecting long and short needles throughout. Graphite and quartz inclusions were also observed. All of these properties are consistent with garnet.

The chemical composition for each wafer was obtained

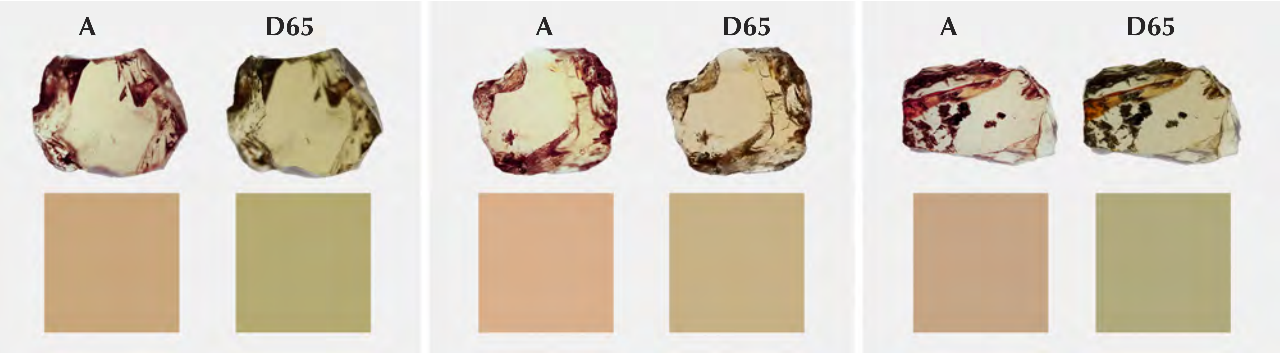

Figure 51. Top: Photos of three garnet wafers under incandescent light and fluorescent light (a daylight-equivalent imitation). Bottom: Calculated color panels of three garnet wafers under CIE A illumination and CIE D65 illumination. Photos by Ziyin Sun.

with a ThermoFisher iCAP Q ICP-MS coupled with a New Wave Research UP-213 laser ablation unit. We concluded that this type of material contains 39.79%–52.66% spessartine, 21.71%–32.03% pyrope, 3.17%–7.28% almandine, 16.87%–22.46% grossular, 0.38%–0.72% goldmanite, and 0.11%–0.19% uvarovite (see detailed table at https://www.gia.edu/gems-gemology/spring-2017-gem-news-pyrope-high-grossular-component). Based on the garnet classification from Stockton and Manson ("A proposed new classification for gem-quality garnets," Winter 1985 *G&G*, pp. 205–218), this material should be classified as pyrope-spessartine. The V_2O_3, MgO, and MnO oxide wt.% are similar to the group 5 color change garnets previously reported (K. Schmetzer et al., "Color-change garnets from Madagascar: Variation of chemical, spectroscopic and colorimetric properties, *The Journal of Gemmology*, Vol. 31, No. 5–8, 2009, pp. 258–259). However, these garnets contains much higher grossular component (16.78%–22.46%) than those reported by Schmetzer et al. (3.02%–10.23% grossular). To our knowledge, the chemical composition of this type of color-change garnet has never been reported before.

The color of the three wafers was quantitatively calculated by using the visible spectra (Z. Sun et al., "Vanadium and chromium bearing pink pyrope garnet: characterization and quantitative colorimetric analysis," Winter 2015 *G&G*, pp. 348–369). The color of each wafer can be presented by using CIE $L^*a^*b^*$ and RGB color coordinates, as seen online in table 2. The calculated color panels of three wafers under daylight-equivalent lighting (CIE D65 illumination) and incandescent lighting (CIE A illumination) were shown in the bottom row of figure 51. The three wafers were also photographed under both fluorescent light and incandescent light to compare with the panels in the top row of figure 51.

One way to judge the quality of a color-change stone is to plot the color pair in the CIE 1976 color circle. Good color-change pairings show a large hue angle difference, small chroma difference, and large chroma values (see table 2). The color coordinates of the three wafers were plotted in the CIE 1976 color circle found online. The color change of this material is not very significant, but is definitely observable.

Ziyin Sun and Jonathan Muyal
GIA, Carlsbad

Aaron C. Palke
University of Queensland and Queensland Museum
Brisbane, Australia

SYNTHETICS AND SIMULANTS

Plastic amber imitation in a rosary. The Dubai Central Laboratory (DCL) receives almost all types of ambers, natural and treated (e.g. heated, dyed, reconstructed) as well as amber imitations for identification. Amber rosaries (prayer beads) are increasingly popular in Middle East countries, especially the United Arab Emirates and Arabian Gulf countries.

Recently DCL received a rosary for amber identification. The yellow and yellowish brown color, structure, and size of the 102 beads were identical (figure 52, left). At first glance, even with a well-trained eye, this rosary could easily be misidentified as exclusively natural amber. Testing revealed that the rosary was strung with 71 heat-treated amber beads and 31 Bakelite plastic beads.

Spot RIs of the amber beads were 1.53; observation between crossed polarization of most beads revealed anomalous double refraction with strained colors. Stress spangles and brown thread-like substances are the most noticeable inclusions in these beads; these features are commonly seen in heat-treated amber. The spot RIs of the plastic beads was around 1.64. Aggregate and anomalous double refraction reaction was observed under the polariscope and gas bubbles and swirl marks were the main inclusions.

The most interesting aspect of the specimen was its reaction under long-wave UV. The amber showed moderate to strong chalky greenish blue and yellow fluorescence, but the plastic appeared brown (figure 52, right).This reaction was very useful for differentiating between the two materials.

Figure 52. Left: The rosary shows yellow to yellowish brown color in daylight-equivalent lighting (left). Right: The rosary under long-wave UV. The amber shows a moderate to strong chalky greenish blue and yellow reaction, but the plastic appears brown. Photo by Nazar Ahmed Ambalathveettil.

To confirm the identity of each material, we analyzed their infrared spectra with attenuated total reflectance (ATR) mode (figure 53). Spectrum A displayed main peaks at 1716.4 and 1161.1 cm^{-1}, consistent with amber. The main peaks of Spectrum B were at 1650.8, 1600.7, and 1218.8 cm^{-1}. After comparison with spectrum A and the spectra of other plastics, spectrum B confirmed the spot RI's identification of this sample as Bakelite plastic.

This rosary is an excellent example of the importance of testing and disclosure, because even an experienced person could not differentiate between the amber and Bakelite beads with the unaided eye.

Nazar Ahmed Ambalathveettil (nanezar@dm.gov.ae), Mohamed Karam, and Sutas Singbamroong
Gemstone Unit, Dubai Central Laboratory
Dubai, United Arab Emirates

Mixed-type treated red HPHT synthetic diamond. A multiple-treatment process involving irradiation and HPHT annealing can produce pink to red color in natural and synthetic diamonds; specimens treated by this process have been on the market for over 10 years. To the best of our knowledge, nearly 95% of the studied red HPHT synthetic diamonds treated by the multi-treatment process are classified as type Ib or type IIa. Recently, we examined a treated red HPHT-grown synthetic diamond which was confirmed to be mixed type (IaA + IaB + Ib).

The 0.27 ct round brilliant sample, graded as Fancy Dark red (figure 54), had a metallic inclusion under the table. The DiamondView image showed strong red fluorescence and cuboctahedral growth structure; the latter is a typical feature of HPHT-grown diamonds (figure 55). Ni-related defects at 883.1/884.8 nm and 793.6 nm were revealed by a photoluminescence (PL) spectrum at liquid-nitrogen temperature with two different laser excitations (532 and 785 nm). The H2 defect corresponding to a sharp peak at 986.2 nm and the NV center associated with a strong peak at 637 nm were also found. In addition, the Fourier-transform infrared (FTIR) absorption spectrum (figure 56) confirmed the material was an uncommon type of IaA + IaB + Ib, with absorptions at 1282 cm^{-1} (A center), at 1175 cm^{-1} (B center), and at 1131 and 1344 cm^{-1} (C center), respectively (again, see figure 56). This mixed type is similar to that observed in treated natural diamonds. A moderate 1450 cm^{-1}

Figure 53. IR spectra of the two specimens, with ATR method applied. Spectrum A represents natural amber, with typical peaks at 1716.4 and 1161.1 cm^{-1}. Spectrum B's main peaks at 1650.8, 1600.7, and 1218.8 cm^{-1} indicate that it is Bakelite plastic.

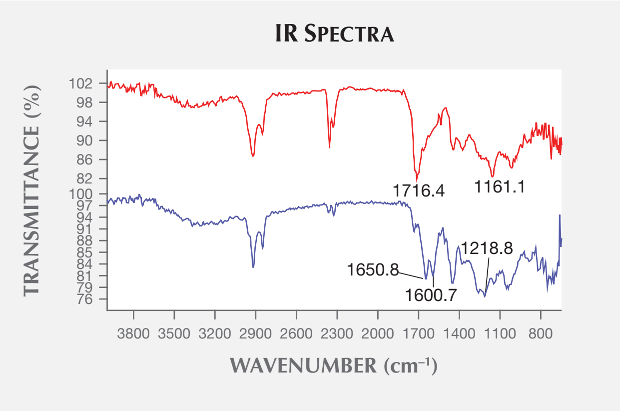

Figure 54. This 0.27 ct Fancy Dark red specimen is a multi-step treated HPHT synthetic diamond. Photo by Meili Wang.

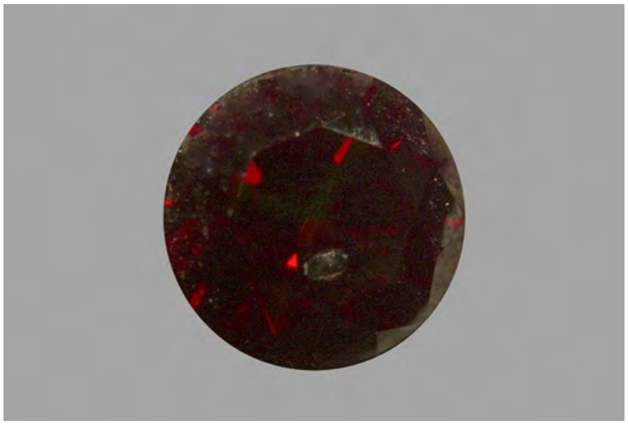

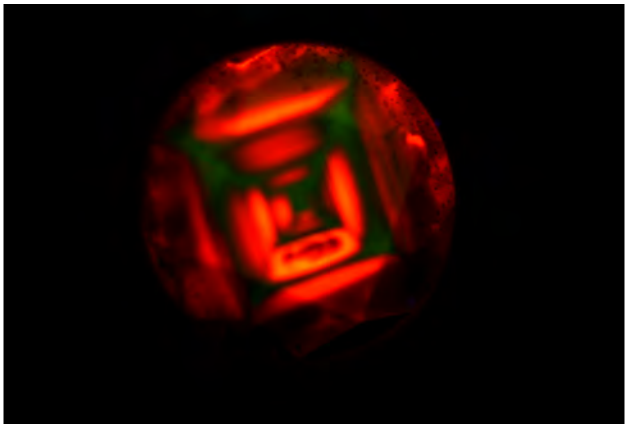

Figure 55. The DiamondView fluorescence image shows cuboctahedral growth structure, a typical feature in HPHT-grown diamonds. Photo by Wen Han.

absorption (H1a), which correlates with irradiation and subsequent annealing (Clark et al., "Absorption spectra of natural and irradiated diamonds," *Proceedings of the Royal Society of London A*, Vol. 234, 1956, pp. 363–381), was also present. Thus, this diamond was identified as a multi-step treated HPHT synthetic diamond, with irradiation and HPHT annealing indicated as treatment processes.

Although most of the recent treated red HPHT synthetic diamonds are reported to be type Ib or type IIa (e.g, Fall 2016 Lab Notes, pp. 308–309; C.M. Breeding and J.E. Shigley, "The 'type' classification system of diamonds and its importance in gemology," Summer 2009 *G&G*, pp, 96–111), such diamonds with mixed type Ia + Ib are available in the jewelry market, as exemplified by this study. Therefore, caution is still needed to distinguish such treated synthetic diamonds from treated stones of natural origin, as they may show similar characteristics.

Meili Wang and Guanghai Shi
China University of Geosciences, Beijing

Joe C.C. Yuan
Taidiam Technology (Zhengzhou) Ltd., China

Figure 56. FTIR spectroscopy reveals that this diamond is type Ia + Ib, with the existence of aggregated nitrogen atoms (A center at 1282 cm^{-1} and B center at 1175 cm^{-1}) and isolated nitrogen (C center at 1131 and 1344 cm^{-1}) impurities. The H1a absorption at 1450 cm^{-1}, correlating with irradiation and subsequent annealing, is also observed.

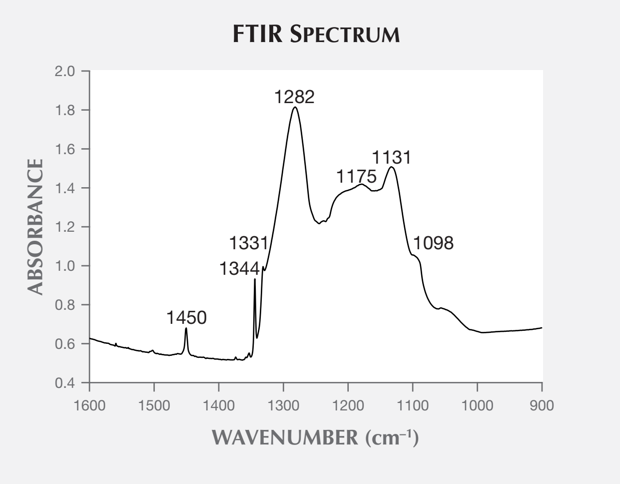

TREATMENTS

Filled calcite with pronounced phosphorescence. Asterism, chatoyancy, color change, and play-of-color are phenomena that are caused by the interaction of light with the host's structure or from its inclusions. Fluorescence, on the other hand, is the emission of light by a substance that has absorbed light or other electromagnetic radiation. Fluorescent materials immediately cease to glow when the radiation source is turned off; phosphorescent specimens continue to emit light for variable periods after the radiation ceases. Previous studies (Spring 2005 Lab Notes, pp. 46–47; Summer 2012 Lab Notes, pp. 139–140) have reported on the misnomer "night glowing pearls," which are in fact not pearls at all but round rocks of mineral species that exhibit phosphorescence. Most of this material in the Chinese market has been treated in a variety of ways and in fact does not phosphoresce naturally.

A partially carved white ovoid with a greasy luster and golden paint within the low-relief carved features (figure 57, left) was submitted for identification to the Lai Tai-An Gem Lab. The submitting client claimed it was a "night glowing pearl." The object weighed 796.71 ct and measured 48 mm in diameter. A spot RI reading of 1.59 and an SG of approximately 2.66 indicated that the object was most likely calcite. This was later confirmed by FTIR and Raman (figure 58) analysis. Initial exposure to short-wave (254 nm) and long-wave (365 nm) UV light (cabinet and lamp respectively) failed to elicit any initial visible reaction; however, both short-wave and long-wave UV did initiate some fluorescence after about 15 minutes. When observed in a dark environment, moderate green phosphorescence lasting more than 10 minutes was noted, with strong whitish phosphorescence concentrated in one area (see figure 57, right).

Microscopic inspection of the area showing the white phosphorescence revealed that the reaction originated from within the object, and did not emanate from the entire outer surface. The microscope revealed a few tiny bubbles comprised of solid epoxy resin (figure 59, left). This translucent epoxy acted as a plug to an opening into the (assumed

Figure 57. The calcite object (left, in daylight-equivalent light) showing a moderate green overall phosphorescence after short-wave UV exposure (right). The object emits a very strong whitish phosphorescence from one area, as seen in the center of the right image. Photos by Lai Tai-An Gem Lab.

hollowed out) interior, where a highly phosphorescent material was placed to create the calcite's glowing effect. It was therefore understandable why this small capped area showed the strongest reaction (figure 59, right).

The trade name "night glowing pearl" used in Asian markets mostly refers to natural fluorite, but some fluorite is treated with a coating containing rare earth elements (REE) such as europium (Eu), dysprosium (Dy), or neodymium (Nd) to add or enhance phosphorescence. The sample submitted was calcite, consisting mainly of calcium, as confirmed by energy dispersive X-ray fluorescence (EDXRF). However, no Eu, Dy, Nd, or any other REE were detected, proving the material was not luminiferous. It therefore seems more logical that the phosphorescence originated from material below the ovoid's surface.

It is interesting to note that the same client also submitted a jadeite jade sphere that was fashioned and treated in a similar manner. The cap on the jadeite piece used to plug the void was itself a piece of jadeite. Since destructive testing was not permitted on either item, analysis of their interiors was not possible. This technique of placing a phosphorescent material inside a hollowed-out stone object appears to be applicable to any material, so those in the trade should be aware when examining similar objects.

Larry Tai-An Lai (service@laitaian.com.tw)
Lai Tai-An Gem Laboratory, Taipei

ERRATUM

In the J.C. Zwaan et al. Winter 2015 article on alluvial sapphires from Montana, in the lower right corner of the Mg-Fe-Ti ternary plot (p. 385), the label "Ti × 100" should be "Ti × 10."

Figure 58. Raman analysis identified the material as calcite (peaks at 279 and 1086 cm^{-1}, blue trace). Cavities were filled with epoxy resin (peaks at 638, 1112, and 1608 cm^{-1}, pink trace).

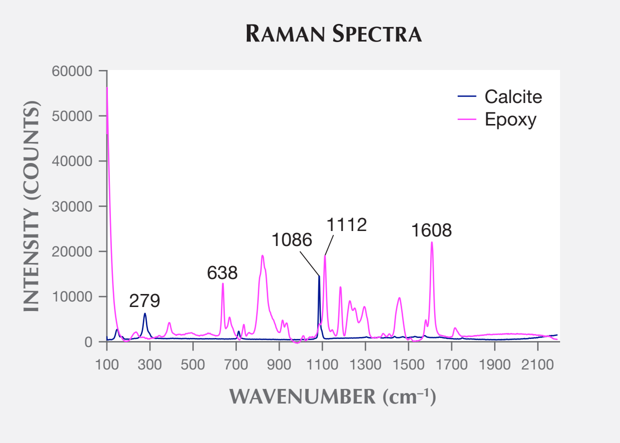

Figure 59. Left: Tiny bubbles were observed in the cavity under magnification. Field of view 6.2 mm. Right: The filled cavity showed stronger phosphorescence because the epoxy resin is more transparent than its calcite host. Field of view 11.6 mm. Photos by Lai Tai-An Gem Lab.

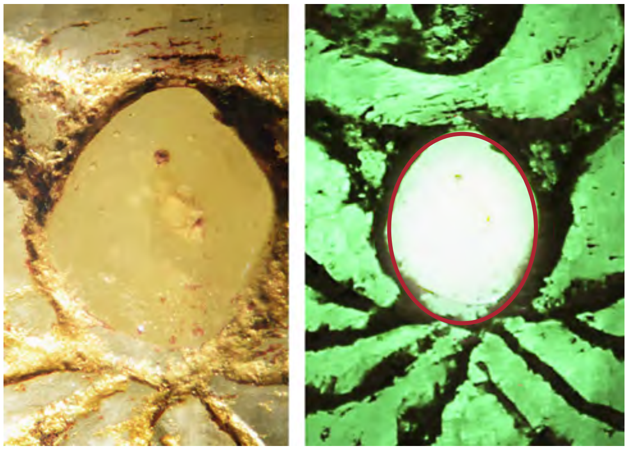

LETTERS

Nacken Synthetic Emeralds: Additional Information

In a recently published study on synthetic emeralds grown by Prof. R. Nacken (K. Schmetzer et al., Winter 2016 *G&G*, pp. 368–392), three different types of flux-grown crystals and faceted samples were described. The vast majority of the synthetic emeralds, comprising several hundred samples, fell within two groups designated types 1 and 2. Most of these had been obtained either from a parcel donated by Nacken to the Deutsches Museum in Munich or from material that had remained in Nacken's family and was now in the possession of his grandsons. Upon examination, all crystals and faceted samples of types 1 and 2 were found to contain irregularly shaped seeds of colorless beryl. In contrast, only a few synthetic emeralds of another type, designated type 3, were discovered. These lacked colorless seeds and had come from the collection of the late F.H Pough, who in turn had acquired the crystals from G.O. Wild. Existing documentation shows that Wild possessed a parcel of Nacken synthetic emeralds during the period after 1945 and donated various samples to friends and colleagues for research and related purposes.

In 1936, the German government decided to affiliate the private Institute for Gemstone Research, located in Idar-Oberstein and directed by G.O. Wild, with the University of Frankfurt. Nacken was named director of the joint entity, with Wild remaining the local leader for activities in Idar-Oberstein. A close collaboration between Wild and Nacken during 1936 and 1937 has long been apparent from known writings, but no direct information about the synthetic emeralds in Wild's possession has previously been available. Wild's son, K.E. Wild, had seen the parcel with Nacken synthetic emeralds in the 1950s and 1960s, while working in his father's office, but no further background about those samples was given to him at the time (K.E. Wild, pers. comms., 2016, 2017).

A new development, however, serves to unveil further details. A document authored by Nacken and dated May 30, 1937, was recently found in the historical archive of the city of Idar-Oberstein (Stadtarchiv Idar-Oberstein, Department 2b, File I B, No. 94). The four-page summary, written to the head of the local administration for the District of Birkenfeld, reports goals and tasks of the Institute for Gemstone Research. In the section covering scientific research, the following is written (translated from German): "Examination of properties related to crystal growth and synthesis of gemstones. These experiments already resulted in the production of synthetic emeralds."

From this short statement, it becomes apparent that growth of synthetic gem materials was one of the specific research topics undertaken or at least planned at the Institute. Equally logical then is the corollary that Wild, being the local representative in Idar-Oberstein, would have had access to the synthetic materials grown in relation to the Institute's research projects. Although no additional information is provided in Nacken's report, the timing would support a conclusion that at least some experiments related to the growth of synthetic emeralds were performed in the 1930s, with Nacken attempting to improve the technique by which he had successfully synthesized emeralds in the 1920s. Presumably, he would have tried to avoid larger colorless zones within the synthetic crystals, as such areas are easily observable, especially in faceted samples. Thus, taking into account all known circumstances, current evidence would seem to suggest that Nacken's type 3 flux-grown synthetic emeralds without colorless seeds were a result of experiments performed in the 1930s, subsequent to the growth of type 1 and type 2 synthetic emeralds with colorless seeds in the 1920s.

Karl Schmetzer
Petershausen, Germany